MOLECULAR PRINTBOARDS AS GENERAL PLATFORMS FOR PROTEIN IMMOBILIZATION

MOLECULAR PRINTBOARDS AS GENERAL PLATFORMS FOR PROTEIN IMMOBILIZATION

PROEFSCHRIFT

ter verkrijging van

de graad van doctor aan de Universiteit Twente,

op gezag van de rector magnificus,

prof. dr. W.H.M. Zijm,

volgens besluit van het College voor Promoties

in het openbaar te verdedigen

op vrijdag 21 september 2007 om 13.15 uur

door

Manon Julia Wilhelmina Ludden

geboren op 29 oktober 1977

te Oldenzaal

Dit proefschrift is goedgekeurd door:

Promotoren: prof. dr. ir. J. Huskens

prof. dr. ir. D. N. Reinhoudt

Voor mijn ouders en Vincent

Contents

Contents

1

General introduction

The immobilization of biomolecules to surfaces is a widely studied topic, and the applications thereof are numerous.[1,2] Antibody-immobilization, for instance, is crucial in medical diagnostic systems that are currently in use, such as immunoassays.[3] The immobilization of cells is also of huge importance from a medical diagnostic point of view for the diagnosis of several infectious diseases such as the detection of the human immunodeficiency virus.[4] Also in relatively simple medical diagnostic tests, such as in the determination of the glucose level of blood, protein immobilization is crucial.[5]

An important issue in the process of biomolecule immobilization is the functional attachment of biomolecules to surfaces.[6,7] Therefore, systems need to be developed in which nonspecific adsorption of biomolecules is inhibited and orientation can be controlled, in order to preserve (biomolecular) function. Immobilization through covalent interactions or physisorption is not attractive since the percentage of functional proteins present at the surface and the tunability of these systems are rather low.

Supramolecular chemistry has been applied for the immobilization of proteins to surfaces.[8-10] The advantage of supramolecular protein immobilization is the tunability: proteins can be reversibly attached to surfaces, and the position and orientation of the proteins can be controlled in this process.[11] In order to enhance binding affinities, multivalent supramolecular interactions may be employed. Multivalency is described as the simultaneous binding of multiple functionalities on one entity with multiple complementary functions on another entity.[12] Multivalency allows tuning the thermodynamic and kinetic properties of supramolecular systems. The combination of supramolecular chemistry and multivalency has been applied in the stable positioning of molecules at surfaces in a non-covalent manner.[13]

β-Cyclodextrin (βCD) is a well known host for various small hydrophobic organic molecules in aqueous environments.[14] βCD self-assembled monolayers (SAMs) are ordered and densely packed, and have been extensively characterized.[15,16] Binding constants of monovalent guest molecules to a single βCD cavity of these SAMs are comparable to binding constants of the respective molecules to βCD in solution.[14,16] All guest-binding sites in the βCD SAM are equivalent and independent, and the use of multivalent[17,18] host-guest interactions allows the formation of kinetically stable assemblies, and thus local complex formation e.g. by patterning, so that these surfaces can be viewed as "molecular printboards".[19,20]

The research described in this thesis is focused on the controlled attachment of proteins and cells to the molecular printboard in a supramolecular manner, through multivalent orthogonal linkers. The applied linkers consist of two parts, one side is designed in such a manner that interaction with the molecular printboard is possible, and the other side is designed for specific attachment to proteins.

Chapter 2 gives a literature review about the development of βCD molecular printboards. Also multivalent systems used to attach proteins or cells to surfaces are discussed.

In Chapter 3, the stepwise assembly of a noncovalent capsule, based on two calix[4]arenes, to the molecular printboard is described. This system employs βCD host-guest and electrostatic interactions between the capsule halves as the orthogonal interaction pairs. The possibility of stepwise assembly and breakdown of the capsule is also demonstrated.

In Chapter 4 the controlled attachment of streptavidin (SAv) to the molecular printboard is described. SAv is bound through mono- and divalent linkers. This allows the use of different assembly schemes, such as a stepwise assembly scheme, which opens the possibility for heterofunctionalization of SAv. Heterofunctionalization is shown with fluorescein-labeled biotin and with a functional protein, biotinylated cytochrome *c* (bt-cyt *c*). The surface concentration of bt-cyt *c* on the molecular printboard can be determined by UV/vis and scanning electrochemical microscopy, and is compared to theoretical values.

In Chapter 5 the heterofunctionalization of SAv is applied to construct (complex) bionanostructures at the molecular printboard. These bionanostructures consist of antibody complexes (or parts thereof) immobilized by multiple orthogonal binding

motifs. The specificity of the build-up of these structures is addressed in patterning studies. The application of the molecular printboard is discussed in the realm of the selective attachment of cells to antibodies present at the molecular printboard, and the immobilization of proteins on βCD SAMs in microchannels.

Chapter 6 presents a supramolecular manner for the prevention of nonspecific adsorption of proteins to the molecular printboard. A monovalent blocking agent is developed which consist of a hexa(ethylene glycol) chain to prevent nonspecific adsorption and an adamantyl functionality for specific interaction to the molecular printboard. This method is shown to be well suited for the prevention of nonspecific interactions of a range of proteins to the molecular printboard. The method still allows the specific attachment of proteins through orthogonal linkers in a multivalent fashion to the molecular printboard, as is shown for SAv, the mono-his-tagged maltose binding protein (His$_6$-MBP) and bovine serum albumin (BSA). The effectiveness of various coverages of the blocking agent is compared to the more traditional poly(ethylene glycol) (PEG) SAMs.

Chapter 7 shows the application of the concept developed in Chapter 6, for the prevention of nonspecific protein adsorption to the molecular printboard for the attachment of histidine-tagged proteins to surfaces. Titration experiments, and the modeling thereof, of His$_6$-MBP with the molecular printboard is discussed. The possibility of surface patterning is demonstrated by patterning studies with the fluorescent DsRed modified with four histidine tags. For the α-His-tagged 20S proteasome, the possibility of specific immobilization is discussed.

1.1   References

1. F. E. Ahmed, *Curr. Genomics* **2006**, *7*, 399-426.
2. H. C. Ma, K. Y. Horiuchi, *Drug Discov. Today* **2006**, *11*, 661-668.
3. A. Barraud, H. Perrot, V. Billard, C. Martelet, J. Therasse, *Biosens. Bioact.* **1993**, *8*, 39-48.
4. L. J. Wysocki, V. L. Sato, *Proc. Natl. Acad. Sci. USA* **1978**, *75*, 2844-2848.
5. F. Ahmad, A. Christenson, M. Bainbridge, A. P. M. Yusof, S. Ab Ghandi, *Biosens. Bioelectron.* **2007**, *22*, 1625-1632.
6. K. Tomizaki, K. Usui, H. Mihara, *ChemBioChem* **2005**, *6*, 782-799.

7.   M. Ueda, A. Tanaka, *Biotech. Adv.* **2000**, *18*, 121-140.

8.   A. Fragoso, J. Caballero, E. Almirall, R. Villalonga, R. Caro, *Langmuir* **2002**, *41*, 4467-4471.

9.   G. Y. Liu, N. A. Amro, *Proc. Natl. Acad. Sci. USA* **2002**, *99*, 5165-5170.

10.   S. A. Miscoria, J. Desbrieres, G. D. Barra, P. Labbé, *Anal. Chim. Acta* **2006**, *578*, 137-144.

11.   S. Gilead, E. Gazit, *Supramol. Chem.* **2005**, *17*, 87-92.

12.   M. Mammen, S.-K. Choi, G. M. Whitesides, *Angew. Chem. Int. Ed.* **1998**, *37*, 2754-2794.

13.   O. Crespo-Biel, B. Dordi, D. N. Reinhoudt, J. Huskens, *J. Am. Chem. Soc.* **2005**, *127*, 7594-7600.

14.   M. V. Rekharsky, Y. Inoue, *Chem. Rev.* **1998**, *98*, 1880-1901.

15.   M. W. J. Beulen, J. Bügler, B. Lammerink, F. A. J. Geurts, E. M. E. F. Biemond, K. G. C. van Leerdam, F. C. J. M. van Veggel, J. F. J. Engbersen, D. N. Reinhoudt, *Langmuir* **1998**, *14*, 6424-6429.

16.   M. W. J. Beulen, J. Bügler, M. R. de Jong, B. Lammerink, J. Huskens, H. Schönherr, G. J. Vancso, B. A. Boukamp, H. Wieder, A. Offenhäuser, W. Knoll, F. C. J. M. van Veggel, D. N. Reinhoudt, *Chem. Eur. J.* **2000**, *6*, 1176-1183.

17.   J. Huskens, A. Mulder, T. Auletta, C. A. Nijhuis, M. J. W. Ludden, D. N. Reinhoudt, *J. Am. Chem. Soc.* **2004**, *126*, 6784-6797.

18.   A. Mulder, T. Auletta, A. Sartori, S. Del Ciotto, A. Casnati, R. Ungaro, J. Huskens, D. N. Reinhoudt, *J. Am. Chem. Soc.* **2004**, *126*, 6627-6636.

19.   J. Huskens, M. A. Deij, D. N. Reinhoudt, *Angew. Chem. Int. Ed.* **2002**, *41*, 4467-4471.

20.   T. Auletta, B. Dordi, A. Mulder, A. Sartori, S. Onclin, C. M. Bruinink, M. Péter, C. A. Nijhuis, H. Beijleveld, H. Schönherr, G. J. Vancso, A. Casnati, R. Ungaro, B. J. Ravoo, J. Huskens, D. N. Reinhoudt, *Angew. Chem. Int. Ed.* **2004**, *43*, 369-373.

2

Molecular printboards: versatile platforms for the creation and positioning of supramolecular assemblies and materials*

In this chapter the development of molecular printboards, which are tailor-made surfaces functionalized with receptor (host) molecules, is described. Such substrates can be used for the binding of complementary ligand (guest) molecules through multivalent interactions. Supramolecular multivalent interactions are ideal to attain a quantitative and fundamental understanding of multivalency at interfaces. Because of their quantitative interpretation, the focus is on the following two multivalent systems: (i) the interaction of β-cyclodextrin host surfaces with multivalent hydrophobic guest molecules, and (ii) the vancomycin-oligopeptide system. Furthermore, systems that allow orthogonal attachment of proteins and cells to surfaces are discussed; more specifically, streptavidin monolayers for the immobilization of biotinylated proteins and NiNTA receptor surfaces for the multivalent binding of histidine-tagged proteins. In the last sections patterning of proteins and cell attachment to surfaces is discussed.

2.1   Introduction

The benefits of nanotechnology arise from the new material properties that emerge when matter is structured at the nanometer (nm) scale. Whereas some properties already become apparent when inspected with a bulk technique, as for example the optical properties of nanoparticles in a solution,[1,2] more sophisticated science, and therefore applications, are involved when use is made of the properties of individual nanostructures,[3] and/or when information processing occurs between nanostructures.[4] In the former case, for example for the biomedical use of nanoparticles,[5] the outer surface of the nanostructure needs to be equipped with specific functional groups which allow the formation of desired interactions. In the latter case, for example in molecular electronics, surface attachment and positioning are of paramount importance in order to predetermine how and in which directions the information processing can take place.[6,7]

Thus in all cases, the interface chemistry of the nanostructures and/or the substrates onto which they are placed is the key to the functioning of the individual nanostructures or of the devices that are composed of them. Fine tuning of the specificity and strength of the interactions that occur at this interface between the nanostructure and its environment are of utmost importance. Usually, when designing a functional nanosystem, the perspective is from the nanostructure and its properties, and the interface is changed *ad hoc* to go as easily and quickly as possible to the functional device structure. Conceptually, however, it is attractive to decouple the interface design from the nanostructure fabrication in order to have the best engineering control over the interface properties. This implies the development of generally applicable interface chemistries for the fine-tuning of assembly and interaction properties of the nanostructures.

Regarding the concept of controlled positioning of molecules, assemblies and particles on substrates, binding stoichiometry, binding strength, binding dynamics, packing density and order, and reversibility emerge as important tuning parameters. Covalent immobilization does not offer sufficient flexibility over most of these criteria. Physisorption or chemisorption do offer reversibility and error correction and therefore the potential of dense packing with high order, but the predictability of binding stoichiometry and thermodynamic binding parameters is small and thus the practical control is limited. Supramolecular interactions, for example of designed

host-guest or receptor-ligand types, constitute a solution to the control of these parameters.

Self-assembled monolayers offer an easy way to the immobilization of receptors and ligands for such receptors. The fixation to a substrate automatically leads to a multivalent display of such supramolecular interaction sites, the density of which is a separate control parameter in the binding of (multivalent) complementary binding partners. Multivalency,[8,9] which describes the interaction between multiple interacting sites on one entity with multiple interacting sites on another, is therefore the underlying principle governing the stabilities and dynamics of such systems and offers the main way to control the binding properties of any entity binding to a substrate, i.e. through systematic variation and optimization of the number of interacting sites, the intrinsic binding strength of an individual interacting pair, and the geometry of the multivalent building blocks.

Apart from the nanotechnological implications described and reviewed here, multivalency has a profound impact on biology.[8,10] Contacts between cells and viruses or bacteria are initiated by multivalent protein-carbohydrate interactions.[11-17] Whereas their monovalent parent interactions are fairly weak, the combined multivalent display at such biological interfaces makes the interactions strong, so that true recognition occurs which for example is the onset of, for example, endocytosis. Qualitatively this pathway is quite well understood, but quantitative details often lack for such systems. The supramolecular interface systems reviewed here can thus be seen as model systems for biological interfaces and their study can lead to a more quantitative understanding of multivalent binding at their biologically more relevant sister systems in the biochemical field.

In this chapter, systems that display multivalent interactions at interfaces are covered. Apart from the cyclodextrin[18]-based host-guest chemistry at interfaces and in aqueous solutions between substrates, the vancomycin-oligopeptide and the NiNTA-His-tag systems, reported by the Whitesides and Tampé groups, respectively, the oriented attachment of streptavidin to surfaces, patterning of proteins at surfaces, and the attachment of cells to surfaces are covered. Although the concept of multivalency at interfaces is introduced via the more well-spread multivalency in solution, here only examples are given which have direct analogs with existing surface systems, in part also because such multivalent solution systems have been reviewed before.[2,8,19] After explaining how a quantitative interpretation of multivalent systems at interfaces can

be obtained, which is the key to the control over the binding properties of designed supramolecular adsorbing entities, the more practical nanotechnological implications for positioning and materials assembly are discussed, as well as some biotechnological implications.

2.2 Multivalency

Multivalency describes the multivalent interactions that occur between a multivalent host and a multivalent guest.[8-10,19] The most simple situation occurs when a divalent guest and a divalent host interact to form a divalent 1:1 complex. Multivalent systems are characterized by (an) intra-complex (further simply called intramolecular) assembly step(s) following an initial, intermolecular binding event. This makes such systems distinctly different, both thermodynamically and kinetically, from monovalent (between two monovalent entities) and multiply monovalent (between a multivalent and multiple monovalent entities) systems which lack such intramolecular steps (Figure 2.1).
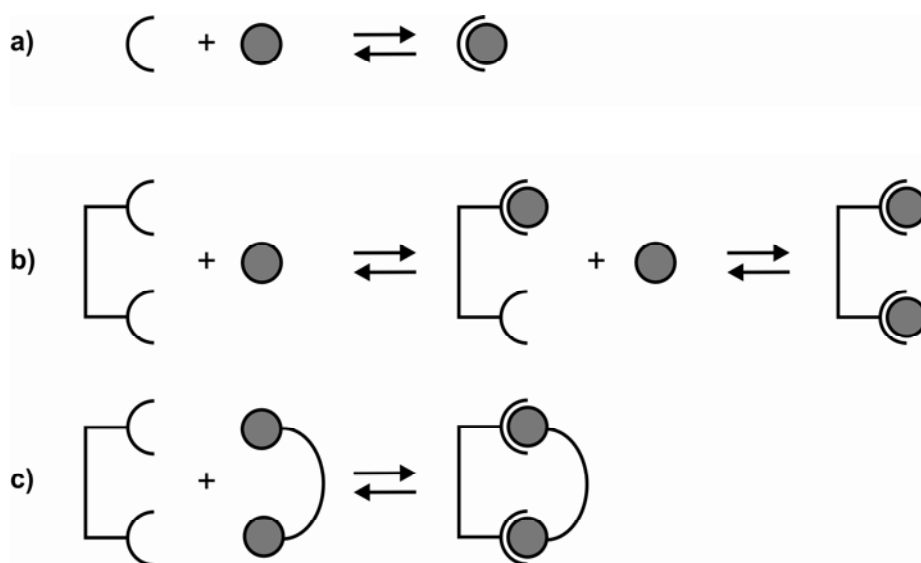

Figure 2.1 Schematic modes of binding for monovalent (a), multiple monovalent (b), and multivalent interactions (c).

2.2.1 Multivalency in solution

A quantitative comparison between the inter- and intramolecular binding events in a multivalent interaction can be accomplished most clearly by adopting the effective

concentration (C_{eff}) or effective molarity terminology (*EM*).[9] Effective concentration represents a probability of interaction between two complementary, interlinked entities and symbolizes a "physically real" concentration of one of the interacting functionalities as experienced by its complementary counterpart. The concept of effective concentration originates from the field of polymer chemistry where it was introduced to account for intramolecular cyclization reactions in polymer synthesis.[20,21] Effective concentration is conceptually similar to the more generally used effective molarity.[22] Whereas effective concentration is based on concentrations calculated or estimated from physical geometries of complexes, effective molarity denotes the ratio of intra- and intermolecular rate or association constants.[22]

It has been argued before[9,23,24] that, although effective concentration and effective molarity are conceptually very closely related, it can be beneficial to keep the two terms separated in the analysis of quantitative thermodynamic data for multivalent systems. When effective molarity is used as an empirical quantity relating the overall stability constant of the multivalent system to the one of the monovalent parent system, the effective concentration is then the theoretical prediction, e.g. from molecular modeling incorporating linker lengths, flexibilities, etc., of that quantity, and thus provides a theoretical estimate of what *EM* should be when only statistical, entropic, and multivalency factors are taken into account. Therefore, the comparison between the two provides a handle to evaluate whether additional, cooperative effects occur: when $EM = C_{eff}$, the data can be explained by assuming independent, non-cooperative interactions only, while when it is observed that $EM \neq C_{eff}$, this may indicate the existence of positively ($EM > C_{eff}$) or negatively ($EM < C_{eff}$) cooperative effects. Note that cooperativity implies a change of interaction strength upon occupation of a neighboring binding site. Cooperativity effects or the lack thereof are otherwise notoriously difficult to ascertain quantitatively in multivalent systems compared to multiply monovalent systems for the latter of which tools such as Scatchard and Hill plots have been very useful. It has been shown that such tools fail to work for multivalent systems,[25] because of the occurrence of intramolecular binding events, as noted above. Many quantitatively investigated solution systems have been described, but only in rare cases an attempt is made to dissect possible multivalency and cooperativity effects. An analysis as described above has been made to describe the thermodynamics of binding of the divalent complex between a bis-adamantyl calix[4]arene guest and a bis-cyclodextrin host (Figure 2.2).[23] The

comparison between the overall 1:1 binding constant of this divalent complex and the intrinsic monovalent binding constant yielded an *EM* of approx. 3 mM, while a C_{eff} of (minimally) 2 mM was estimated from the linker lengths of the guest and host in the monovalently linked intermediate. This excellent agreement, together with the fact that the binding enthalpy of the divalent complex was twice the value for the monovalent complex, led to the conclusion that this divalent system could be well described with multivalency effects only, thus without cooperativity. A similar reasoning has been found to hold for other solution systems as well.[9]
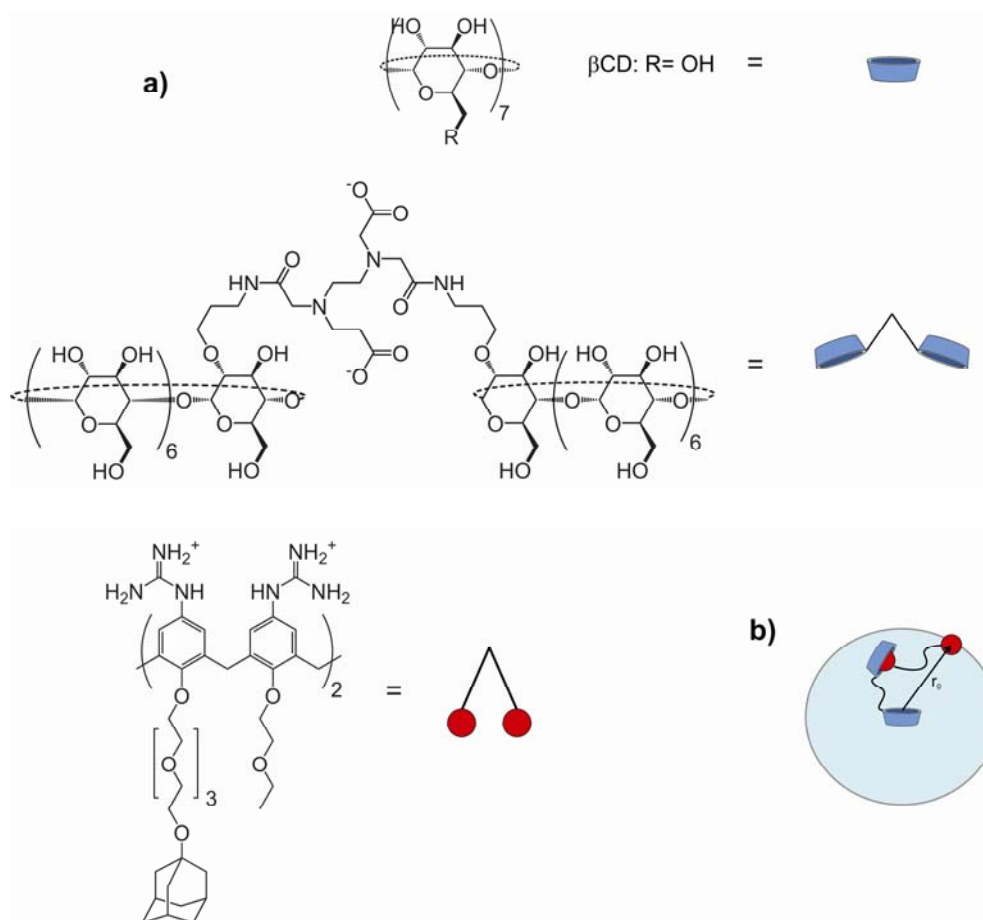
Figure 2.2 *Host and guest molecules: β-cyclodextrin (βCD), an EDTA-linked βCD dimer, and a bis(adamantyl)-calix[4]arene[23] (a); Schematic representation of the concept of effective concentration (C_{eff}) for the interaction between the EDTA-linked βCD dimer, and the bis(adamantyl)-calix[4]arene in solution (b).[23,24]*

The interaction between vancomycin and D-alanine-D-alanine (D-Ala-D-Ala) and D-alanine-D-lactate (D-Ala-D-Lac) and multivalent derivatives thereof has been

thoroughly studied by Whitesides and coworkers.[26-32] Vancomycin (Figure 2.3) is an important member of the group of glycopeptide antibiotics that are active against gram-positive bacteria. The D-Ala-D-Ala motif represents the carboxy-terminus of gram-positive bacteria that are susceptible to vancomycin, whereas the D-Ala-D-Lac motif represents the carboxy-terminus of gram-positive bacteria that are resistant to vancomycin. Solution studies revealed that the interaction between Van and D-Ala-D-Lac is much weaker than the interaction between vancomycin and D-Ala-D-Ala, due to the absence of one hydrogen bond. It was also shown that a dimeric derivative of Van, Van-R_d-Van (R_d = NHCH$_2$C$_6$H$_4$CH$_2$NH; Figure 2.3), binds stronger to a divalent D-Ala-D-Lac derivative by means of multivalency.
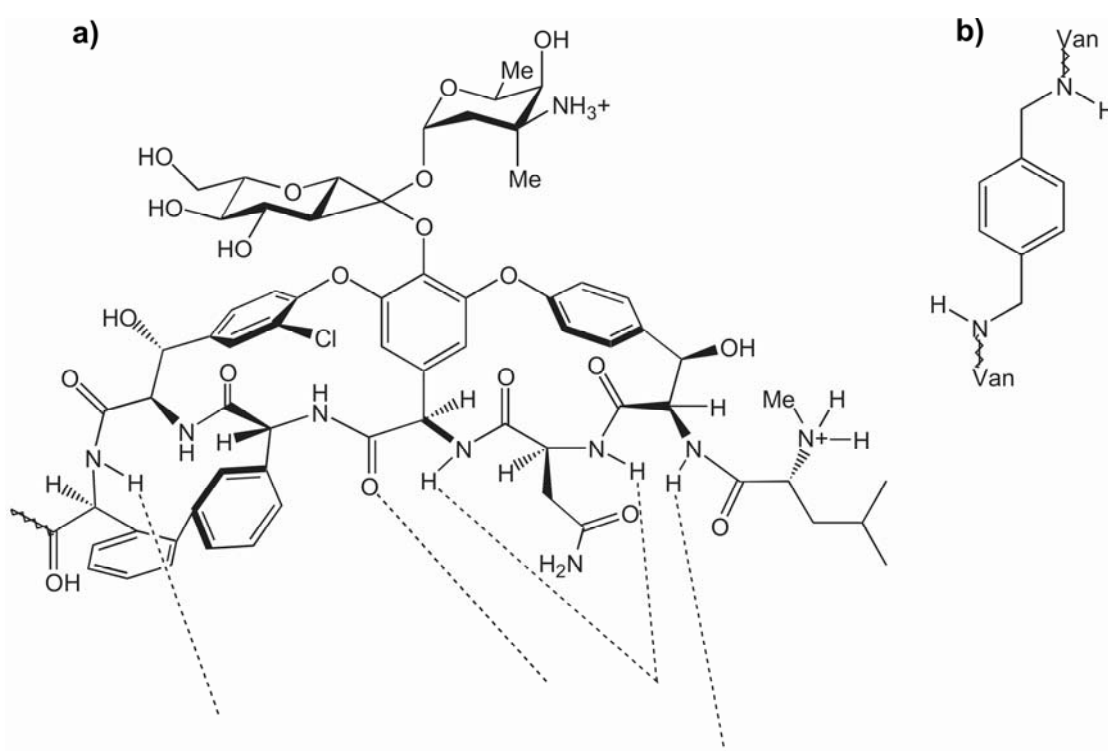
Figure 2.3 *Structures of vancomycin (a) and dimeric vancomycin (b). Dotted lines indicate hydrogen bonds involved in ligand interactions.*

2.2.2   Multivalency at interfaces

Several years ago, self-assembled monolayers[33] (SAMs) of a β-cyclodextrin (βCD) heptathioether derivative on gold (Figure 2.4) were reported,[34,35] at that stage a logical extension of the ongoing efforts to immobilize various receptors on surfaces, e.g. for sensor development. These βCD SAMs have been extensively characterized with a plethora of analytical techniques. The main conclusions were that: (i) the molecules formed a monolayer with the secondary sides of the βCD ring exposed to the solution,

(ii) they were densely packed in the alkyl regions of the adsorbate, and (iii) the SAMs were comparatively well-ordered, leading to a βCD cavity lattice periodicity of approximately 2 nm, which was confirmed by atomic force microscopy (AFM).[34]
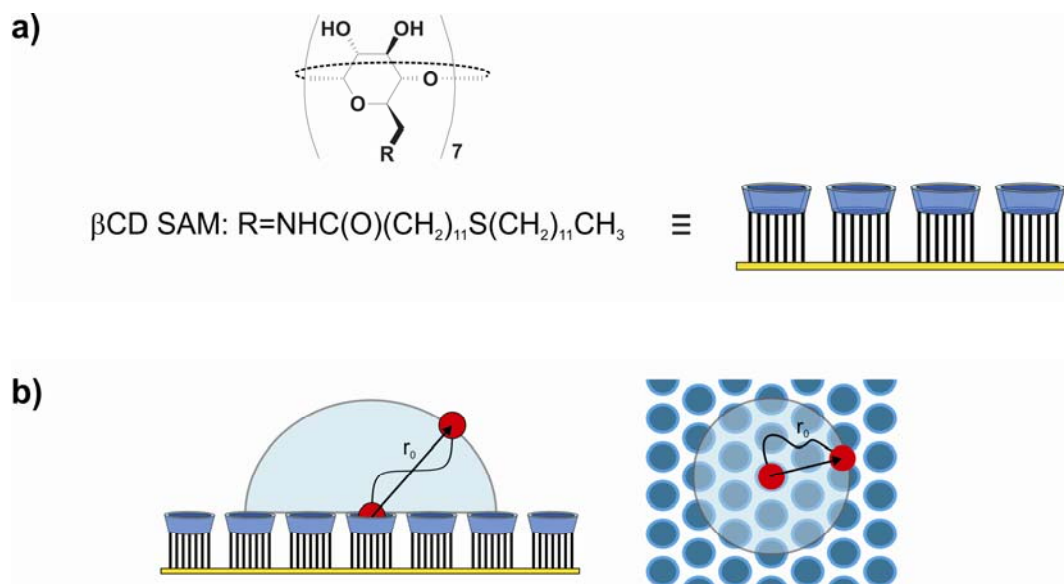
Figure 2.4 *(a) βCD SAM on gold;[34] (b) Schematic representation of the concept of effective concentration for the interaction between the bis(adamantyl)-calix[4]arene (Figure 2.2) and the βCD SAM.[23,24]*

Initial host-guest studies, performed with small monovalent guests, showed that the molecular recognition properties of the βCD cavities were unaltered by the surface immobilization as was exemplified by (i) the identical stability constants obtained for these guests in binding to the βCD SAMs and to native βCD in solution,[36] and (ii) AFM pull-off experiments with a variety of guests immobilized on an AFM tip.[37-39] The association and dissociation rates were fast on the experimental timescales, as was to be expected for such monovalent systems, providing rapid reversibility to the system, which was thought to be beneficial when sensor systems were envisaged.

Only for larger steroidal guests, an influence of the alkyl portion of the βCD adsorbate was observed,[36] most likely due to the fact that, in case of binding to native βCD, such guests normally protrude from the cavity at both sides of the βCD molecules. In the same study[36] a different SAM architecture consisting of a monothiol βCD derivative was applied, and indications for binding of (the same steroidal) guests by two immobilized βCD cavities simultaneously were observed for the first time.

A paradigm shift of the view of these βCD SAMs occurred upon the initial work[40] using adamantyl-functionalized poly(propylene imine) (PPI) dendrimers[41] (Figure 2.5). With increasing dendrimer generation, and thus with increasing number of adamantyl-βCD SAM interactions, slower dissociation kinetics were observed, indicating a shift from reversible to irreversible binding. For the larger dendrimer generations, even individual dendrimer molecules could be visualized using AFM showing that they were attached strongly enough to withstand the forces exerted by the AFM tip. At that moment it became apparent that such receptor-functionalized surfaces, rather than being rapidly interchanging sensor substrates, could be used as assembly platforms for larger entities with considerable complexation lifetimes. Hence, they were coined the term "molecular printboards".[40]
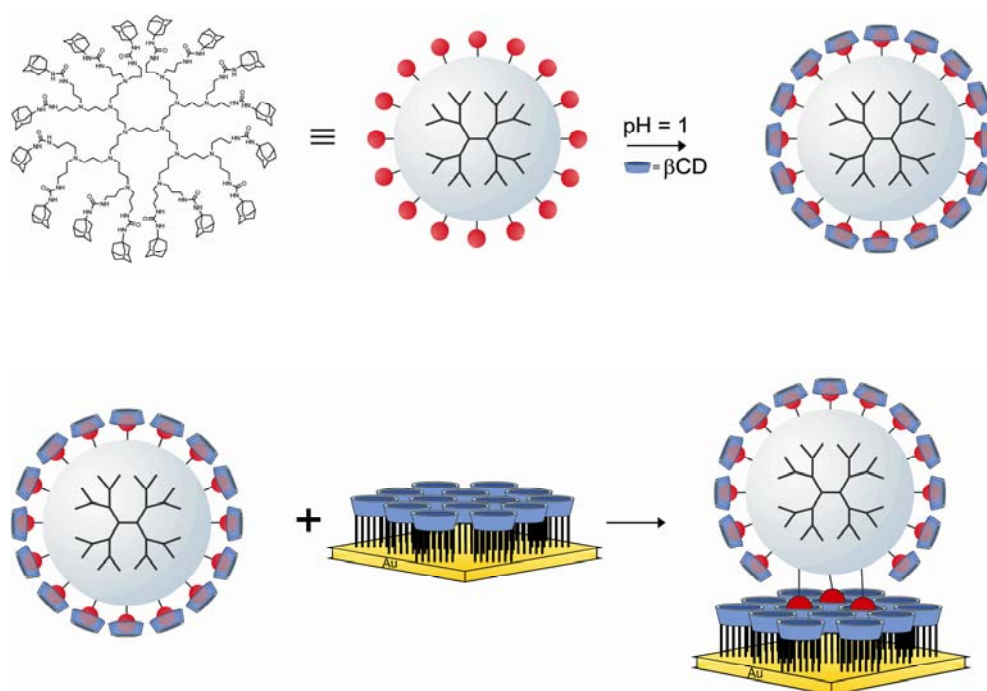
Figure 2.5 *Generation-3 adamantyl-functionalized poly(propylene imine) dendrimer and the formation of water-soluble assemblies by βCD complexation (top), and the adsorption of these assemblies onto a βCD SAM on gold (bottom).*[40]

It will become clear that the ultimate key to the control over binding thermodynamics and kinetics and even to stimulus-dependent control arises from multivalency. By tuning the type of monovalent interaction, the number of such interactions, and the epitope density and their geometry on both multivalent guest and host platforms, one can vary the association and dissociation rates practically at will so that the whole

range from labile to stable complexes can be accessed. The number of interactions needed to obtain kinetically stable assemblies can be rather low, even for interaction motifs with moderately weak intrinsic interaction strengths.

The divalent calix[4]arene guest described above (Figure 2.2) in the solution systems was also studied regarding its binding to the molecular printboard.[23] A clear distinction with the solution system was the fact that the overall binding constant at the molecular printboard was 2-3 orders of magnitude larger than in solution. This effect was, however, again fully attributable to multivalency: the stability constant increase (from about 10^7 M^{-1} for binding to the βCD dimer, shown in Figure 2.2, to $10^9 - 10^{10}$ M^{-1} for binding to the molecular printboard) was fully due to a higher C_{eff} (of approx. 0.2 M) at the molecular printboard because in the (smaller) probing volume, compared to solution, resided a larger number of accessible host molecules (Figure 2.4b).

The interaction between vancomycin and D-Ala-D-Ala and D-Ala-D-Lac has also been studied at surfaces. Whitesides and coworkers developed mixed SAMs on gold that consist of adsorbates with N^{α}-Ac-L-Lys-D-Ala-D-Ala (L*) and carboxylic acid groups, the mole fractions of which were both about 0.5.[29,42] To these monolayers, the adsorption of vancomycin was compared to the adsorption of a divalent vancomycin derivative (Figure 2.3) using surface plasmon resonance (SPR) spectroscopy.[43-45] These SPR experiments indicated that the binding of vancomycin to L* at a SAM was comparable to binding in solution, a similar conclusion observed above for small guests binding to the molecular printboard. It was also established that binding of the divalent vancomycin derivative to the SAM was much stronger than the binding of the monomeric vancomycin derivative, and that the interaction was biospecific.

Similar mixed SAMs on gold, consisting of adsorbates with N^{α}-Ac-L-Lys-D-Ala-D-Lac (L*^{2}) and with carboxylic acid groups, were prepared in order to mimic the surfaces of cells that are resistant to vancomycin. The affinity of vancomycin for such SAMs was 300-fold less than for SAMs consisting of L*. The divalent vancomycin derivative, however, interacted much stronger with these surfaces; the dissociation rate was about 100 times slower than that of vancomycin. This supports the hypothesis that multivalency contributes to the antibacterial activity against vancomycin-resistant bacteria.[29,46]

The examples discussed above all describe the binding of multivalent guests for which the binding stoichiometries followed logically from their structure and were thus predictable. In contrast, although a qualitative shift from kinetically labile to stable interactions had been observed,[40] the dendrimeric guest systems proved harder to study since their binding stoichiometry to the molecular printboard could only be estimated from basic molecular modeling. The key to a quantitative understanding of the multivalent dendrimer systems came from the use of the electroactive ferrocenyl-functionalized PPI dendrimers (Figure 2.6) which provided an independent experimental measure of the numbers of interactions.[47,48] On the one hand, the overall binding constants determined by SPR, of the still thermodynamically reversible dendrimer generations 1-3 could be evaluated in terms of multivalency. A model for describing the multivalency effects in a quantitative fashion for the binding of such highly multivalent molecules at the βCD interfaces was developed incorporating the effective concentration concept as well as possible competition with monovalent hosts or guests in solution.[24] All dendrimer data led as well to the conclusion that all binding enhancement stemmed solely from the multivalency effect.
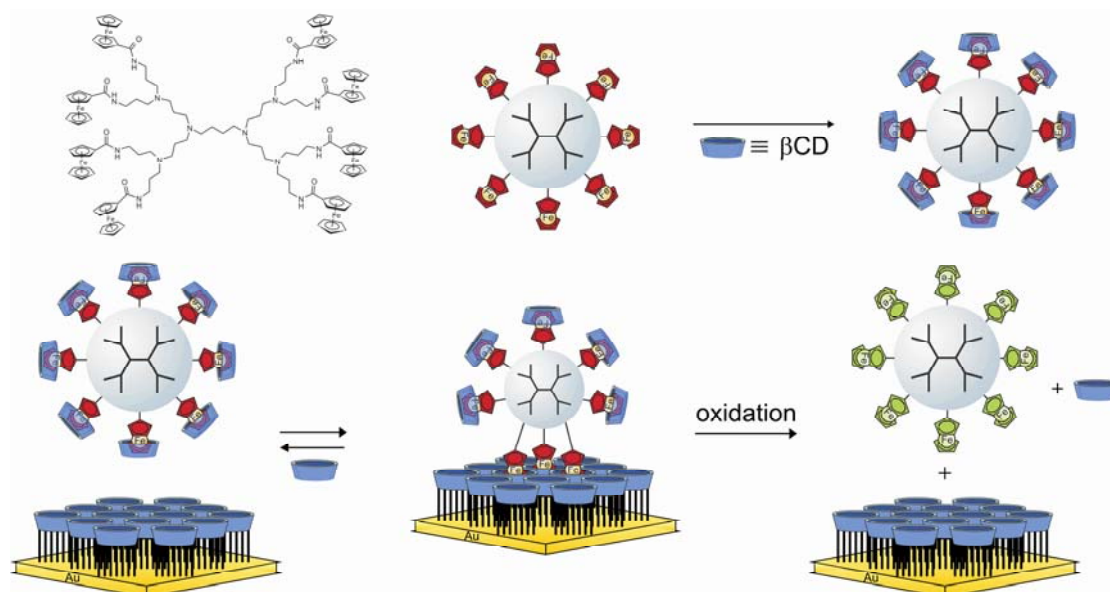
Figure 2.6 *Generation-2 ferrocenyl-functionalized PPI dendrimer and its formation of water soluble assemblies with βCD (top); the adsorption of the dendrimer-βCD assembly at the molecular printboard and the electrochemically induced desorption from the molecular printboard (bottom).*[47,48]

On the other hand, the surface coverages of electroactive ferrocenyl groups, after assembly of a full monolayer of these dendrimers on a βCD SAM (Figure 2.6), as determined by cyclic voltammetry, were compared to the known surface coverage of the βCD host molecules. This provided ratios of bound *vs.* unbound ferrocenyl groups, and thus in a direct fashion the binding stoichiometries (Figure 2.7).[47] This electrochemical stoichiometry determination method also worked for the higher generations 4 and 5, which showed too slow dissociation rates to allow stability constant determinations by SPR. Straightforward extension of the thermodynamic model nevertheless provides reliable *K* value predictions for such systems as well.

$\Gamma_{Fc}/\Gamma_{\beta CD} = 4$ $\Gamma_{Fc}/\Gamma_{\beta CD} = 2$ $\Gamma_{Fc}/\Gamma_{\beta CD} = 1.33$ $\Gamma_{Fc}/\Gamma_{\beta CD} = 1$
$P_b = 1$ $P_b = 2$ $P_b = 3$ $P_b = 4$
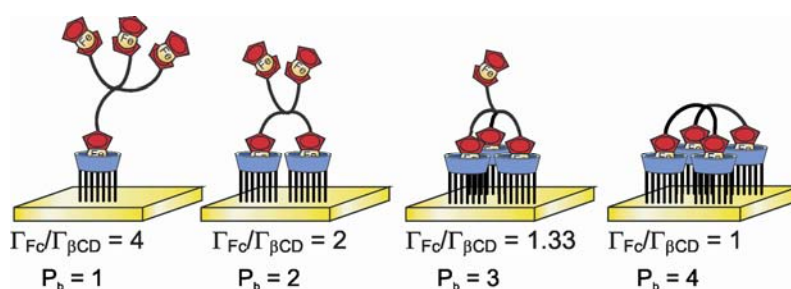
Figure 2.7 *Schematic representation of the four possible binding modes of the generation-1 ferrocenyl dendrimer to the molecular printboard with the number of bound sites, p_b, and the predicted coverage ratios, $\Gamma_{\beta CD}/\Gamma_{Fc}$, depicted below.[47]*

Comparison of the experimentally observed binding stoichiometries for these dendrimers to molecular models revealed a straightforward geometric rule for the binding stoichiometry. As long as a dendritic branch can stretch without violating common bond lengths and angles to reach a neighboring free βCD binding site at the molecular printboard it will bind, thus contributing to the overall stoichiometry. This was confirmed by modifying the dendrimer skeleton and the spacer length between the dendrimer amino-endgroups of the parent dendrimers and the ferrocenyl groups attached to them.[48] These modifications led to different binding stoichiometries but always followed this geometric rule. Since replacing the ferrocenyl groups by adamantyl moeities does not change the geometry of the dendrimers significantly, the stoichiometry data for the ferrocenyl dendrimers could be directly applied to the adamantyl dendrimers, thus allowing thermodynamic data for the latter to be interpreted quantitatively as well.

In conclusion, careful extension of the multivalency of the model guest systems, together with the well-defined properties of the molecular printboard, allowed the obtainment of quantitative thermodynamic data and interpretations for multivalent binding events occurring at these interfaces. The data and the model lead to the following conclusions:[24] (i) binding events at these molecular printboards are commonly explained by multivalency only, without the need for assuming cooperativity, and (ii) crude molecular models (e.g. CPK) suffice to estimate whether an unused binding site of the guest can reach a neighboring free host site and thus provide easy estimates of the (maximal) binding stoichiometry even when these are not experimentally accessible. The mathemathical model also provides a clearcut way to estimate dissociation rate constants,[24] although experimental dissociation measurements are bound to be convoluted with mass transport limitation effects.

2.3   Stable positioning and directed assembly at molecular printboards: towards supramolecular materials and devices

Although perhaps unexpected initially, weak supramolecular interactions, when used in a multivalent fashion can provide thermodynamically and kinetically stable assemblies, both in solution and at interfaces. This stability may be put to use by noting that it implies that: (i) when the assembly occurs at an interface, the complex remains at the position where it was originally formed, (ii) directed assembly can therefore be applied to obtain patterns of such supramolecular complexes, and (iii) additional building blocks with other or identical binding motifs can be employed in subsequent assembly steps to extend the supramolecular structure, thus leading to supramolecular materials. Paragraph 2.3.1 deals with the stable assembly and stimulus-dependent reversal of various types of multivalent supramolecular entities, from small molecules to polymers, onto the molecular printboards, and basic motifs for extending the assemblies to larger systems, while the truly materials systems, including nanoparticle assembly, are covered in paragraph 2.3.2.

2.3.1   Patterning at printboards

The earlier work on adamantyl dendrimers had already shown the imaging and thus strong binding of individual dendrimer molecules at the molecular printboard. Nevertheless, these individual dendrimer molecules were arranged in an unordered

fashion, randomly spread over the substrate.[40] Directed assembly was achieved with the divalent calix[4]arene guest molecule (Figure 2.2) using microcontact printing (μCP) to obtain micrometer-sized patterns of these molecules on the molecular printboard.[49] The guest molecules were found exclusively in the areas of preceding contact between the microcontact printing stamp and the substrate, even after extensive rinsing with water or salt solutions. Only rinsing with 10 mM βCD, in order to induce competition for binding the adamantyl guest sites, led to appreciable, i.e. noticeable by AFM, desorption. Comparison with patterns printed onto OH-functionalized SAMs showed that the assembly on the molecular printboard was governed by specific, multivalent host-guest interactions. Very similar results were obtained using the adamantyl-functionalized PPI dendrimers.[50]

In order to allow the visualization of fluorescent molecules, βCD SAMs on silicon oxide and glass were developed.[51] Although the monolayer formation in this case constitutes a three- or four-step covalent procedure, these SAMs showed a βCD coverage and guest binding characteristics that were fully comparable to the βCD SAMs on gold. Several divalently binding fluorescent guests, consisting of a fluorescent moiety and two adamantyl functionalized ethyleneglycol chains fixed to a synthetic core, were applied to these SAMs, and similar binding behavior and specificity were observed as for the calix[4]arene guest on the βCD SAMs on gold.[52] For one of these dye molecules, a fluorescent titration curve was obtained, from which a stability constant was derived that was fully in line with data obtained for the gold substrates.[51] The application of two dyes, one in a printing step and the second one in a subsequent solution assembly step, showed that alternating patterns of dyes could be obtained.[52] The second dye was found almost exclusively in the areas left vacant after the preceding printing step, which showed that the first dye was bound in a stable fashion and that exchange of dyes in the subsequent solution assembly step did not occur to a noticeable extent. More high-resolution patterning, down to line widths of approx. 200 nm, was achieved by dip-pen nanolithography, using the calix[4]arene, an adamantyl dendrimer, and the fluorescent dye guest molecules as the ink.

One of the divalent fluorescent guest molecules was also used in the binding to cyclodextrin vesicles of about 100 nm.[53] Binding constants found were similar to values obtained for flat βCD SAMs. Vesicles consisting of both α- and β-cyclodextrin of varying ratios were employed to test the hypothesis of receptor clustering in these

mobile layered architectures.[54] Indeed, binding of the divalent dyes showed that binding to vesicles with a fraction of βCD always yielded significantly higher binding constants than expected when assuming random mixing of these receptors. Whether this clustering stems from demixing of the receptor molecules in the vesicles before guest binding or from active clustering upon guest binding is an unsolved issue.

Patterning the adamantyl dendrimers on the molecular printboard on silicon oxide provided one of the first cases of the use of two orthogonal interaction motifs for the formation of more complex architectures.[55] Whereas the affinity of the positively charged dendritic cores for negatively charged fluorescent dye molecules was already proven in solution following the "dendrimer molecular box" paradigm developed by Meijer,[41] the application of a solution of a negatively charged fluorescent dye to a substrate patterned by µCP with the adamantyl dendrimers led to localization of the dyes in the dendrimer-printed areas only.[55] This two-step procedure therefore succumbed to an architecture where the dendrimers were bound by multivalent host-guest interactions whereas the dyes were immobilized inside the dendrimer cores by electrostatic interactions. An even more complicated architecture was developed by printing lines of dendrimers in one direction, subsequently printing one dye in an orthogonal direction, and finally assembling a second dye from solution (Figure 2.8). This yielded a dicolored block pattern, again showing good selectivity and directionality even for these electrostatically bound dyes.[55]
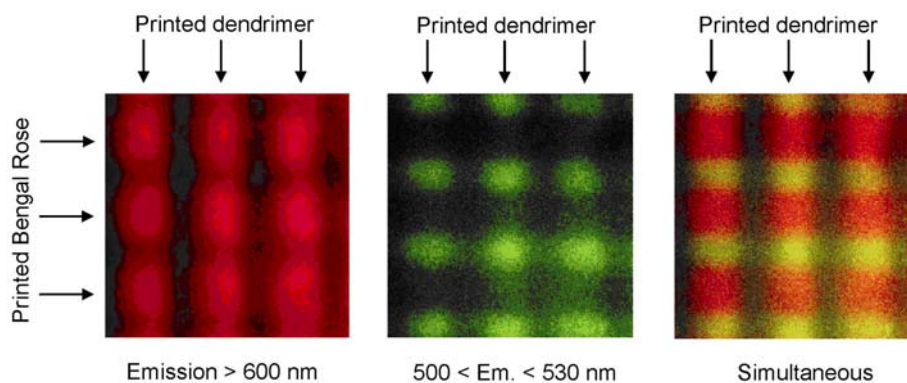
Figure 2.8 *Confocal microscopy images (50×50 μm²) after μCP of the generation-5 adamantyl dendrimer on the molecular printboard on glass, followed by cross printing of Bengal Rose, and subsequent filling with fluorescein.[55] The substrate was simultaneously excited at 488 nm and 543 nm and images were recorded by measuring the emission above 600 nm (left), between 500 and 530 nm (center). The image on the right shows the overlay image.*

In the study discussed above, the binding of adamantyl derivatives to the molecular printboard can only be reversed by competition with a host in solution.[49] This becomes progressively more difficult with increasing numbers of interactions of the multivalent complexes, as was for example indicated by SPR titrations of the adamantyl-terminated dendrimers. Totally irreversible adsorption was also observed for polymers functionalized with *t*-butylphenyl or adamantyl groups.[56] SPR and AFM showed that such polymers showed strong adsorption and a very efficient use of all or most endgroups. This behavior led to a drastic change of conformation of the polymers from an on average spherical shape in solution to a completely flattened thin layer of less than 1 nm when adsorbed on the molecular printboard. This adsorption proved completely irreversible by competition with monovalent guests or hosts from solution which was to be expected from the strong multivalency effect for such highly multivalent systems.

Bifunctional polymers consisting of vancomycin and fluorescein were prepared by Whitesides *et al.*, and adsorbed to SAMs consisting of D-Ala-D-Ala and tri(ethylene glycol) (TEG) groups (Figure 2.9).[57] SPR studies revealed that the adsorbed polymer desorbed only very slowly from the surface (k_{off} = 10^{-6} s^{-1}). When soluble ligand was added, however, the dissociation constant increased by a factor of about 50. This very

strong interaction to the surface was attributed to multivalent interactions between the multiple vancomycin groups at the polymer and multiple D-Ala-D-Ala groups present on the SAM. The fluorescein groups present at the polymer directed the assembly of anti-fluorescein antibodies towards the polymer (Figure 2.10). It appeared that the affinity of the antibody for binding to the SAM was enhanced by a factor of 570 due to divalency. Thus the bifunctional polymer functions as a bridge between the SAM and the immunoglobin through two independent interactions, the polyvalent interaction between the SAM and the polymer, and the divalent interaction between the immunoglobin and the polymer. These polymers could thus be used for the direction of antibodies towards cell surfaces.
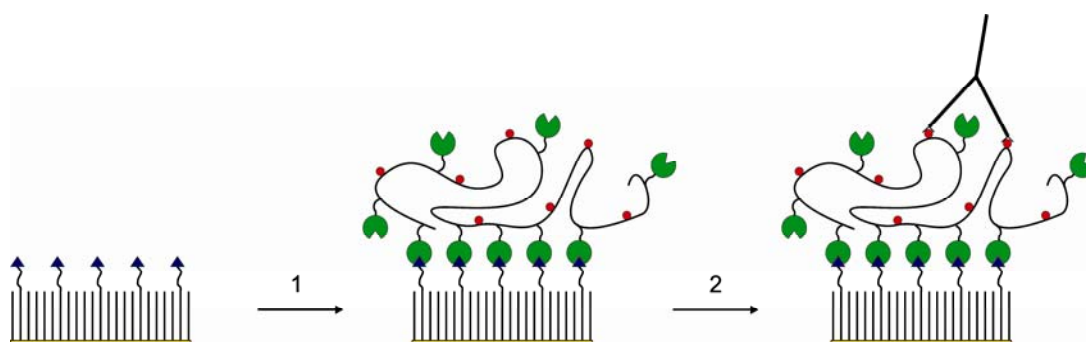
Figure 2.9 *The adsorption of a bifunctional polymer presenting vancomycin and fluorescein groups to SAMs consisting of D-Ala-D-Ala groups and tri(ethylene glycol) groups (1); the adsorption of an anti-fluorescein antibody to such SAMs to which the bifunctional vancomycin-fluorescein polymer was adsorbed (2).*[57]

To introduce the possibility of desorption by an external stimulus, the electroactive ferrocenyl PPI dendrimers were subsequently explored.[47-49] It was noted before that oxidation of the ferrocenyl groups to ferrocenium cations leads to a strongly reduced affinity of these groups for the βCD cavity. Thus the externally triggered desorption by electrochemical oxidation of molecular printboard-adsorbed ferrocenyl dendrimers was envisaged. The binding of ferrocenyl dendrimers to the molecular printboard was studied using cyclic voltammetry (CV). Apart from the tool to study binding stoichiometry,[47] CV also provided proof of the envisaged assembly and disassembly scheme (Figure 2.6). Oxidation of the ferrocenyl groups of a full monolayer of ferrocenyl dendrimers on the molecular printboard, which occurred for all ferrocenyl groups at the same potential, led to complete desorption of the dendrimers, as also

indicated by the combination of CV with SPR.[48] Subsequent reduction showed that only part of the oxidized dendrimers were reduced back and re-adsorbed, thus leading to lower charge densities for subsequent CV scans. When the same dendrimers were added to the electrolyte solution which was in contact with the Fc dendrimer monolayer, oxidation led to complete desorption, but upon reduction the dendrimer monolayer was fully reconstituted by replenishment of Fc dendrimers from the electrolyte solution (Figure 2.10). This procedure was found to be fully reversible at various scan rates.
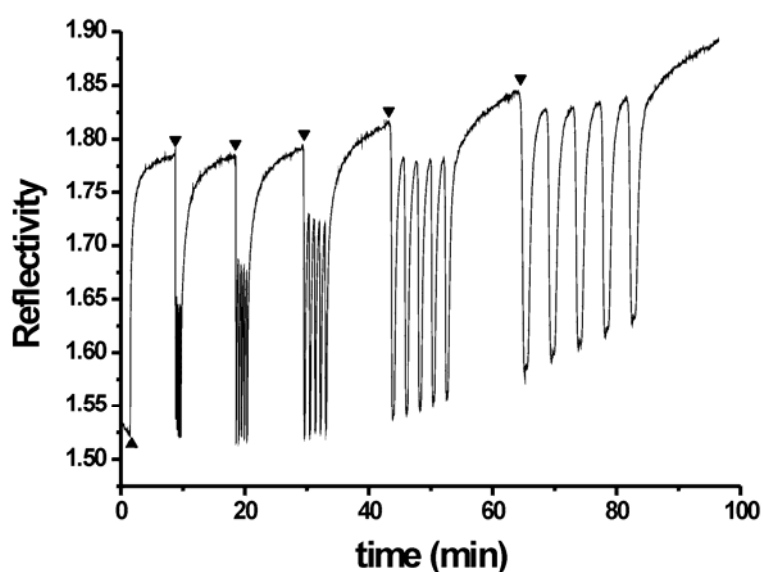
Figure 2.10 *SPR response of the* molecular printboard *with generation-3 ferrocenyl dendrimer in solution while performing cyclic voltammetry at different scan rates:* ▲ *= injection of 6.3 μM aqueous solution of the dendrimer with 10 mM βCD at pH = 2;* ▼ *= 5 scans at 100 mV/s, 50 mV/s, 25 mV/s, 10 mV/s, and 5 mV/s from left to right.*[48]

The (latent) power of multivalent host-guest interactions at interfaces lies in part in the easy conceptual transfer to various building blocks and substrate types. Apart from flat surfaces, also 3D objects such as nanoparticles can be functionalized with host or guest motifs with the aim of assembling materials.

From the stoichiometry data, it was clear that the adamantyl dendrimers have many unused guest groups when adsorbed on the molecular printboard. Consequently, such dendrimer monolayers can be viewed as guest-functionalized layers which in turn allow the adsorption of host-functionalized species. On the other hand, the spherical

nature of βCD gold nanoparticles ensures that their subsequent adsorption again leads to a host-functionalized surface. Thus, the repeated application of dendrimers and nanoparticles has led to a supramolecular layer-by-layer assembly scheme (Figure 2.11), where each step was self-limiting and in which uncontrolled aggregation was prevented since both building blocks were applied from separate solutions.[58] SPR, UV/Vis, ellipsometry and AFM all indicated a linear growth of the multilayer structures upon increase of the number of assembly steps, with a thickness increase of about 2 nm per bilayer.
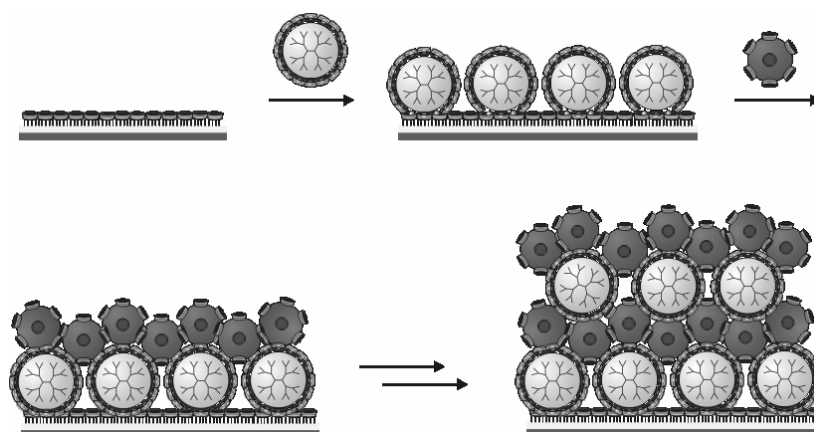
Figure 2.11 *Layer-by-layer assembly scheme for the alternating adsorption of generation-5 adamantyl-terminated PPI dendrimers and βCD-functionalized gold nanoparticles onto the molecular printboard.*[58]

2.3.2 Devices

As shown above, the use of multivalent interactions can lead to both thermodynamically and kinetically stable assemblies at interfaces. This stability has been shown to allow localized surface assembly, i.e. patterning, as well as materials buildup in a layer-by-layer (LBL) fashion. The combination of the two holds a powerful paradigm for the construction of three-dimensional nanostructures of supramolecular materials. Various surface patterning strategies were applied to make patterned βCD monolayers with adsorption-resistant monolayers in the areas in between, with the aim of directed layer-by-layer assembly of the adamantyl dendrimers and βCD gold nanoparticles.[59] This proved impossible mainly because of limited selectivity of adsorption of the adamantyl dendrimers due to nonspecific interactions with the inert SAM areas. Two other nanofabrication schemes, however,

were successful. First, supramolecular LBL assembly was performed on PDMS relief stamps.[59] Subsequent nanotransfer printing led to the transfer of the complete, intact assemblies from the stamp-substrate contact areas only onto the βCD SAM substrate. This allowed the formation of nanostructures with lateral dimensions in the μm range and a height in the nm range. Truly 3D nanostructures, with sub-100 nm sizes in all three dimensions, were obtained through the use of nanoimprint lithography (NIL).[60,61] NIL was used to create polymer templates with nm lateral dimensions onto which βCD SAM formation and supramolecular LBL assembly was performed (Figure 2.12). As a last step, lift-off of the polymer template allowed the concomitant removal of any nonspecifically adsorbed material, while the structures assembled on the βCD SAM areas remained intact.
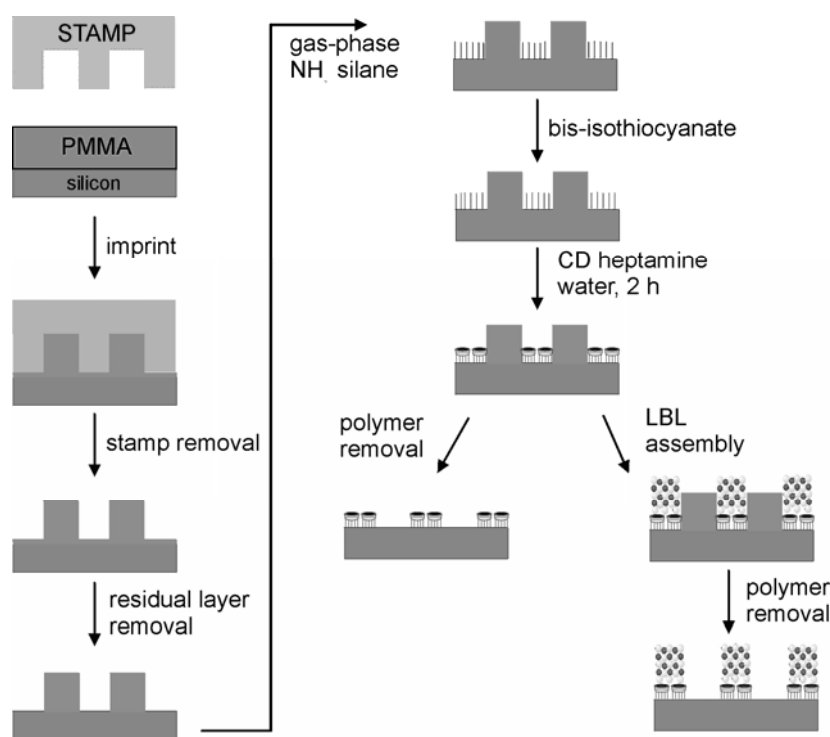
Figure 2.12 Integrated nanofabrication scheme incorporating nanoimprint lithography, (patterned) βCD SAM formation, and layer-by-layer assembly of adamantyl dendrimers and βCD gold nanoparticles.[60]

Current activities in this direction focus on the use of larger nanoparticles, e.g. for potential photonic crystal applications. To this respect, 60 nm silica nanoparticles have been equipped with βCD host molecules.[62] These showed aggregation in

solution with adamantyl dendrimers as well as specific binding to dendrimer monolayers adsorbed on the molecular printboard, similar to the behavior of the, much smaller, βCD gold nanoparticles discussed above. When the adamantyl dendrimers were microcontact printed onto the molecular printboard in micrometer-sized areas, the βCD silica nanoparticles faithfully adsorbed to the dendrimer-functionalized SAM areas. This again confirms the use of the guest-functionalized adamantyl dendrimers as a kind of supramolecular glue for the adsorption of host-functionalized entities onto the molecular printboards.

Dendrimer-stabilized gold nanoparticles have been used for the localized growth of metal structures using electroless deposition.[50] To this aim, βCD complexed, dendrimer-stabilized gold nanoparticles were microcontact printed onto the molecular printboard. Consecutive electroless deposition of copper, initiated by the localized gold nanoparticles, led to the controlled growth of metallic copper structures in the contacted areas with a height of over 60 nm. Current activities are in the area of nanotransfer printing of gold topped electrode structures onto ferrocenyl dendrimers for the construction of molecular electronic devices.[63,64]

2.4   The attachment of proteins and cells to surfaces

Protein attachment, in such a way that the protein is attached to the surface in a stable fashion and remains functional, is one of the key aspects of many different systems involving protein immobilization.[65-70] There are several methods for the attachment of proteins to surfaces such as physisorption and chemisorption,[71,72] but in those systems, not many factors of protein adsorption can be controlled at will and the functionality of the adsorbed protein is decreased dramatically.[73] Ideally, when adsorbing proteins to surfaces one would be able to control adsorption rates, immobilization orientation, and thereby functionality. When controlling these parameters, one can very specifically design systems for specific purposes, such as biosensors.

2.4.1   Protein-resistant surfaces

One of the major issues in protein immobilization at surfaces is the control over nonspecific interactions of proteins to the surface. Nonspecific protein adsorption is

highly unfavorable because it causes high background noises and false positives in medical diagnostic systems.

Throughout literature different strategies are utilized to prevent nonspecific interactions from occurring, such as the addition of bovine serum albumin and/or surfactants to protein solutions.[74-76] A more elegant manner of avoiding nonspecific adsorption, however, is the use of very specific monolayers that resist the adsorption of proteins. The mechanism of protein adsorption to the surface is depicted in Figure 2.13. Two major parts can be distinguished in this process, adsorption of the protein to the surface (a), reorganization of the protein on the surface, in the form of denaturation (d) and lateral diffusion of the protein on the surface (b). Once adsorbed, a protein can desorb from the surface (a, c, e), but in most cases the protein remains irreversibly adsorbed to the surface (f) or is exchanged with proteins from solution (g). For designing surfaces that possess protein-repellent characteristics, the adsorption step (a) should be blocked.[77]
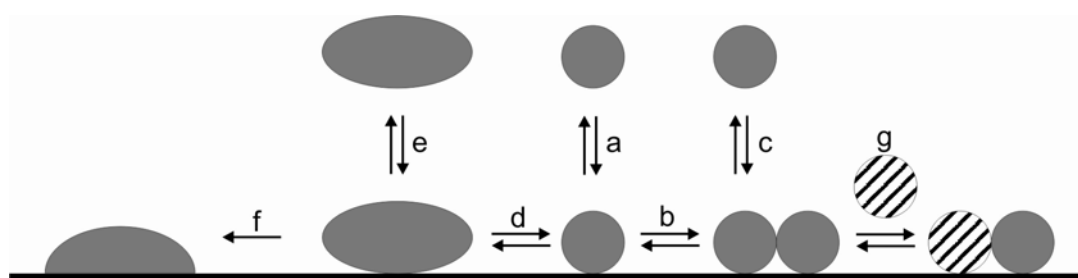
Figure 2.13 *Protein adsorption at surfaces, showing the adsorption (a), lateral diffusion (b), desorption (a, c, e), denaturation (d), irreversible adsorption (f), and exchange with proteins from solution (g).*[77]

Much research has been devoted to the mechanisms that are responsible for the protein-resistant characteristics of these surfaces. In general, surfaces that are protein repellent, have the following characteristics:[78] i) they are hydrophilic, ii) they include hydrogen-bond acceptors, iii) they do not include hydrogen-bond donors,[79] and iv) their overall charge is neutral.[80] In literature, however, also papers that describe SAMs consisting of mannitol are reported as being protein resistant. These SAMs contain a large number of hydrogen-bond donors, but in fact, they resist the adsorption of fibroblasts longer than the well known poly(ethylene glycol) (PEG) surfaces, which satisfy all criteria described above.[81] The mechanism for protein resistance of these

mannitol SAMs is different from the mechanism that is applicable to surfaces that do meet the criteria listed above, but the actual mechanism is not clear.

More research has been devoted to the mechanisms underlying the protein-repellent characteristics of the adsorbates that posses the "standard" features listed above. The mechanism behind the protein repellent characteristics of these surfaces is not completely understood, because the processes that are involved in nonspecific protein adsorption to surfaces are not studied easily with kinetics or thermodynamics, but there are a few important features which can be mentioned.

Degennes and Andrade, who were among the first to investigate the PEG SAMs and their ability to suppress nonspecific protein adsorption, showed in calculations that the protein resistance from PEG SAMs are related to weak Van der Waals interactions between the SAM and the protein. In this respect, the density of the SAMs has a larger impact than the length of the ethylene glycol unit.[82] They also showed that when the density of PEG SAMs is kept constant, an increase in the number of PEG units has a positive effect on the ability of the SAM to resist the nonspecific adsorption of proteins.[83] According to their mechanism, water molecules are expelled out of the PEG layer upon proteins approaching the surface. This is thermodynamically not favorable, and thus gives rise to steric repulsion. This steric repulsion contributes to the protein-resistant properties of the PEG SAMs.

The protein resistance of PEG SAMs could theoretically be accounted for by Szleifer and coworkers, who made use of the single-chain mean-field (SCME) theory, which shows that a high density of short PEG chains ($n \geq 6$) are also protein repellent. They could however not explain this at a molecular level.[84] Grunze *et al.* showed that the chain conformation flexibility of the PEG chains at a surface is of major importance.[85] They found that the PEG chains that adopt a helical conformation are excellent protein repellent. They also showed that the interaction between H_2O and the SAM is important; actually the general idea is that this is the most important aspect of surfaces that are protein repellent.[86-89] Therefore, the chemical properties of surfaces are also believed to be important in protein resistance, since this is an important factor in determining the state of hydration.[86] Sum frequency studies have shown that PEG chains on Au adopt a helical conformation and that PEG chains on Ag are in a trans configuration, and are more densely packed. The SAMs with a helical conformation are shown to interact more strongly with water.[89,90]

Wettability is often mentioned as an indication for the protein-resistant capacity of SAMs. Up to date, however, no real correlation between wettability and protein resistance of SAMs has been shown. For example, SAMs terminating in hexa(ethylene glycol) (HEG) appear to be very protein resistant while their wettability is only average. This was also confirmed by the studies of Harder *et al.*[90]

2.4.2 Orthogonal attachment of proteins to surfaces

Control over the orientation of immobilized proteins is of utmost importance in many biotechnological systems.[91-94] This can be acquired using linker systems.[45,95] Such a linker has two different moieties: one that interacts with the surface, and one that interacts with the molecule to be attached to the surface. When both sides of such a linker molecule do not interfere with each other, the linker is regarded as an "orthogonal linker".[96,97] The advantages of using such orthogonal linkers are several, such as control over the distance between the target (bio)molecule and the surface, control over adsorption density, and even control over adsorption and desorption rates.

2.4.2.1 Attachment of (strept)avidin to surfaces

The (strept)avidin-biotin couple is a useful and versatile tool in many bioanalytical applications.[98] Streptavidin (SAv), a protein isolated from *Streptomyces avidinii*, is very closely related to avidin, and both are homo-tetrameric proteins.[99,100] Each subunit contains a binding site for D-biotin, which is vitamin H (Figure 2.14). The association constant for the biotin-(strept)avidin interaction is about 10^{15} M^{-1},[101-104] which is the strongest non-covalent interaction known in nature. Binding of SAv to biotin takes place in a non-cooperative manner.[105] For applications, SAv is preferred over avidin, since it does not contain glycoamino acids, which results in a lower isoelectric point, and as a consequence less nonspecific adsorption is observed.
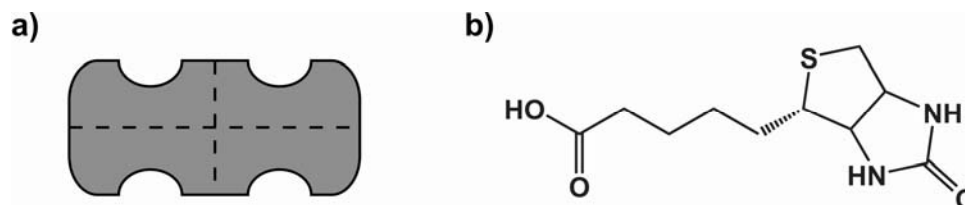
Figure 2.14 Schematic representation of (strept)avidin (a) and biotin (b).

Layers of SAv on surfaces can be a useful tool for the further attachment of proteins, since many proteins are available with a biotin functionality, or can easily be equipped with one. The challenge of assembling a SAv system on a surface was taken-up around 1989.[106]

There are two schemes for preparing monomolecular layers of SAv. The first deals with SAMs on gold or silver. For this purpose long chain thiols bearing a biotin head group have been synthesized to form (mixed) SAMs on Ag and Au surfaces, which could be subsequently functionalized with SAv. In the second scheme, the Langmuir-Blodgett-Kuhn (LBK) technique is applied, in which a functional monolayer is prepared at the air/water interface by spreading a lipid solution onto a volatile solvent and thereafter compressing the amphiphilic molecules to the desired lateral density.

Both types of SAv-layers have been characterized extensively using, amongst others, ellipsometry, SPR, fluorescence measurements, and neutron reflectivity. All these methods showed that the solvent exposed biotin binding pockets are still available. In these layers good ordering of SAv is observed which allowed the 2D-crystallization of SAv.

Such SAv layers allow for the build-up of more complex multilayer systems, since the upper two biotin binding pockets are available for further hetero-functionalization. In general, the biotin-(strept)avidin couple has been used very often in immunoassays, an example of which has been described by Spinke *et al*.[107] They describe a system in which SAv is attached to a biotin-functionalized substrate, and subsequently functionalized with biotinylated Fab fragments specific to the human gonadotrophin (HCG) hormone. Thereafter HCG was shown to bind to this system (Figure 2.15a). After 24 h of exposure to a high concentration of biotin, the biotin surface was regenerated.

In a series of articles, the attachment of cytochrome *c* (cyt *c*) to SAv SAMs (Figure 2.15b) was studied.[108-111] The results showed that a macroscopically ordered film of adsorbed cyt *c* molecules can be produced when a single, high-affinity type of noncovalent binding occurs between the protein and the substrate. The cyt *c* in this layer is highly oriented. By comparison with cyt *c* directly bound to lipid bilayers it was also shown that the SAv layer in between does not affect the macroscopic molecular orientation of cyt *c*.

In an extensive review Wilchek and Bayer showed hat the avidin-biotin technology can be applied in the development of e.g immunoassays as displayed in Figure

2.15c.[112] Examples of immunoassays developed with the avidin-biotin technology include sensors as developed by Guesdon *et al.*,[113] and Kohen *et al.*[114] It was concluded that this technology can be used in quantitative enzyme-immunoassays, since the enzymes did not have to be bound covalently to surfaces.

Anzai *et al.* showed that it is possible to obtain multilayers based on biotin-labeled poly(amine)s and avidin.[115] They showed that this buildup was really due to the biotin-labeling of the dendrimers, since non-biotinylated dendrimers did not result in multilayer formation. Depending on the type of dendrimers used, different types of multilayers are formed, of which the avidin/poly(amine)s yielded the best monomolecular avidin layers, whereas the use of randomly branched and linear poly(amine)s yielded multilayers of avidin (Figure 2.15d1, 2.15d2, and 2.15d3 respectively).

2.4.2.2 The orthogonal attachment of proteins through NiNTA linkers to surfaces

In immobilized metal affinity chromatography (IMAC), the *N*-nitrilotriacetate (NTA)-hexahistidine- (His$_6$-) tag chelator couple is a powerful tool for the purification of proteins.[116] Proteins, labeled with a (small) His tag, a short fused sequence of histidines, are purified by the ability of the His-tag to bind to a Ni^{2+}-NTA complex. NTA is a tetradentate ligand which forms a hexagonal complex with divalent metal ions like Ni^{2+}, Co^{2+}, Cu^{2+}, and Zn^{2+} (Figure 2.16).[117] This way, four of the six binding sites at the metal ion are occupied, leaving two binding positions available for binding to a His$_6$-sequence. This interaction can be reversed by the addition of imidazole or EDTA, imidazole competes with the His$_6$-sequence for coordination to Ni^{2+}, EDTA competes with NTA for coordination to Ni^{2+}. Especially this reversibility makes the system interesting because it allows the reversible attachment of proteins to surfaces. The NiNTA-His-tag strategy is more and more applied in controlled immobilization, i.e. in orientation-specific binding and 2D organization of proteins at interfaces.[118-121] Multivalent attachment of His-tagged proteins is an important issue, since it allows for the stable and specific attachment of proteins to these surfaces.
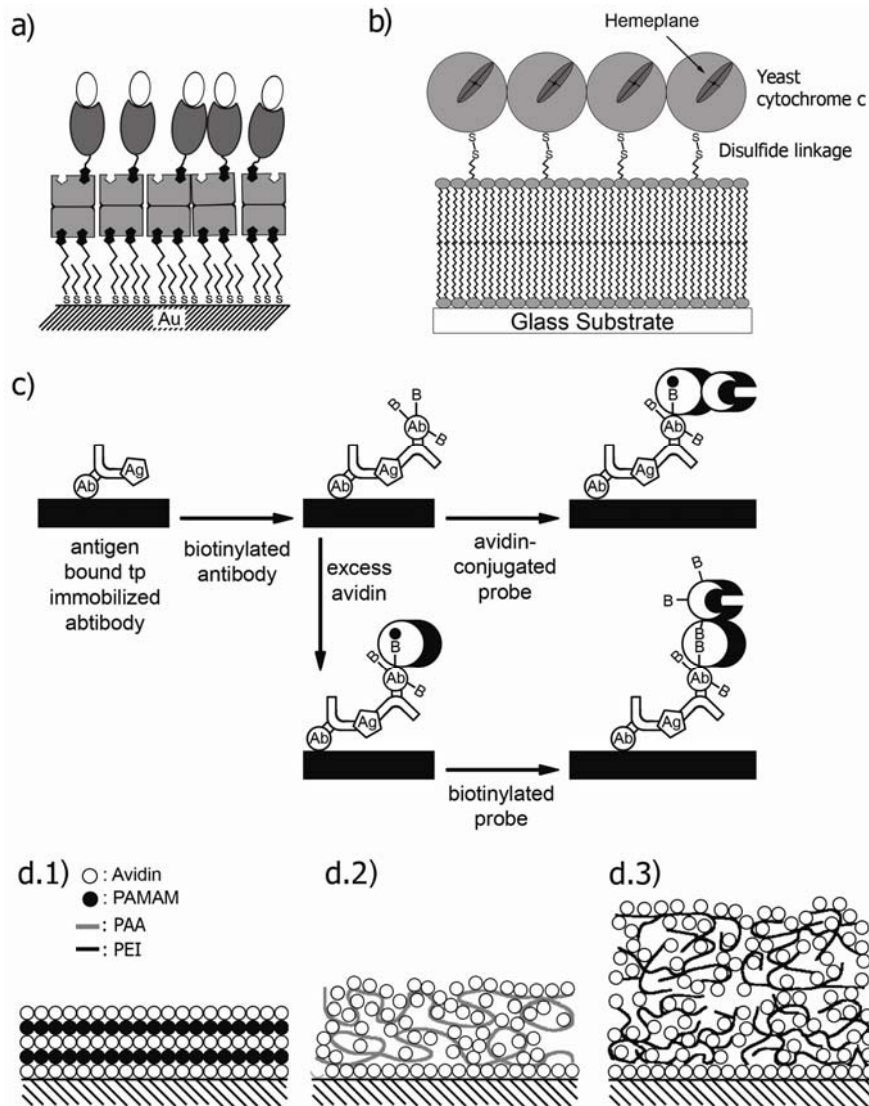
Figure 2.15 *Multilayers based on SAv-biotin interactions: HCG sensor as developed by Spinke et al.[107] (a), cyt c attachment to surface-immobilized SAv[108-111] (b), biotin-avidin technology as applied in the development of immunoassays[112] (c), attachment of SAv-dendrimer multilayers[115] (d).*
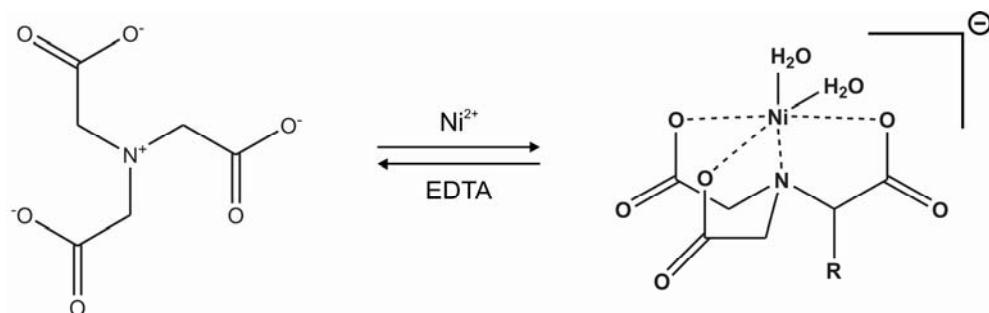
Figure 2.16 *N-nitrilotriacetate is converted into the NiNTA complex by adding Ni^{2+}. Complexation can be reversed by adding EDTA.[117]*

High affinity receptors were designed by incorporating multiple NTA moieties into single molecular entities.[122] The binding process of oligo-His tags (His_6 or His_{10}) to such entities with 1-4 NTA headgroups, leading to 2-8 possible coordination bonds, was studied in detail.[122] His_6 and His_{10} have 6 and 10 coordination possibilities, respectively. This means that theoretically the number of histidines on a tag are fewer or more than the demand of the chelators, which is called redundancy (Figure 2.17). The multivalency principle dictates an increase of the complex stability with increasing valency. The system, however, remains switchable, as addition of EDTA or imidazole leads to decomplexation.
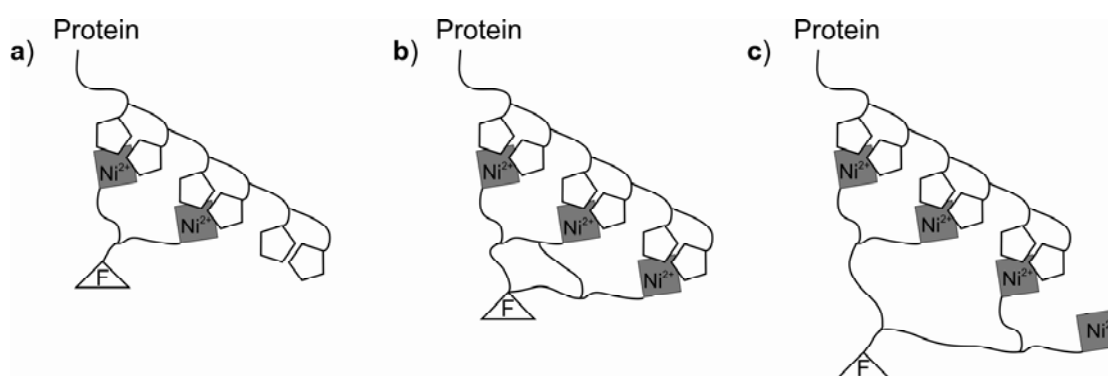
Figure 2.17 *Schematics of valencies and redundancy for interactions between a His_6-tagged protein and di-, tri-, and tetravalent NiNTA receptors: redundancy of the His groups of the His_6 tag (a), complementary valency, no redundancy (b), redundancy of chelator groups (F represents a fluorophore) (c).[122]*

Isothermal titration calorimetry (ITC) experiments revealed several issues. One of the consequences of redundancy is that complex stoichiometries depend on the absolute concentrations of the binding partners. Low concentrations of binding partners led to 1:1 complexes but at higher concentrations or a deficiency in one of the binding partners, other complex stoichiometries could not be excluded. ITC also showed that for higher valencies a substantial redundancy in histidines was required to reach an enthalpy of binding in line with the expected number of coordination bonds. This indicates that steric constraints interfered with full coordination. For the multivalent complexes, high entropy losses were reported. This is attributed to a huge loss of conformational freedom of the flexible spacers upon complexation. Due to the redundancy of chelator groups as presented in Figure 2.17c only a small amount of His_6 or His_{10} is necessary to dissociate the complex.[122]

Tampé and coworkers combined the possibilities of the NiNTA-His-tag couple with self-assembled monolayers (SAMs). They designed chelator lipids for the reversible immobilization of His-tag-fused proteins at self-assembled lipid interfaces.[123] Chelator-lipid monolayers have some advantages for the immobilization of proteins at surfaces, such as (i) the possibility of coating nearly every surface by various techniques, (ii) the lateral organization and pattern formation because of the phase behavior of these lipid films,[124] and (iii) their biocompatibility. When Langmuir monolayers were formed of the NTA lipids, complex formation between Ni^{2+} and NTA was demonstrated at the air/water interface. The Ni^{2+} binding capability of the NTA groups was not compromised by the presence of the lipid. Since His-tagged proteins interact with the Ni^{2+} center through the imidazole ring of the histidine groups, imidazole is a suitable model compound for the testing of ligand binding to the NiNTA complex. The binding between imidazole and the NiNTA complex appeared to be specific, and the binding could be reversed by adding EDTA, because of its superior binding to Ni^{2+}. Since two histidines are required for stable complex formation with one NiNTA group, there is hardly any nonspecific interaction expected between proteins without a His_6-tag and a NiNTA-modified surface since the His is not a rare amino acid, and therefore the presence of two neighboring His groups is also very rare. This was confirmed by epifluorescence studies and film balance measurements.[117] From these studies, it could also be concluded that the binding process and pattern formation of histidine-tagged molecules were directly triggered by complex formation of the chelator lipid, and that the binding was specific.

Multivalency was first observed in a system in which Green Fluorescent Protein (GFP) was immobilized through specific binding on chelator-lipid-rich domains of a phase segregated monolayer.[120] When GFP was immobilized at such a surface, EDTA concentrations well above 1 mM were needed in order to desorb GFP from the surface. This very stable immobilization was attributed to the high surface concentration of binding sites present in the condensed lipid domains, and thus a high effective concentration. Approximately nine binding sites were present underneath a single GFP so that rebinding to unoccupied chelator lipids could easily occur. Further evidence for multivalent interactions between a His_6 tag and the NTA groups came from experiments involving immobilization of His_6-tagged proteins on chelating lipid membranes with chelators at different surface concentrations.[125] Pair formation

between a rhodamine-labeled, His-tagged peptide by an 7-nitro-2,1,3-benzoxadiazol-4-yl- (NBD-) labeled chelator lipid was demonstrated using fluorescence energy transfer spectroscopy at the monolayer interface as well as in solution. Also the dissociation of the complex by adding EDTA was shown this way. A very low percentage of nonspecifically bound protein was observed. FRET kinetic studies on this system showed that the binding (dissociation) constant was 3.0 ± 0.4 μM. From fluorescence correlation spectroscopy (FCS), a dissociation constant of 4.3 ± 0.8 μM could be deduced. Kinetically stable immobilization of the proteins at the chelator interfaces for at least 60 minutes was observed.

The stable immobilization and orientation of proteins on flat, biocompatible supports are a prerequisite for structural and mechanic studies of proteins. Therefore multivalent interactions play a major role in surface attachment of these proteins.[120,126] It was already shown that the chelator-lipid NiNTA surfaces are highly biocompatible, and that multipoint attachment of proteins to these layers is possible.[45,127] The 20S proteasome (Figure 2.18) was His-tagged specifically at the α-positions,[119] and immobilized at a chelator-lipid interface. SPR measurements showed the specific immobilization of these proteins to the lipid chelator surface. The proteasome remained stable at the surface, and the protein complex could only be removed from the surface by 0.1 M EDTA. Lateral mobility of the proteasome on the surface was also proven in these experiments. Also the biological activity of the attached proteasome was demonstrated by SPR. This stable, specific immobilization of the proteasome to the metal chelator surface led to elucidation of the molecular mechanism of the catalytic activity of these protein complexes.[118,119]
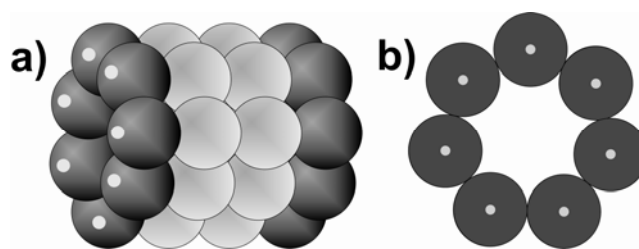

Figure 2.18 *20S Proteasome, His-tagged at the α-terminus: side view (a), front view (b), His$_6$-tag (•).*[119]

So far, only surfaces consisting of *monovalent* chelator lipids have been discussed. However, SAMs were also prepared with *multivalent* chelator lipids. There was a

considerable decrease in dissociation rate for the dissociation of a His-tagged protein (His$_6$-infar2) from the multivalent surface compared to the monovalent surface.[128] The low dissociation rate constant allowed orthogonal protein immobilization. The high stability of the multivalent NTA SAM towards His$_6$ tags also allowed the patterning of these SAMs.[128]

2.4.3   Patterning of proteins

The ability to pattern proteins on surfaces has many applications, such as the fabrication of multi-analyte biosensors, clinical assays, and the modulation of cell-substrate interactions in biomaterials and tissue engineering. Important to note is that proteins immobilized at surfaces are more stable than proteins in solution due to the higher concentration of proteins at the surface.[129] An important issue is the patterning of proteins in such a way that orientation and functionality can be controlled, since proteins easily lose their activity due to unfolding processes that can occur once attached to a surface.[130] There are different manners of patterning of proteins on surfaces. In this section, only systems will be discussed in which µCP is used and no or only little activity loss of the protein due to immobilization is expected.

A well known technique for obtaining protein-patterned substrates is µCP.[131] This technique is simple, inexpensive and effective. However, there is no precise control over pattern position, and non-uniform patterns can be obtained due to deformation of the stamp. There are different manners in which µCP can be applied in this field. Kohli *et al.*[132] have made well-defined 3-D layered bionanocomposite patterns, containing alternating layers of polyelectrolytes, dendrimers, and amphiphilic proteins. The biological activity could be predicted by co-immobilization of macromolecular structures such as dendrimers or polyelectrolyte multilayers (PEMs). Dendrimers can serve as functional frames to encapsulate small molecules needed by the protein. PEMs are robust, easy to fabricate and have tunable architectures. A (patterned) PDMS stamp first spincoated with a secondary alcohol dehydrogenase (SADH), and subsequently spincoated with a poly(amidoamine-organosilicon) (PAMAMOS) dendrimer. This stamp served as a template for the growth of PEMs. Thereafter the pattern grown on the stamp was transferred to the substrate.

A nice aspect of this system is that, in between PEMs, different enzymes can be sandwiched in order to catalyze sequential reactions. When transferred to a substrate,

the multilayer architecture could be checked by fluorescent labeling of the protein and of the dendrimer. Fluorescence spectroscopy proved the coexistence of both layers. The electrostatic interactions between the enzymes, dendrimers, and PEMs are responsible for stabilizing the multilayered structures. Furthermore, this approach relies on topographical contrast, rather than on chemical contrast. This leads for example to less nonspecific protein adsorption on the substrate.

The NiNTA-His-tag systems as described by Tampé can be applied in the patterning of proteins.[133] In their approach, protein patterning relies on molecular and surface multivalency. Patterns of mono- and bis-NTA SAMs, both mixed with a matrix thiol containing no NTA units, were assembled into microarrays by dispensing the thiol solutions into a hydrophobic grid, which was obtained by μCP. These surfaces had already been proven to be biocompatible.[128] In this way, the concentration of the NTA moieties inside an element of the array could be controlled, as well as the type of chelator head. To these surfaces, the extracellular domain of the type I interferon receptor subunit ifnar2 bearing a hexa histidine- or a decahistidine-tag (His_6-infnar2 or His_{10}-ifnar2) was immobilized. It appeared that not only molecular multivalency, but also surface multivalency plays an important role in the attachment of a His-tagged protein to the surface, since a strong dependence of the dissociation kinetics on the surface concentration of bis-NTA was observed: the lower the bis-NTA density, the faster the protein dissociated from the surface. Thereafter, on one chip, arrays with different densities of mono- and bis-NTA were fabricated. Binding studies were in this case performed with His_6-ifnar2 and followed by SPR imaging (Figure 2.19). Again, very different dissociation kinetics were observed for mono- and bis-NTA domains, which are strikingly clear at a concentration of 15 mol% bis-NTA. His_6-Ifnar2 dissociated significantly slower from bis-NTA domains than from mono-NTA surfaces. Even at a surface loading of 30 mol% of mono-NTA, the His_6-ifnar2 dissociated much faster than at a domain which was loaded with 15 mol%, even though the surface concentration of NTA sites was the same. A striking aspect of this system is that proteins do not have to be adsorbed on stamps, or undergo harsh conditions such as used in photolithography which are processes that always reduce the activity of the immobilized protein, and are therefore less biocompatible.
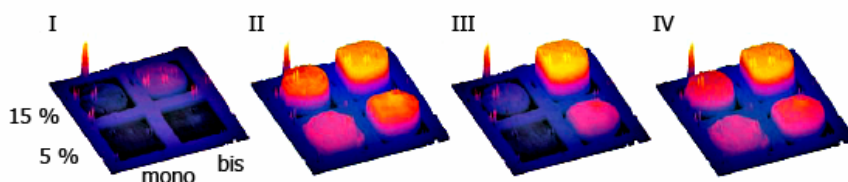
Figure 2.19 *SPR images of a comparative protein-binding experiment with 5 and 15 mol% mono- and bis-NTA. I) after conditioning by treatment with 10 mM Ni^{2+} ions and 200 mM imidazole, II) after immobilization of His_6-ifnar2, III) after eluation with 40 mM imidazole, IV) after reloading His_6-ifnar2.[133]*

The Whitesides group made use of μCP on reactive mixed SAMs to yield substrates on which biotin and benzenesulfonamide were patterned.[134] Benzenesulfonamides bind to carbonic anhydrase (CA) of which the interaction in solution and on SAMs has been studied.[44] Both the patterned biotin and benzesulfonamide surfaces were obtained by μCP. Subsequently, the patterned biotin substrates were analyzed in different methods: i) incubation of the substrates in an antibiotin mouse IgG_1-Alexa 488 conjugate, and ii) in a sandwich experiment in which SAv is first bound to the biotinylated surface. The edge resolution of the patterns obtained in the sandwich experiment was better than the resolution obtained in the experiment with the antibiotin IgG. From SPR experiments it could be concluded that there is a significant difference between SAMs in which the biotin functionality was inserted through μCP, or by immersing the SAM in a solution with biotin ligand, the coupling trough μCP is 90% larger than that accomplished via immersion. For the binding of CA, SAMs with benzenesulfonamides were also prepared by μCP and immersion. The binding of CA was more than 90% reversible on both types of samples. The amount of CA bound to surfaces obtained via μCP, however, was only 75% compared to the samples obtained through immersion.

2.4.4 Cells at surfaces

The attachment of cells to surfaces is an important issue in several research fields,[135,136] including the development of supports for the immobilization of cells in bioreactors, substrates for tissue engineering, and in diagnostics of diseases such as the acquired immunodeficiency syndrome (AIDS)[137] and cancer.[138] The attachment of cells to surfaces is mediated by multivalent interactions, and is therefore strong.

Cells adhere to different surfaces, which is necessary in order to perform their normal metabolism, proliferation, and differentiation. The biological matrix that makes this possible is made up of different insoluble proteins and glycoaminoglycans that are referred to as the extracellular matrix (ECM).[139] The primary responsibility of the ECM is to mediate the adhesion of cells to surfaces.[140] Most of the ECM proteins contain the arginine glycine aspartic acid (RGD) tripeptide sequence, and this (short) peptide is responsible for cell adhesion to surfaces.[141,142]

Self assembly of peptides on surfaces can lead to unique substrates to which cells can attach. Model substrates developed for cell attachment should have several characteristics in order to be useful:[143] i) the substrate onto which cells should be adsorbed, should present structurally defined ligands in a homogeneous environment at the interface, and the density of ligands at the surface should be controllable, ii) the substrate must be protein resistant, so that immobilized ligands are not obstructed when proteins adsorb, iii) the model substrate should be compatible with routine methods used for the characterization of cells.

The PEG SAMs as developed by Whitesides are suitable for this purpose, since they are protein resistant, and can be mixed with different ligands allowing the insertion of ligands which allow specific interactions. A study by Mrksich *et al.* showed the adhesion of Swiss 3T3 cells on SAMs prepared from a mixed monolayer containing tri(ethylene glycol) (TEG) moieties and the peptide Gly-Arg-Gly-Asp (GRGD).[144,145] It appeared that cells spread efficiently when the peptide was present in a 0.01 to 1.0% density. Not only the density of the peptide appeared to be important, but also that the TEG group could not be interchanged with a hexa(ethylene glycol) (HEG) group, in which case fewer cells attached to the surface.

The development of dynamic substrates for cell attachment is an important one, since dynamic substrates allow mechanistic studies of the pathways by which cells respond to changes in their environment. A good example of dynamic substrates to which orthogonal attachment of cells is possible, is described by Whitesides and Mrksich.[146,147] They have prepared SAMs that incorporate alkanethiolates terminated in two different electroactive moieties, an electroactive quinone ester (QE) and an O-silyl hydroquinone (SHQ) that can respond to electrical potentials by releasing attached ligands to which a peptide containing the RGD sequence is attached (Figure 2.20). Nonspecific interactions of cells with the surface were circumvented by using tri(ethylene glycol)-terminated disulfides as matrix elements. Swiss 3T3 fibroblast

cells were attached to these patterned SAMs. These cells only attached to the spots were the ligand was patterned, and not in between on the TEG SAM. When a potential of +650 mV was applied to these SAMs, the cells were only released from the areas in which SHQ groups were attached. When a potential of -650 mV was applied, only the cells in the QE areas were released.
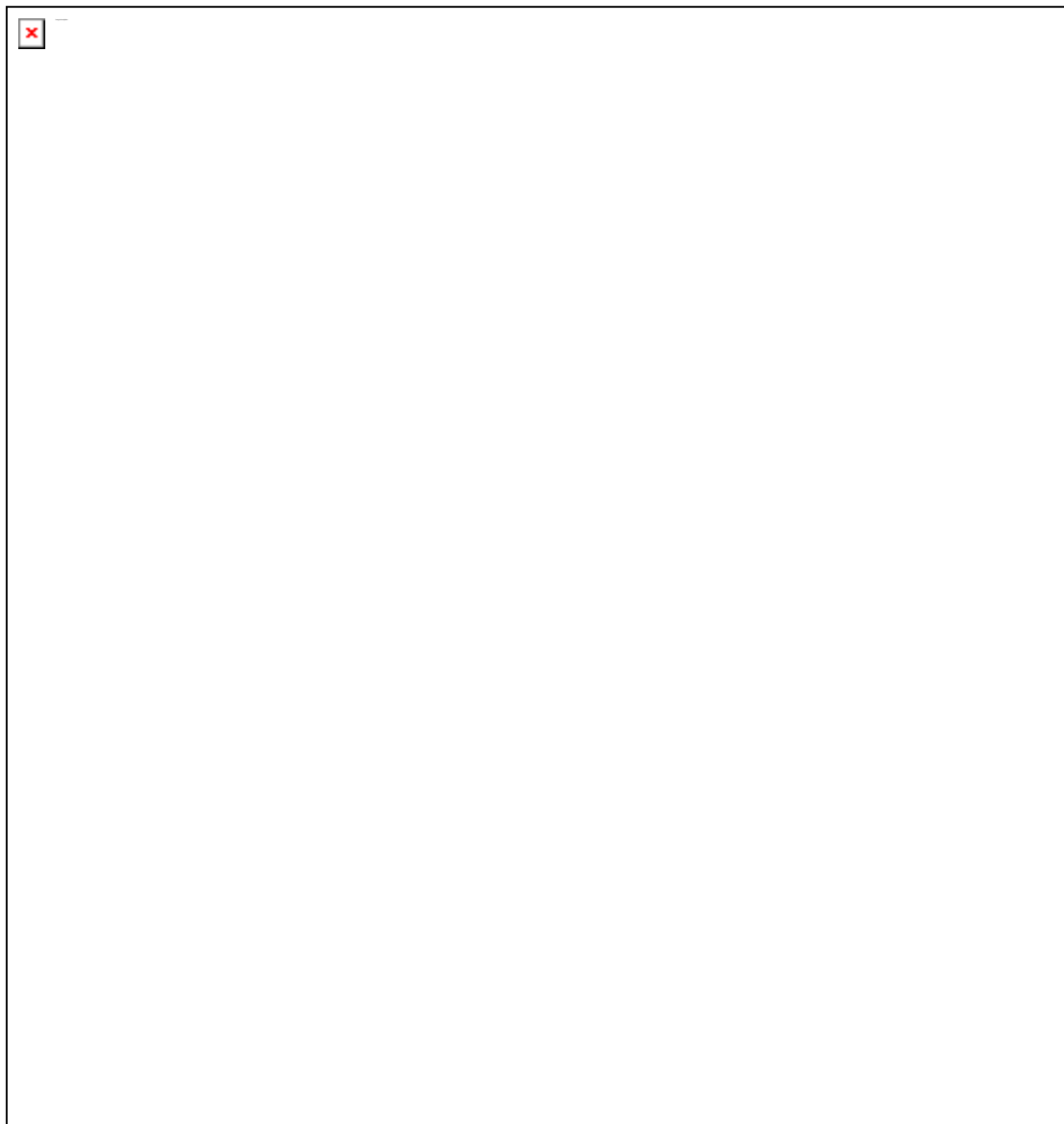

Figure 2.20 *Preparation of dynamic substrates for cell attachment. Sequential preparation of a SAM containing QE moieties and the RGD sequence, and the electrochemically induced desorption of the RGD sequence (a). Sequential preparation of a SAM containing SHQ moieties and the RGD sequence, and the electrochemically induced desorption of the RGD sequence (b).[147]*

An important issue in nature is the clustering of receptors at cell surfaces.[148,149,150,151] Therefore, substrates at which the density of ligands can be controlled can reflect natural situations. Kahne *et al.* used SAMs modified with carbohydrate ligands as model systems to elucidate mechanisms behind cell-surface carbohydrate-protein interactions.[152] In previous studies they found that the solution affinities of carbohydrate ligands for BP lectins did not correlate with their polyvalent degree of affinity. To elucidate whether this change is caused by immobilization of the carbohydrate ligands to the surface (orientation effect) or to clustering of the carbohydrate ligands on the surface (density-dependent polyvalent effect) they prepared surfaces of different carbohydrates in different concentrations to the surface. With SPR spectroscopy they were able to establish that the latter hypothesis is correct. Making use of the principle of clustering of ligands to induce binding to cells, Herbert *et al.* prepared SAMs containing patterns of different concentrations of peptides containing the RGD motive.[153] Observations made 24 h after cell seeding in a serum-free medium revealed that cell adherence was maximal at the sites where most peptide was present. The cells were attached to the surface with the RGD moieties by specific receptor-ligand interactions, in a multivalent fashion.

2.5   Conclusions & outlook

The different systems discussed in this chapter all show, each in their own way, that multivalency is an important tool for the understanding of different biological processes, for the interactions between proteins and receptor surfaces, and for the application of non-biological nanostructures at surfaces. Multivalency allows for the stable interaction between molecules to enhance the effectiveness of antibiotics and the elucidation of the mechanism of protein complexes. It allows the stable patterning of proteins to surfaces, as well as cell adhesion to surfaces. It also enables the stable positioning of molecules on surfaces to create nanostructures.

Molecular printboards offer numerous applications, especially when employing multivalent interactions for assembling all kinds of building blocks. Whereas the thermodynamics is now well understood for the few printboard systems discussed here, the quantitative interpretation of multivalent interactions at biological interfaces, such as real cell membranes, is conspicuously lacking. Reliable data on multivalent kinetics at interfaces is also not available at this time of writing, but new surface

diffusion mechanisms can be envisaged of which the implications for science and the applications can only be speculated upon.

A clear trend is also envisaged in the direction of orthogonal multivalent interactions to create more complex nanostructures at interfaces and to attach proteins and cells at surfaces. For now only limited numbers of examples are at hand; examples being the electrostatic interaction of negatively charged dyes in the positively charged cores of adamantyl dendrimers adsorbed to βCD SAMs,[55] and the orthogonal attachment of cells to surfaces.[133,134] Procedures in which proteins or cells are attached in a multivalent fashion to a surface yield stable and functional protein surfaces that can be used for many different applications. An important factor here is that selective, multivalent attachment of proteins to specific areas of substrates does not depend on direct patterning of proteins, but on the patterning of linkers to a substrate. This omits the direct protein patterning step, and thereby the step in which protein activity can be expected to decrease. More examples are needed for a better quantitative understanding of heterotropic multivalency, both in solution and at interfaces, but without doubt their development will lead to much more complex (bio)systems and (bio)materials.

2.6   References

1.   J. P. Wilcoxon, B. L. Abrams, *Chem. Soc. Rev.* **2006**, *35*, 1162-1194.

2.   M. C. Daniel, D. Astruc, *Chem. Rev.* **2004**, *104*, 293-346.

3.   L. N. Dinh, S. E. Hayes, A. E. Wynne, M. A. Wall, C. K. Saw, B. C. Stuart, M. Balooch, A. K. Paravastu, J. A. Reimer, *J. Mat. Sci.* **2002**, *37*, 3953-3958.

4.   H. J. Krenner, S. Stufler, M. Sabathil, E. C. Clark, P. Ester, M. Bichler, G. Abstreiter, J. J. Finley, A. Zrenner, *New. J. Phys.* **2005**, *7*, 1-27.

5.   V. Sambhy, M. M. MacBride, B. R. Peterson, A. Sen, *J. Am. Chem. Soc.* **2006**, *128*, 9798-9808.

6.   H. Yu, L. Luo, K. Beverly, J. F. Stoddart, H-R. Tseng, J. R. Heath, *Angew. Chem. Int. Ed.* **2003**, *42*, 5706-5711.

7.   D. R. Stewart, D. A. A. Ohlberg, P. A. Beck, Y. Chen, R. S. Williams, *Nano Lett.* **2004**, *4*, 133-136.

8.   M. Mammen, S.-K. Choi, G. M. Whitesides, *Angew. Chem. Int. Ed.* **1998**, *37*, 2754-2794.

9.   A. Mulder, J. Huskens, D. N. Reinhoudt, *Org. Biomol. Chem.* **2004**, *2*, 3409-3424.

10.   A. Varki, *Glycobiology* **1993**, *3*, 97-130.

11.   M. N. Matrosovich, L. V. Mochalova, V. P. Marinina, N. E. Byramova, N. V. Bovin, *FEBS Lett.* **1990**, *272*, 209-212.

12.   G. D. Glick, P. L. Toogood, D. C. Wiley, J. J. Skehel, J. R. Knowles, *J. Biol. Chem.* **1991**, *266*, 23660-23669.

13.   A. Spaltenstein, G. M. Whitesides, *J. Am. Chem. Soc.* **1991**, *113*, 686-687.

14.   S. Sabesan, J. Ø. Duus, S. Neira, P. Domaille, S. Kelm, J. C. Paulson, K. Bock, *J. Am. Chem. Soc.* **1992**, *114*, 8363-8375.

15.   W. J. Lees, A. Spaltenstein, J. E. Kingery-Wood, G. M. Whitesides, *J. Med. Chem.* **1994**, *37*, 3419-3433.

16.   G. B. Sigal, M. Mammen, G. Dahmann, G. M. Whitesides, *J. Am. Chem. Soc.* **1996**, *118*, 3789-3800.

17.   S.-K. Choi, M. Mammen, G. M. Whitesides, *J. Am. Chem. Soc.* **1997**, *119*, 4103-4111.

18.   For comprehensive reviews about cyclodextrin chemistry see: *Chem. Rev.* **1998**, *98*.

19.   J. D. Badjic, A. Nelson, S. J. Cantrill, W. B. Turnbull, J. F. Stoddart, *Acc. Chem. Res.* **2005**, *38*, 723-732.

20.   W. Kuhn, *Kolloid Z.* **1934**, *68*, 2-15.

21.   H. Jacobsen, W. H. Stockmayer, *Chem. Phys.* **1950**, *18*, 1600-1606.

22.   L. Mandolini, *Adv. Phys. Org. Chem.* **1986**, *22*, 1-111.

23.   A. Mulder, T. Auletta, A. Sartori, S. Del Ciotto, A. Casnati, R. Ungaro, J. Huskens, D. N. Reinhoudt, *J. Am. Chem. Soc.* **2004**, *126*, 6627-6636.

24.   J. Huskens, A. Mulder, T. Auletta, C. A. Nijhuis, M. J. W. Ludden, D. N. Reinhoudt, *J. Am. Chem. Soc.* **2004**, *126*, 6784-6797.

25.   G. Ercolani, *J. Am. Chem. Soc.* **2003**, *125*, 16097-16103.

26.   I. J. Colton, J. D. Carbeck, J. H. Rao, G. M. Whitesides, *Electrophoresis* **1998**, *19*, 367-382.

27.   J. H. Rao, L. Yan, B. Xu, G. M. Whitesides, *J. Am. Chem. Soc.* **1999**, *121*, 2629-2630.

28. J. H. Rao, J. Lahiri, L. Isaacs, R. M. Weis, G. M. Whitesides, *Science* **1998**, *280*, 708-711.

29. J. H. Rao, L. Yan, J. Lahiri, G. M. Whitesides R. M. Weiss, H. S. Warren, *Chem. Biol.* **1999**, *6*, 353-359.

30. J. H. Rao, J. Lahiri, R. M. Weis, G. M. Whitesides, *J. Am. Chem. Soc.* **2000**, *122*, 2698-2710.

31. J. H. Rao, I. J. Colton, G. M. Whitesides, *J. Am. Chem. Soc.* **1997**, *119*, 9336-9340.

32. J. H. Rao, G. M. Whitesides, *J. Am. Chem. Soc.* **1997**, *119*, 10286-10290.

33. A. Ulman, *An Introduction to Ultrathin Organic Films: From Langmuir-Blodgett to Self-Assembly*, Academic Press: Boston, U.S.A. **1996**, *96*, 1533-1554.

34. M. W. J. Beulen, J. Bügler, B. Lammerink, F. A. J. Geurts, E. M. E. F. Biemond, K. G. C. van Leerdam, F. C. J. M. van Veggel, J. F. J. Engbersen, D. N. Reinhoudt, *Langmuir* **1998**, *14*, 6424-6429.

35. M. W. J. Beulen, J. Bügler, M. R. de Jong, B. Lammerink, J. Huskens, H. Schönherr, G. J. Vancso, B. A. Boukamp, H. Wieder, A. Offenhäuser, W. Knoll, F. C. J. M. van Veggel, D. N. Reinhoudt, *Chem. Eur. J.* **2000**, *6*, 1176-1183.

36. M. R. de Jong, J. Huskens, D. N. Reinhoudt, *Chem. Eur. J.* **2001**, *7*, 4164-4170.

37. H. Schönherr, M. W. J. Beulen, J. Bügler, J. Huskens, F. C. J. M. van Veggel, D. N. Reinhoudt, G. J. Vancso, *J. Am. Chem. Soc.* **2000**, *122*, 4963-4967.

38. S. Zapotoczny, T. Auletta, M. R. de Jong, H. Schönherr, J. Huskens, F. C. J. M. van Veggel, D. N. Reinhoudt, G. J. Vancso, *Langmuir* **2002**, *18*, 6988-6994.

39. T. Auletta, M. R. de Jong, A. Mulder, F. C. J. M. van Veggel, J. Huskens, D. N. Reinhoudt, S. Zou, S. Zapotoczny, H. Schönherr, G. J. Vancso, L. Kuipers, *J. Am. Chem. Soc.* **2004**, *126*, 1577-1584, and references cited therein.

40. J. Huskens, M. A. Deij, D. N. Reinhoudt, *Angew. Chem. Int. Ed.* **2002**, *41*, 4467-4471.

41. J. J. Michels, M. W. P. L. Baars, E. W. Meijer, J. Huskens, D. N. Reinhoudt, *J. Chem. Soc. Perkin Trans. 2* **2000**, 1914-1918.

42. L. Yan, C. Marzolin, A. Terfort, G. M. Whitesides, *Langmuir* **1997**, *13*, 6704-6712.

43. S.-W. Tam-Chang, H. A. Biebuyck, G. M. Whitesides, N. Jeon, R. G. Nuzzo, *Langmuir* **1995**, *11*, 4371-4382.

44. M. Mrksich, J. R. Grunwell, G. M. Whitesides, *J. Am. Chem. Soc.* **1995**, *117*, 12009-12010.

45. G. B. Sigal, C. Bamdad, A. Barberis, J. Strominger, G. M. Whitesides, *Anal. Chem.* **1996**, *68*, 490-497.

46. U. N. Sundram, J. H. Griffin, *J. Am. Chem. Soc.* **1996**, *118*, 13107-13108.

47. C. A. Nijhuis, J. Huskens, D. N. Reinhoudt, *J. Am. Chem. Soc.* **2004**, *126*, 12266-12267.

48. C. A. Nijhuis, F. Yu, W. Knoll, J. Huskens, D. N. Reinhoudt, *Langmuir* **2005**, *21*, 7866-7876.

49. T. Auletta, B. Dordi, A. Mulder, A. Sartori, S. Onclin, C. M. Bruinink, C. A. Nijhuis, H. Beijleveld, M. Péter, H. Schönherr, G. J. Vancso, A. Casnati, R. Ungaro, B. J. Ravoo, J. Huskens, D. N. Reinhoudt, *Angew. Chem. Int. Ed.* **2004**, *43*, 369-373.

50. C. M. Bruinink, C. A. Nijhuis, B. Dordi, M. Péter, O. Crespo-Biel, T. Auletta, A. Mulder, H. Schönherr, G. J. Vancso, J. Huskens, D. N. Reinhoudt, *Chem. Eur. J.* **2005**, *11*, 3988-3996.

51. S. Onclin, A. Mulder, J. Huskens, B. J. Ravoo, D. N. Reinhoudt, *Langmuir* **2004**, *20*, 5460-5466.

52. A. Mulder, S. Onclin, M. Péter, J. P. Hoogenboom, H. Beijleveld, J. ter Maat, M. F. García-Parajó, B. J. Ravoo, J. Huskens, N. F. van Hulst, D. N. Reinhoudt, *Small* **2005**, *1*, 242-253.

53. P. Falvey, C. W. Lim, R. Darcy, T. Revermann, U. Karst, M. Giesbers, A. T. M. Marcelis, A. Lazar, A. W. Coleman, D. N. Reinhoudt, B. J. Ravoo, *Chem. Eur. J.* **2005**, *11*, 1171-1180.

54. C. W. Lim, B. J. Ravoo, D. N. Reinhoudt, *Chem. Commun.* **2005**, 5627-5629.

55. S. Onclin, J. Huskens, B. J. Ravoo, D. N. Reinhoudt, *Small* **2005**, *1*, 852-857.

56. O. Crespo-Biel, M. Péter, C. M. Bruinink, B. J. Ravoo, D. N. Reinhoudt, J. Huskens, *Chem. Eur. J.* **2005**, *11*, 2426-2432.

57. S. J. Metallo, R. S. Kane, R. E. Homlin, G. M. Whitesides, *J. Am. Chem. Soc.* **2003**, *125*, 4534-4540.

58. O. Crespo-Biel, B. Dordi, D. N. Reinhoudt, J. Huskens, *J. Am. Chem. Soc.* **2005**, *127*, 7594-7600.

59. O. Crespo-Biel, B. Dordi, P. Maury, M. Péter, D. N. Reinhoudt, J. Huskens, *Chem. Mater.* **2006**, *18*, 2545-2551.

60. P. Maury, O. Crespo-Biel, M. Péter, D. N. Reinhoudt, J. Huskens, *MRS Symp. Proc.* **2006**, *901E*, 0901-Rb12-01.1-9.

61. P. Maury, M. Péter, O. Crespo-Biel, X. Y. Ling, D. N. Reinhoudt, J. Huskens, *Nanotechnology* **2007**, *18*, 044007.

62. V. Mahalingam, S. Onclin, M. Péter, B. J. Ravoo, J. Huskens, D. N. Reinhoudt, *Langmuir* **2004**, *20*, 11756-11762.

63. C. A. Nijhuis, J. ter Maat, S. Z. Bisri, M. H. H. Weusthof, C. Salm, J. Schmitz, B. J. Ravoo, J. Huskens, D. N. Reinhoudt, submitted.

64. C. A. Nijhuis, *PhD Thesis*, University of Enschede, The Netherlands, **2006**.

65. K. Zhang, M. R. Diehl, D. A. Tirrell, *J. Am. Chem. Soc.* **2005**, *127*, 10136-10137.

66. H. Zhu, M. Snyder, *Curr. Opin. Chem. Biol.* **2003**, *7*, 55-63.

67. N. L. Rossi, C. A. Mirkin, *Chem. Rev.* **2005**, *105*, 1547-1562.

68. C. M. Niemeyer, *Angew. Chem. Int. Ed.* **2001**, *40*, 4128-4158.

69. E. Katz, I. Willner, *Angew. Chem. Int. Ed.* **2004**, *43*, 6042-6108.

70. L. Tiefenauer, R. Ros, *Coll. Surf. B* **2002**, *23*, 95-114.

71. K. M. McLean, S. L. McArthur, R. C. Chatelier, P. Kingshott, H. J. Griesser, *Coll. Interface Sci. B* **2000**, *17*, 23-35.

72. A. Biebricher, A. Paul, P. Tinnefeld, A. Gölzhäuser, M. Sauer, *J. Biotech.* **2004**, *112*, 97-107.

73. S. V. Rao, K. W. Anderson, L. G. Bachas, *Mikrochim. Acta.* **1998**, *128*, 127-143.

74. W. Senarate, L. Andruzzi, C. K. Ober, *Biomacromolecules* **2005**, *6*, 2427-2448.

75. C. P. Quinn, *et al.*, *Emerg. Infect. Dis.* **2002**, *8*, 1103-1110.

76. M. Kyo, T. Yamamoto, H. Motohashi, T. Kamiya, T. Kuroita, T. Tanaka, J. D. Engel, B. Kawakami, M. Yamamoto, *Genes to Cells* **2004**, *9*, 153-164.

77. M. Mrksich, *Cell. Mol. Life. Sci.* **1998**, *54*, 653-662.

78. R. G. Chapman, E. Ostuni, L. Yan, G. M. Whitesides, *Langmuir* **2000**, *16*, 6927-6936.

79. R. G. Chapman, E. Ostuni, S. Takayama, R. E. Holmlin, L. Yan, G. M. Whitesides, *J. Am. Chem. Soc.* **2000**, *122*, 8303-8304.

80. R. E. Holmlin, X. Chen, R. G. Chapman, S. Takayama, G. M. Whitesides, *Langmuir* **2001**, *17*, 2841-2850.

81. Y.-Y. Luk, M. Kato, M. Mrksich, *Langmuir* **2000**, *16*, 9604-9608.

82. S. I. Jeon, J. H. Lee, D. Andrade, P. G. de Gennes, *J. Coll. Interf. Sci.* **1991**, *142*, 149-158.

83. S. I. Jeon, J. D. Andrade, *J. Coll. Interf. Sci.* **1991**, *142*, 159-166.

84. J. Satulovsky, M. A. Carignano, I. Szleifer, *Proc. Natl. Acad. Sci. USA* **2000**, *97*, 9037-9041.

85. R. L. C. Wang, H. J. Kreuzer, M. Grunze, *J. Phys. Chem. B* **1997**, *101*, 9767-9773.

86. N. A. M. Besseling, *Langmuir* **1997**, *13*, 2113-2122.

87. D. C. Rau, V. A. Parsegian, *Science* **1990**, *249*, 1278-1281.

88. E. Ostuni, R. G. Chapman, E. Homlin, S. Takayama, G. M. Whitesides, *Langmuir* **2001**, *17*, 5605-5620.

89. K. Feldman, G. Hähner, N. D. Spencer, P. Harder, M. Grunze, *J. Am. Chem. Soc.* **1999**, *121*, 10134-10141.

90. P. Harder, M. Grunze, R. Dahint, G. M. Whitesides, P. E. Laibinis, *J. Phys. Chem. B* **1998**, *102*, 426-436.

91. S. Chen, L. Liu, J. Zhou, S. Jiang, *Langmuir* **2003**, *19*, 2859-2864.

92. K. K. Chittur, *Biomaterials* **1998**, *19*, 357-369.

93. B. Lu, M. R. Smith, R. O'Kennedy, *Analyst* **1996**, *121*, 29R-32R.

94. J. Turková, *J. Chromatogr. B* **1999**, *722*, 11-31.

95. D. L. Johnson, L. L. Martin, *J. Am. Chem. Soc.* **2005**, *127*, 2018-2019.

96. M. C. T. Fyfe, J. F. Stoddart, *Coord. Chem. Rev.* **1999**, *183*, 139-155.

97. H. Hofmeier, U. S. Schubert, *Chem. Commun.* **2005**, 2423-2432.

98. M. Wilchek, E. A. Bayer, *Anal. Biochem.* **1988**, *171*, 1-32.

99. N. M. Green, *Methods in Enzymology*, **1990**, 51-67.

100. M. González, C. E. Argaraña, G. D. Fidelio, *Biomol. Eng.* **1999**, *16*, 67-72.

101. N. M. Green, *Advances in Protein Chemistry* **1975,** Ed. M. C. Anson, J. T. Edsell, Acad. Press, New York, 85-133.

102. M. J. Swamy, Biochem. *Mol. Biol. Int.* **1995**, *36*, 219-225.

103. A. Chilkoti, P. S. Stayton, *J. Am. Chem. Soc.* **1995**, *117*, 10622-10628.

104. M. González, L. A. Bagatolli, I. Echabe, J. L. R. Arrondo, C. E. Argaraña, C. R. Cantor, G. D. Fidelo, *J. Biol. Chem.* **1997**, *272*, 11288-11294.

105. M. L. Jones, G. P. Kurzban, *Biochemistry* **1995**, *34*, 11750-11756.

106. R. Blankenburg, P. Meller, H. Ringsdorf, C. Salesse, *Biochemistry*, **1989**, *28*, 8214-8221.

107. J. Spinke, M. Liley, H.-J. Guder, L. Angermaier, W. Knoll, *Langmuir* **1993**, *9*, 1821-1825.

108. P. L. Edmiston, J. E. Lee, S-S. Cheng, S. S. Saavedra, *J. Am. Chem. Soc.* **1997**, *119*, 560-570.

109. L. L. Wood, S-S. Cheng, P. L. Edmiston, S. S. Saavedra, *J. Am. Chem. Soc.* **1997**, *119*, 571-576.

110. P. L. Edmiston, S. S. Saavedra, *Biophys. J.* **1998**, *74*, 999-1006.

111. P. L. Edmiston, S. S. Saavedra, *J. Am. Chem. Soc.* **1998**, *120*, 1665-1671.

112. M. Wilchek, E. A. Bayer, *Anal. Biochem.* **1988**, *171*, 1-32.

113. J.-L. Guesdon, T. Ternynck, S. Avrameas, *J. Histochem. Cytochem.* **1979**, *27*, 1131-1139.

114. F. Kohen, Y. Amir-Zaltsman, C. J. Strasburger, E. A. Bayer, M. Wilcheck, *Complementary Immunoassays* **1987**, Ed. W. P. Collins, 57-69.

115. J. I. Anzai, Y. Kobayashi, N. Nakamura, M. Nishimura, T. Hoshi, *Langmuir* **1999**, *15*, 221-226.

116. J. Porath, J. Carlsson, I. Olsson, G. Belfrage, *Nature* **1975**, *258*, 589-599.

117. C. Dietrich, L. Schmitt, R. Tampé, *Proc. Natl. Acad. Sci. USA* **1995**, *92*, 9014-9018.

118. S. Hutschenreiter, A. Tinazli, K. Model, R. Tampé, *EMBO J.* **2004**, *23*, 2488-2497.

119. I. T. Dorn, R. Escrich, E. Seemüller, R. Guckenberger, R. Tampé, *J. Mol. Biol.* **1999**, *288*, 1027-1036.

120. I. T. Dorn, K. Pawlitschko, S. C. Pettinger, R. Tampé, *Biol. Chem.* **1998**, *379*, 1151-1159.

121. D. R. Shnek, D. W. Pack, D. Y. Sasaki, F. H. Arnold, *Langmuir* **1994**, *10*, 2382-2388.

122. S. Lata, A. Reichel, R. Brock, R. Tampé, J. Piehler, *J. Am. Chem. Soc.* **2005**, *127*, 10205-10215.

123. L. Schmitt, C. Dietrich, R. Tampé, *J. Am. Chem. Soc.* **1994**, *116*, 8485-8491.

124. H. M. McConnell, *Annu. Rev. Phys. Chem.* **1991**, *42*, 171-195.

125. I. T. Dorn, K. R. Neumaier, R. Tampé, *J. Am. Chem. Soc.* **1998**, *120*, 2753-2763.

126. S. Lata, J. Piehler, *J. Anal. Chem.* **2005**, *77*, 1096-1105.

127. L. Nieba, S. E. Nieba-Axmann, A. Persson, M. Hämäläinen, F. Edebratt, A. Hansson, J. Lidholm, K. Magnusson, Å. Frostell Karlsson, A. Plückthun, *Anal. Biochem.* **1997**, *252*, 217-228.

128. A. Tinazli, J. L. Tang, R. Valiokas, S. Picuric, S. Lata, J. Piehler, B. Liedberg, R. Tampé, *Chem. Eur. J.* **2005**, *11*, 5249-5259.

129. J. Parrado, J. Bautista, *Biosci. Biotech. Biochem.* **1995**, *59*, 906-907.

130. P. Ringler, G. E. Schulz, *Science* **2003**, *302*, 106-109.

131. Y. Xia, G. M. Whitesides, *Angew. Chem. Int. Ed.* **1998**, *37*, 550-575.

132. N. Kohli, R. M. Worden, I. Lee, *Chem. Commun.* **2005**, 316-318.

133. R. Valiokas, G. Klenkar, A. Tinzali, R. Tampé, B. Liedberg, J. Piehler, *ChemBioChem* **2006**, *7*, 1325-1329.

134. J. Lahiri, E. Ostuni, G. M. Whitesides, *Langmuir* **1999**, *15*, 2055-2060.

135. R. Langer, D. A. Tirrell, *Nature* **2004**, 487-492.

136. J. J. Pancrazio, J. P. Whelan, D. A. Borkholder, W. Ma, D. A. Stenger, *Ann. Biomed. Eng.* **1999**, *27*, 697-711.

137. I. V. Jani, G. Janossy, D. W. G. Brown, F. Mandy, *Lancet Infect. Dis.* **2002**, *2*, 243-250.

138. M. Balic, N. Dandachi, G. Hofmann, H. Samonigg, H. Loibner, A. Obwaller, A. Van der Kooi, A. G. J. Tibbe, G. V. Doyle, L. W. M. M. Terstappen, T. Bauernhof, *Cyt. Part B* **2005**, *68B*, 25-30.

139. N. Boudreau, M. Bissell, *Curr. Opin. Cell Biol.* **1998**, *10*, 640-646.

140. A. Huttenlocher, R. R. Sandborg, A. F. Horwitz, *Curr. Opin. Cell. Biol.* **1995**, *7*, 697-706.

141. M. D. Pierschbacher, E. Ruoslahti, *Nature*, **1984**, *309*, 30-33.

142. E. Ruoslahti, M. D. Pierschbacher, *Science*, **1987**, *238*, 491-497.

143. M. Mrksich, *Chem. Soc. Rev.* **2000**, *29*, 267-273.

144. B. T. Houseman, M. Mrksich, *J. Org. Chem.* **1998**, *63*, 7552-7555.

145. C. Roberts, C. S. Chen, M. Mrksich, V. Martichonok, D. E. Ingber, G. M. Whitesides, *J. Am. Chem. Soc.* **1998**, *120*, 6548-6555.

146. X. Jiang, R. Ferrigno, M. Mrksich, G. M. Whitesides, *J. Am. Chem. Soc.* **2003**, *125*, 2366-2367.

147. W. S. Yeo, M. Mrksich, *Langmuir* **2006**, *22*, 10816-10820.

148. L. L. Kiessling, J. E. Gestwicki, L. E. Strong, *Curr. Opin. Chem. Biol.* **2000**, *4*, 696-703.

149. J. E. Gestwicki, L.L. Kiessling, *Nature* **2002**, *415*, 81-84.

150. T. B. H. Geijtenbeek, R. Torensma, S. J. van Vliet, G. C. F. van Duijnhoven, G. J. Adema, Y. van Kooyk, C. G. Figdor, *Cell* **2000**, *100*, 575-585.

151. T. B. H. Geijtenbeek, D. S. Kwon, R. Torensma, S. J. van Vliet, G. C. F. van Duijnhoven, J. Middel, I. L. M. H. A. Cornelissen, H. S. L. M. Nottet, V. N. KewalRamani, D. R. Littman, C. G. Figdor, Y. van Kooyk, *Cell* **2000**, *100*, 587-597.

152. N. Horan, L. Yan, H. Isobe, G. M. Whitesides, D. Kahne, *Proc. Natl. Acad. Sci. USA* **1999**, *96*, 11782-11786.

153. C. B. Herbert, T. L. McLernon, C. L. Hypolite, D. N. Adams, L. Pikus, C-C. Huang, G. B. Fields, P. C. Letourneau, M. D. Distefano, W. S. Hu, *Chem. Biol.* **1997**, *4*, 731-737.

3

Self-assembly of a molecular capsule based on ionic interactions in solution and at the molecular printboard*

*In this chapter the self-assembly of a molecular capsule based on ionic interactions between two oppositely charged calix[4]arenes (**1** and **2**) in solution and at the molecular printboard is discussed. Calix[4]arene **1** is functionalized at the lower rim with four adamantyl moieties, through which stable positioning at the β-cyclodextrin (βCD) molecular printboard is enabled. At the upper rim four guanidinium moieties are present to enable capsule formation with tetrasulfonate calix[4]arene **2**. Isothermal titration calorimetry (ITC) studies proved the formation of the capsule in solution. By means of surface plasmon resonance (SPR) spectroscopy the association constant for capsule formation at the surface was determined as well as the repeated build-up and subsequent breakdown of the capsule at the molecular printboard. It turned out, that capsule formation at the molecular printboard ($K_a = 3.5 \times 10^6 \ M^{-1}$) is comparable to capsule formation in solution ($K_a = 7.5 \times 10^5 \ M^{-1}$).*

3.1   Introduction

Multivalent interactions are widespread in nature[1] and supramolecular chemistry,[1,2,3] and describe the simultaneous binding of multiple guest entities on one molecule to multiple host entities on another.[4] Multivalent binding processes differ markedly from monovalent binding processes, e.g. they consist of both inter- and intramolecular interactions, and dissociation is in general slow and can be influenced by a competitor in solution.[4]

Multivalent interactions are not only important in nature, but they are also crucial when one wants to develop stable assemblies at surfaces.[5,6] Multivalent interactions can provide such high binding constants that molecules can be positioned on molecular printboards in a both thermodynamically and kinetically stable fashion.[7] Furthermore, multivalent host-guest interactions allow for controllable adsorption and desorption by variation of the type and number of host-guest interactions. By making use of host-guest interactions, it becomes possible to build nanosized structures in a controlled fashion at the molecular printboard.[8-10] The same interactions can also be exploited for creating patterns of molecules on surfaces through supramolecular microcontact printing (μCP) or dip-pen nanolithography (DPN).[11]

Much research has already been performed on the formation of non-covalent containers in solution, most of them being based on hydrogen bonding[12,13] and on metal-ligand interactions.[14-17] Applications for those containers are for example the encapsulation of drugs and the active transport or delivery of these drugs,[18] or for catalysis.[19] There are, however, only a few cases in which capsules are self-assembled at a surface. In these cases, the bottom part of the capsule is immobilized directly at the solid substrate via self-assembly of thiols on gold, such as the attachment of a resorcin[4]arene-based carceplex in a SAM on gold, which has been reported before.[20,21] Another example is the formation of a molecular cage based on metal-ligand coordination, which has been achieved at a surface, while one of the components was immobilized to a gold support.[22]

The use of electrostatic interactions for the formation of capsules has been extensively shown in solution.[23-27] In this chapter the use of orthogonal host-guest and ionic interactions, which allow a stepwise build-up and breakdown of a capsule at the molecular printboard, is described. The capsule consists of a calixarene, which is

modified at the lower rim with four adamantyl moieties to ensure binding to the molecular printboard, and at the upper rim with guanidinium moieties to enable binding to a second calixarene with four tetrasulfonate moieties at the upper rim. Both the assembly in solution and at the surface is discussed and a comparison is made.

3.2   Results and discussion

3.2.1   System

The capsule that is assembled in solution and at the molecular printboard consists of calix[4]arenes **1** and **2** (Chart 3.1a). The bottom part of the capsule is calix[4]arene **1**, the lower rim of which is modified with four tetra(ethylene glycol) chains which each possess an adamantyl functionality, while the upper rim is modified with four guanidinium groups to enable interaction with **2** and increase water solubility. The top part of the capsule is the tetrasulfonate calix[4]arene **2**. The resulting capsule is based on the ionic interactions between the two oppositely charged upper rims of these calix[4]arenes. In Chart 3.1b the capsule comprised of **1** and **2** is depicted. The molecular printboard has been introduced previously (Chapter 2).
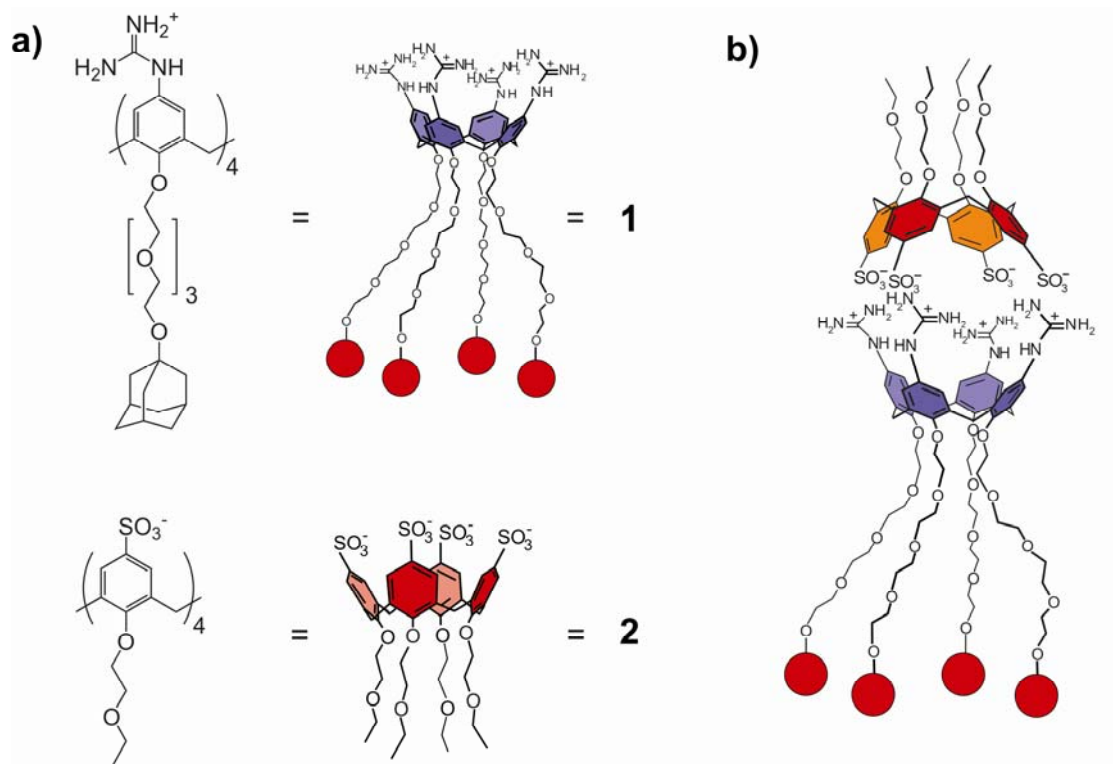

Chart 3.1 *a) Building blocks used in this study: tetraguanidinium calix[4]arene (**1**), and tetrasulfonate calix[4]arene (**2**); b) capsule **1·2**.*

3.2.2 Synthesis of calix[4]arene 1 and calix[4]arene 2

Tetrasulfonate calix[4]arene **2** was synthesized according to literature procedures.[28] Tetraguanidinium calix[4]arene **1** was synthesized as outlined in Scheme 3.1, and as follows:[29] 1-Adamantyl tetraethyleneglycol tosylate was reacted with tetrahydroxy-*p-tert*-butylcalix[4]arene **3** at 80 °C in dry DMF using NaH as a base to give the tetra(adamantyl tetraethylene glycol)-functionalized calix[4]arene **4**. Substitution of the *tert*-butyl for nitro groups by an *ipso*-nitration reaction using glacial acetic acid and nitric acid gave tetranitro-calix[4]arene **5**. Low temperature and dry conditions are prerequisites for this reaction in order to prevent elimination of the adamantoxy groups under the strongly acidic conditions used. Reduction of the nitro groups using hydrazine monohydrate and Pd/C in absolute ethanol gave the tetraamine calix[4]arene **6** in nearly quantitative yield. Introduction of the BOC-protected guanidinium groups using bis-BOC-thiorea was performed under the conditions reported by Qian[30] and led to the formation of **7**. Specific removal of the BOC groups was achieved using 2 N HCl in dioxane, giving the desired product **1** as a tetrachloride salt.
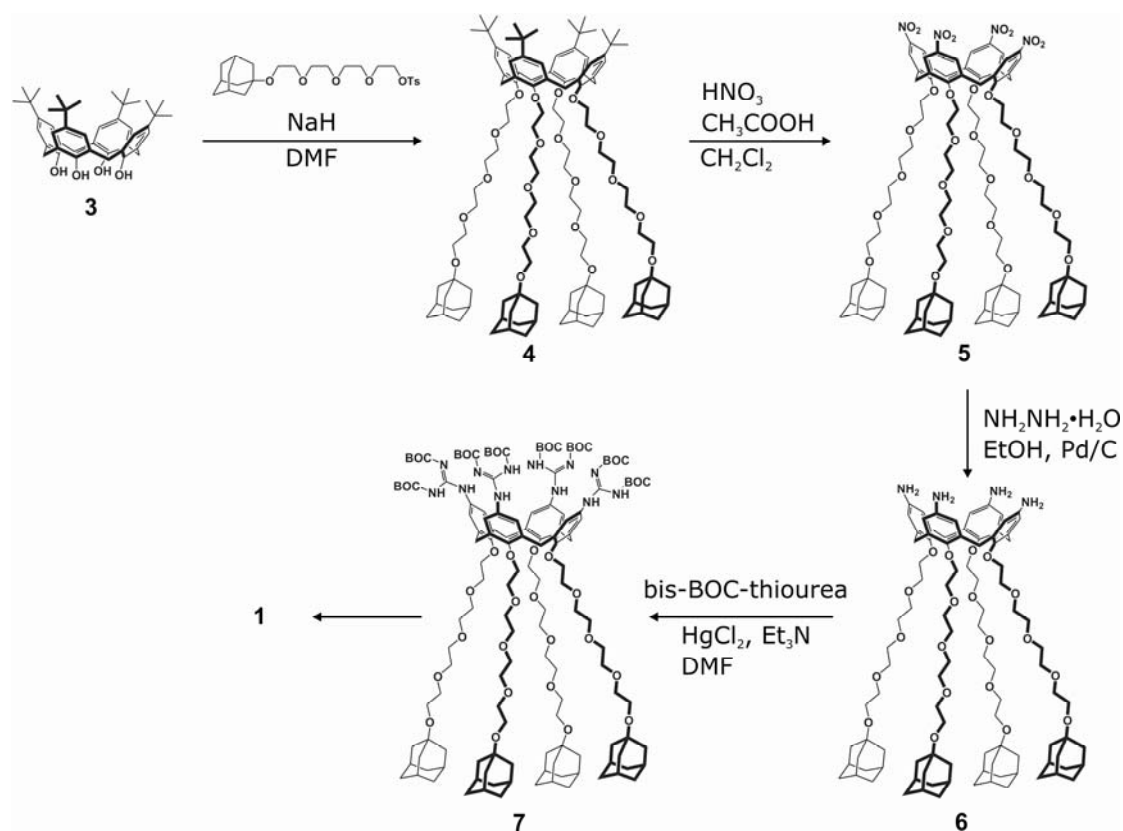
Scheme 3.1 Synthetic route towards tetraguanidinium calix[4]arene 1.

3.2.3 Formation of the molecular capsule 1•2 in solution

Water solubility of tetrasulfonate calix[4]arene **2** is ensured through the charged groups and by the ethylene glycol chains attached respectively at the upper and lower rims of the calix[4]arene scaffold. Also tetraguanidinium calix[4]arene **1** possesses four charges and long ethylene glycol chains for this purpose, however, precipitation was observed upon mixing the two components in water. This is a consequence of the neutralization of the charges upon capsule formation and of the presence of the four adamantyl groups which further limit the water solubility of the assembly. Upon addition of βCD again a clear aqueous solution was obtained, caused by the inclusion of the adamantyl groups in the βCD cavities, rendering the complex more water soluble.

The binding constant for capsule formation in solution was studied by isothermal titration calorimetry (ITC) in H_2O containing βCD (1.0×10^{-2} M). The presence of βCD in both cell and burette makes sure that no heat effects are monitored due to the βCD-adamantyl interactions. An ITC titration of 5.0×10^{-4} M **2** to 5.0×10^{-5} M **1** showed a 1:1 binding event (Figure 3.1a and b). The positive values for both ΔH^o (2.5 kcal•mol^{-1}) and $T\Delta S^o$ (10.5 kcal•mol^{-1}) account for an endothermic, entropy-driven process. As found for similar systems, the formation of molecular capsules based on ionic interactions is driven by the desolvation of the charged groups upon complex formation. Highly ordered solvent molecules are released into the bulk solvent thus resulting in a gain in entropy which is reflected in the positive value for $T\Delta S^o$. The unfavorable value of ΔH^o suggests that the enthalpy needed to desolvate the charged groups overrides the enthalpy gained by the self-assembly process. The data obtained from the titration were successfully fitted to a 1:1 binding model giving an association constant K_a of $(7.5 \pm 1.2) \times 10^5$ M^{-1}.

The formation of a well-defined assembly was also proven by ESI mass spectrometry and ^{1}H NMR studies in which the formation of aggregates could be ruled out, since no broadening of the NMR signals could be observed.

The binding of **1** to βCD was also studied by means of ITC. A 1.0×10^{-4} M solution of βCD was titrated to a 2.25×10^{-5} M solution of calix[4]arene **1**. The resulting enthalphogram (Figure 3.1c) is indicative of the formation of a 4:1 assembly, as suggested by the presence of an inflection point at a molar ratio of 4. Fitting showed that $\Delta H^o = -7.1$ kcal/mol, and $K_i = 2.9 \times 10^4$ M^{-1}.
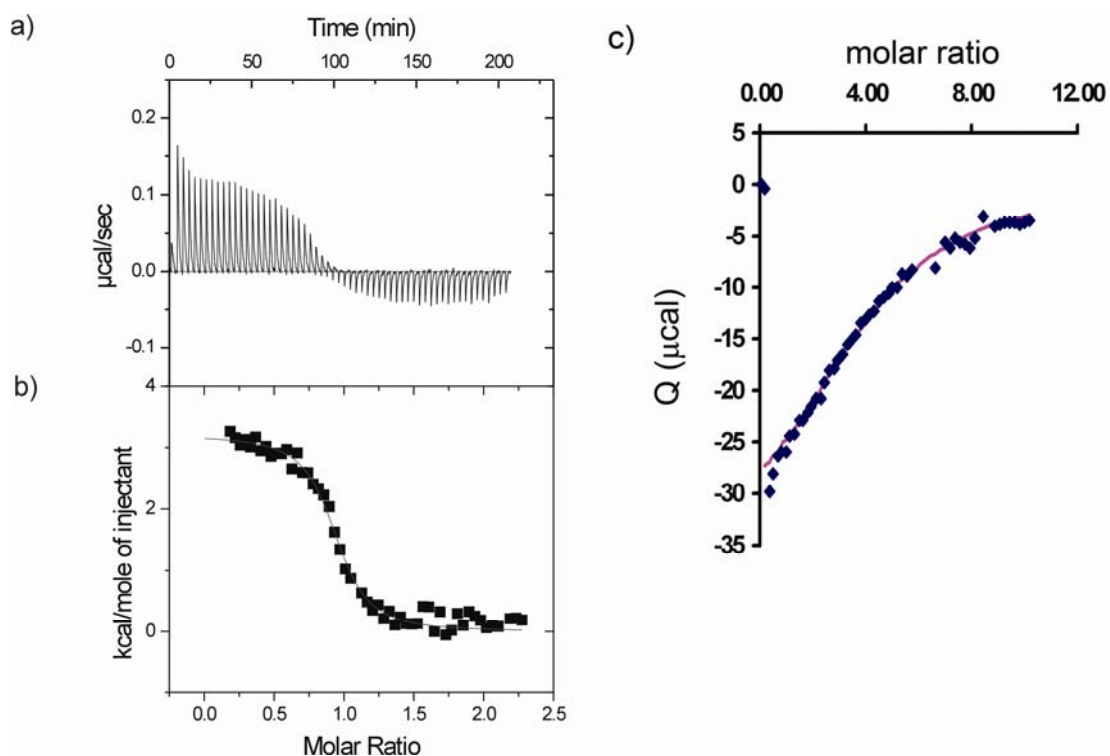
Figure 3.1 Calorimetric titration of **1** (5×10^{-5} M) with **2** (5×10^{-4} M) in H_2O containing βCD (1×10^{2} M) and KCl (1×10^{-2} M) at 298 K. Data of heat evolution with injection of **2** (a). Resulting binding curve (markers) and best fit (line) to a 1:1 model (b). Calorimetric titration of **1** (1.0×10^{-4} M) with βCD (2.3×10^{-5} M) in H_2O (c), binding curve (markers) and best fit (line) to a 4:1 model.

3.2.4 Formation of the molecular capsule 1•2 at the molecular printboard

It is important for the build-up of the capsule at the molecular printboard (Scheme 3.2) that the attachment of adamantyl-modified calix[4]arene **1** is stable. Therefore, the adsorption and (attempted) desorption thereof were studied first.
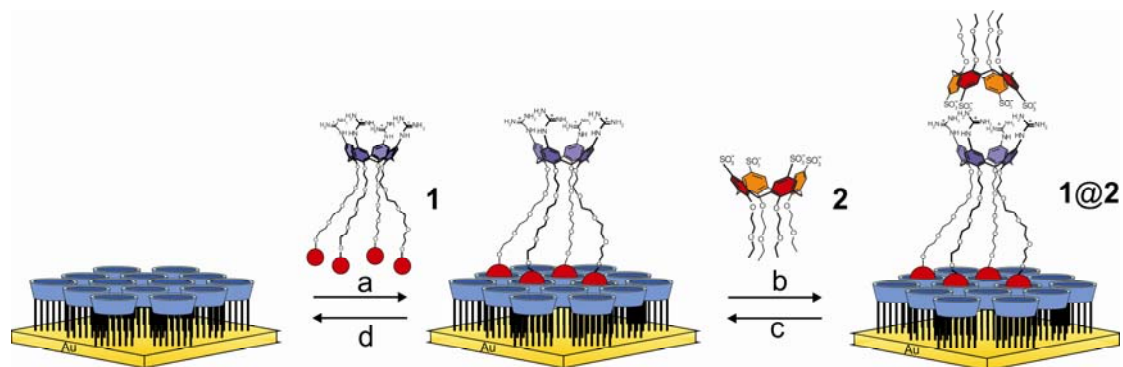
Scheme 3.2 *Schematic representation of the build-up (a,b) and subsequent breakdown (c,d) of the capsule* **2**@**1** *at the molecular printboard.*

In an SPR experiment, **1** was adsorbed at the molecular printboard at a βCD background of 4 mM. The binding of **1** to the molecular printboard proved to be irreversible, as it appeared impossible to remove **1** by extensive rinsing procedures in which competition was induced by using a high concentration of 8 mM native βCD in solution (Figure 3.2 left). Similarly, rinsing with 1 M KCl did not result in the removal of **3**. This is explained by the multivalency model as described previously.[7,31] The association constant of **3** to the molecular printboard is expected to be in the order of ~10^{15} M^{-1}. In contrast, subsequent rinsing procedures with ethanol and 2-propanol did result in the removal of **3** from the surface (Figure 3.2 right), by weakening the intrinsic hydrophobic interaction strength ($K_{i,s}$) between the βCD cavities and the adamantyl functionalities. Thus we have shown that the lower halve of the capsule can be strongly immobilized at the molecular printboard in aqueous solutions, but that the application of organic solvents provides a way of removing it from the surface again as this lowers $K_{i,s}$ and thus the stability of the assembly as a whole.
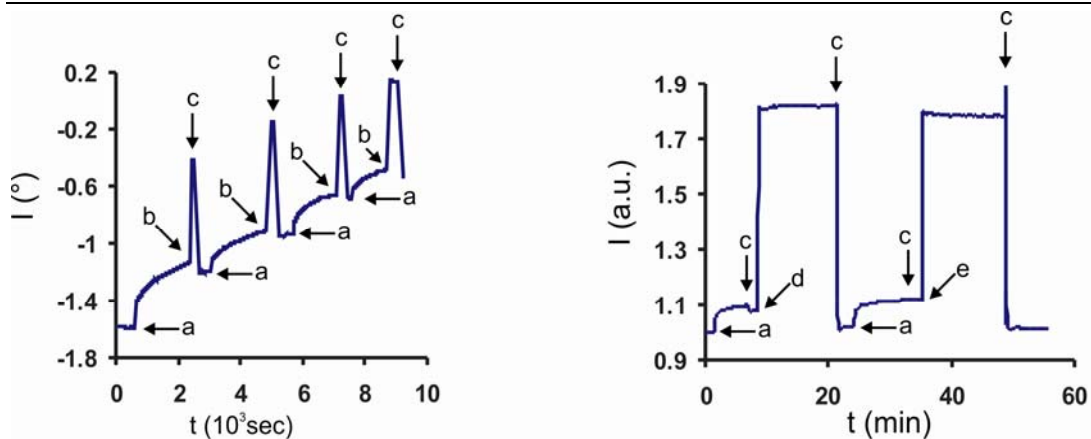
Figure 3.2 SPR sensogram for the adsorption of **1** followed by attempted desorption with βCD (left) and ethanol and 2-propanol (right) at molecular printboards; 0.1 mM **1** in 4 mM βCD (a), 8 mM βCD (b), 4 mM βCD (c), ethanol (d), and 2-propanol (e).

SPR titrations of the addition of **2** to a monolayer of **1** on the molecular printboard were performed, and fitted to a Langmuir isotherm (Figure 3.3). The association constant was $(3.5 \pm 1.6) \times 10^6$ M^{-1}, which is slightly higher than the association constant found in solution (7.5×10^5 M^{-1}). This could be due to some form of positive cooperativity, resulting from stronger electrostatic interactions of the many calixarenes **1** at the surface. However, the slightly higher association constant found on the surface compared to solution cannot be due to the formation of a 1:2 complex, because in that case an 8+/4- ion pair is to be expected, which should give rise to an association constant of approx. 10^{12} M^{-1}. It is obvious that the association constant observed here is far lower than this value.
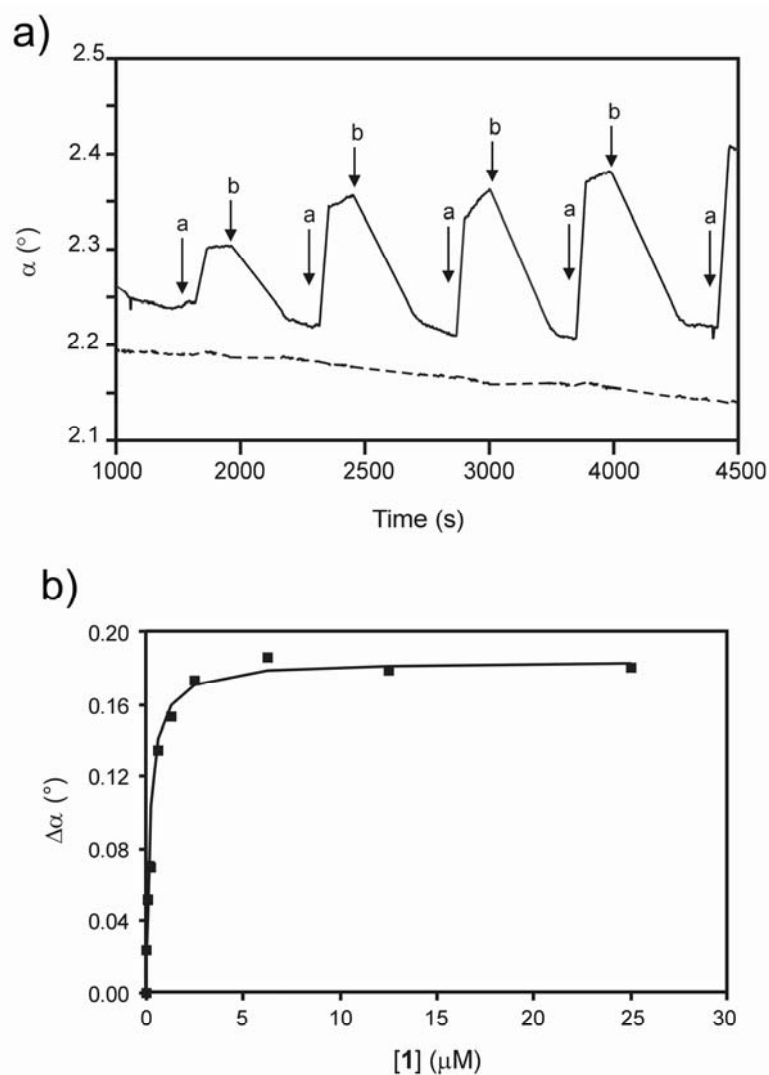
Figure 3.3 *a) Part of the SPR sensogram for the titration of increasing amounts of **2** to the molecular printboard saturated with **1** (solid line) and to the molecular printboard (dashed line). Additions of increasing amounts of a 1 × 10⁻⁵ M solution of **2** are depicted. (All solutions in 1 × 10⁻² M aqueous KCl). b) Data points (markers) and best fit (line) for the change in SPR angle of the monolayer of **1**@molecular printboard as a function of the concentration of **2** (right).*

The capsule could be built up in two steps at the molecular printboard, and broken down again in two steps (Scheme 3.2: a→b→c→d). This assembly and disassembly process can clearly be followed by SPR spectroscopy (Figure 3.4). First a monolayer of **1** was formed at the molecular printboard (Scheme 3.2 and Figure 3.4, step a). Subsequently, **2** was attached through ionic interactions on top of the monolayer of **1** (Scheme 3.2 and Figure 3.4, step b). At this point, the capsule is present at the molecular printboard. The stepwise assembly of the capsule is followed by the

stepwise disassembly of the capsule. First, a rinsing procedure with 1 M KCl was performed (Scheme 3.2 and Figure 3.4, step c), in which the top part of the capsule, **2**, was removed by weakening of the ionic interactions due to charge screening at this high salt concentration. As noted before, this rinsing step does not affect the binding of **3** at the molecular printboard. After restoring the 10^{-2} M KCl background solution, a rinsing procedure with 2-propanol was applied in order to remove the bottom part of the capsule (step d). Hereafter the molecular printboard appeared to be clean, since the whole procedure could be repeated without loss of efficiency (Figure 3.4).
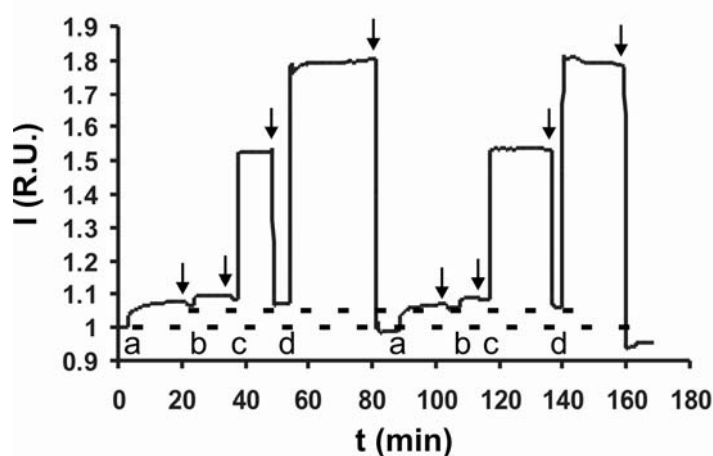
Figure 3.4 *SPR sensogram showing the stepwise assembly and the subsequent stepwise disassembly of the molecular capsule **2@1** at the molecular printboard. The arrows (↓) indicate a background change to 10 mM aqueous KCl; a indicates adsorption of **3** (0.1 mM in 4.0 mM βCD + 10 mM KCl); b indicates adsorption of **2** (0.1 mM in 4.0 mM βCD + 10 mM KCl); c indicates desorption of **2** by 1 M KCl and d indicates desorption of **1** by 2-propanol.*

3.3   Conclusions

In this chapter it has been shown that a molecular capsule, based on ionic interactions, can be assembled in solution and on the surface. At the surface the capsule was built through a non-covalent, stepwise procedure which involves a multipoint attachment of the lower building block through a tetravalent adamantyl-βCD interaction. The upper building block was attached through ionic interactions to the lower building block.

In conclusion, these results show that multivalency can result in such strong binding that weaker, orthogonal interactions can be employed in subsequent steps to make more complex assemblies. Furthermore, it emphasizes the versatility of the molecular printboards as a building platform onto which assemblies can be constructed and removed again at will.

3.4   Acknowledgements

The work presented in this chapter was performed in collaboration with Alart Mulder, Francesca Corbellini, and Andrea Sartori.

3.5   Experimental section

General

All moisture-sensitive reactions were carried out under nitrogen atmosphere. Most of the solvents and all reagents were obtained from commercial sources and used without further purification. All dry solvents were prepared according to standard procedures and stored over molecular sieves.

Substrate preparation

Gold substrates for SPR (BK7 glass/2-4 nm Ti/50 nm Au), were obtained from Ssens B.V., Hengelo, The Netherlands. Gold substrates were cleaned by dipping them in piranha (1:3 mixture of concentrated H_2SO_4 and 30% H_2O_2) for 5 s. (*Warning:* piranha should be handled with caution; it can detonate unexpectedly.) After thorough rinsing with Millipore water, they were placed for 10 min in absolute EtOH in order to remove the oxide layer. Subsequently the substrates were placed in a freshly prepared 0.1 mM solution of βCD heptathioether for 16 h at 60 °C. The samples were subsequently rinsed 3 times with $CHCl_3$, EtOH and Millipore water. All solvents used in the monolayer preparation were of p.a. grade.

SPR measurements

SPR titration measurements were performed in a two-channel vibrating mirror angle scan setup based on the Kretschmann configuration, described by Kooyman and co-

workers.[32] Light from a 2 mW HeNe laser is directed onto a prism surface by means of a vibrating mirror. The intensity of the light is measured by means of a large-area photodiode. This setup allows the determination of changes in plasmon angle with an accuracy of 0.0028 °. The gold substrate with the monolayer was optically matched to the prism using an index matching oil. All solutions were made using Millipore water and all solutions were filtered through nanopore filters prior to use.

In a typical experiment a cell placed on top of a βCD monolayer was filled with 800 μL of a 10 mM KCl solution. After stabilization of the SPR signals, the βCD monolayer in one of the cells was saturated with **3** by replacing 720 μL of the buffer solution with a 10 mM KCl buffer solution containing 0.1 mM of **3** and 5 mM of βCD. The system was equilibrated while monitoring the SPR angle change. After stabilization of the SPR signal (typically 30 min) both cells were rinsed with a 10 mM KCl solution by repeatedly replacing 720 μL of the cell solutions with 720 μL of the buffer solution (7 times). Titrations with **2** were performed by systematically replacing an increasing amount of buffer solution with a solution of **2** (1-100 μM) in 10 mM KCl for both cells. Between additions, the cells were rinsed by repeatedly replacing 720 μL of the cell solution with 720 μL of a 1 M KCl solution (7 times). The initial KCl concentration was restored by replacing 720 μL of the cell solutions with 720 μL Millipore water, and subsequent rinsing with 10 mM KCl using the procedure outlined above. Binding constants given above are based on three independent SPR titrations.

The SPR experiments in which the capsule build-up was investigated were performed on a Resonant Probes GmbH SPR instrument. The instrument consists of a HeNe laser (JDS Uniphase, 10 mW, $\lambda = 632.8$ nm) of which the laser light passes through a chopper that is connected to a lock-in amplifier (EG&G 7256). The modulated beam is directed through two polarizers (OWIS) to control the intensity and the plane of polarization of the light. The light is coupled via a high index prism (Scott, LaSFN9) in the Kretschmann configuration to the backside of the gold-coated substrate which is optically matched through a refractive index matching oil (Cargille; series B; $n_D^{25°C} = 1.7000 \pm 0.0002$) at the prism, mounted on a θ-2θ goniometer, in contact with a Teflon cell with a volume of 39 μl and a diameter of 5 mm. The light that leaves the prism passes through a beam splitter, and subsequently the s-polarized light is directed to a reference detector, and the p-polarized light passes through a lens which focuses

the light onto a photodiode detector. Laser fluctuations are filtered out by dividing the intensity of the p-polarized light (I_p) by the intensity of the s-polarized light (I_s). All measurements were performed at a constant angle by reflectivity tracking, and at a flowrate of 0.5 ml/min.

Calorimetry

The titration experiments were carried out using a Microcal VP-ITC microcalorimeter with a cell volume of 1.4115 mL. The formation of the assembly **1•2** has been studied adding aliquots of a 0.5 mM solution of **2**, in the burette, to a 0.05 mM solution of **1**, in the calorimetric cell, and monitoring the heat change after each addition. Dilution experiments showed that, at the experimental concentrations employed here, none of the species showed any detectable aggregation in water. The thermodynamic parameters given above are based on three independent calorimetric titrations. Titration curves were fitted with a 1:1 model using a least-squares fitting procedure and the association constant and enthalpy of binding as independent fitting parameters.

3.6   References

1.   A. Varki, *Glycobiology* **1993**, *3*, 669-672.

2.   F. Hof, S. L. Craig, C. Nuckolls, J. Rebek Jr., *Angew. Chem Int. Ed.* **2002**, *41*, 1488-1508.

3.   G. Decher, *Science* **1997**, *277*, 1232-1237.

4.   M. Mammen, S. K. Choi, G. M. Whitesides, *Angew. Chem. Int. Ed.* **1998**, *37*, 2754-2794.

5.   T. Auletta, B. Dordi, A. Mulder, A. Sartori, S. Onclin, C. M. Bruinink, M. Peter, C. Nijhuis, H. Beijleveld, H. Schonherr, G. J. Vancso, A. Casnati, R. Ungaro, B. J. Ravoo, J. Huskens, D. N. Reinhoudt, *Angew. Chem. Int. Ed.* **2004**, *43*, 369-373.

6.   C. A. Nijhuis, F. Yu, W. Knoll, J. Huskens, D. N. Reinhoudt, *Langmuir* **2005**, *21*, 7866-7874.

7.   J. Huskens, A. Mulder, T. Auletta, C. A. Nijhuis, M. J. W. Ludden, D. N. Reinhoudt, *J. Am. Chem. Soc.* **2004**, *126*, 6784-6797.

8.   O. Crespo-Biel, B. Dordi, D. N. Reinhoudt, J. Huskens, *J. Am. Chem. Soc.* **2005**, *127*, 7594-7600.

9.   O. Crespo-Biel, B. Dordi, P. Maury, M. Péter, D. N. Reinhoudt, J. Huskens, *Chem. Mater.* **2006**, *18*, 2545-2551.

10. V. Mahalingam, S. Onclin, M. Péter, B. J. Ravoo, J. Huskens, D. N. Reinhoudt, *Langmuir* **2004**, *20*, 11756-11762.

11. C. M. Bruinink, C. A. Nijhuis, M. Péter, B. Dordi, O. Crespo-Biel, T. Auletta, A. Mulder, H. Schönherr, G. J. Vancso, J. Huskens, D. N. Reinhoudt, *Chem. Eur. J.* **2005**, *11*, 3988-3996.

12. J. Rebek Jr., *Chem Soc. Rev.* **1996**, *25*, 255-264.

13. J. Rebek Jr., *Chem. Commun.* **2000**, 637-643.

14. P. Jacopozzi, E. Dalcanale, *Angew. Chem. Int. Ed. Engl.* **1997**, *36*, 613-615.

15. U. Radhakrishnam, M. Schweiger, P. J. Stang, *Org. Lett.* **2001**, *3*, 3141-3143.

16. N. Takeda, K. Umemoto, K. Yamaguchi, M. Fujita, *Nature* **1999**, *398*, 794-796.

17. M. Fujita, K. Umemoto, M. Yoshizawa, N. Fujita, T. Kusukawa, K. Biradha, *Chem. Commun.* **2001**, 509-518.

18. Y. K. Kryschenko, S. R. Seidel, D. C. Muddiman, A. I. Nepomuceno, P. J. Stang, *J. Am. Chem. Soc.* **2003**, *125*, 9647-9652.

19. R. Warmuth, E. F. Maverick, C. B. Knobler, D. J. Cram, *J. Org. Chem.* **2003**, *68*, 2077-2088.

20. B. H. Huisman, D. M. Rudkevich, A. Farrán, W. Verboom, F. C. J. M. Van Veggel, D. N. Reinhoudt, *Eur. J. Org. Chem.* **2000**, *2*, 269-274.

21. B. H. Huisman, D. M. Rudkevich, F. C. J. M. Van Veggel, D. N. Reinhoudt, *J. Am. Chem. Soc.* **2001**, *40*, 1892-1896.

22. S. Levi, P. Guatteri, F. C. J. M. van Veggel, G. J. Vancso, E. Dalcanale, D. N. Reinhoudt, *Angew. Chem. Int. Ed.* **2001**, *40*, 1892-1896.

23. M. Wehner, T. Schrader, P. Finocchiaro, S. Failla, G. Consiglio, *Org. Lett.* **2000**, *2*, 605-608.

24. R. Zadmard, T. Schrader, T. Grawe, A. Kraft, *J. Org. Chem.* **2003**, *68*, 6511-6521.

25. R. Fiammengo, P. Timmerman, F. de Jong, D. N. Reinhoudt, *Chem. Commun.* **2000**, 2313-2314.

26. G. V. Oshovsky, D. N. Reinhoudt, W. Verboom, *J. Org. Chem.* **2006**, *71*, 7441-7448.

27. F. Corbellini, L. di Costanzo, M. Crego-Calama, S. Geremia, D. N. Reinhoudt, *J. Am. Chem. Soc.* **2003**, *125*, 9946-9947.

28. R. Fiammengo, P. Timmerman, J. Huskens, K. Versluis, A. J. R. Heck, D. N. Reinhoudt, *Tetrahedron* **2002**, *58*, 757-764.

29. F. Corbellini, A. Mulder, A. Sartori, M. J. W. Ludden, A. Casnati, R. Ungaro, J. Huskens, M. Crego-Calama, D. N. Reinhoudt, *J. Am. Chem. Soc.* **2004**, *126*, 17050-17058.

30. K. S. Kim, L. Qian, *Tetrahedron Lett.* **1993**, *34*, 7677-7680.

31. A. Mulder, T. Auletta, A. Sartori, S. Del Ciotto, A. Casnati, R. Ungaro, J. Huskens, D. N. Reinhoudt, *J. Am. Chem. Soc.* **2004**, *126*, 6627-6636.

32. A. T. M. Lenferink, R. P. H. Kooyman, J. Greve, *J. Sens. Actuators B* **1991**, *3*, 261-265.

4

Attachment of streptavidin to the molecular printboard through orthogonal host-guest and protein-ligand interactions*

Streptavidin (SAv) is attached to β-cyclodextrin (βCD) molecular printboards through orthogonal host-guest and SAv-biotin interactions. The utilized orthogonal linkers consist of a biotin functionality for binding to SAv and one or two adamantyl functionalities to enable host-guest interactions at the molecular printboard. The orthogonality of the binding motifs and the stability of the divalent linker at the molecular printboard allowed the stepwise assembly of the complex, by first adsorbing the linker, followed by SAv. Furthermore, this stepwise assembly allowed the controlled hetero-functionalization of surface-immobilized SAv with biotin-4-fluorescein and cytochrome c. The results presented here show the versatility of orthogonal interactions for the buildup of (bio)molecular nanostructures at interfaces, and the control over protein binding affinity through externally designed, multivalent linkers with the ability of hetero-functionalization of the immobilized protein.

4.1   Introduction

The attachment of proteins at surfaces is important for various fields, such as bioanalytical, biochemical, and biophysical research.[1-6] A strong attachment between the protein and the surface is deemed essential, as well as that binding at the surface is specific, and that the biomolecule of interest is not denatured at the surface.[6] Furthermore, proteins are often used as building blocks at surfaces for the assembly of larger structures.[7,8] The precise and controlled attachment of biomolecules is also a key issue in biotechnology. Streptavidin (SAv) often serves as a model protein in such studies, because of its robustness and its extensive characterization.[9-18]

There are several methods by which proteins can be attached to a surface, such as covalent attachment through primary amines at the protein surface,[19] attachment via a biochemically engineered His$_6$-tag at the protein to a nickel(II)-complexed nitrilotriacetate (NiNTA) linker,[20-24] or via a SAv-biotin linkage.[7] In most of these manners, however, kinetics and thermodynamics of adsorption and desorption can not be controlled at will. In the NiNTA-His-tag system,[24,25] however, multivalent chelator head groups can be applied, and thus proteins can be immobilized at NiNTA surfaces with high affinities, specificities, a well-defined stoichiometries, and even controlled orientation.

Monolayers of biotin have been employed before for the attachment of SAv to surfaces.[7,26-31] In these studies, it has been shown that the attachment of SAv to a biotin monolayer occurs through the use of two biotin binding pockets of SAv, and that the two remaining biotin binding pockets are available for further functionalization with biotinylated (bio)molecules. Such SAv monolayers therefore can serve as platforms for further bio-functionalization, e.g. for the development of hormone sensors as shown by Knoll *et al.*[7]

Cytochrome *c* (cyt *c*) is a small (12.2 kDa) redox protein with one heme centre, that has been studied extensively.[32-34] The redox potentials of the different class I cyt *c* vary between +200 and +350 mV (*vs.* SHE).[34-36] Heme, which is the iron complex of protoporphyrin IX, is a rigid and planar molecule, having four pyrrole groups which are linked by methylene bridges to form a tetrapyrrole ring. The heme group as it is present in cyt *c* is covalently bound to the polypeptide chain. An important function of cyt *c* is the electron transfer between cytochrome *c* reductase and cytochrome *c* oxidase.

The adsorption of cyt *c* to SAMs has been studied before.[37-39] Fragoso *et al.* for instance have described the surface immobilization of cyt *c* via adamantyl moieties that are incorporated in the protein to βCD SAMs on Ag. They showed that cyt *c*, when bound in a supramolecular fashion to a surface, is more stable than when physisorbed to a surface.[40]

The aim of this work is the controlled attachment of a protein to a surface with respect to kinetics, thermodynamics and orientation, and with the potential of stimulated desorption.[41] Through the stepwise assembly of SAv to the molecular printboard, controlled hetero-functionalization of SAv is possible, which is impossible in solution, with the potential to control the orientation of the protein towards the surface upon immobilization. Firm attachment of the protein at the surface is achieved using appropriately functionalized linkers, while the protein is still in a liquid-like environment. In this chapter, the attachment of SAv to the molecular printboard through host-guest interactions using orthogonal linkers is discussed. The aim is to combine the robust, well-known SAv-biotin interaction motif for the formation of protein constructions with the versatility of the βCD host-guest interaction motif, for tuning the kinetics, thermodynamics and orientation of the immobilized SAv to the molecular printboard. Therefore, two linkers were developed, both with a biotin functionality to enable binding to SAv, and with one or two adamantyl functionalities to enable binding to the molecular printboard. Surface plasmon resonance (SPR) spectroscopy, atomic force microscopy (AFM), X-ray photoelectron spectroscopy (XPS) and fluorescence spectroscopy were employed (i) to probe specificity of the interactions, (ii) to investigate the orthogonality of the binding motifs, (iii) to study the adsorption and desorption properties of the SAv-linker complexes, (iv) to probe the different assembly schemes for SAv attachment, and (v) to show the possibility of controlled hetero-functionalization of SAv when immobilized in a stepwise manner to the surface. At first this will be shown with a fluorescently labeled biotin moiety, and subsequently with the biotinylated protein cyt *c*. The preservation of electrochemical function of the immobilized cyt *c* after adsorption will be shown by UV/vis absorption and by scanning electrochemical microscopy (SECM), both of which allowed the determination of the surfaceconcentration. The SECM experiments on the molecular printboard are a modification of the route developed before for ferrocene-terminated

dendrimers but had to be optimized because a monolayer of cyt *c* offers much less redox equivalents.[42]

4.2   Results and discussion

4.2.1   System

For the attachment of SAv to the molecular printboard, which are introduced in Chapter 2, two orthogonal linkers were developed, each with a biotin functionality to enable binding to SAv, and one (**1**) or two (**2**) adamantyl functionalities to enable host-guest interactions with the βCD cavities at the surface (Chart 4.1).
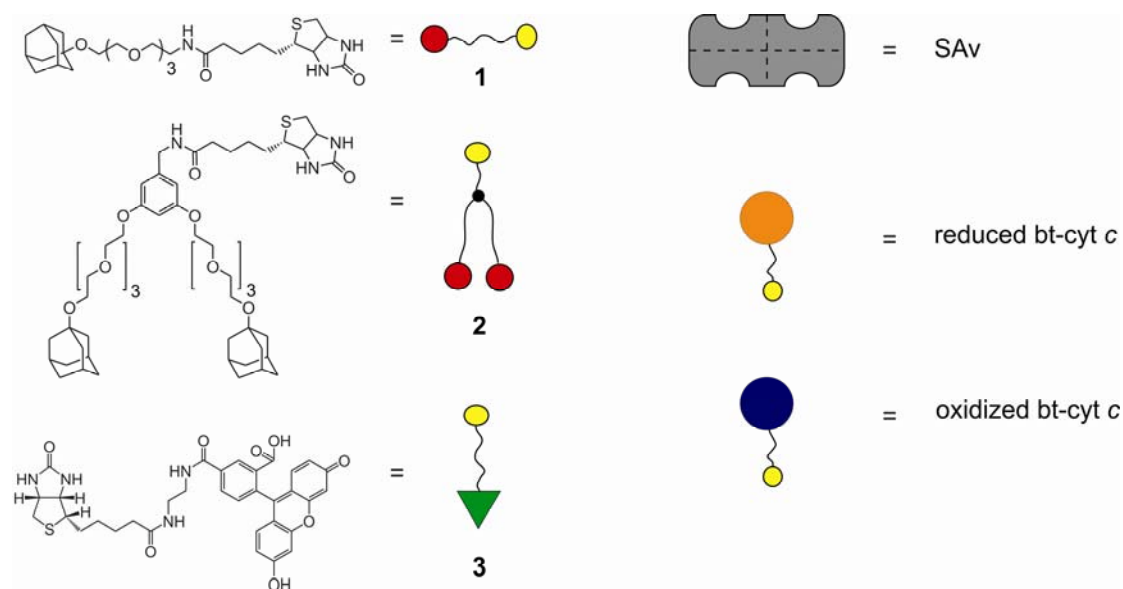

Chart 4.1 *Building blocks used in this study: monovalent linker (**1**), divalent linker (**2**), biotin-4-fluorescein (**3**), SAv, reduced cyt c, and oxidized cyt c.*

The syntheses of **1** and **2** are outlined in Scheme 4.1. Starting materials **5** and **8** were synthesized according to literature procedures.[43] The monovalent linker (**1**) was synthesized from **5** in three subsequent steps. The bromide functionality of the monoadamantyl-functionalized tetra(ethylene glycol) bromide **5** was converted into a phthalimide functionality upon reaction with potassium phthalimide in toluene to yield **6**. The phthalimide functionality was converted into an amino group upon reaction with hydrazine monohydrate in ethanol to yield **7**. Upon reaction of **7** with (+)-biotin 4-nitrophenyl ester, the linker **1** was obtained. The divalent linker (**2**) was prepared from **8** in one step, upon reaction with (+)-biotin 4-nitrophenyl ester.
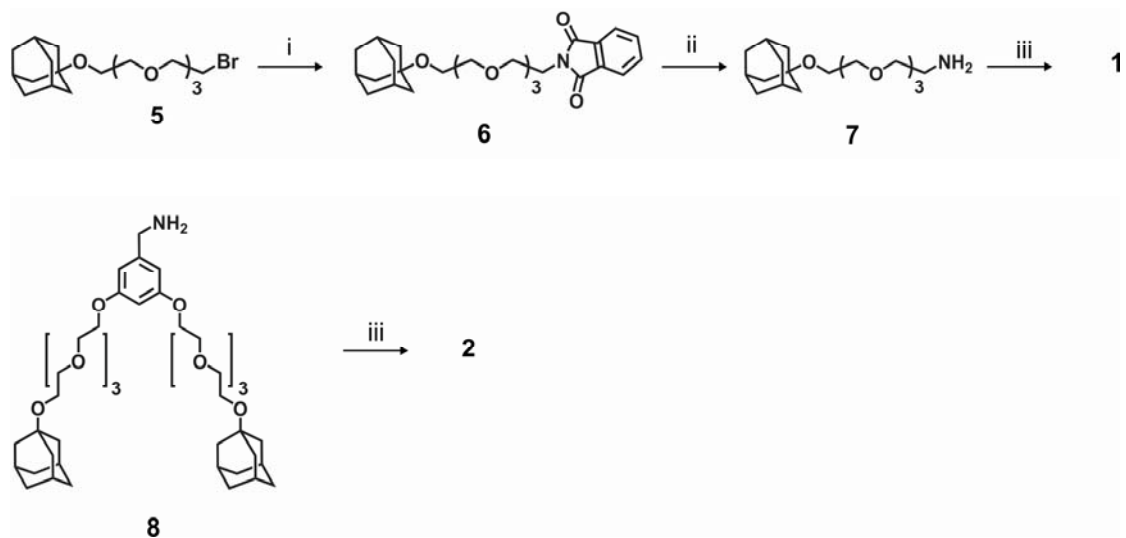
Scheme 4.1 *Synthesis routes towards the monovalent and divalent linkers **1** and **2**: i) potassium phthalimide in DMF, 60 °C, stirring overnight; ii) $N_2H_4 \cdot H_2O$ in ethanol, reflux, stirring overnight; iii) (+)-biotin-4-nitrophenyl ester in DMF and Et_3N, r.t., stirring overnight.*

Scheme 4.2 shows the various adsorption modes that can be envisaged for the adsorption of SAv to the molecular printboard. The potential advantage of using orthogonal interactions is that the order of putting together the interaction motifs can be varied. The consequence of this versatility for our system is that the linkers can be bound in solution to SAv by the biotin-SAv interaction followed by adsorption to the molecular printboard (Scheme 4.2, routes A and B), or that the linkers can be first adsorbed to the molecular printboard followed by SAv attachment (Scheme 4.2, routes C and D). For studying assembly schemes A and B, βCD SAMs on gold were placed in a flow cell, and studied by surface plasmon resonance (SPR) spectroscopy. Protein and linker were dissolved together in 10 mM phosphate buffered saline (PBS). The protein concentration used was 1.3×10^{-7} M, while a linker concentration of 1×10^{-4} M was used, unless stated otherwise. This large linker-to-protein ratio ensures that all biotin binding pockets of SAv are occupied. All solutions were flowed over the molecular printboard through the liquid cell, and the flow rate was controlled by a peristaltic pump.
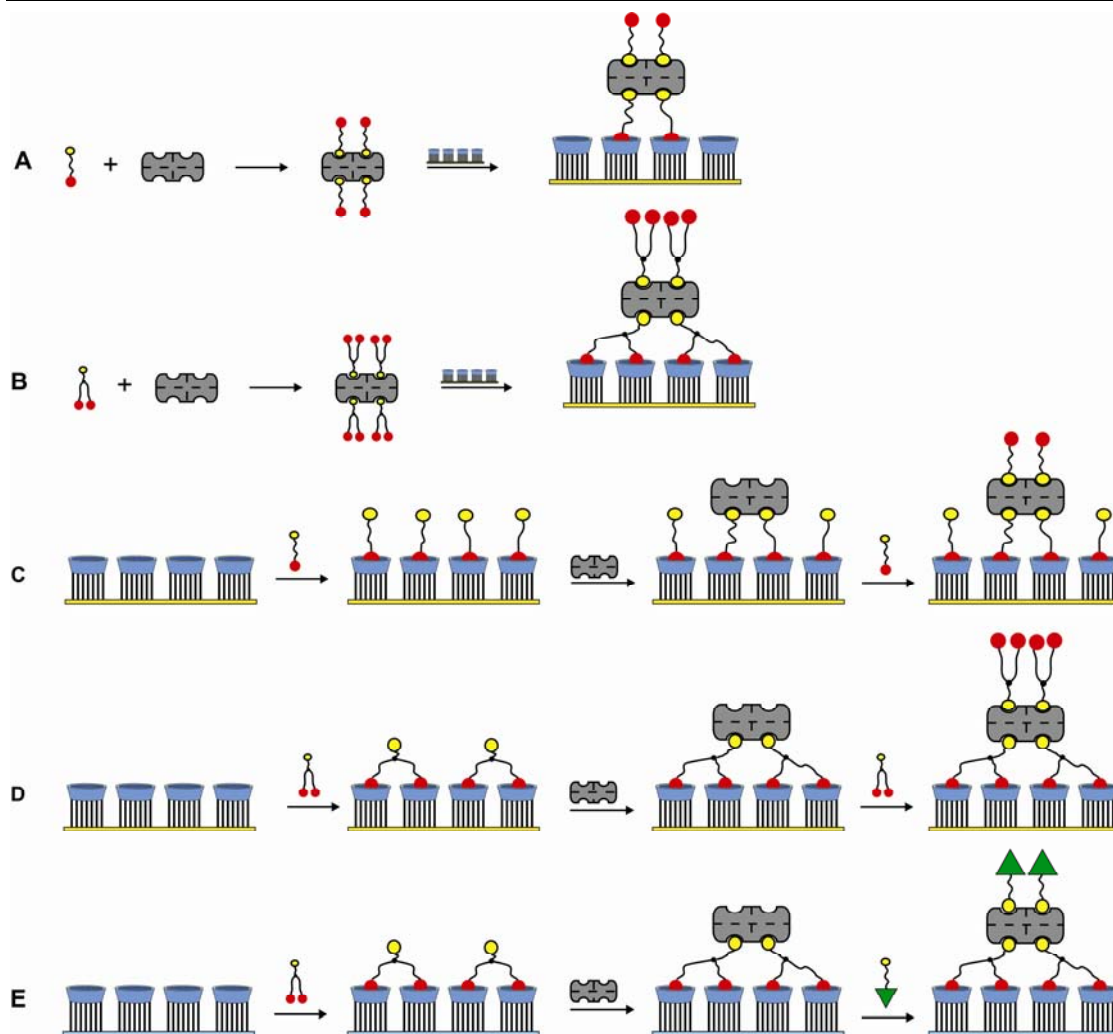
Scheme 4.2 *Adsorption schemes for the assembly of SAv at the molecular printboard through monovalent and divalent linkers.*

4.2.2   Immobilization of streptavidin at the molecular printboard

For the specific attachment of SAv to the molecular printboard via orthogonal linkers, the reduction of nonspecific adsorption is very important. Therefore, several SPR experiments were performed to investigate the conditions for reducing or eliminating nonspecific interactions of SAv to the surface. Nonspecific adsorption of SAv to the molecular printboard is flow rate-dependent (data not shown). When flow rates below 0.4 ml/min were used, the nonspecific adsorption of SAv appeared to be considerable. Flow rates of 0.4 ml/min or higher reduced the nonspecific adsorption to the surface to some extent. Therefore, all subsequent experiments were performed at a flow rate of 0.5 ml/min. Nonspecific adsorption of SAv still occurred, and rinsing with a 10 mM βCD solution led only to partial restoration of the signal (Figure 4.1, black curve). An experiment in which SAv was saturated with 1×10^{-4} M natural biotin

(Figure 4.1, dark grey curve), showed much less nonspecific adsorption. Similarly, adsorption of SAv at a 1 mM βCD background (light grey curve), showed that the nonspecific interactions of SAv to the molecular printboard were strongly reduced, most likely through competition introduced by βCD in solution.
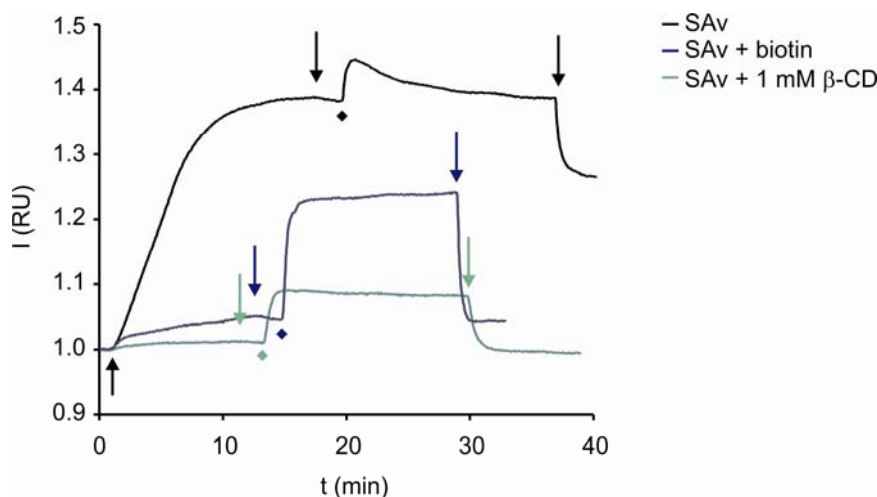

Figure 4.1 *SPR sensograms recorded for the adsorption and (attempted) desorption of SAv in the absence (black curve) or presence of 1 × 10^{-4} mM biotin (dark grey curve) or 1 mM of βCD (light grey curve). Symbols indicate switching of solutions in the SPR flow cell: SAv with or without biotin or βCD in PBS (↑), PBS (↓), 10 mM βCD in PBS (♦).*

In order to test the binding specificity of the linkers towards the molecular printboard, the adsorption of each linker to the molecular printboard was compared to their adsorption to 11-mercapto-1-undecanol SAMs. Such OH-terminated SAMs resemble molecular printboards regarding polarity, but lack the specific host-guest recognition sites. Figure 4.2 shows the SPR sensograms of these adsorption experiments. From Figure 4.2 it is clear that none of the linkers adsorbed to the OH-terminated SAMs. Both linkers however did adsorb to the molecular printboard. This implies that the βCD cavity is needed to ensure binding of the linkers, and thus that the adsorption of the linkers to the molecular printboard is specific.
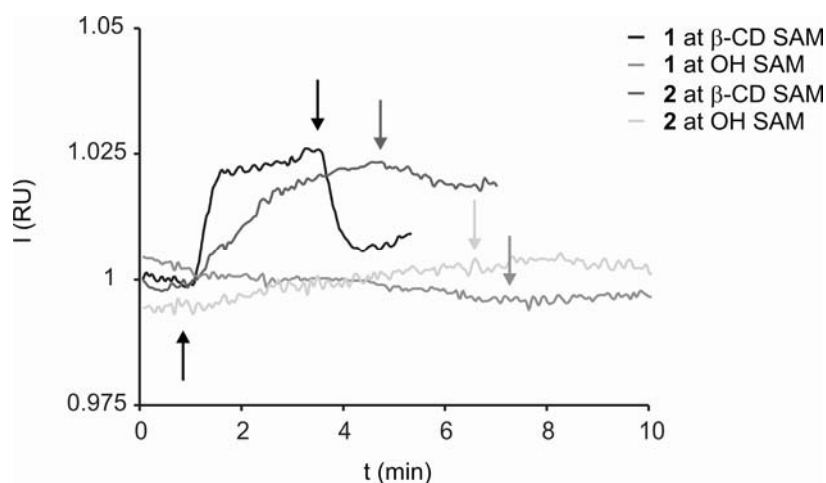
Figure 4.2 *SPR sensograms recorded for the adsorption and (attempted) desorption of the monovalent and divalent linkers to the molecular printboard and 11-mercapto-1-undecanol SAMs in PBS buffer with 1 mM βCD. Symbols indicate switching of solutions in the SPR flow cell: linker with or without 1 mM βCD in PBS (↑), PBS or 1 mM βCD PBS (↓).*

Figure 4.3a shows six SPR sensograms representing the adsorption of the SAv, bound to the monovalent linker (**1**) in solution, at βCD concentrations up to 10 mM, to the molecular printboard. It can be seen that, when the βCD concentration in the buffer was increased, less SAv adsorbed to the surface. When the SAv-monovalent linker complex was flowed over the βCD surface at low βCD concentrations, followed by a rinsing procedure with 10 mM βCD, the baseline was restored. In contrast, when the SAv-monovalent linker complex was flowed over the surface at higher βCD concentrations, some SAv remained at the surface.

Figure 4.3b shows the SPR sensograms for the adsorption of SAv, coupled to the divalent linker (**2**) in solution, to the molecular printboard at βCD concentrations up to 10 mM. At all βCD concentrations the SAv-divalent linker complex adsorbed to the surface in comparable amounts. After a rinsing procedure with 10 mM βCD in solution, it appeared impossible to remove the protein-divalent linker complex from the surface.
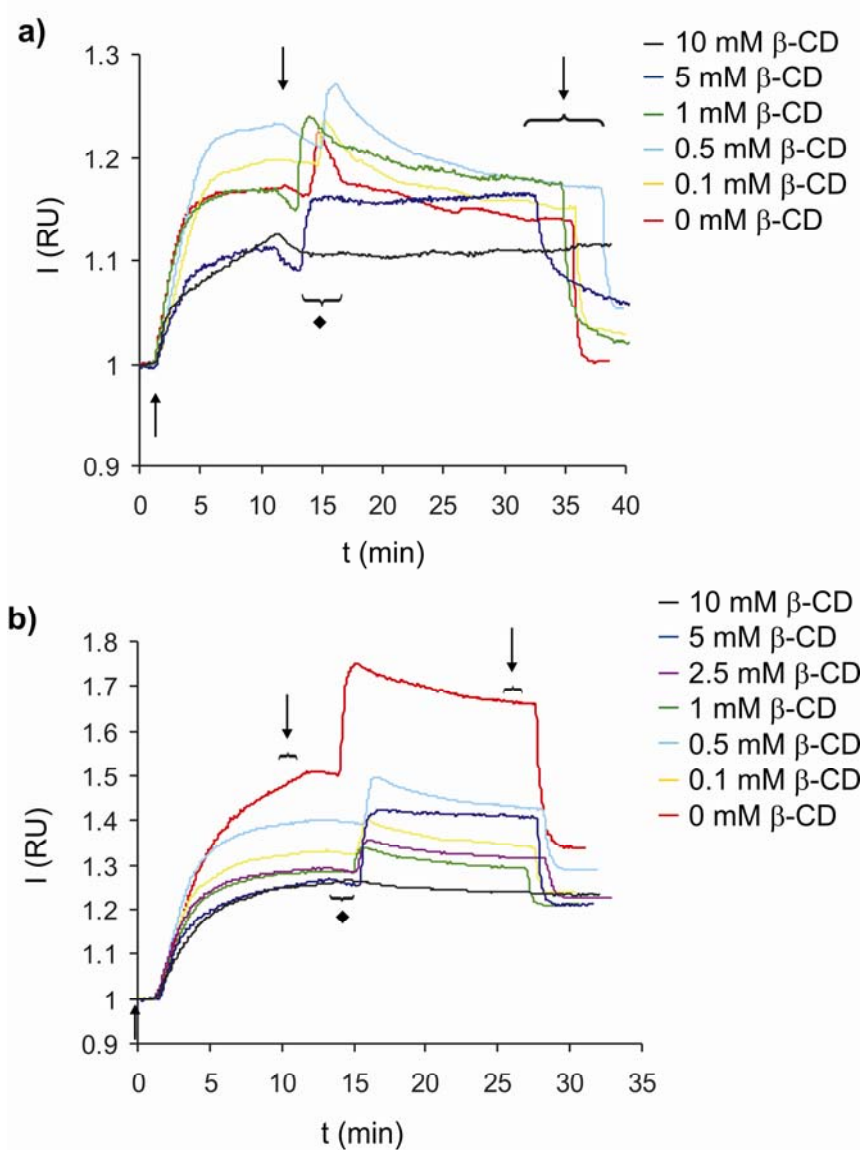
Figure 4.3 *SPR sensograms recorded for the adsorption and (attempted) desorption of SAv complexed to monovalent linker **1** (a) and divalent linker **2** (b) at the molecular printboard at increasing βCD concentrations. Symbols indicate switching of solutions in the SPR flow cell: SAv with mono- or divalent linker in PBS (↑), PBS (↓), 10 mM βCD in PBS (♦).*

From Figure 4.3 can be concluded that, at all βCD concentrations, SAv can be attached to the molecular printboard, with either the mono- or the divalent linker. This emphasizes the importance of the presence of host-guest interactions between the adamantyl functionalities of the linker and the βCD cavity at the SAM. When SAv was attached through the monovalent linker to the molecular printboard, at the lower βCD concentrations, all attached material could be removed from the surface, while at

higher βCD concentrations, most material remained. When the divalent linker was used for attachment, the complex could not be removed from the surface through competition with 10 mM βCD. This difference in binding behavior between mono- and divalent linkers can be explained by examining the valency of the SAv/linker complexes at the molecular printboard. When SAv is complexed with the monovalent linker in solution, four adamantyl functionalities are present at the complex (Scheme 4.2A). From previous studies it is known that a compound attached to the molecular printboard via four or more adamantyl functionalities can not be removed from the surface through competition with a high concentration of βCD in solution (see Chapter 3).[44] This means that, when the adsorbed protein can be desorbed, it must be bound through one to three interactions. The most likely number of interactions with linker **1**, however, will be two, since this corresponds with the expected orientation of SAv with two of its four binding pockets towards the surface (Scheme 4.2A). Complexation of the divalent linker to SAv results in a complex with eight adamantyl functionalities. Analogously this complexation is expected to be tetravalent at the βCD SAM interface (Scheme 4.2B), which is in agreement with the observation that it cannot be removed from the surface. Thus, this method allows choosing between reversible and irreversible complexation to the surface, simply by changing the valency of the host-guest interactions directed towards the surface.

To further investigate the valency effect of the linker on the adsorption of SAv to the molecular printboard, two SPR titrations were performed in which the concentration of SAv was kept constant at 1.3×10^{-7} M and the concentration of the linker was increased stepwise from 0.77 to 7.7 equivalents for the monovalent linker and from 0.38 to 7.7 equivalents for the divalent linker. For both the monovalent and divalent linkers, the experiments were performed at a βCD concentration of 1 mM to suppress nonspecific adsorption of SAv to the surface.

The SPR sensograms at varying linker **1**-SAv ratios are shown in Figure 4.4a. SAv was complexed to linker **1** in solution. Figure 4.4a shows that, after adsorption, only at the highest linker concentration, the original baseline was restored after desorption by inducing competition with 10 mM βCD. At lower linker concentrations, the complex also adsorbed at the surface, but after inducing competition with 10 mM βCD, some of the complex remained at the surface. The SPR sensograms at varying divalent linker-SAv ratios are shown in Figure 4.4b. SAv was complexed to the

divalent linker **2** in solution as well. In this case, adsorption was stronger at higher linker concentrations and, under all conditions, only relatively small fractions could be removed.
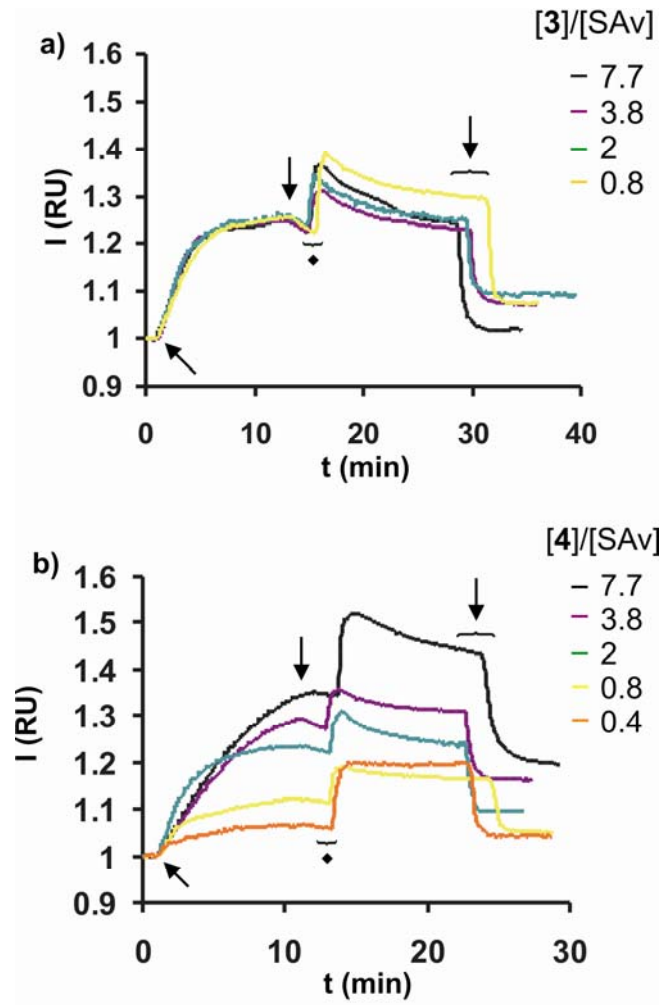
Figure 4.4 *SPR sensograms recorded for the adsorption and (attempted) desorption of SAv at an increasing [**1**]/[SAv] ratio (a) and [**2**]/[SAv] ratio (b). Symbols indicate switching of solutions in the SPR flow cell: SAv-linker in 1 mM βCD in PBS (↑), 1 mM βCD in PBS (↓), 10 mM βCD in PBS (♦).*

The SPR sensograms confirmed that there is a difference in binding of SAv to the molecular printboard between the mono- and divalent linkers in these concentration series. When SAv is adsorbed to the surface when linked to the monovalent linker, the binding of the SAv-monovalent linker complex to the surface is reversible at high linker concentrations, because it can be removed after adsorption by competition with 10 mM βCD in solution. At lower concentrations of the monovalent linker however,

more nonspecific interactions are apparent, leading to only partial removal of the monovalent linker-SAv complex from the surface. This is most likely caused by the presence of empty SAv binding pockets at low linker concentrations. When SAv is adsorbed to the surface through the divalent linker, the adsorption at higher linker concentrations is stronger, due to the formation of specific tetravalent interactions. The complex cannot be removed, neither at high concentrations caused by the high valency, nor at low concentrations due to nonspecific interactions.

4.2.3   Stepwise binding of streptavidin to the molecular printboard

As a last test the SAv-linker complexes were built up at the surface in a stepwise fashion (Scheme 4.2, routes C and D). Also in these experiments, a βCD concentration of 1 mM in PBS was used to suppress nonspecific adsorption of SAv to the surface. First, the linker was flowed over the surface, followed by SAv, and finally linker again, to occupy the free biotin-binding sites at the SAv side exposed to the solution. In Figure 4.5 the combined SPR graphs are depicted. After adsorption of the monovalent linker (**1**) (grey line, Figure 4.5), the baseline was restored upon rinsing with 1 mM βCD. When SAv was flowed over this surface, only some nonspecific adsorption was observed. When the linker was flowed over this surface again, it reversibly adsorbed to the surface, giving an increase in SPR signal comparable to the initial linker adsorption, indicating that many βCD sites were still accessible. For the divalent linker (black line; Figure 4.5), it can be seen that the linker remained at the surface after adsorption and rinsing with buffer containing 1 mM βCD. When SAv was flowed over the surface subsequently, a strong adsorption was observed. After adsorption of SAv, the divalent linker was flowed over the SAv surface, and this adsorption was again irreversible. Thus it is clear that only the divalent linker allows a reliable stepwise buildup of the SAv complex and thus a controlled functionalization of SAv, potentially with two different linkers.
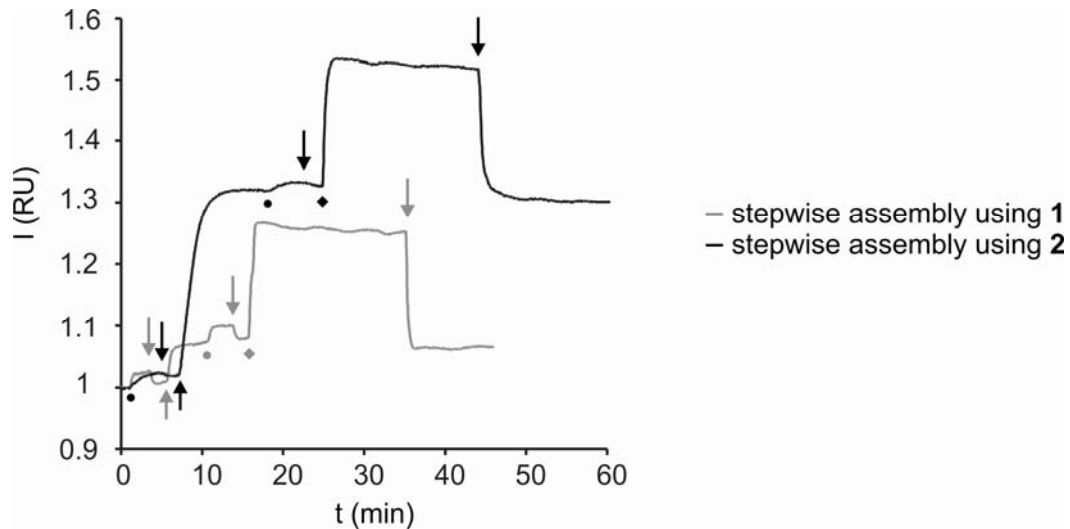
Figure 4.5 *SPR sensograms for the stepwise adsorption of the SAv-linker complex at the molecular printboard. The black and grey curves represent the adsorption via the mono- and divalent linkers respectively. Symbols indicate switching of solutions in the SPR flow cell: linker (●),PBS containing 1 mM βCD (↓), SAv (↑), PBS containing 10 mM βCD (♦).*

XPS studies were performed in order to follow the different adsorption steps. Therefore the following substrates were studied: a βCD SAM, a βCD SAM fully covered with divalent linker, and a βCD SAM fully covered with divalent linker and on top of that SAv. Although the absolute values differed considerably from the theoretically expected values, it could be concluded from the relative trends (Table 4.1) that the organic layer thickness increased in each adsorption step, as indicated by the decrease of the Au(4f) signal. Upon protein adsorption, the N(1s) signal increased, confirming the adsorption of SAv.

Table 4.1 *Experimental and theoretical (in brackets) atomic percentages as determined by XPS of a bare βCD SAM, a βCD SAM covered with the divalent linker 2, and the βCD SAM covered with the divalent linker 2 and SAv.*

SAM	C (1s)	N(1s)	O(1s)	S(2p)	Au(4f)
βCD	37.1 (31.8)	2.5 (1.1)	6.4 (5.5)	2.5 (1.1)	51.7
βCD + **2**	46.9 (40.2)	3.5 (3.0)	13.5 (6.0)	2.2 (1.3)	33.7
βCD + **2** + SAv	49.3	6.6	2.2	1.5	25.1

The stepwise assembly of SAv can be extended to patterning of the molecular printboard. Patterned surfaces were obtained by microcontact printing (μCP) the divalent linker onto the molecular printboard and subsequently flowing SAv over the sample. The adsorption of SAv to the specifically patterned surface was followed *in situ* by an atomic force microscope (AFM) equipped with a liquid cell. Imaging in a liquid cell not only allows the possibility to follow the adsorption of SAv *in situ* in a liquid-like environment, but also ensures the monitoring of the process at the very same spot. Other advantages are that, due to imaging in a liquid, capillary forces are excluded; therefore the forces exerted by the scanning tip to the surface are at least two orders of magnitude less than in air. Potential damage to the protein layer is minimized this way.

Polydimethylsiloxane (PDMS) stamps were treated by ozone and UV irradiation to render them hydrophilic, and placed in a 1×10^{-4} M aqueous solution of the divalent linker. Subsequently, the stamps were blown dry in a stream of N_2, and placed in contact with the βCD SAMs on gold. The samples were rinsed with water, dried, and before assembling them into the liquid cell they were imaged in contact mode AFM in air in order to verify the presence and quality of the divalent linker patterns (Figure 4.6a, left). The height of the patterns from the topography image shown in Figure 4.6a was estimated by cross section analysis to be about 0.5 nm (Figure 4.6a, right). This corresponds to the theoretically height of the adsorbed divalent linker.

Subsequently, the samples were assembled into the liquid cell that was filled with deionized water, and again height images were recorded in contact mode (Figure 4.6b, left). After this step, 10 ml of 5×10^{-7} M SAv was flowed through the cell at a 1 mM βCD background concentration in order to suppress nonspecific interactions. Afterwards, water was flowed through the cell and AFM images were recorded in

contact mode (Figure 4.6c, left). The cross section analysis of the AFM image gave a height of about 2.7 nm (Figure 4.6c, right), indicating the successful adsorption of SAv. Subsequently, 10 mM βCD was flowed through the liquid cell followed by flushing with water, after which again an AFM height image was recorded in water. After this last rinsing step, a slight decrease in height was observed. Initially this was attributed to material removal by rinsing with βCD but zooming out to a larger scan area showed that the height decrease was present only in the area where we initially scanned for a longer time (Figure 4.7). Thus the decrease in height is attributed to some compression or removal of the protein by the scanning tip. The AFM experiments showed that the attachment of SAv only occurred at the areas pre-patterned by the divalent linker. There were no signs of nonspecific SAv adsorption on the bare βCD sites, indicating excellent specificity under these conditions.
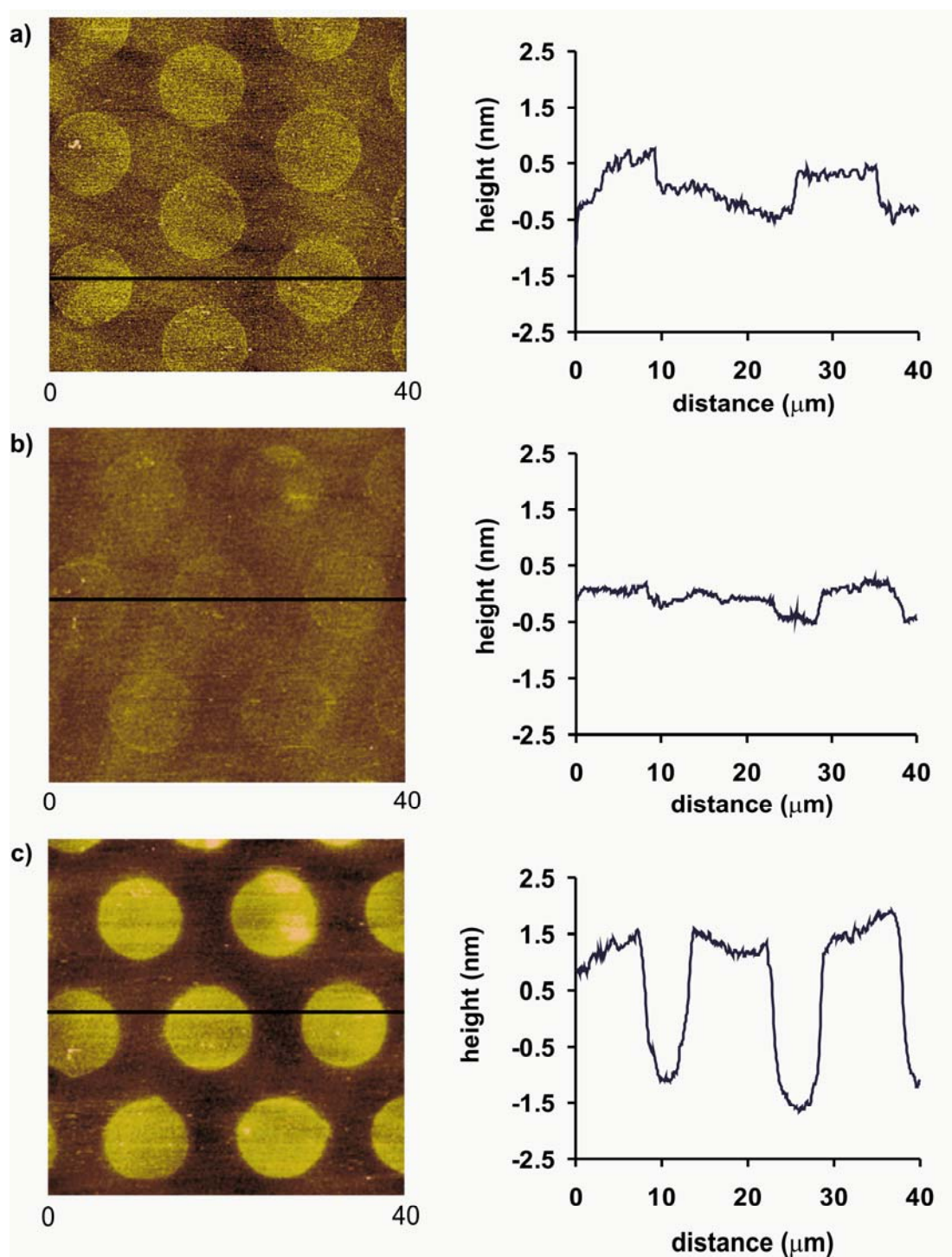
***Figure 4.6** Contact mode AFM height images (left; z range 5 nm) with cross sections performed across the shown lines (right) recorded in air (a) or water (b,c) after printing the divalent linker **2** onto the molecular printboard (a), after transfer of the sample to water (b), and after subsequent SAv adsorption (c).*
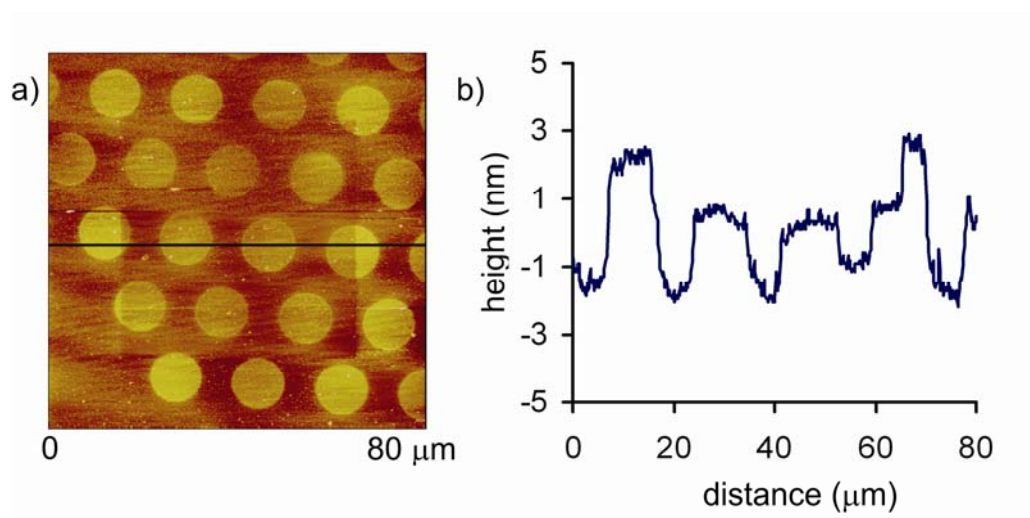
Figure 4.7 *(a) AFM height image (at z range 10 nm) recorded in air after printing the divalent linker and subsequent SAv adsorption, showing some material removal in the previously scanned area; (b) cross section performed across the line shown in the image.*

4.2.4 Hetero-functionalization of streptavidin

In order to show controlled hetero-functionalization at the stepwise immobilized SAv, an experiment was performed in which the divalent linker was printed on a βCD SAM on glass after which SAv was attached on top of the linker, followed by the attachment of fluorescein-labeled biotin (Scheme 4.2E). Cyclodextrin SAMs on glass were prepared as described before.[55] Printing of the divalent linker **2** was performed as described above for the patterning of βCD SAMs on gold. The patterned substrates were placed in a liquid cell, and for one sample SAv was flowed over the substrate at a βCD concentration of 1 mM. Subsequently fluorescein-labeled biotin was flowed over the surface. The samples were dried in a stream of N_2, and examined with fluorescence microscopy (Figure 4.8).
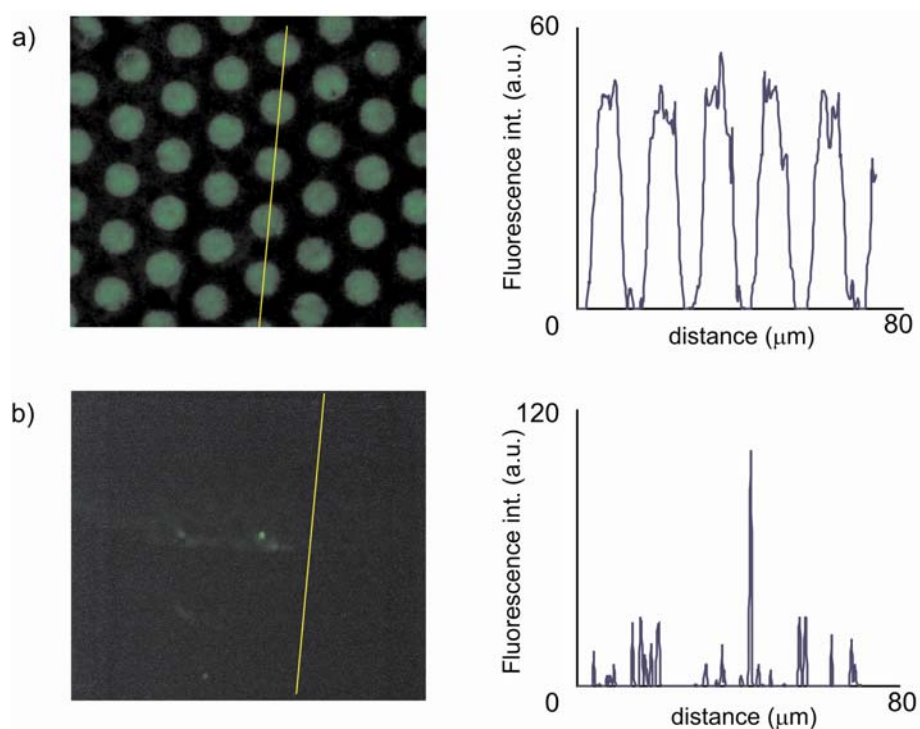
Figure 4.8 *Fluorescence image and line scan recorded after printing the divalent linker (**2**) followed by the selective attachment of SAv to the patterned areas, and subsequent attachment of fluorescein-labeled biotin to the available biotin binding pockets at SAv (a); Fluorescence image and line scan recorded after printing the divalent linker (**2**), and subsequent flow of fluorescein-labeled biotin over the patterned surface (b).*

The image presented in Figure 4.8a confirms the results obtained by SPR experiments in which the SAv complex was built up at the surface in a stepwise manner. The fluorescence patterns clearly indicate the presence of free binding pockets available for subsequent biotin binding after the SAv assembly step. The complete absence of fluorescence in the non-contacted areas shows the excellent specificity of the binding of the fluorescent-labeled biotin. Figure 4.8b shows a fluorescence image of the same process, but without SAv attachment. The absence of a pattern confirms again that the interactions are specific.

4.2.5   Application of the adsorption scheme for the immobilization of the functional protein cytochrome *c*

Hetero-functionalization of SAv was also performed with cyt *c*, which was chosen for several reasons. In the first place, these type of redox enzymes are often used in diagnostic equipment, and second, it allows the determination of the cyt *c* surface concentration in different manners, such as by UV/vis, and electrochemical measurements. The attachment of biotinylated cytochrome *c* (bt-cyt) *c* to molecular printboards is envisaged as depicted in Scheme 4.3. The biotinylation of cyt *c* was performed according to literature procedures with biotin-LC-NHS, which has a spacer arm of 2.24 nm.[45] The reaction mixture contained a 15-fold excess of linker relative to protein, therefore cyt *c* can be biotinylated with on average more than one biotin functionality.
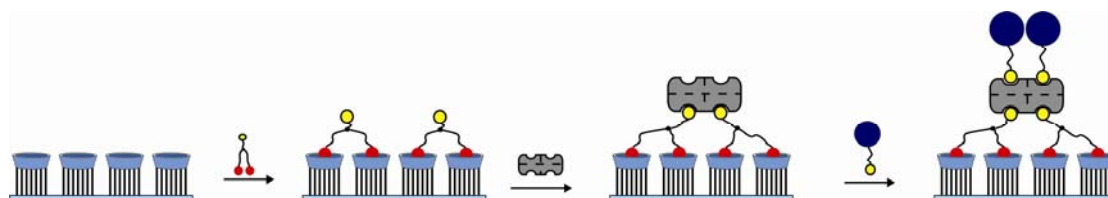
Scheme 4.3 *Stepwise adsorption of **3** and SAv to the molecular printboard, followed by the hetero-functionalization with bt-cyt c.*

To test the specificity of bt-cyt *c* binding to the SAv layer, two surface plasmon resonance (SPR) experiments were performed, in which SAv was immobilized to the molecular printboard via **2** (ex-situ), and then in a separate experiments, cyt *c* and bt-cyt *c* were flowed over the surface (Figure 4.9). From both the sensograms depicted in Figure 4.9, SAv adsorption can be clearly observed. The subsequent flow of cyt *c*, however, did not result in an increase in signal intensity, therefore it can be concluded that cyt *c* was not adsorbed onto the SAv layer (Figure 4.9a). In the second experiment, in which bt-cyt *c* was utilized, a change in signal intensity was observed (Figure 4.9b). This leads to the conclusion that bt-cyt *c* attaches in a specific manner to the SAv layer.
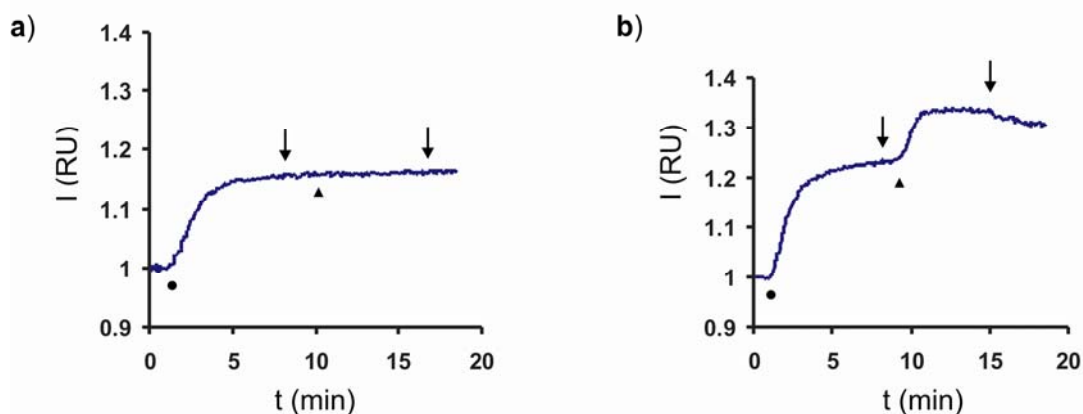
Figure 4.9 *SPR sensograms for the attempted adsorption of cyt c to SAv immobilized at the molecular printboard. The adsorption of SAv to a **3**-covered molecular printboard followed by a flow of non-biotinylated cyt c (a) or of bt-cyt c (b). Symbols indicate: (●) SAv in PBS containing 1 mM βCD, (▲) cyt c (a) or bt-cyt c (b) in PBS containing 1 mM βCD, (↓) switching to PBS buffer containing 1 mM βCD.*

In order to verify the stoichiometry of the binding scheme shown in Scheme 4.3, the surface concentration of bt-cyt c was determined by UV/vis and electrochemistry. Biotinylated cyt c has in the oxidized form an ε of 2.8 cm^2/mg at λ = 408 nm. Determination of the absorbance (A) at 408 nm can be used for the determination of the cyt c concentration. In order to determine the surface concentration of bt-cyt c on the molecular printboard-immobilized SAv, glass substrates were covered on both sides with divalent linker by immersion in a 1×10^{-4} M solution of **2**, followed by adsorption of SAv, and finally bt-cyt c was attached. Subsequently four or five samples were placed together in the UV/vis setup and UV/vis spectra were recorded (Figure 4.10). From the absorbance at 408 nm a surface concentration of $(2.4 \pm 0.5) \times 10^{-11}$ mol/cm^2 could be determined.
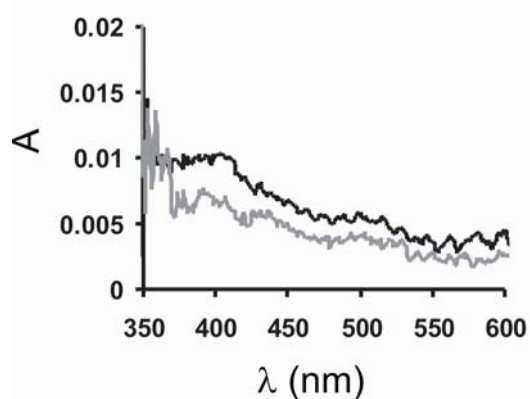
Figure 4.10 *UV/vis-spectra of 8 (-) or 10 (-) βCD SAMs on glass substrates covered with bt-cyt c on SAv on* **3**.

Scanning electrochemical microscopy (SECM) studies on bt-cyt *c* attached to SAv were performed in order to determine the surface concentration of bt-cyt *c* in an electrochemical manner. Therefore, surfaces with bt-cyt *c* were prepared as described above. The sample was mounted in an SECM setup, which used a Ag/AgCl reference electrode and a disk-shaped carbon ultra-microelectrode (UME) of 3.5 μm (Figure 4.11). The redox reactions that occur at the UME and at the surface are listed below.

$[Ru(NH_3)_6]^{3+} + e^-$ ⇌ $[Ru(NH_3)_6]^{2+}$ at the UME

$[Ru(NH_3)_6]^{2+} + [cyt\ c]_{ox}$ ⇌ $[Ru(NH_3)_6]^{3+} + [cyt\ c]_{red}$ at the surface
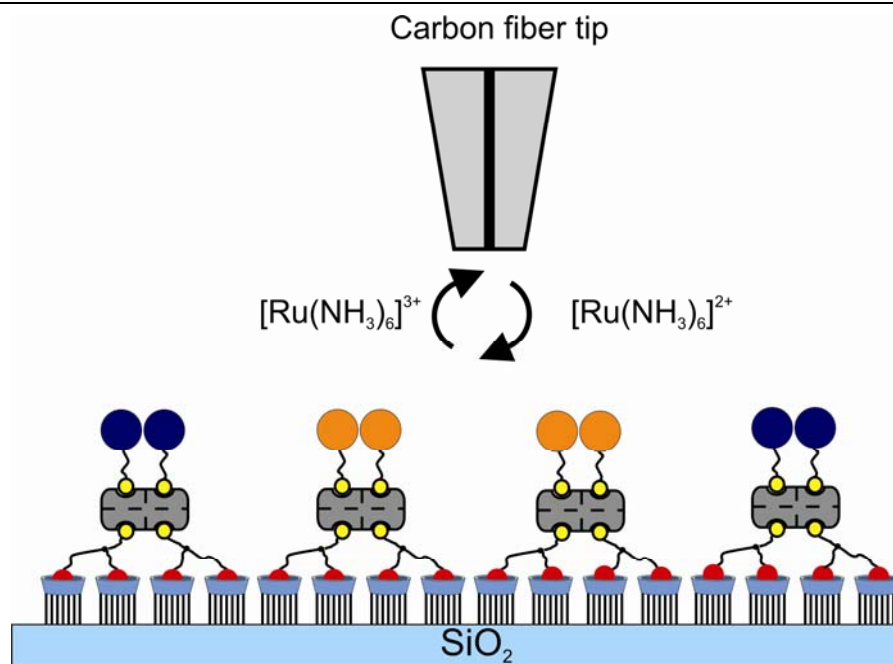
Figure 4.11 *Schematics of the SECM experiment. [Ru(NH₃)₆]³⁺ is reduced at the tip and diffuses to the molecular printboard where it reduces (oxidized) bt-cyt c. Thereafter, [Ru(NH₃)₆]³⁺ diffuses back to the UME, which results in a negative feedback current.*

The UME was positioned in a distance d of 10 μm from the surface and a potential pulse of E_T = -0.35 V was applied to the UME in order to reduce the mediator $[Ru(NH_3)_6]^{3+}$. Chronoamperograms of the UME current were recorded during the pulse. This sequence was repeated multiple times at the same location and at different distances from the surface while the horizontal position was not changed (Figure 4.12). First, a 10 s pulse was applied to the UME positioned 10 μm above the surface (Figure 4.12, curve 1). The pulse was repeated at the same location (Figure 4.12, curve 2). For reference purposes, another pulse experiment was performed far away from any surface (Figure 4.12, curve 3).

Figure 4.12 SECM amperograms in which pulse times are in each case 10 s; first pulse 10 μm from the surface (curve 1, second pulse 10 μm from the surface second pulse (curve 2), third pulse 300 μm from the surface (curve 3).

Almost all cyt c is reduced within the first pulse of about 10 s by a bimolecular electron transfer reaction between $[Ru(NH_3)_6]^{2+}$ and oxidized cyt c (Figure 4.12, curve 1). During this rea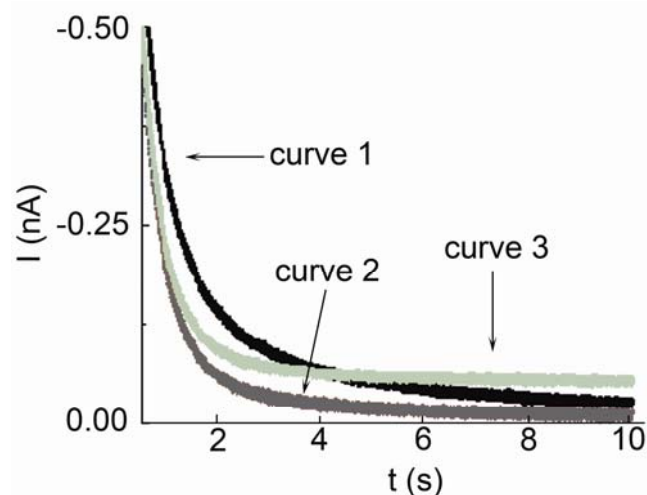ction $[Ru(NH_3)_6]^{3+}$ is regenerated. After diffusion to the UME, it enhances the UME current compared to the same pulse experiment above an inert sample at which no reaction of the mediator is possible. However, the bimolecular reaction can only be sustained as long as oxidized cyt c is available at the surface. Therefore a second pulse at the same location produces much lower currents (Figure 4.12, curve 2). This chronoamperogram is identical to one obtained at the same distance above an bare glass sample. It can be considered as a background signal. For times < 0.1 s it results from double layer charging currents and for longer times it is controlled by the hindered diffusion of $[Ru(NH_3)_6]^{3+}$ from the solution bulk through the gap between UME and sample to the active UME area. Curve 1 and curve 2 merge at around 10 s indicating the time when the oxidized cyt c is exhausted during the first pulse. The current resulting from hindered diffusion (Figure 4.12, curve 2) depends on the distance between the UME and its insulating sheaths to the sample. If the working distance is enlarged (Figure 4.12, curve 3), the diffusion is less effectively hindered and the currents are larger than in Figure 4, curve 2. However, for t < 4 s, the currents during the first pulse at 10 μm distance (Figure 4.12, curve 1) are larger than the currents at large distances (Figure 4.12, curve 3). This is a clear proof that the enhancement of the UME currents in curve 1 is a result of the chemical mediator

recycling at the substrate surface. The electrical charge Q used to convert the cyt c at the surface was obtained by integrating the current difference between the first and the second pulse at $d = 10$ μm (curve 1 minus curve 2). The radius r_S of the sample region that is affected by the oxidation can be approximated by considering the average diffusion length of the $[Ru(NH_3)_6]^{2+}$ generated at the UME (Figure 4.13). With the known[46] diffusion coefficient of $D = 7.4 \times 10^{-6}$ cm^2/s[1] the average diffusion length within the pulse time τ is $(2D\tau)^{1/2}$ and the modified radius at the sample is

$$r_S = (2D\tau - d^2)^{1/2} \qquad (1)$$

From r_S the modified area can be estimated as $A = \pi r_S^2$. Form the Q, r_S and the number $n = 1$ of transferred electrons per cyt c molecule and the Faraday constant F, the surface concentration Γ is obtained.

$$\Gamma = Q / (n\,F\,\pi\,r_S^2) \qquad (2)$$

The estimation according to Eq. (1) and (2) leads to a value of $\Gamma = (2.2 \pm 0.5) \times 10^{-11}$ mol cm^{-2} (Table 4.2). This values compares well with the surface concentration determined by UV/vis (see above). This confirms that all or most all of the cyt c units are electrochemically functional and accessible when immobilized according to this assembly scheme.
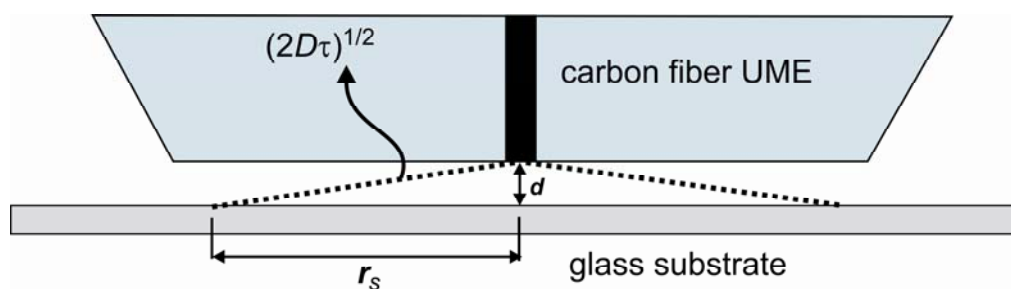

Figure 4.14 *Estimation of the radius of the modified sample region by the diffusion of the UME-generated $[Ru(NH_3)_6]^{2+}$.*

Table 4.2 *Calculation of the surface concentration of bt-cyt c from five independent SECM pulse experiments; for all experiment r_T = 3.5 μm, d = 10 μm, D = 7.4 × 10^{-6} cm^2/s[1].*

τ / s	Q / (10^{-9} As)[a]	r_S / (10^{-4} cm)[b]	Γ / (10^{-11} mol cm^{-2})[c]
5	0.402	85.44	1.82
10	0.707	121.2	1.59
10	1.23	121.2	2.76
10	1.05	121.2	2.36
20	2.04	171.7	2.28

[a] Integrated difference of chronoamperometric currents of the first and the second pulses. [b] Calculated according to Eq. (1). [c] Calculated according to Eq. (2).

Since both the size and molecular weight of SAv and cyt *c* are known, a theoretical estimate about their concentration on the molecular printboard can be made. The dimensions of SAv (2.5 nm × 3 nm × 5 nm) allow the attachment of two molecules of cyt *c*, which is a globular protein with dimensions less than 2 nm.[47] Thus the projected area of cyt *c* on SAv is smaller than the area per biotin-binding site.[48] The biotin-binding pockets on SAv are positioned 2 nm from each other.[49] Nevertheless, when viewing the size of cyt *c*, and the distance between the biotin-binding pockets of SAv, 1:1 SAv : cyt *c* binding is also possible, because bt-cyt *c* has probably multiple biotin groups.

The coverage of the molecular printboard on glass is not known, but is expected to be comparable to the concentration on gold (8 × 10^{-11} mol/cm^2).[50] Four βCD cavities host one SAv, and one SAv hosts one or two cyt *c* molecules. Thus a coverage of cyt *c* is expected to be between 25% and 50% of the βCD concentration on the surface, *i.e.* $\Gamma_{\text{cyt } c}$ is expected to be between 2 × 10^{-11} and 4 × 10^{-11} mol/cm^2. The values found by UV and SECM correspond quite well with this range.

Comparable systems in which cyt *c* was bound to a SAv layer showed an excess of cyt *c* at the surface after immobilization.[28] The SAv layer formed on top of a biotinylated surface consisted of 2.6 × 10^{-12} mol/cm^2 SAv molecules, and 8.8 × 10^{-12} mol/cm^2 cyt *c* molecules. On a molecularly flat surface, the theoretical concentration of cyt *c* corresponds to 2.2 × 10^{-11} mol/cm^2.[51] The nonspecifically bound cyt *c* is attributed to bad packing of the SAv layer (which was only 60 % of a fully packed

layer) which allowed cyt *c* to be nonspecifically immobilized at the biotin SAM.[28] In the case described in this chapter, there is excellent control over the packing of the SAv layer, probably owing to the dynamic supramolecular interactions applied in this system, and a notable absence of nonspecific adsorption.

4.3 Conclusions

In this chapter, it has been shown that it is possible to attach a protein, in this case SAv, to the molecular printboard through orthogonal host-guest and protein-ligand interactions. Both the mono- and divalent linker can be used in this assembly process as was shown by SPR. It was possible to reduce nonspecific interactions between SAv and the molecular printboard by adding 1 mM βCD. Also, when all biotin-binding pockets of SAv are occupied, the nonspecific interactions were reduced. From SPR experiments in which the βCD concentration or the [linker]/SAv ratio was varied it was concluded that, when the monovalent linker is used, SAv is complexed to the surface through two adamantyl-cyclodextrin interactions, while in the case of the divalent linker, the binding is tetravalent. Alternative to assembly of the linker-SAv complex in solution followed by adsorption to the molecular printboard, it has also been shown that the assembly of the protein-divalent linker complex can be done a stepwise fashion at the surface, leaving the upper two binding pockets of SAv available for further (hetero-)functionalization. This scheme was not possible with the monovalent linker, because the binding of this linker to the surface is thermodynamically not strong enough. The stepwise assembly of SAv to the molecular printboard was also proven by AFM imaging, which showed that the height of the SAv-linker complex attached to the molecular printboard was about 2.7 nm. From experiments with fluorescently labeled biotin, it could be concluded that the upper biotin binding pockets were indeed available for further functionalization, in this case proving controlled hetero-functionalization as well. Both AFM imaging and fluorescence studies showed that the attachment of SAv was very specific, and that there was no detectable nonspecific interaction of SAv to the molecular printboard. The hetero-functionalization was also shown with the functional protein cyt *c*. This allowed the quantification of the protein coverage by UV/vis and SECM. The approach that has been used here for the attachment of SAv to a surface. and that all

or most of the cyt *c* was electrochemically functional when using our immobilization strategy as proven by UV/vis and SECM. Furthermore, it was possible to determine the cyt *c* surface concentration from the UV/vis and the SECM experiments. This study shows that the protein surface concentration on top of the SAv layer is in agreement with the expected binding stoichiometry of the resulting bionanostructure. The approach presented here for the attachment of SAv to the surface shows that multivalency plays an important role in the adsorption of proteins to surfaces. The stepwise adsorption of SAv to the surface through the divalent linker enables the use of the biotin binding pockets that are directed towards the solution for the binding of other, biotinylated (bio/macro)molecules. βCD is a cyclic oligosaccharide, and interactions between the hydrophobic βCD cavity and hydrophobic amino acids of proteins will occur.[52-54] However, this appeared not to interfere with the biomolecules used in this system. It is difficult to predict whether βCD will interfere with other biological systems, but in case of the stepwise assembly onto the SAv layer by the further (hetero)functionalization of the free binding pockets, βCD does not need to be present. The approach presented here can be used for further build-up and patterning of (bio) molecular nanostructures at interfaces, especially by further functionalization of the unused biotin binding sites of SAv immobilized in the stepwise fabrication method.

4.4   Experimental section

General

All materials and reagents were used as received, unless stated otherwise. The syntheses of **5** and **8** have been reported previously.[43] Biotin-4-fluorescein was bought from Sigma Aldrich and used as received. All moisture sensitive reactions were carried out under an argon atmosphere. ^{1}H NMR spectra were recorded on Varian Unity 300 MHz and Varian Inova 400 MHz spectrometers. Spectra are reported in ppm downfield from TMS as an internal standard. FAB-MS and MALDI-MS spectra were recorded with a Finnigan MAT 90 spectrometer using *m*-NBA as a matrix and a PerSpective Applied Biosystems Voyager-De-RP spectrometer, respectively. Analytical TLC was performed using Merck prepared plates (silica gel 60 F-254 on aluminum).

Cytochrome *c* was bought at Sigma and biotinylated with Sulfo-NHS-LC-biotin (Pierce) according to literature procedures.[55]

Synthesis

Triethylene glycol phthalimide-ethyl adamantyl ether 6. Compound **5** (1.0 g, 2.6 mmol) and potassium phthalimide (482 mg, 2.6 mmol) were mixed in DMF (30 ml) and allowed to reflux for 10 h while stirring. The precipitate was filtered off after cooling to room temperature, and washed with DMF. The residue was concentrated under vacuum. The product was a yellowish oil (yield 75%).

^{1}H NMR (300 MHz, CDCl$_3$, TMS) δ: 7.90 (m, 2H, ArH), 7.70 (m, 2H, ArH), 3.86 (t, 2H, AdO*CH$_2$*CH$_2$), 3.75-3.70 (t, 2 H, N*CH$_2$*CH$_2$), 2.65-2.55 (m, 12H, O*CH$_2$CH$_2$*O), 2.15 (m, 3H, CH$_2$*CH*CH$_2$Ad), 1.76-1.75 (m, 6H, CH*CH$_2$*CAd), 1.64-1.58 (m, 6H, CH*CH$_2$*CHAd); ^{13}C NMR: δ (ppm) 169.0, 132.1, 127.6, 70.5, 70.2, 67.8, 66.1, 43.1, 39.2, 38.1, 36.4, 30.4; MS (FAB-MS): *m/z* calcd for [M+H^{+}] 458.3, found 458.3.

Triethylene glycol amine-ethyl adamantyl ether 7. Compound **6** (1.4 g, 3.1 mmol) was dissolved in ethanol. The mixture was heated to reflux, subsequently, hydrazine monohydrate (0.17 g, 3.4 mmol) was added. The mixture was allowed to reflux for 1 h. Thereafter, the mixture was allowed to cool to room temperature, and 6 M hydrochloric acid was added to obtain a slightly acidic solution. Subsequently, the mixture was refluxed for 1 h. After cooling to room temperature the phthalhydrazine was filtered off. The residue was concentrated under vacuum. The product was a colorless oil (yield 90%).

^{1}H NMR (300 MHz, CDCl$_3$, TMS) δ: 3.75-3.50 (m, 16H, O*CH$_2$CH$_2$*O + O*CH$_2$*CH$_2$NH$_2$), 2.85 (t, 2H, *CH$_2$*NH$_2$), 2.15 (m, 3H, CH$_2$*CH*CH$_2$Ad), 1.76-1.75 (m, 16H, CH*CH$_2$*CAd), 1.64-1.58 (m, 6H, CH*CH$_2$*CHAd); ^{13}C NMR: δ (ppm): 73.9, 73.7, 73.3, 69.0, 68.5, 67.5, 66.5, 66.3, 66.1, 65.9, 57.5, 55.5, 37.8, 32.5, 26.8; MS (FAB-MS): *m/z* calcd for [M+H^{+}] 327.2, found 327.5.

Triethylene glycol biotin-ethyl adamantyl ether 1. Compound **7** (297 mg, 0.650 mmol) was dissolved in DMF (2 ml) and Et$_3$N (0.1 ml, 0.7 mmol). To this solution (+)-biotin-4-nitro-phenyl ester (238 mg, 0.650 mmol) was added. This was stirred overnight at room temperature. Subsequently, diethyl ether was added dropwise, and

the product precipitated. The product was redissolved in DMF, and precipitated again by adding diethyl ether dropwise. The product was a white solid (yield 60%).

^{1}H NMR (400 MHz, D$_2$O, TMS) δ: 6.8 (t, 2H; CO*NH*), 5.6 (s, 2H, CH$_2$*NH*CH$_2$), 4.45 (m, 1H, NH*CH*CH$_2$), 4.25 (m, 1H, NH*CH*CH), 3.65-3.45 (m, 12H, O*CH$_2$CH$_2$*O), 3.39 (m, 2H, *CH$_2$*NHCO), 3.10 (m, 1H, *CH*CHCH$_2$), 2.85 (d, 1H, S*CH$_2$*CH), 2.65 (s, 1H, S*CH$_2$*CH), 2.10 (t, 2H, CO*CH$_2$*CH$_2$), 2.05 (m, 3H, CH$_2$*CH*CH$_2$Ad), 1.75-1.45 (m, 12H, CH*CH$_2$*CAd + CH$_2$*CH2CH2CH2*CH), 1.60-1.58 (m, 6H, CH*CH$_2$*CHAd); ^{13}C NMR: δ (ppm) 170.0, 73.8, 73.4, 73.3, 68.9, 67.5, 66.8, 66.3, 58.0, 56.5, 55.5, 54.5, 51.9, 49.5; MS (MALDI TOF): *m/z* calcd for [M+H^{+}] 553.8, found 553.2.

1-Biotin-3-(3,5-di(tetraethylene glycol adamantyl ether) benzyl amide 2. Compound **8** (250 mg, 0.330 mmol) was dissolved in DMF, and a few drops of triethylamine were added, followed by (+)-biotin-4-nitrophenyl ester (238 mg, 0.650 mmol). The mixture was stirred overnight at room temperature. The product was precipitated by adding diethyl ether dropwise. The product was redissolved in DMF and precipitated again by adding diethylether dropwise (3 times). The product was a white solid (yield 55%).

^{1}H NMR (400 MHz, CDCl$_3$, TMS) δ: 6.55 (s, 2H; ArH), 6.39 (s, 1H; ArH), 4.49 (t, 2 H; N*CH*CH + N*CH*CH$_2$), 4.13 (t, , 4H; ArO*CH$_2$*), 3.86 (m, 6H, AdO*CH$_2$* + C*CH$_2$*NH), 3.76-3.65 (m, 18H, O*CH$_2$CH$_2$*O + C*CH$_2$*NH), 3.60 (m, 8H, AdOCH$_2$*CH$_2$* + *CH$_2$*CH$_2$OAr), 2.16 (m, 3H, CH$_2$*CH*CH$_2$Ad), 1.75-1.76 (m, 18H, CH*CH$_2$*CAd + CH$_2$*CH$_2$CH$_2$CH$_2$*CH), 1.68-1.58 (m, 12H, CH*CH$_2$*CHAd); ^{13}C NMR: δ (ppm): 162.0, 160.0, 105.0, 82.0, 80.5, 79.2, 78.0, 77.5, 71.2, 70.5, 69.5, 68.8, 67.0, 61.0, 58.8, 56.0, 55.5 ppm; MS (MALDI TOF): *m/z* calcd for [M+H^{+}] 987.3, found 987.2.

Monolayer preparation

Gold substrates for SPR (BK7 glass/2-4 nm Ti/50 nm Au), XPS (BK 7 glass/2-4 nm Ti/200 nm Au) and AFM (Si wafer/2-4 nm Ti/20 nm Au) were obtained from Ssens B.V., Hengelo, The Netherlands. Gold substrates were cleaned by dipping them in piranha (1:3 mixture of concentrated H$_2$SO$_4$ and 30% H$_2$O$_2$) for 5 s. (*Warning:* piranha should be handled with caution; it can detonate unexpectedly.) After thorough rinsing with Millipore water, they were placed for 10 min in absolute EtOH. Subsequently the substrates were placed in a freshly prepared 0.1 mM solution of

βCD heptathioether for 16 h at 60 °C. The samples were subsequently rinsed 3 times with CHCl$_3$, EtOH and Millipore water.[56] The 11-mercapto-1-undecanol SAMs were prepared by placing clean gold substrates overnight in an ethanolic solution of 11-mercapto-1-undecanol. The samples were rinsed 3 times with dichloromethane, ethanol, and Millipore water. All solvents used in the monolayer preparation were of p.a. grade. βCD monolayers on glass were prepared as described earlier.[57]

SPR

SPR measurements were performed on a Resonant Probes GmbH SPR instrument. The instrument consists of a HeNe laser (JDS Uniphase, 10 mW, λ = 632.8 nm) of which the laser light passes through a chopper that is connected to a lock-in amplifier (EG&G 7256). The modulated beam is directed through two polarizers (OWIS) to control the intensity and the plane of polarization of the light. The light is coupled via a high index prism (Scott, LaSFN9) in the Kretschmann configuration to the backside of the gold-coated substrate which is optically matched through a refractive index matching oil (Cargille; series B; $n_D^{25°C}$ = 1.7000 ± 0.0002) at the prism, mounted on a θ-2θ goniometer, in contact with a Teflon cell with a volume of 39 μl and a diameter of 5 mm. The light that leaves the prism passes through a beam splitter, and subsequently, the s-polarized light is directed to a reference detector, and the p-polarized light passes through a lens which focuses the light onto a photodiode detector. Laser fluctuations are filtered out by dividing the intensity of the p-polarized light (I_p) by the intensity of the s-polarized light (I_s). All measurements were performed at a constant angle by reflectivity tracking.

A Reglo digital MS-4/8 Flow pump from Ismatec with four channels was used. In this flow pump, Tygon R3607 tubings with a diameter of 0.76 mm were used, obtained from Ismatec.

The SPR experiments were performed in a flow cell with a volume of 3.9×10^{-2} ml, under flow. Apart from the experiments that are flow rate-dependent, a continuous flow of 0.5 ml/min was used. Before a new experiment was started, the gold substrates were rinsed thoroughly with 10 mM βCD in 10 mM PBS containing 150 mM NaCl, and 10 mM PBS containing 150 mM NaCl. Experiments were started after the baseline was stable. When the solution had to be changed, the pump was stopped, and immediately after changing the solution the pump was switched on again.

Microcontact printing (μCP)

PDMS stamps were prepared by casting a 10:1 (v/v) mixture of poly(dimethylsiloxane) and curing agent (Sylgard 184, Dow Corning) against a patterned silicon master. After curing of the stamps overnight, they were mildly oxidized in an ozone plasma reactor (Ultra-Violet Products Inc., model PR-100) for 60 min to render them hydrophilic. Subsequently, they were inked by soaking them in a 10^{-5} M aqueous solution of the divalent linker (**2**) for 20 min. The master employed to prepare the PDMS stamps had hexagonally oriented 10 μm circular features separated by 5 μm, Before printing, the stamps were blown dry in a stream of N_2. The stamps were applied manually and without pressure control for 10 min onto the βCD SAMs on gold and then carefully removed. For every printing step, a new stamp was used. The substrates were thoroughly rinsed with water after printing.

AFM

The AFM experiments were performed on a Nanoscope IIIa (Veeco, Digital Instruments, USA) multimode atomic force microscope equipped with a J-scanner (maximum scan size about 170×170 μm^2). The instrument was operated in contact mode, setting the feedback mechanism such to ensure a constant force between the tip and the sample. The *in situ* AFM experiments were also performed in tapping mode (non-contact mode) in liquid but the results found were not different from those obtained in contact mode. Commercially available triangular Si_3N_4 cantilevers with a nominal spring constant of about 0.32 Nm^{-1} were used both in air and in liquid. The total force applied to the surface in air was less than 10 nN. The *in situ* experiments were performed using a liquid cell supplied by the manufacturer of the instrument. The available volume of the cell was about 50 μl. The sample and the cell were sealed together using a rubber ring. The images were recorded at scan speeds between 1 and 1.5 Hz (1 Hz: 1 line/s).

Fluorescence Microscopy

Fluorescent images were made using an Olympus inverted research microscope IX71 equipped with a mercury burner U-RFL-T as light source and a digital camera Olympus DP70 (12.5 million-pixel cooled digital color camera) for image acquisition.

Blue excitation light (450 nm $\leq \lambda \leq$ 480 nm) and green emission light ($\lambda \geq$ 515 nm) was filtered using a U-MWB Olympus filter cube.

XPS

XPS was performed on a PHI Quantera SXM, using a monochromated Al K$_\alpha$ X-ray source with an energy of 1486.6 eV. The X-ray beam with a diameter of 100 μm and a power of 25 W was scanned over an area of 300 x 700 μm^2. Survey scans (1100-0 eV) were collected at 45° take-off angle and at a pass energy of 224 eV (0.4 eV step size). Element scans were collected with a pass energy of 112 eV (0.2 eV step size). Samples were neutralized with low energy Ar$^+$ ions and electrons. Atomic concentrations were calculated using Multipak 8.0 software from PHI.

UV/vis spectroscopy

βCD SAMs on glass substrates were consecutively immersed in a 1 mM solution of **2**, a 1.0×10^{-7} M SAv solution, and finally in a 1.0×10^{-7} M solution of bt-cyt *c*. In between these steps a rinse step with PBS buffer was applied. Four or five glass substrates, *i.e.* 8 or 10 cyt *c* modified SAMs, were placed in a Varian Cary 300 Bio instrument which was set in the double beam mode, using 5 non-covered glass substrates as a reference. The substrates were placed perpendicular to the beam, and the glass substrates covered the whole area of the beam.

SECM

A home-built SECM was used consisting of a stepper motor positioning system (Märzhäuser, Wetzlar, Germany) and a CHI701 potentiostat (CH Instruments, Austin, TX, USA). Experiments were carried out in a three-electrode configuration and was operated via home-built software. The carbon fiber UME (working electrode) had a radius r_T = 7 μm and the $RG = r_{glass} / r_T$ = 30 (r$_{glass}$ is the radius of the insulating glass shielding). A Pt wire served as auxiliary electrode, and was used together with a Ag/AgCl reference electrode, to which all potentials are referred to. Measurements were performed in 0.1 mM of [Ru(NH3)$_6$]Cl$_3$ and 0.1 mM of ferrocenemethanol (Fc-CH$_3$OH) in 0.1 M Na$_2$SO$_4$. Initially the UME was positioned far from the surface, and then approached the surface with the help of the SECM setup by monitoring the steady-state current of Fc-CH$_3$OH oxidation at E_T = 0.2 V at the UME until the

current stayed constant when the insulating sheath of the UME mechanically touched the surface. The UME was retracted 10 μm from this point for the pulse experiments. Subsequent the potential was switched to E_T = -0.35 V in order to reduce $[Ru(NH_3)_6]^{3+}$.

4.5   References

1.   K. Zhang, M. R. Diehl, D. A. Tirrell, *J. Am. Chem. Soc.* **2005**, *127*, 10136-10137.

2.   H. Zhu, M. Snyder, *Curr. Opin. Chem. Biol.* **2003**, *7*, 55-63.

3.   N. L. Rosi, C. A. Mirkin, *Chem. Rev.* **2005**, *105*, 1547-1562.

4.   C. M. Niemeyer, *Angew. Chem. Int. Ed.* **2001**, *40*, 4128-4158.

5.   E. Katz, I. Willner, *Angew. Chem. Int. Ed.* **2004**, *43*, 6042-6108.

6.   L. Tiefenauer, Ros, R., *Coll. Surf. B* **2002**, *23*, 95-114.

7.   W. Knoll, M. Zizlsperger, T. Liebermann, S. Arnold, A. Badia, M. Liley, D. Piscevic, F. J. Schmitt, J. Spinke, *Coll. Surf. A* **2000**, *161*, 115-137.

8.   D. Zhou, A. Bruckbauer, L. Ying, C. Abell, D. Klenerman, *Nano Lett.* **2003**, *3*, 1517-1520.

9.   A. Chilkoti, P. S. Stayton, *J. Am. Chem. Soc.* **1995**, *117*, 10622-10628.

10.   M. González, C. E. Argaraña, G. D. Fidelio, *Biomol. Eng.* *1999*, *16*, 67-72.

11.   N. M. Green, *Meth. Enzymol.* **1990**, *184*, 51-67.

12.   L. A. Klumb, V. Chu, P.S. Stayton, *Biochemistry* **1998**, *37*, 7657-7662.

13.   C. Rosano, P. Arosio, M. Bolognesi, *Biomol. Eng.* **1999**, *16*, 5-12.

14.   P. C. Weber, M. W. Patoliano, L. D. Thompson, *Biochemistry* **1992**, *31*, 9350-9354.

15.   T. Sano, C. R. Cantor, *Proc. Natl. Acad. Sci. USA* **1995**, *92*, 3180-3184.

16.   M. J. Swamy, *Biochem. Biomol. Biol. Int.* **1995**, *36*, 219-225.

17.   M. González, L. A. Bagatolli, I. Echabe, J. L. R. Arrondo, C. E. Argaraña, C. R. Cantor, G. D. Fidelio, *J. Biol. Chem.* **1997**, *272*, 11288-11294.

18.   W. A. Hendrickson, A. Pähler, J. L. Smith, Y. Satow, E. A. Merritt, *Proc. Natl. Acad. Sci. USA* **1989**, *80*, 2190-2194.

19.   A. Biebricher, A. Paul, P. Tinnefeld, A. Gölzhäuser, M. Sauer, *J. Biotech.* **2004**, *112*, 97-107.

20.   I. T. Dorn, K. R. Neumaier, R. Tampé *J. Am. Chem. Soc.* **1998**, *120*, 2753-2763.

21. J. F. Hainfeld, W. Liu, *J. Struct. Biol.* **1999**, *127*, 185-198.

22. U. Rädler, J. Mack, N. Persike, G. Jung, R. Tampé, *Biophys. J.* **2000**, *79*, 3144-3152.

23. L. Schmitt, C. Dietrich, R. Tampé, *J. Am. Chem. Soc.* **1994**, *116*, 8485-8491.

24. S. Lata, A. Reichert, R. Brock, R. Tampé, J. Piehler, *J. Am. Chem. Soc.* **2005**, *127*, 10205-10215.

25. A. Tinazli, J. Tang, R. Valiokas, S. Pićurić, S. Lata, J. Piehler, B. Liedberg, R. Tampé, *Chem. Eur. J.* **2005**, *11*, 5249-5259.

26. R. Blankenburg, P. Meller, H. Ringsdorf , C. Salesse, *Biochemistry* **1989**, *28*, 8214-8221.

27. S. A. Darst, M. Ahlers, P. H. Meller, E. W. Kubalek, R. Blankenburg, H. O. Ribi, H. Ringsdorf, R. D. Kornberg, *Biophys. J.* **1991**, *59*, 387-396.

28. P. L. Edmiston, S. S. Saavedra, *J. Am. Chem. Soc.* **1998**, *120*, 1665-1671.

29. A. Schmidt, J. Spinke, E. Bayerl, W. Knoll, *Biophys. J.* **1992**, *63*, 1185-1192.

30. S. Zhao, W. M. Reichert, *Langmuir* **1992**, *8*, 2785-2791.

31. W. Müller, H. Ringsdorf, E. Rump, X. Zhang, L. Angermaier, W. Knoll, J. Spinke, *J. Biomater. Sci. Polymer Edn.* **1994**, *6*, 481-495.

32. "*Cytochrome c, a multidisciplinary approach*", Eds. R. A. Scott, A. G. Mauk, **1996**, University Science books, Sauslito, California.

33. D. Keilin, E. F. Hartree, *Biochem. J.* **1945**, *39*, 289-292.

34. G. Battistuzzi, M. Borsari, M. Sola, *Antioxid. Redox Signaling* **2001**, *3*, 279-291.

35. G. Battistuzzi, M. Borsari, M. Sola, *Eur. J. Inorg. Chem.* **2001**, 2989-3004.

36. G. Battistuzzi, M. Borsari, F. Francia, M. Sola, *Biochemistry* **1997**, *36*, 16247-16258.

37. J. Deere, M. Serantomi, K. J. Edler, B. K. Hodnett, J. G. Wall, E. Magner, *Langmuir* **2004**, *20*, 532-536.

38. A. S. Haas, D. L. Pilloud, K. S. Reddy, G. T. Babcock, C. C. Moser, J. K. Blasie, P. L. Dutton , *J. Phys. Chem. B*, **2001**, *105*, 11351-11362.

39. A. Fantuzzi, M. Fairhead, G. Gilardi, *J. Am. Chem. Soc.* **2004**, *126*, 5040-5041.

40. A. Fragoso, J. Caballero, E. Almirall, R. Villalonga, R. Caro, *Langmuir* **2002**, *18*, 5051-5054.

41. C. A. Nijhuis, F. Yu, W. Knoll, J. Huskens, D. N. Reinhoudt, *Langmuir* **2005**, *21*, 7866-7876.

42. C. A. Nijhuis, J. K. Sinha, G. Wittstock, B. J. Ravoo, D. N. Reinhoudt, *Langmuir* **2006**, *22*, 9770-9775.

43. A. Mulder, S. Onclin, M. Péter, J. P. Hoogenboom, H. Beijleveld, J. ter Maat, M. F. García-Parajó, B. J. Ravoo, J. Huskens, N. F. van Hulst, D. N. Reinhoudt, *Small*, **2005**, *1*, 242-253.

44. F. Corbellini, A. Mulder, A. Sartori, M. J. W. Ludden, A. Casnati, R. Ungaro, J. Huskens, M. Crego-Calama, D. N. Reinhoudt, *J. Am. Chem. Soc.* **2004**, *126*, 17050-17058.

45. Pierce, catalogue **2006**.

46. S. E. Pust, D. Scharnweber, S. Baunack, G. Wittstock, *J. Electrochem. Soc.* **2007**, *154*, C508-C514.

47. G. Bodo, *Biochim. Biophys. Acta* **1957**, *25*, 428-429.

48. P. L. Edminston, S. S. Saavedra, *J. Am. Chem. Soc.* **1998**, *120*, 1665-1671.

49. Z. Ding, R. B. Fong, C. L. Long, P. S. Stayton, A. S. Hoffman, *Nature* **2001**, *411*, 59-62.

50. C.A. Nijhuis, *Ph. D. thesis*, University of Twente, Enschede, **2006**.

51. P. L. Edmiston, J. E. Lee, S-S. Cheng, S. S. Saavedra, *J. Am. Chem. Soc.* **1997**, *119*, 560-570.

52. A. Cooper, *J. Am. Chem. Soc.* **1992**, *114*, 9208-9209.

53. A. Cooper, M. Lovatt, M. A. Nutley, *J. Incl. Phen. Mol. Rec. Chem.* **1985**, *25*, 85-88.

54. D. Rozema, S. H. Gellman, *J. Am. Chem. Soc.* **1995**, *117*, 2373-2374.

55. A-L. Levonen, A. Landar, A. Ramachandran, E. K. Ceaser, D. A. Dickinson, G. Zanoni, J. D. Morrow, V. M. Darley-Usmar, *Biochem. J.* **2004**, *378*, 373-382.

56. M. W. J. Beulen, J. Bügler, B. Lammerink, F. A. J. Geurts, E. M. E. F. Biemond, K. G. C. van Leerdam, F. C. J. M. van Veggel, J. F. J. Engbersen, D. N. Reinhoudt, *Langmuir* **1998**, *14*, 6424-6429.

57. S. Onclin, A. Mulder, J. Huskens, B. J. Ravoo, D. N. Reinhoudt, *Langmuir* **2004**, *20*, 5460-5466.

5

Build-up of complex bionanostructures at molecular printboards: towards applications*

In this chapter, the build-up of (complex) bionanostructures is described, consisting of stepwise immobilized streptavidin (SAv) on molecular printboards. Patterning studies are shown in which SAv, biotinylated protein A (bt-PA) and an Fc fragment of an immunoglobin G (IgG-Fc) are applied. The build-up of this assembly was investigated by SPR spectroscopy, as well as fluorescence measurements. These results were the basis of a further study, in which antibodies (ABs) are attached to the molecular printboard in different manners. Mouse IgG (MIgG) was attached via biotinylated goat anti-mouse IgG (bt-GαMIgG) and via biotinylated protein G (bt-PG). Subsequently, two monoclonal ABs (MABs), biotinylated CRIS-7 and B-B12, are immobilized on the molecular printboard, serving as a platform for $CD3^+CD4^+$ and $CD3^+CD8^+$-lymphocyte detection. Linearity studies show that the relation between seeded cells and counted cells is approximately linear. Furthermore, ABs were immobilized in a micro-chip made-up of one large channel that splits up into four smaller channels. It is shown that all four microchannels could be addressed separately, and that ABs can be selectively attached in these channels.

5.1   Introduction

There has been considerable interest in the build-up of bionanostructures at surfaces for sensing purposes. Examples of such biosensing devices which employ (complex) bionanostructures at surfaces are the development of a HGC sensor by Knoll *et al.*,[1] and the sensor types described in a review by Wilchek.[2] Main issues of antibody (AB), and in general protein, immobilization are orientation, functionality, and specificity.[3-10]

Antibody-antigen assays are some of the most common medical diagnostic tools, commonly requiring immobilization of antibodies (ABs) on the sensor surface.[11,12] Control over orientation when immobilizing ABs to surfaces for sensor purposes is of utmost importance, since this determines for a large part the effectiveness of the ABs to detect antigens.[13-18] One way to achieve this is by using Fc receptors, such as protein A (PA), protein G (PG), or protein A/G (PA/G).[19-22] An AB binds with its Fc fragment to PA or PG, thus presenting the Fab fragments of the AB towards the solution, which thus become capable of binding antigens present in the solution.

The stepwise binding of streptavidin (SAv) to the molecular printboard via a divalent linker allows hetero-functionalization of the immobilized SAv as shown in Chapter 4. In this chapter, it will be shown that the hetero-functionalization of SAv at βCD self-assembled monolayers (SAMs), can be used for the attachment of (parts of) ABs, or their Fc fragments. Different assembly modes of ABs at surfaces will be demonstrated. Assembly of an AB via fused a biotin (bt) functionality will be compared to the assembly of the same AB, but via bt-PG. The assembly of such bionanostructures was investigated by surface plasmon resonance (SPR) and fluorescence spectroscopy, and atomic force microscopy (AFM). We will also show that the use of thus immobilized IgGs can be used in cell-count systems. Furthermore, it will be shown that microchannels can be functionalized in a stepwise manner with βCD SAMs. It will be shown that it is possible to exploit the host-guest chemistry, developed for planar substrates, in microchannels. Subsequently, previously introduced protein immobilization schemes will be applied to the attachment of antibodies in these microchannels. Furthermore, the addressability of individual channels for localized antibody assembly will be investigated, and the selectivity of the antibody recognition will be studied.

5.2   Results and discussion

5.2.1   Patterning of a human IgG-Fc fragment

βCD and the SAMs thereof have been introduced in Chapter 2. The stepwise adsorption of SAv to the molecular printboard via a divalent linker allows hetero-functionalization of the immobilized SAv as shown in Chapter 4. In order to functionalize SAv with ABs, a biotinylated AB (bt-AB) or a biotinylated Fc receptor protein, such as protein A (PA) or protein G (PG), is needed. In the first part of this study, the assembly of biotinylated protein A (bt-PA) and the Fc fragment of a human IgG (IgG-Fc) (Chart 5.1) is described.
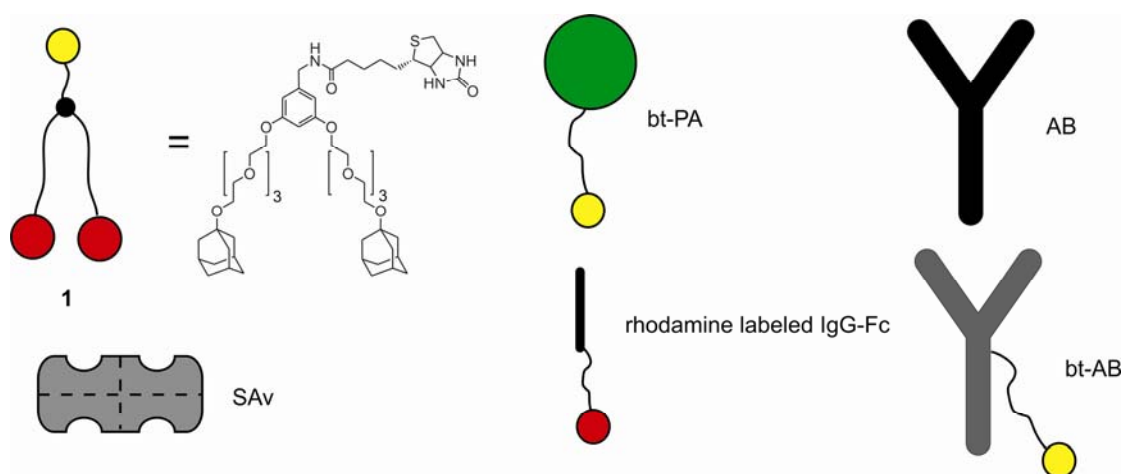

Chart 5.1 *Building blocks used in this study: divalent adamantyl-biotin linker (**1**), SAv, bt-PA, rhodamine-labeled IgG-Fc, and the general structure of an AB, and bt-AB.*

The assembly process is depicted in Scheme 5.1. First the divalent adamantyl (Ad)-biotin linker **1** is bound to the molecular printboard, followed by the attachment of SAv, yielding immobilized SAv, with two biotin binding pockets available for further functionalization as explained in Chapter 4. Bt-PA is attached to these biotin-binding pockets. This protein serves as an Fc receptor, so that IgG-Fc can be attached on top (Scheme 5.1). Thus, in this assembly scheme, three orthogonal, non-covalent interactions are present: βCD-Ad, SAv-biotin, and bt-PA-IgG-Fc.
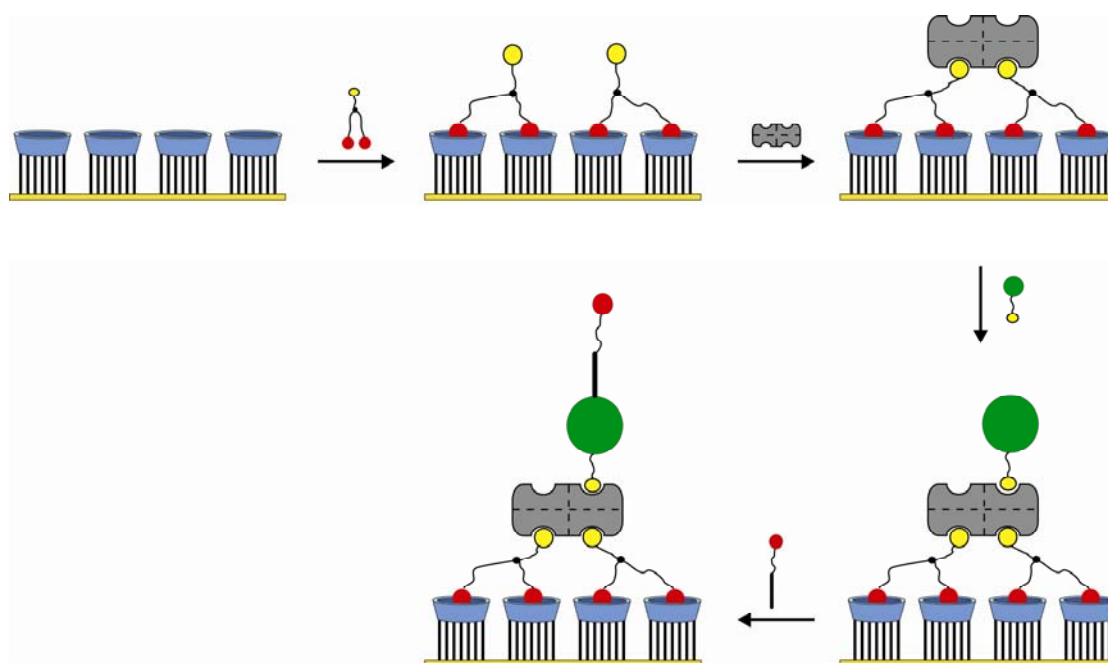
Scheme 5.1 *Build-up of a bionanostructure composed of **1**, SAv, bt-PA, and rhodamine-labeled IgG-Fc at the molecular printboard.*

When considering the assembly of different proteins on top of each other, the sizes and shapes of the different proteins need to be taken into account. For SAv (58 kDa; 2.5 nm × 3 nm × 5 nm) immobilized via two biotin-binding pockets to a surface, the spacing between the remaining free biotin-binding pockets is about 2 nm.[23] PA and PG are globular proteins with sizes of 42 kDa and 60 kDa respectively, corresponding to diameters of ~3 nm and ~6 nm. This means that these Fc receptors can only bind to SAv in a 1:1 ratio at best. ABs are even larger (~150 kDa) and are Y-shaped. Thus the binding ratio of AB to Fc receptor and SAv can never be larger than 1.

SPR experiments showed that both bt-PA and IgG-Fc have significant nonspecific interactions with the molecular printboard in phosphate buffered saline (PBS) (Figures 5.1a and b). Adding 1 mM βCD to the PBS buffer appeared to be sufficient to minimize nonspecific adsorption of bt-PA to the molecular printboard (Figure 5.1.a) Alternatively, 1×10^{-7} M BSA was used to block the molecular printboard. It appeared that IgG-Fc did not attach to the molecular printboard which was blocked by BSA. As shown below, SAv fulfills a similar blocking function in the assembly of the bionanostructure.
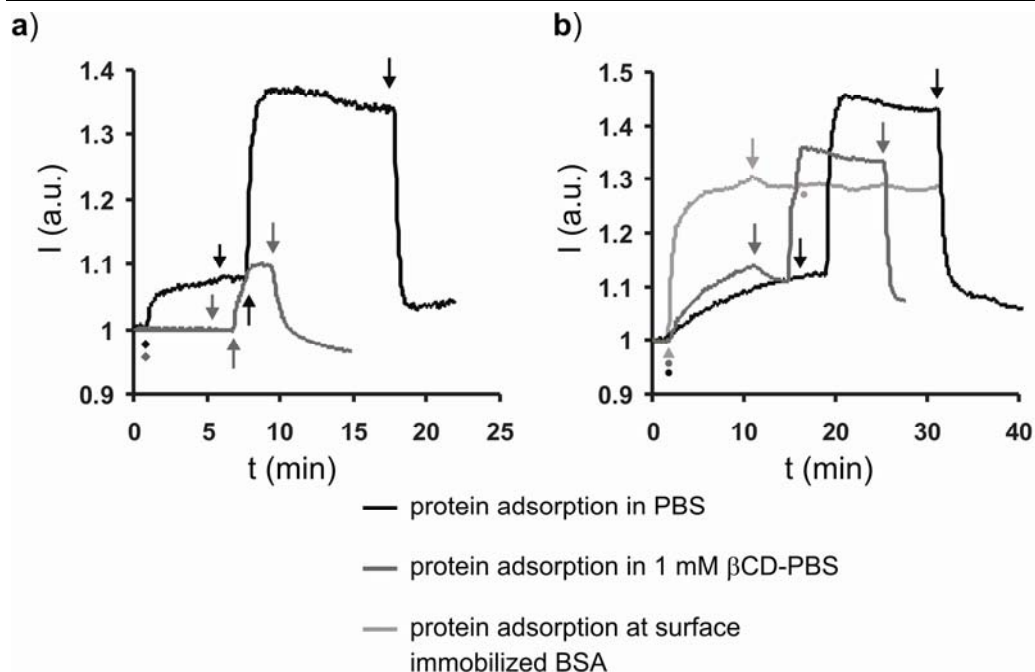
Figure 5.1 SPR sensograms representing: adsorption of bt-PA to molecular printboards (a), and the adsorption of IgG-Fc to molecular printboards (b). Symbols indicate switching the flow to (♦) bt-PA, (●) IgG-Fc, (↓) buffer, and (↑) 10 mM βCD in PBS.

For the complete assembly as depicted in Scheme 5.1, a gold substrate with a βCD SAM was immersed in a 1 mM aqueous solution of **1**. Subsequently, the substrate was rinsed with water, dried in a stream of N_2, and was mounted into the SPR setup. Consecutively, SAv, bt-PA, and IgG-Fc were flowed over the substrate, while in between these different steps PBS buffer containing 1 mM βCD was flowed over the substrate to avoid protein-protein interactions in solution (Figure 5.2).
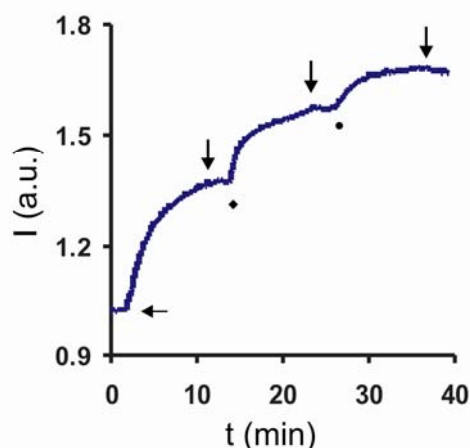

Figure 5.2 SPR sensogram representing the assembly of the bionanostructure. Symbols indicate switching the flow to (←) SAv, (↓) buffer, (♦) bt-PA, and (●) IgG-Fc.

107

Patterned bionanostructures according to Scheme 5.1 were obtained by microcontact printing (μCP) of divalent linker **1** onto the molecular printboard on glass, followed by flowing SAv, bt-PA, BSA, and IgG-Fc over the sample. The use of BSA minimizes nonspecific interactions to the non-patterned areas. For fluorescence microscopy imaging of the final structure, the IgG-Fc was labeled with lissamine-rhodamine according to a literature procedure,[24] and patterns of **1** on the molecular printboard were prepared as described in Chapter 4. The samples were rinsed with water, dried, and assembled in the flow setup. SAv was flowed over the substrate in 1 mM βCD PBS buffer. Subsequently bt-PA was flowed over the substrate in the presence of 1 mM βCD, followed by BSA and IgG-Fc. In between the assembly steps PBS was flowed over the substrate to avoid interactions in solution between the different proteins.

After assembling all proteins at the surface, the substrate was removed from the liquid cell, and imaged with a fluorescence microscope. Figure 5.3 (left) confirms the selective build-up of the SAv-PA-IgG-Fc bionanostructure on the surface only in the areas where **1** was printed in the first step. A series of reference experiments in which either linker, SAv, or bt-PA were omitted showed no pattern formation at all, indicating the essential role of each of the components in this system to form the build-up. The fluorescence microscopy image obtained for the experiment in which bt-PA was omitted (Figure 5.3 right) clearly shows that the presence of SAv also suppresses nonspecific interactions of IgG-Fc to βCD SAMs similar to the function of BSA in the empty areas (see above).
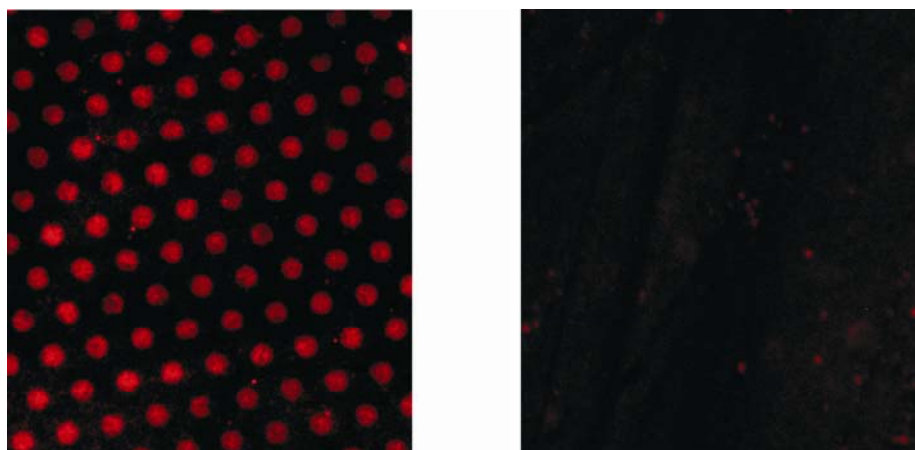
Figure 5.3 *Fluorescence microscopy images of a patterned bionanostructure prepared by microcontact printing of **1**, followed by adsorption of SAv, bt-PA, and rhodamine-labeled IgG-Fc (left; Scheme 5.1), and of the experiment in which bt-PA is omitted (right).*

5.2.2 Antibodies at the molecular printboard

Scheme 5.2a presents a schematic approach for the attachment of complete ABs via two different assembly methods. The first (Scheme 5.2a) employs biotinylated goat anti-mouse IgG (bt-GαMIgG) which is bound through its biotin functionality to the SAv layer at the molecular printboard. Mouse IgG (MIgG) can subsequently interact with the AB. The assembly method (Scheme 5.2b), employs bt-PG for the attachment of MIgG.
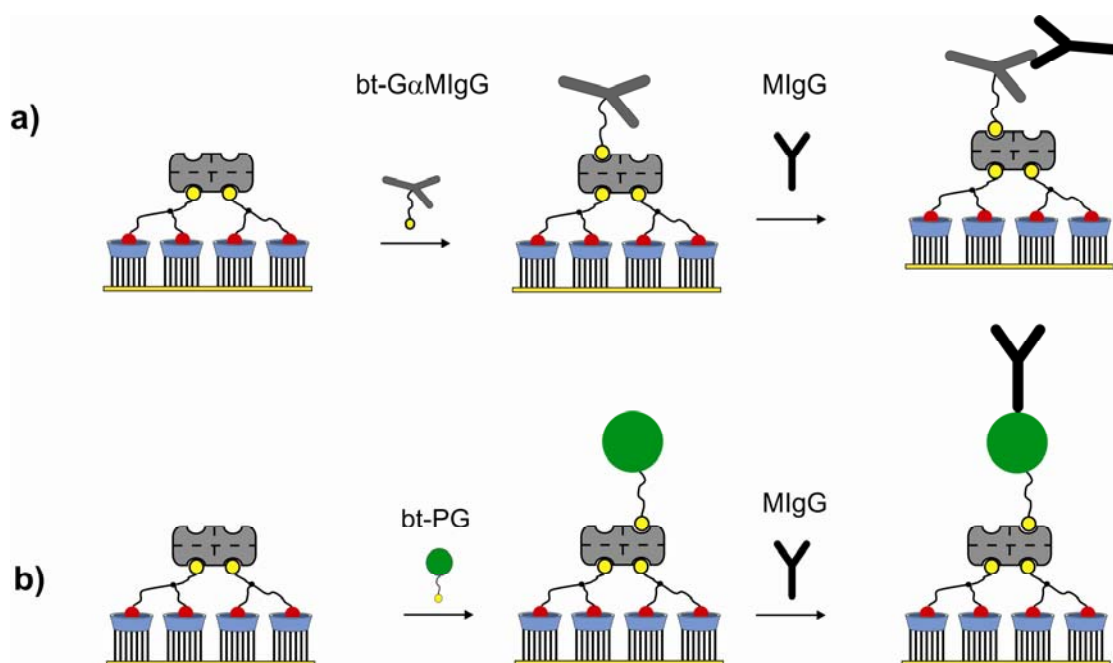
Scheme 5.2 *Two different routes for the attachment of ABs to the molecular printboard coated with **1** and SAv, via bt-GαMIgG (a) and via bt-PG (b).*

SPR experiments were performed to investigate possible nonspecific interactions of the different ABs to the molecular printboard. As expected from the results with IgG-Fc (see above), also the complete ABs showed nonspecific interactions to the printboard (Figure 5.4a). Adding 1 mM βCD to the PBS buffer did not solve the problem of nonspecific attachment of the ABs (Figures 5.4b and d). As in the case with the IgG-Fc, preceding adsorption of BSA led to the complete suppression of these nonspecific interactions (Figures 5.4c and e).
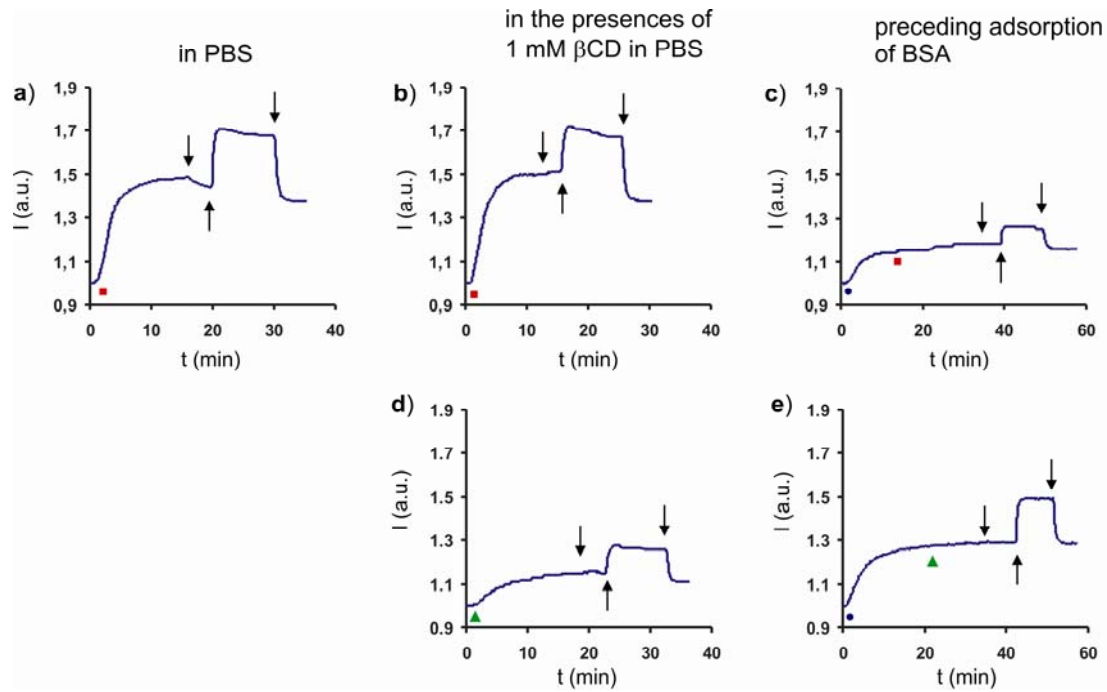
Figure 5.4 *SPR sensograms displaying the nonspecific attachment of two different ABs at the molecular printboard: adsorption of bt-GαMIgG in PBS, in the absence (a) or the presence (b) of 1 mM βCD, or with preceding adsorption of BSA (c); adsorption of MIgG in PBS containing 1 mM βCD (d) or with preceding adsorption of BSA (e). Symbols indicate switching the flow to: (■) bt-GαMIgG, (↓) buffer (with (b,d) or without (a,c,e) 1 mM βCD) (↑) indicates flow of 10 mM βCD, (●) BSA, and (▲) MIgG.*

SPR sensograms of the assemblies according to Scheme 5.2 are depicted in Figure 5.5. In Figure 5.5a the assembly consisting of bt-GαMIgG and MIgG is depicted (Scheme 5.2a). The SPR signal increased upon AB flow, but this increase was rather small, while the ABs are large proteins (150 kDa, compared to 58 kDa for SAv). Also the attachment via bt-PG as shown in Figure 5.5b appeared feasible, however, also in this case the increase in SPR signal corresponding to the adsorption of AB remained rather low.

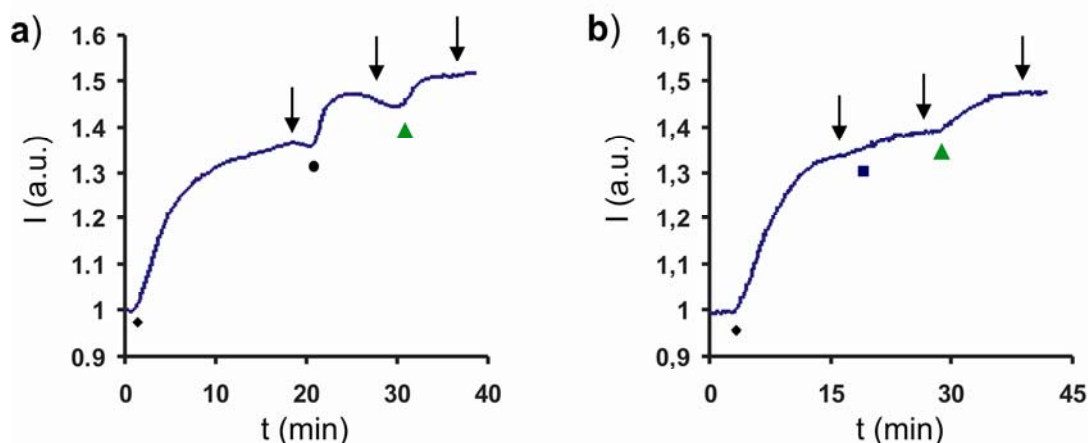***Figure 5.5*** *SPR sensograms of the assembly of ABs at the molecular printboard via the routes shown in Schemes 5.2a and b. Symbols indicate: (♦) SAv (onto **1** at the molecular printboard), (↓) buffer, (•) bt-GαMIgG, (▲) MIgG, and (■) bt-PG.*

AFM experiments were performed to check the different assembly steps. Five samples were prepared according to Schemes 5.2a and b. The substrates were fully covered with protein, and a small scratch with the AFM tip was made on the samples from which the height of the protein layer could be measured (Table 5.1).

The height of SAv is the same as measured in the patterning AFM experiments described in Chapter 4. The height increases after the different adsorption steps are lower than would be expected based on the sizes of the different proteins, especially for the AB adsorption steps. This may be due to the high compressibility of the adsorbed proteins, and partly due to the fact that the packing of the ABs at the surface is probably not ideal, due to the different sizes and shapes of the proteins present in the bionanostructures at the molecular printboard, or to the specific binding of a particular antibody with its antigen such that the major part of the antigen is located next to the antibody binding site which would result in only a limited increase in the total height of the complex. Nevertheless, the results clearly indicate that also complete ABs can be immobilized using this supramolecular assembly scheme.

Table 5.1 *Heights measured in AFM scratching experiments on fully protein-covered βCD SAMs made according to Scheme 5.2*

Assembly	Height (nm)
SAv	2.5
SAv•bt-GαMIgG	4.0
SAv•bt-GαMIgG•MIgG	5.7
SAv•bt-PG	3.5
SAv•bt-PG•MIgG	5.9

5.2.3 Molecular printboards as platforms for cell attachment: towards cell count systems

AB-coated substrates can be used for the detection of cells.[26-31] Lymphocytes for instance, are key indicators for the diagnosis and the monitoring of malignancies, auto-immune disorders, and infections.[32] Lymphocytes can be divided into: i) natural killer cells, ii) $CD19^+$ B cells, and iii) $CD3^+$ T cells. The latter can be subdivided into $CD4^+$ T cells and $CD8^+$ T cells (Figure 5.6).[33] The enumeration of $CD4^+$ T-lymphocytes is needed for monitoring *e.g.* the infection stage of the human immunodeficiency virus (HIV) and the HIV stage of patients. For children, also the $CD4^+/CD8^+$ ratio is required.
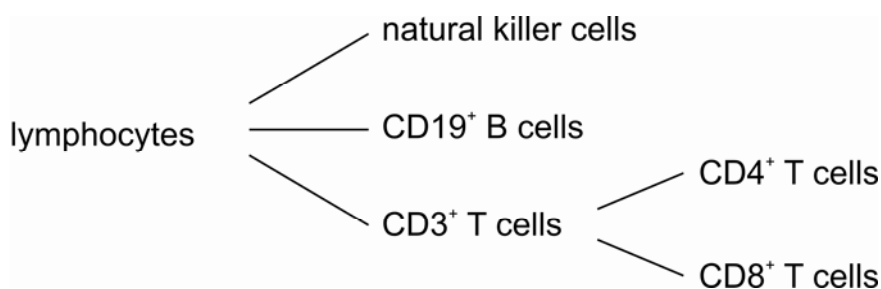
Figure 5.6 *Subdivision of lymphocytes.*

Flow cytometry is the preferred method for $CD4^+$ enumeration, because it is very efficient and accurate. However, since it is also expensive, application of this technology in resource-poor countries can not be afforded. In literature cell enumeration methods have been described that are based on surface detection techniques.[26-31] The advantage is that these are more cost-effective, and the obtained results can be easily quantified. Most of the AB surfaces used for this purpose are non-organized, which has an effect on the total number of cells that can be bound.

For the attachment of CD3$^+$ lymphocytes to surfaces, monoclonal antibodies (MABs) directed against CD3$^+$ lymphocytes should be immobilized. Two MABs were used here for this purpose, one from a CRIS-7 clone, and one from a B-B12 clone. The MAB from the CRIS-7 clone is on average mono-biotinylated. This means that this MAB can be attached directly to streptavidin (Scheme 5.3 route a). B-B12 however, does not have a biotin functionality and must therefore be assembled via an Fc receptor. The advantage of using an Fc receptor is that the Fc part of the AB is directed towards the surface, and the Fab part, which is capable of binding antigens, is directed towards the solution interface. Thus, the surface density of Fab portions on the surface which are directed upwards is potentially enhanced.
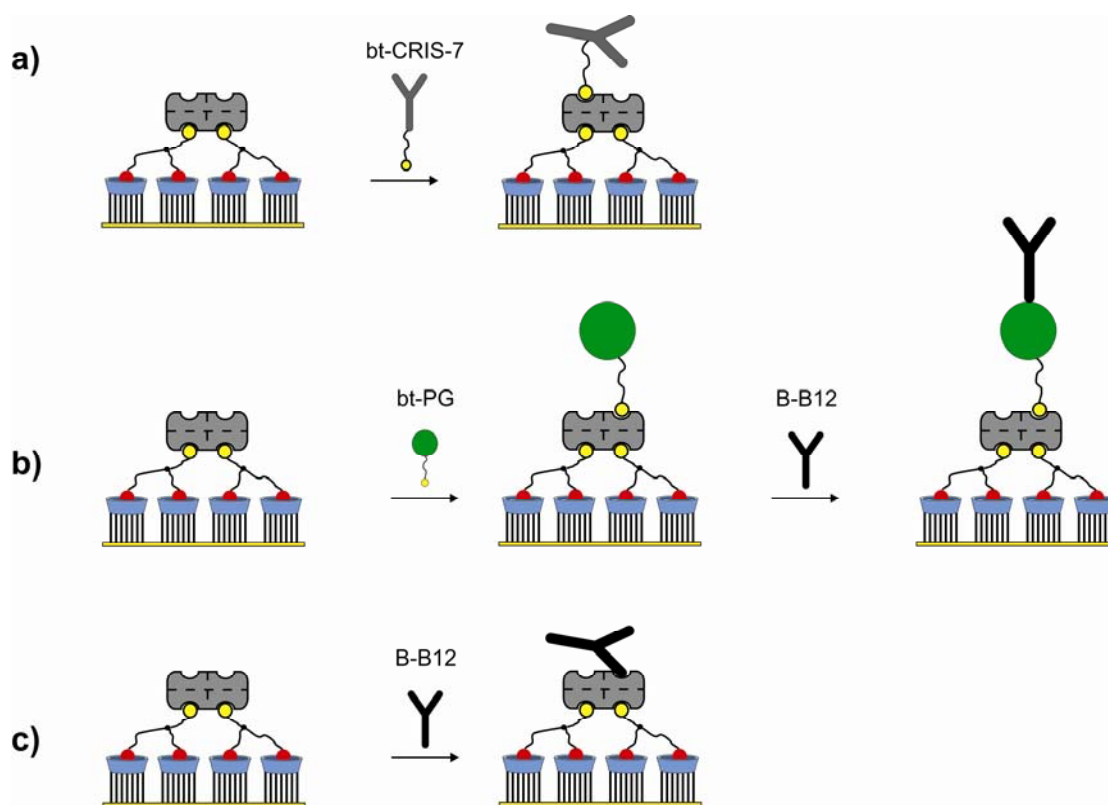
Scheme 5.3 *AB bionanostructures used for the cell attachment: molecular printboards coated with **1** and SAv: via bt-CRIS-7 (a), via B-B12 onto bt-PG (b), and via B-B12 directly immobilized (nonspecifically) at SAv on the molecular printboard (c).*

Dot-blot experiments were performed to check which of the Fc receptor proteins (PA or PG) is best suitable to bind the B-B12 MAB.[34] To this purpose, spots of the B-B12 MAB were made on nitrocellulose membranes followed by immobilization of PA or

PG on these spots. Subsequently the spots were developed by adding a specific horseradish peroxidase (HRP) (PA-HRP or PG-HRP) to the spots. Good binding to the B-B12 MAB was correlated with strong chemiluminescent signals. From the dot-blot-experiments, it became clear that bt-PA does not bind the B-B12 MAB very strongly. Bt-PG appeared to have strong binding to the B-B12 MAB and was therefore used in subsequent experiments preparing the bionanostructures according to Scheme 5.3b.

The binding of the bt-CRIS-7 MAB and the B-B12 MAB to SAv layers at molecular printboards according to Scheme 5.3a and b was investigated by SPR spectroscopy (Figure 5.7). βCD SAMs on gold substrates were immersed in an aqueous solution of 1 mM of **1**. Subsequently the samples were rinsed with water, carefully dried and assembled in the SPR setup. For the experiment with the bt-CRIS-7 MAB, SAv was flowed over the substrate, followed by a short flow of 1 mM βCD in PBS. Subsequently, 10^{-7} M bt-CRIS-7 in 1 mM βCD PBS was flowed over the surface (Figure 5.7a). For the structures consisting of the B-B12 MAB, SAv was adsorbed and 10^{-7} M bt-PG followed by a flow of 10^{-7} or 10^{-6} M of the B-B12 MAB (Figures 7b and c respectively).
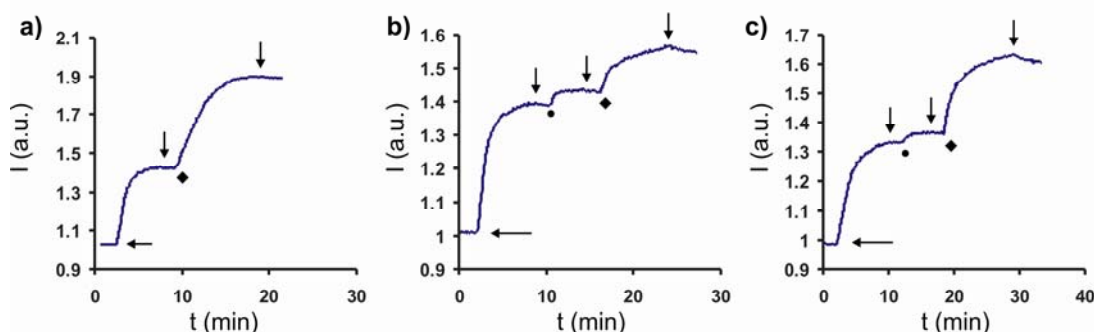
Figure 5.7 *SPR sensograms of the adsorption of SAv to the molecular printboard, followed by the adsorption of bt-CRIS-7 (Scheme 3a) (a) or bt-PG with subsequent B-B12 adsorption (Scheme 3b) from a 10^{-7} M (b) and a 10^{-6} M solution of the B-B12 MAB (c). Symbols indicate: SAv (←), PBS (↓), bt-PG (•), and the bt-CRIS-7 MAB or the B-B12 MAB(♦).*

The SPR sensograms in Figure 5.7 show the assembly of both the CRIS-7 and the B-B12 MABs. Figure 5.7a shows a relatively high signal when the CRIS-7 MAB was bound to the surface. When this is compared to the binding of the B-B12 MAB to bt-

PG at equal AB concentration (Figure 5.7b), it appeared that the latter binding was significantly lower, which indicates that less material was bound to the surface. This can potentially be attributed to a slower association kinetics for the B-B12 MAB. The SPR experiment depicted in Figure 5.7c shows the binding of the B-B12 MAB to bt-PG at an AB concentration of 10^{-6} M. This resulted in more binding, but still not as much as observed for the CRIS-7 MAB.

CRIS-7 is a MAB that is on average mono-biotinylated. These biotin moieties can be attached to different free amino groups present at the outside of the MAB. Therfore, not all Fab fragments will be directed upwards. The build-up via bt-PG is more difficult to interpret. The density of PG on the SAv layer is not known, but since PG (60 kDa) is about the same size as SAv it can be safely assumed that there is not a 2:1 binding of bt-PG to SAv. This means that the PG density is probably about the same as for SAv. On this PG layer an AB layer can be formed.

Surface-immobilized cells were detected by fluorescence microscopy. Hoechst 33342 is a general DNA-binding dye, coloring all cells present at the surface. CD4FITC, CD3PE, and CD8APC are dye-labeled ABs that are directed to specific proteins present in the cell membrane (CD4, CD3, and CD8 respectively). Molecular printboards were prepared on glass substrates which were immersed in a 1 mM aqueous solution of **1**. After rinsing with water, the substrates were mounted in a flow setup, and all protein components were sequentially flowed over the substrate. SAv was flowed over in PBS at a βCD concentration of 1 mM, other proteins were flowed over the substrate in PBS. The B-B12 MAB was also flowed directly over the self-assemblies on molecular printboards to prepare non-specifically bound B-B12 MAB surfaces (Scheme 5.3c). After attachment of the proteins, the samples were taken out of the flow setup, and rinsed carefully with PBS. Subsequently, 200 μl of a suspension of lymphocytes (1×10^5 cells/μl) which had been stained with Hoechst 33342 and CD4FITC, was put on top of the substrate, and the cells were incubated for 30 min at RT in the dark. The cell suspension was removed from the substrate, and the substrate was placed under the fluorescence microscope and Hoechst 33342 fluorescence microscopy images were recorded to determine the optimal washing procedure. After several wash steps the number of cells, stained with Hoechst 33352 did not decrease anymore, and both CD4FITC (displayed in red) and Hoechst 33342 (displayed in green) were imaged (Figure 5.8). By comparison these two recorded

images the specificity of cell adsorption can be determined. Cells which are only stained with Hoechst 3334 are regarded as being nonspecifically adsorbed, cells stained both by Hoechst 3334 and CD4FITC are regarded as being specifically immobilized.

The samples in which the B-B12 MAB was bound specifically through bt-PG showed the least amount of nonspecifically adsorbed cells. Since the results from cell adsorptions at the B-B12 surface prepared from 10^{-7} M and 10^{-6} M concentrations of B-B12 seemed to give similar results, linearity studies were performed on the B-B12 surface prepared from a 10^{-7} M solution.
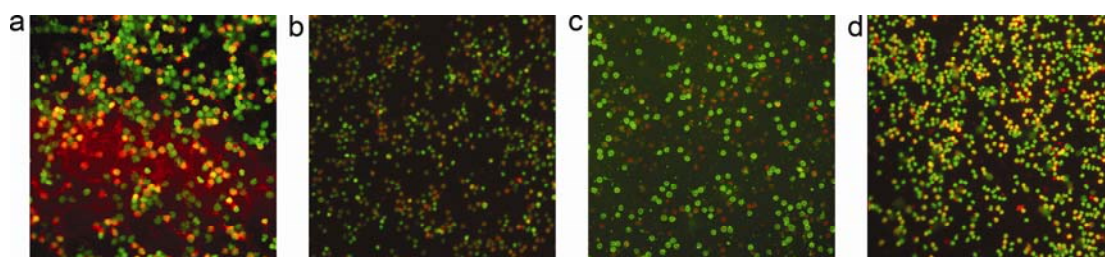
Figure 5.8 *Overlays of fluorescence microscopy images for the different cell adsorption experiments according to Scheme: 5.3a prepared from [AB] = 1 × 10⁻⁷ M (a), 5.3b prepared from [AB] = 1 × 10⁻⁷ M (b), 5.3b prepared from [AB] = 1 × 10⁻⁶ M (c), and 5.3c prepared from [AB] = 1 × 10⁻⁷ M (d). Hoechst 33342 is depicted in green and CD4FITC is depicted in red.*

For the linearity study, four substrates onto which B-B12 was immobilized via bt-PG (Scheme 5.3b) were prepared, and each sample was incubated for 30 min at RT in the dark, with a different concentration of lymphocytes on each sample. The concentration of lymphocytes, as determined by flow cytometry, contained 8500 lymphocytes/μl, of which 6200 CD3$^+$ T cells/μl (3500 CD3$^+$CD4$^+$ T cells/μl and 2700 CD3$^+$CD8$^+$ T cells/μl). Four lymphocyte suspensions were prepared by dilution of the original cell suspension with PBS. From these numbers the expected numbers of cells per image, (60% of the seeded cells due to the manner in which the cells are brought in contact with the surface) can be calculated (Table 5.2).

Table 5.2 *Results of linearity studies on four samples prepared according to Scheme 5.3b: numbers of seeded cells, theoretically expected cells and the immobilized cells that were visualized by fluorescence microscopy imaging. The number of expected cells is 60% of the number of seeded cells.*

	Seeded cells (#/μl)	Expected CD3$^+$ cells (#/image)	Experimental CD3$^+$ cells (#/image)
Sample 1	2016	1199	1253 ± 62
Sample 2	1005	598	424 ± 27
Sample 3	503	299	159 ± 4
Sample 4	248	148	43 ± 4

The cell suspensions were removed after 30 min from the substrate, and the substrate was rinsed 3 times. Thereafter, cells were incubated with a solution containing Hoechst 33342, CD3PE, CD4FITC, and CD8APC to color the cells in different manners, as described above. Subsequently, fluorescence images were recorded in three different spots on the sample, from CD3PE (depicted in red), CD4FITC (depicted in green), and CD8APC (depicted in cyan). In Figure 5.9 overlay images are presented of the samples with the highest and the lowest cell concentrations. The specificity of the cell adsorption measured on all substrates is similar, and comparable to the experiments showed above.
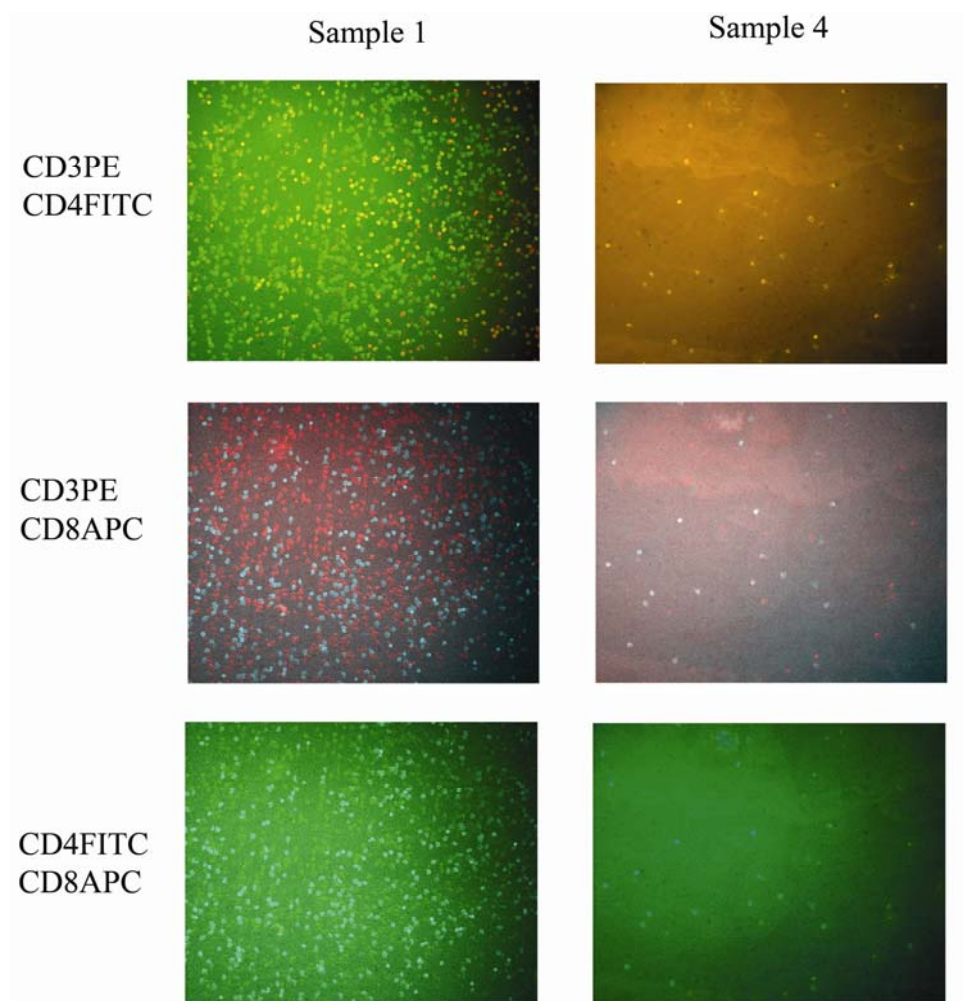
Figure 5.9 *Fluorescence microscopy images of the linearity studies (Scheme 5.3b) sample 1 and 4). CD3$^+$ cells are depicted in red, CD4$^+$ cells are depicted in green, and CD8$^+$ cells are depicted in cyan.*

Figure 5.10 shows linearity plots of the cell experiments. The expected numbers of cells were calculated by assuming that all CD3$^+$ T cells are captured on a surface under ideal conditions, which is 60% of the total amount of cells put on top of the sample. The theoretical number of captured cells is not reached, in particular not for lower numbers of seeded cells. However, all cell species at the surface show an approximately linear relationship, indicating that the molecular printboard can potentially be used for the detection of CD3$^+$ cells by ABs.

Figure 5.10 *Linearity plots showing the number of counted cells plotted versus the number of seeded cells of cell adsorption according to Scheme 5.3b. CD3$^+$ cells (blue), CD3$^+$CD4$^+$ cells (red), and CD3$^+$CD8$^+$ cells (green). The offset of the slopes were set as zero. Error bars indicate the standard deviations of cell numbers counted in three different areas.*

5.2.4   Molecular printboards inside microchannels: towards protein assays
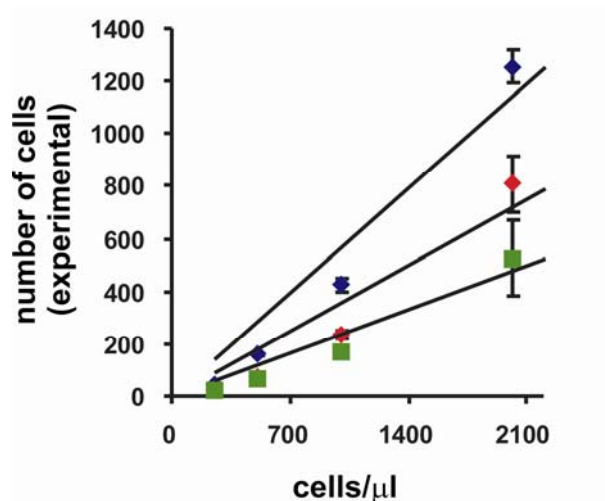
The strive for miniaturization is important in biological assays, since it allows faster diagnostics, with small amounts of sample, and therefore lower costs.[35-37] There are currently numerous applications for these microchips.[38,39] Protein functionality and the inhibition of nonspecific adsorption are key issues in this field. Immunoassays, which involve the immobilization of ABs in microchannels, are an important class of biological assays, since small quantities of antigens can be detected.[40-45]

For the formation of βCD SAMs and the subsequent specific attachment of proteins inside these channels separately, a microchip was fabricated with one large channel (width 390 μm; height 50 μm) which splits into four smaller channels (width 60 μm; height 50 μm), which are separated by 50 μm (Chart 5.2a). The chip was made of glass on silicon. The compounds used in this study are depicted in Chart 5.2.
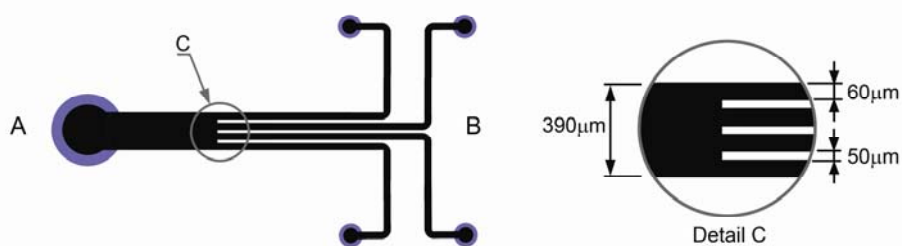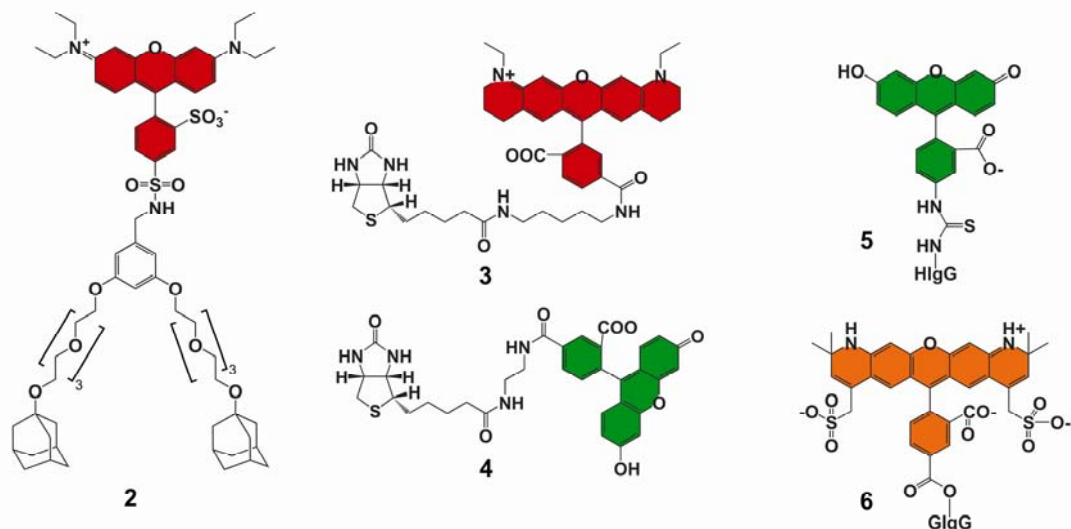
Chart 5.2 *Chip design used in this study (a) and compounds used in the chip study (b): fluorescent dendritic wedge (**2**), Atto 565-biotin (**3**), biotin-4-fluorescein (**4**), HIgG-fluorescein (**5**), Alexafluor 568-GIgG (**6**).*

The formation of βCD SAMs in the microchannels was carried out in three subsequent steps (Scheme 5.4), similar to the procedure described before.[46] In a preceding cleaning procedure, approximately 250 µl fresh piranha was flushed through the chip, every 5 min, for 45 min. After the last piranha flush, water was flushed through the channels followed by drying in a stream of N_2. Thereafter, freshly distilled toluene was flushed through the chip for 10 min. Subsequently a 5 mM solution of N-[3-(trimethoxysilyl)propyl]ethylenediamine (TPEDA) was flowed through the chip for 4 h at room temperature. After this step distilled toluene was flushed through for 15 min, followed by drying of the channels in a stream of N_2. No blocked channels due to polymerization were observed by microscopy. The channels were flushed with ethanol, followed by a flow of 10 mM 1,4-phenylene-diisothiocyanate (DITC) in ethanol for 2 h at room temperature followed by a rinse with ethanol. After drying the chip, Millipore water was flowed through the chip,

121

followed by 10 mM βCD-heptamine in millipore water at pH 8.5 for 2 h at room temperature. This was again followed by a rinse with water, and drying the channels in a stream of N$_2$.
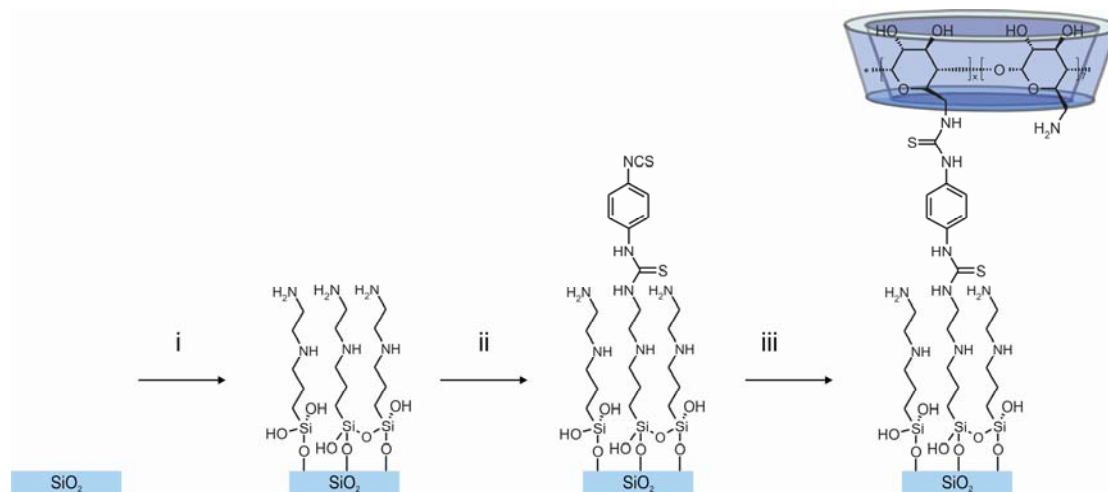
Scheme 5.4 *Synthesis scheme for the preparation of βCD SAMs inside microchannels composed of SiO$_2$ and glass: piranha, followed by TPEDA in freshly distilled toluene, RT, 4 h (i), DITC in ethanol, RT, 2 h (ii), βCD-heptamine in Millipore water pH 8.5, RT, 2 h (iii).*

To test whether or not the βCD immobilization in the channels was successful, and if the host-guest properties of the formed monolayer inside the microchannels is comparable to the host-guest properties at planar βCD substrates, adamantyl-terminated dendritic wedge **2** was immobilized in the channels by rinsing a 0.1 mM solution in 1 mM βCD through the channels for 30 min. The fluorescence image that was recorded after rinsing for 10 min with water (Figure 5.11a) shows clearly that **2** is present in the channels. Subsequently, a rinse with 1 mM βCD was carried out for 10 min, followed by a rinse with water for 10 min. The fluorescence image after this treatment (Figure 5.11b) shows very clearly that **2** is still present, although the intensity is slightly lower. Subsequently 10 mM βCD was flowed through the chip for 20 min followed by a water rinse for 10 min. The fluorescence image that was recorded hereafter (Figure 5.11c) shows that the intensity had dropped significantly, but was not completely removed. Rinsing for 10 min with ethanol did not change much (Figure 5.11d), and only after 10 min with methanol followed by a 10 min water

rinse (Figure 5.11e), the fluorescence of the channels had dropped to almost zero. These results are comparable to the results obtained from experiments in which divalent adamantyl guests were attached to βCD SAMs on gold and glass.[47,48] The possibility of disrupting the host-guest assemblies by organic solvents such as ethanol and methanol has also been shown in Chapter 3. Therefore it can be concluded that this experiment indicates that the interaction between **2** and the channel wall is indeed governed by supramolecular interactions, proving the presence of the βCD SAM inside the channel.
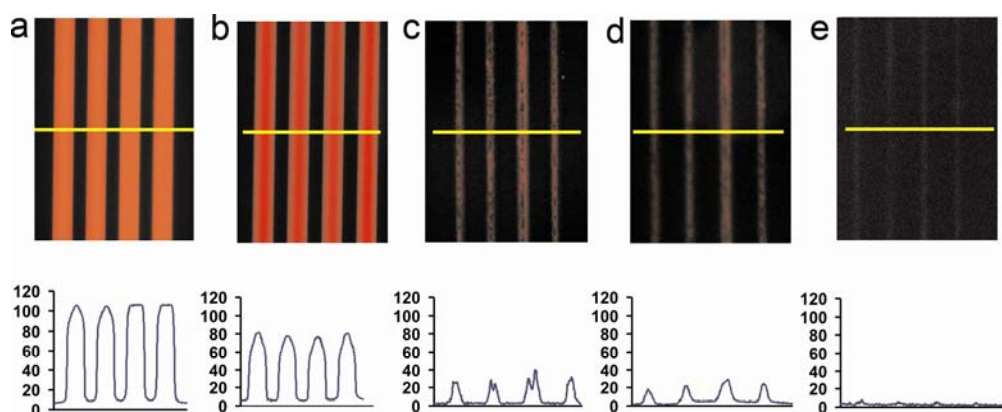
Figure 5.11 *Fluorescence images after the attachment of **5**, and the sequential flowing of water (a), 1 mM βCD and water, (b) 10 mM βCD and water(c), ethanol and water (d), and methanol and water (e).*

To show that the channels can be addressed individually, SAv was assembled in all channels via divalent linker **2**. The latter was adsorbed from inlet A (see Chart 5.2), and from the same side SAv was flowed through the channel subsequently. Two different fluorescently labeled biotin derivatives (**3** and **4**) were flowed from the small inlets at side B through alternating channels to create assemblies according to the procedure shown in Scheme 4.2E (Chapter 4). The flow rate in this experiment was set such that there was sufficient back-pressure in order to prevent mixing, or back-diffusion of the different biotin derivatives in the small channels. After 30 min, millipore water was flowed through the channels, also from side B.

Imaging the channels with green excitation light showed two channels in which **3** was immobilized (Figure 5.12). Imaging with blue excitation light showed that **4** was immobilized in the other two channels. The combined image shows the four channels,

with alternating **3** and **4**, proving the possibility of individual channel functionalization, using intrinsically reversible supramolecular interactions.

Figure 5.12 *Fluorescence microscopy images taken with blue (left) and green (center) excitation light of the chip functionalized with biotin derivatives (**3** and **4**) in alternating channels as described in Scheme 5.2b. The picture at the right shows the combined image.*

For protein assays it is important to show that only specific ABs are detected. This prevents the appearance of e.g. false positives. To prove that this is possible in this system, divalent linker **2** and SAv were immobilized in the βCD-covered channels from side A followed by the immobilization of bt-PA from this side, which results in all channels being covered with bt-PA (Scheme 5.2b). Subsequently, human IgG (HIgG) (**5**) and goat IgG (GIgG) (**6**), were flowed in the reverse direction (From side B) through alternating channels of the chip for 30 min. After rinsing for 20 min it became apparent that only two channels had been modified with a fluorescent IgG (Figure 5.13b): only HIgG immobilization was observed. Goat IgG did not bind to PA, as expected, since this GIgG does not bind to protein A. These experiments showed that the channels can be addressed separately and that the channels can be modified in such a manner that the immobilization of proteins is specific.
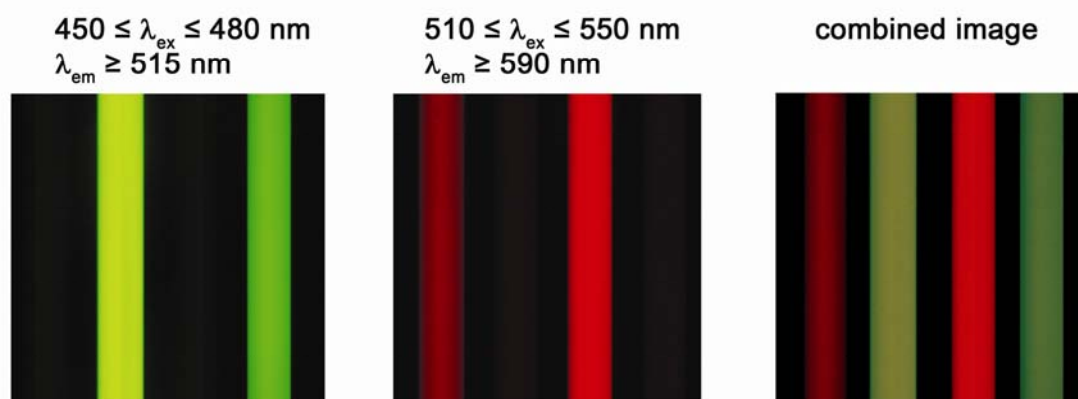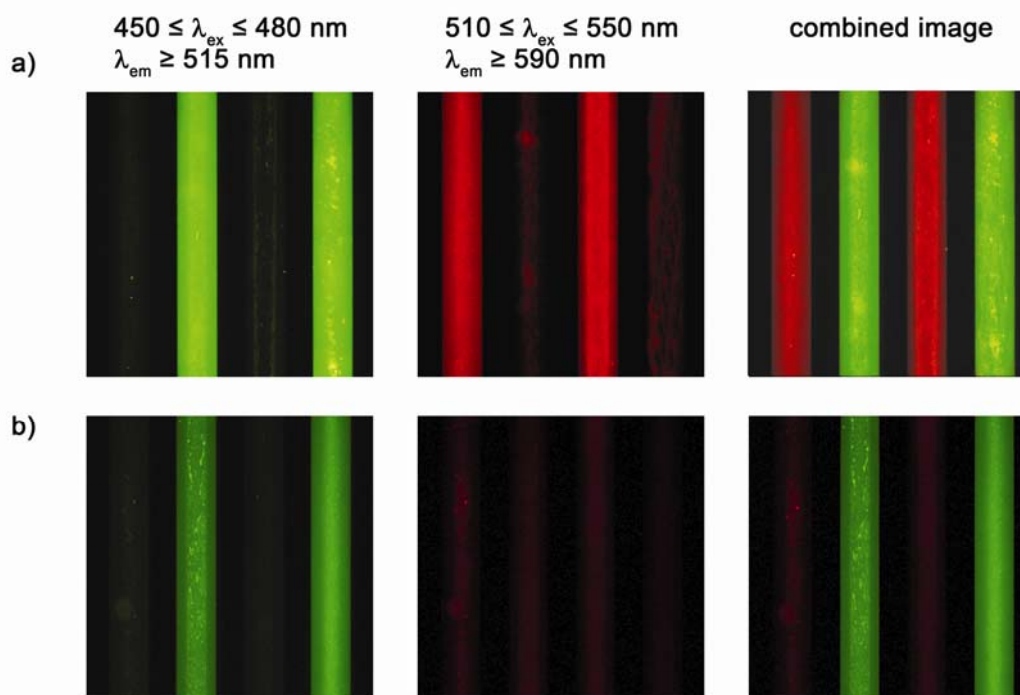
Figure 5.13 *Fluorescence microscopy images taken with blue (left) and green (center) excitation light of the chip functionalized with bt-PA-HIgG and bt-PG-GIgG in alternating channels as described in Schemes 2b and 2c (a), and with bt-PA + HIgG and bt-PA + GIgG in alternating channels (b). The picture at the right show the combined images.*

5.3   Conclusions

In this chapter, it has been shown that SAv, once assembled in a stepwise manner to molecular printboards can be hetero-functionalized with (complex) bionanostructures. These structures, consisting of ABs or their Fc fragment can be patterned on surfaces with a high degree of specificity as shown by fluorescence images of a bionanostructure consisting of **1**, SAv, bt-PA, and rhodamine-labeled IgG-Fc. Bionanostructures consisting of ABs on the molecular printboard can be assembled in different ways, via a biotin functionality, via a biotinylated AB, or via an Fc receptor such as PA or PG. These bionanostructures can be applied in the specific attachment of cells to these surfaces. Different MAB modified surfaces were tested for this purpose, consisting of the bt-CRIS-7 MAB and the B-B12 MAB in different concentrations, assembled via bt-PG, and the B-B12 MAB adsorbed to the molecular printboard in a non-ordered fashion. Surfaces, consisting of the B-B12 MAB and

125

assembled via bt-PG have the least nonspecific cell attachment. Linearity studies were therefore performed on the bionanostructures consisting of the B-B12 MAB. An approximately linear behavior was observed when adsorbing different concentrations of cells to these surfaces. The results shown in this part can possibly applied in new cell-detection systems. Finally, it was shown that βCD SAMs can be assembled in microfluidic channels, and that the properties of these βCD SAMs are comparable to previous studies. The build-up of bionanostructures inside microchannels was proven by fluorescence microscopy. The individual addressability of the different channels was shown in an experiment in which H-IgG was specifically adsorbed. The tools presented in this part can potentially be used for the development of more complex diagnostic systems, to be used e.g. in medical or environmental applications.

5.4   Acknowledgements

5.5   Experimental section

General

Compound **1** was synthesized as described in Chapter 4. Compound **2** was synthesized as described before.[47] All chemicals were used as received. SAv and IgG-FITC from human serum were obtained from Sigma Aldrich. MAB to CD3 from clone CRIS-7 (isotype Mouse IgG2a,κ; 0.526 mg/ml) and MAB to CD3 from clone B-B12 (isotype IgG1,κ; 3.385 mg/ml) were obtained from the Antibodystore. Biotinylation of CRIS-7 was performed by Immunicon. Alexa fluor 568 goat anti-rabbit IgG (H + L) were obtained from Invitrogen, the Netherlands. Hoechst 33342 for DNA staining was obtained from Molecular Probes, Invitrogen, USA. CD3PE, CD4FITC, and CD8APC were obtained from BD Bioscience, USA. The

functionalization of IgG-Fc with rhodamine was performed according to literature procedures. After labeling, the protein:rhodamine ratio was on average 1:2.[49,50]

10 mM phosphate buffered saline (PBS) at pH 7.5 containing 150 mM NaCl was used during experiments.

Monolayer preparation

Gold substrates for SPR (BK7 glass/2-4 nm Ti/50 nm Au) and AFM (Si wafer/2-4 nm Ti/20 nm Au) were obtained from Ssens B.V., Hengelo, The Netherlands. Gold substrates were cleaned by dipping them in piranha (1:3 mixture of concentrated H_2SO_4 and 30% H_2O_2) for 5 s. (*Warning:* piranha should be handled with caution; it can detonate unexpectedly.) After thorough rinsing with Millipore water, they were placed for 10 min in absolute EtOH. Subsequently the substrates were placed in a freshly prepared 0.1 mM solution of βCD heptathioether for 16 h at 60 °C. The samples were subsequently rinsed 3 times with $CHCl_3$, EtOH and Millipore water.[51] βCD monolayers on glass were prepared as described earlier.[46] All solvents used in the monolayer preparation were of p.a. grade.

SPR

SPR measurements were performed on a Resonant Probes GmbH SPR instrument. The instrument consists of a HeNe laser (JDS Uniphase, 10 mW, λ = 632.8 nm) of which the laser light passes through a chopper that is connected to a lock-in amplifier (EG&G 7256). The modulated beam is directed through two polarizers (OWIS) to control the intensity and the plane of polarization of the light. The light is coupled via a high index prism (Scott, LaSFN9) in the Kretschmann configuration to the backside of the gold-coated substrate which is optically matched through a refractive index matching oil (Cargille; series B; $n_D^{25°C}$ = 1.7000 ± 0.0002) at the prism, mounted on a θ-2θ goniometer, in contact with a Teflon cell with a volume of 39 μl and a diameter of 5 mm. The light that leaves the prism passes through a beam splitter, subsequently, the s-polarized light is directed to a reference detector, and the p-polarized light passes through a lens which focuses the light onto a photodiode detector. Laser fluctuations are filtered out by dividing the intensity of the p-polarized light (I_p) by the intensity of the s-polarized light (I_s). All measurements were performed at a constant angle by reflectivity tracking.

A Reglo digital MS-4/8 flow pump from Ismatec with four channels was used. In this flow pump, Tygon R3607 tubings with a diameter of 0.76 mm were used, obtained from Ismatec.

The SPR experiments were performed under a continuous flow of 0.5 ml/min. Before a new experiment was started, the gold substrates were rinsed thoroughly with 10 mM βCD in 10 mM PBS containing 150 mM NaCl, and 10 mM PBS containing 150 mM NaCl. Experiments were started after the baseline was stable. When the solution had to be changed, the pump was stopped, and immediately after changing the solution the pump was switched on again. Concentrations of proteins that were flowed during experiments were 1×10^{-7} M, unless stated otherwise.

Microcontact printing (μCP)

PDMS stamps were prepared by casting a 10:1 (v/v) mixture of poly(dimethylsiloxane) and curing agent (Sylgard 184, Dow Corning) against a patterned silicon master. After curing of the stamps overnight, they were mildly oxidized in an ozone plasma reactor (Ultra-Violet Products Inc., model PR-100) for 60 min to render them hydrophilic. Subsequently, they were inked by soaking them in a 10^{-5} M aqueous solution of the divalent linker (**1**) for 20 min. The master employed to prepare the PDMS stamps had hexagonally oriented 10 μm circular features separated by 5 μm. Before printing, the stamps were blown dry in a stream of N_2. The stamps were applied manually and without pressure control for 10 min onto the βCD SAMs on gold and then carefully removed. For every printing step, a new stamp was used. The substrates were thoroughly rinsed with water. Proteins were flowed over the patterned substrates for 10 min at a flowrate of 0.5 ml/min. In between different protein flows, a rinse of 2 min with PBS was applied.

Atomic force microscopy

For the AFM scratching experiments a custom-built stand-alone AFM was employed.[52] Standard silicon nitride cantilevers with a length of 85 μm, force constant 0.5 N/m and operating frequencies 85 – 130 kHz (in air) purchased from Veeco were used. First, AFM in contact mode was used to produce a 300 nm groove (contact force of 50 nN), by repeatedly scanning the same area in order to remove the adsorbed material and determine *in situ*[53] the thickness of the different assemblies.

Subsequently, the scan size was increased to 1500 nm and imaged in tapping mode. Images contained 256×256 pixels and were recorded at a line frequency of 2 Hz. The calibration of the setup was made with UltraSharp Calibration Gratings from NT-MDT (NT-MDT Co., Russia). Topographical images were quantitatively analysed by means of a scanning probe image processor program (Image Metrology ApS, Lyngby, Denmark).

Dot-Blot experiments

A standard dot-blot protocol was used for these experiments.[34] Different concentrations of B-B12 in PBS were prepared: 500 ng/μl, 50 ng/μl, and 5 ng/μl. Stock solutions of 1 mg/ml of the ligands PA-Horseradish Peroxidase (PA-HRP) and PG-Horseradish Peroxidase (PG-HRP) were prepared in dilution buffer (PBS). Working dilutions were prepared by diluting the ligand stocks 5000-fold using blocking reagent (containing 0.05% Tween-20 and 1% BSA).

Circles ($d = 4$ mm) were drawn on a Protan nitrocellulose transfer membrane (pore size: 0.45 μm) to indicate the regions in which the protein samples would be blotted. Thereafter, 2 μl of the different CD3 MAB solutions were slowly spotted onto the nitrocellulose membrane at the center of the circle using a pipette with a narrow-mouth tip, after which the membrane was left to dry. The nonspecific sites of the membrane (*i.e.* the sites outside the circled areas) were blocked by soaking the membrane in blocking buffer for 1 h at RT. Subsequently, the membranes were removed from the blocking buffer, and incubated. In a solution containing the HRP-conjugate working dilutions for 1 h at RT under shaking. After incubation the membranes were rinsed with wash buffer and left shaking in wash buffer. The wash buffer was replaced every 5 min, and this was repeated 5 times. Thereafter the membranes were incubated in the substrate working solution for 5 min (0.1 ml of working solution per cm^2 membrane). Chemiluminescent images of the dot membranes were recorded on a Kodak Image Station 2000MM.

Lymphocyte suspensions

Peripheral blood (20 ml) was collected into 2 heparinized tubes from healthy donors. Peripheral blood mononuclear cells (PBMC) were isolated using a Ficoll-Paque[TM] Plus (GE Healthcare) density separation method.

One tube of peripheral blood (approximately 10 ml) was diluted with 12 ml PBS supplemented with 0.38% trisodium citrate and 0.5% bovine serum albumine (PBS-TNC-BSA). 6 - 7 ml of the diluted blood is brought onto a layer of 3 ml Ficoll with a density of 1.077 g/cm^3. The tube was centrifuged at 2200 rpm (1000 g) for 20 min at room temperature. The layer on top of the Ficoll (the mononuclear cells) was removed and washed with ~ 40 ml PBS-TNC-BSA once at 1500 rpm for 7 mins at 4 °C and once at 1400 rpm for 6 min at 4 °C. The mononuclear cells were resuspended in RPMI 1640 supplemented with 10% FCS and 1% Antibiotic/Antimycotic solution, and incubated for 1 h at 37 °C in a T75 culture flask. Subsequent the lymphocytes were removed from the suspension, concentrated into 2 ml of PBS and kept on ice.

Cell enumeration by immuno-labeling and image recording

For the linearity experiments, the cell count of the lymphocytes suspension was measured by flow cytometry. Accordingly, four different concentrations of cell suspensions were prepared by diluting the original cell suspension with PBS. The stock solution of lymphocytes contained 8500 lymphocytes/µl, of which 6200 CD3$^+$ T cells/µl (3500 CD3$^+$CD4$^+$ T cells/µl and 2700 CD3$^+$CD8$^+$ T cells/µl). The different CD3$^+$ T cell concentrations in the different dilutions were: 2016 CD3$^+$ T cells/µl (sample 1), 1005 CD3$^+$ T cells/µl (sample 2), 503 CD3$^+$ T cells/µl (sample 3), and 248 CD3$^+$ T cells/µl (sample 4).

A reagent cocktail (230 µl) consisting of 0.5 µl of 1mg/ml Hoechst 33342, 20 µl CD3PE, 20 µl CD4FITC, and 40 µl CD8APC and 150 µl of PBS was added to the samples on which the cell sample had been incubated. The samples were analyzed by fluorescence microscopy. For each sample three areas in the center of the glass slide were imaged.

Microchip

Chips were prepared as follows. After standard cleaning and HNO$_3$ treatment, a silicon wafer (<100>, p-type) was coated with 1.7 µm photoresist (Olin 907.17) and baked for 90 s at 90 °C. Subsequently contact photolithography with an exposure time of 4 s was performed, followed by a 1 min post-exposure bake at 120 °C The photoresist was developed by immersion of 30 s in "dirty" developer and 25 s in

"clean" developer. Subsequently the Bosch process[54] was applied at a rate of 20 μm/min. Photoresist stripping was carried out by rinsing with acetone, followed by 20 min HNO$_3$ treatment and a few min of O$_2$ plasma exposure. To create the inlets, powder blasting foil (BF410) was applied on the other side of the wafer by laminating it at 130 °C. Photolithography through a mask was applied for 20 s. After this the photoresist was developed for 3 min. The inlets were made by powder blasting with Al$_2$O$_3$ grains (29 μm; viahole formation). The inlets had a size of 1 mm at the outside, and 360 μm at the bottom. The powder blasting foil was stripped with acetone and soda. After this procedure the wafer was cleaned in an ultrasonic bath in acetone (20 min) and standard cleaning. Pyrex glass was cleaned by standard cleaning and attached via anodic bonding at 400 °C for 3 min at 400 V, 3 min at 600 V, 3 min at 800 V and finally 10 min at 1000 V. Dicing to separate the microchips on the wafer by a disco dicing saw was carried out after laminating the wafer with a transparent foil on the silicon side. After dicing the foil was detached by 3 min UV irradiation for final cleaning.

Microchip holders were fabricated from black Delrin blocks and Teflon. The chip was placed in a black Delrin custom made holder onto which syringes could be connected via nanoports to create pressure drives flow with a CMA/102 Microdialysis Pump on which 250 μl flat Hamilton syringes were mounted. Syringes were connected to fused silica capillaries (100 μm i.d.) by means of nanoports. The applied flow rate was 2 μl/min in the experiments for the assembly of the βCD SAM. For the assembly of the different proteins and biotin derivatives a flow rate of 4 ml/min for 30 min was used. In between the different assembly steps, PBS buffer was flowed through the chip at a rate of 2 μl/min.

Fluorescence Microscopy

Microchip experiments

Fluorescence microscopy images were made using an Olympus inverted research microscope IX71 equipped with a mercury burner U-RFL-T as light source and a digital camera Olympus DP70 (12.5 million-pixel cooled digital color camera) for image acquisition. Blue excitation (450 nm ≤ λ_{ex} ≤ 480 nm) and green emission (λ_{em} ≥ 515 nm) was filtered using a U-MWB Olympus filter cube. Green excitation (510 nm

≤ λ$_{ex}$ ≤ 550 nm) and red emission (λ$_{em}$ ≥ 590 nm) was filtered using a U-MWG Olympus filter cube.

Cell experiments

Fluorescent images were made using an Nikon ECLIPSE E400 microscope equipped with a 40× objective and 4 filter cubes (Excitation/Dichroic/Emission: 365/400/400; 480/495/510; 546/560/580; 620/660/700), and a CCD camera for image acquisition.

5.6   References

1.   J. Spinke, M. Liley, H.-J. Guder, L. Angermaier, W. Knoll, *Langmuir* **1993**, *9*, 1821-1825.

2.   M. Wilchek, E. A. Bayer, *Anal. Biochem.* **1988**, *171*, 1-32.

3.   J. Turková. *J. Chrom. B* **1999**, *722*, 11-31.

4.   A. Biebricher, A. Paul, P. Tinnefeld, A. Gölzhäuser, M. Sauer, *J. Biotech.* **2004**, *112*, 97-107.

5.   K. Zhang, M. R. Diehl, D. A. Tirrell, *J. Am. Chem. Soc.* **2005**, *127*, 10136-10137.

6.   H. Zhu, M. Snyder, *Curr. Opin. Chem. Biol.* **2003**, *7*, 55-63.

7.   N. L. Rosi, C. A. Mirkin, *Chem. Rev.* **2005**, *105*, 1547-1562.

8.   C. M. Niemeyer, *Angew. Chem. Int. Ed.* **2001**, *40*, 4128-4158.

9.   E. Katz, I. Willner, *Angew. Chem. Int. Ed.* **2004**, *43*, 6042-6108.

10.   L. Tiefenauer, Ros, R., *Coll. Surf. B* **2002**, *23*, 95-114.

11.   D. Q. Tang, D. Y. Tang, D. P. Tang, *Bioprocess. Eng.* **2005**, *27*, 135-141.

12.   C. C. Su, T. Z. Wu, L. K. Chen, H. H. Yang, D. F. Tai, *Anal. Chim. Acta* **2003**, *479*, 117-123.

13.   D. J. O'Shannessy, M. J. Dobersen, R. H. Quarles, *Immun. Lett.* **1984**, *8*, 273-277.

14.   W. L. Hoffman, D. J. O'Shannessy, *J. Immun. Methods* **1988**, *112*, 113-120.

15.   I. N. Chang, J. N. Herron, *Langmuir* **1995**, *11*, 2083-2089.

16.   I. N. Chang, J. N. Lin, J. D. Andrade, J. N. Herron, *J. Coll. Interf. Sci.* **1995**, *174*, 10-23.

17.   J. Buijs, D. D. White, W. Norde, *Coll. Surf. B* **1997**, *8*, 239-249.

18. S. Chen, L. Liu, J. Zhou, S. Jiang, *Langmuir* **2003**, *19*, 2859-2864.

19. B. Akerstrom, T. Brodin, k. Reis, L. Bjorck, *J. Immunol.* **1985**, *135*, 2589-2592.

20. L. J. Janis, F. E. Regnier, *Anal. Chem.* **1989**, *61*, 1901-1906.

21. A. Larsson, *J. Immunol Methods* **1990**, *135*, 273-275.

22. J. G. J. van de Winkel, P. J. A. Capel, *Immun. Today* **1993**, *14*, 215-221.

23. Z. Ding, R. B. Fong, C. L. Long, P. S. Stayton, A. S. Hoffman, *Nature* **2001**, *411*, 59-62.

24. R. P. Haugland, *Methods in Molecular Biology*, ed. W. C. Davis, Totowa: Davis Humana Press Inc., **1995**, *45*, 205-221.

25. C. M. Bruinink, C. A. Nijhuis, M. Péter, B. Dordi, O. Crespo-Biel, T. Auletta, A. Mulder, H. Schönherr, G. J. Vancso, J. Huskens, D. N. Reinhoudt, *Chem. Eur. J.* **2005**, *11*, 3988-3996.

26. P. H. Nibbering, P. C. J. Leijh, R. van Furth, *J. Histochem. Cytomet.* **1985**, *33*, 453-459.

27. L. J. Wysocki, V. L. Sato, *Proc. Natl. Acad. Sci. USA* **1978**, *75*, 2844-2848.

28. T.-W. Chang, *J. Immun. Methods* **1983**, *65*, 217-223.

29. P. Bousso, F. Michel, N. Pardigon, N. Bercovici, R. Liblau, P. Kourilsky, J. P. Abastado, *Immun. Lett.* **1997**, *59*, 85-91.

30. L. Belov, O. de la Vega, C. G. dos Remedios, S. P. Mulligan, R. I. Christopherson, *Cancer Res.* **2001**, *61*, 4483-4489.

31. K. Sekine, A. Revzin, R. G. Tompkins, M. Toner, *J. Immun. Methods* **2006**, *313*, 96-109.

32. C. A. Janeway Jr., P. Travers, M. Walport, M. J. Shlomchik, *Immunobiology: the immunesystem in health and disease*, 6th ed., **2005**.

33. W. M. Comans-Bitter, R. de Groot, R. Van den Beemd, H. J. Neijens, W. C. J. Hop, K. Groeneveld, H. Hoijkaas, J. J. M. Van Dongen, *J. Pediatr.* **1997**, *130*, 388-393.

34. www.abcam.com/technical (**2006**).

35. E. Delamarche, D. Juncker, H. Schmid, *Adv. Mater.* **2005**, *17*, 2911-2933.

36. C. Hultschig, J. Kreutzberger, H. Seitz, Z. Kontur, K. Büssow, H. Lehrach, *Curr. Opin. Chem. Biol.* **2006**, *10*, 4-10.

37. D. N. Breslauer, P. J. Lee, L. P. Lee, *Mol. Biosystems* **2006**, *2*, 97-112.

38. J. Jäger, D. Weichenhan, B. Ivandic, R. Spang, *Stat. Appl. Gen. Mol. Biol.* **2005**, *4*, Art. No. 9.

39. M. Madou, J. Zoval, G. Y. Jia, H. Kido, J. Kim, N. Kim, *Annu. Rev.* **2006**, *8*, 601-628.

40. D. Wild, *The Immunoassay Handbook*, 2nd ed., Nature, Londen, **2001**.

41. E. P. Diamandis, T. K. Christopoulos, *Immunoassays*, Academic Press, San Diego, CA, **1996**.

42. D. S. Hage, *Anal. Chem.* **1999**, *71*, 294R.

43. A. Bange, H. B. Halsall, W. R. Heineman, *Biosens. Bioelectron.* **2005**, *20*, 2488-2503.

44. A. E. Herr, D. J. Throckmorton, A. E. Davenport, A. K. Sigh, *Anal. Chem.* **2005**, *77*, 585-590.

45. A. Ymeti, J. Greve, P. V. Lambeck, T. Wink, S. W. F. M. van Hövell, T. A. M. Beumer, R. R. Wijn, R. G. Heideman, V. Subramaniam, J. S. Kanger, *Nano Lett.* **2007**, *7*, 394-397.

46. S. Onclin, A. Mulder, J. Huskens, B. J. Ravoo, D. N. Reinhoudt, *Langmuir*, **2004**, *20*, 5460-5466.

47. A. Mulder, S. Onclin, M. Péter, J. P. Hoogenboom, H. Beijleveld, J. ter Maat, M. F. Garcia-Parajo, B. J. Ravoo, J. Huskens, N. F van Hulst, D. N. Reinhoudt, *Small* **2005**, *1*, 242-253.

48. A. Mulder, T. Auletta, A. Sartori, S. del Ciotto, A. Casnati, R. Ungaro, J. Huskens, D. N. Reinhoudt, *J. Am. Chem. Soc.* **2004**, *126*, 6627-6636.

49. M. Brinkley, *Bioconj. Chem.* **1992**, *3*, 2-13.

50. K. L. Holms, L. M. Lantz, *Method. Cell Biol.* **2001**, *63*, 185-204.

51. M. W. J. Beulen, J. Bügler, B. Lammerink, F. A. J. Geurts, E. M. E. F. Biemond, K. G. C. van Leerdam, F. C. J. M. van Veggel, J. F. J. Engbersen, D. N. Reinhoudt, *Langmuir* **1998**, *14*, 6424-6429.

52. K. O. van der Werf, C. A. J. Putman, B. G. de Grooth, F. B. Segerink, E. H. Schipper, N. F. van Hulst, J. Greve. *Rev. Sci. Instrum.* **1993**, *64*, 2892-2897.

53. R. F. M. Lobo, M. A. Pereira-da-Silva, M. Raposo, R. M. Faria, O. N. Oliveira, *Nanotechnology* **1999**, *10*, 389-393.

54. A. A. Ayon, R. B. Braff, C. C. Lin, H. H. Sawin, M. A. Schmidt, *J. Electrochem. Soc.* **1999**, *339*, 2730-2736.

6

Molecular printboards as general platforms for protein immobilization: a supramolecular solution to nonspecific adsorption*

In this chapter a supramolecular approach for the prevention of nonspecific protein adsorption at β-cyclodextrin (βCD) molecular printboards is presented. For that reason adamantyl hexa(ethylene glycol) (1) was developed, consisting of an adamantyl group for controlled specific interactions to βCD molecular printboards, and a hexa(ethylene glycol) chain for the inhibition of nonspecific protein adsorption. Aggregation of 1 did not occur up to concentrations of 1 mM and also interactions of 1 with the test protein bovine serum albumin (BSA) could be ruled out. It appeared that already very low concentrations of 1 could be used, when compared to the standard oligo(ethylene glycol)-terminated SAMs developed by Whitesides et al. When 1 was used for the prevention of nonspecific protein adsorption, specific immobilization of proteins through multivalent orthogonal linkers was still possible by effective replacement of the monovalent adamantyl hexa(ethylene glycol).

6.1   Introduction

The attachment of proteins to surfaces is a key step in many biotechnological processes and applications.[1-3] For many of these purposes, one needs control over adsorption strength and reversibility, protein orientation, and retention of biological function. Such requirements can only be met when the binding of the protein to the surface is specific. Moreover, these need to be addressed anew every time another protein is being immobilized. In Chapter 4 the use of β-cyclodextrin (βCD) molecular printboards as a general platform for protein immobilization by small multivalent, orthogonal linker molecules was introduced.[4] In that chapter it was shown that a hard-to-solve interface problem can be converted to a much more easily addressable organic synthetic task. In principle, this methodology allows: (i) control over the binding strength by varying the valency of the linker at the printboard, (ii) control over protein orientation by the bioengineering of a specific binding site for the linker at a predetermined location in the protein, (iii) creation of a solution-like environment by increase of the linker length, and (iv) reversibility by rinsing with solutions of mono- or multivalent competitors. One major issue that was not yet solved in this methodology was the omnipresent problem of nonspecific protein adsorption.

Different options exist to prevent the nonspecific adsorption of proteins to surfaces, such as adding surfactants or bovine serum albumin (BSA) to protein solutions.[5,6] Another well known method is the use of self-assembled monolayers (SAMs) that are "protein-resistant" such as oligo(ethylene glycol) (OEG) SAMs.[7-9] Surfactants inhibit protein-protein interactions and thus nonspecific adsorption of these proteins to surfaces. BSA blocks the surface, so that nonspecific interactions of other proteins at the SAM do not occur. The prevention of nonspecific interactions by using SAMs with OEG chains is attributed to loose packing and the well-hydrated nature of these SAMs.[8] SAMs consisting of hexa(ethylene glycol) appear to be the most protein-resistant, and these monolayers have been widely applied.[7,10,11]

When attaching SAv to the molecular printboard, the addition of 1 mM βCD to the PBS buffer led to the inhibition of nonspecific interactions (Chapter 4).[4] For other proteins, however, this appeared to be insufficient. Non-ionic detergents such as Tween 20 were not useful either, since they also interact with the βCD cavities, and do not prevent nonspecific adsorption sufficiently. Passivating the surface with BSA

was possible, but this does not allow surface regeneration nor does it leave room for experiments in which binding constants of proteins to the surface, attached via specifically interacting sites and/or linkers, are determined.

In this chapter the use of hexa(ethylene glycol) mono(adamantyl ether) is introduced, which forms a dynamic, supramolecularly controlled oligo(ethylene glycol) (OEG) layer at the molecular printboards. This is shown to prevent nonspecific protein adsorption. At the same time it allows replacement by multivalent linker molecules, because multivalent interactions are typically orders of magnitude stronger than monovalent ones.[12] Here it will be shown that the methodology not only applies to the typical test protein streptavidin (SAv), but also to the histidine-(His-)tagged maltose binding protein (His_6-MBP), which functions here as a representative of the class of bioengineered His-tagged proteins.[13,14]

6.2   Results and discussion

6.2.1   System

The compounds used in this study are depicted in Chart 6.1. In order to solve the issue of nonspecific binding, the use of the monovalent supramolecular blocking agent **1** was envisaged, which was designed to have a single adamantyl (Ad) group for a predictable, specific and reversible interaction at the molecular printboard and a hexa(ethylene glycol) chain for preventing nonspecific protein adsorption (Scheme 6.1). The molecular printboard has been described in Chapter 2, the attachment of SAv via the divalent linker **2** to these molecular printboards has been described in Chapter 4. *N*-Nitrilo-triacetic acid-(NTA)-Ad linker **3** was developed for the attachment of His-tagged proteins to the molecular printboard through its Ni^{2+} complex.

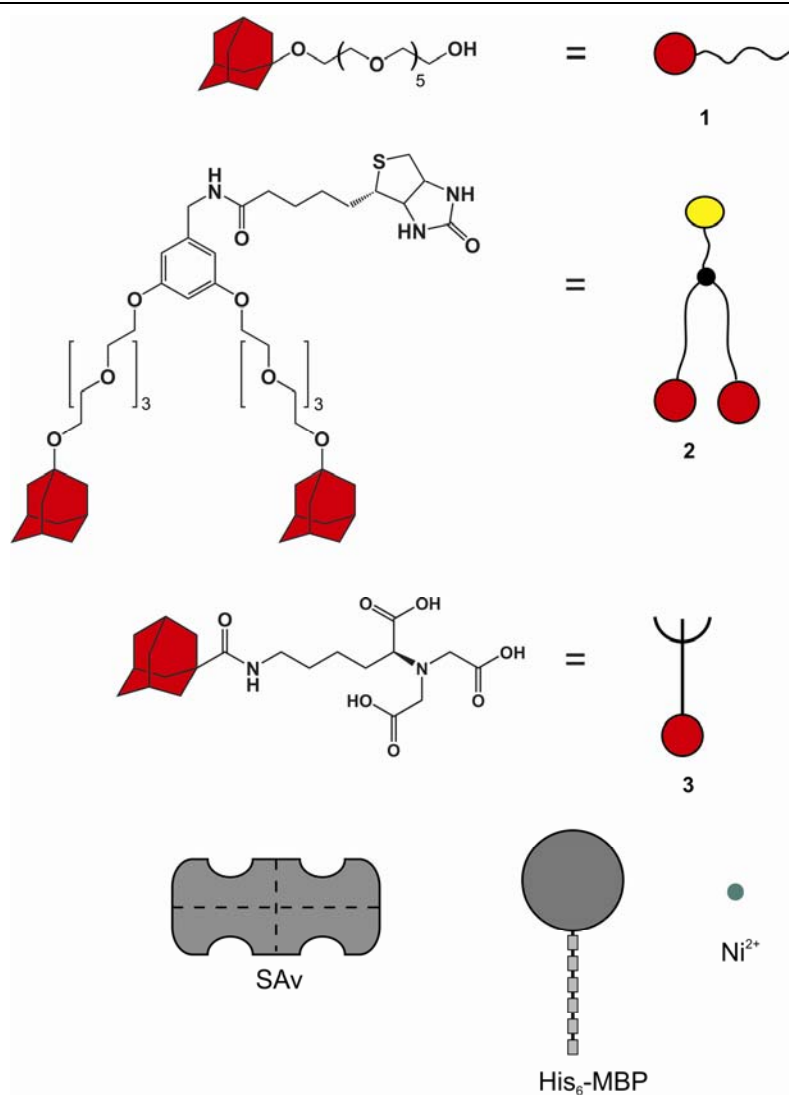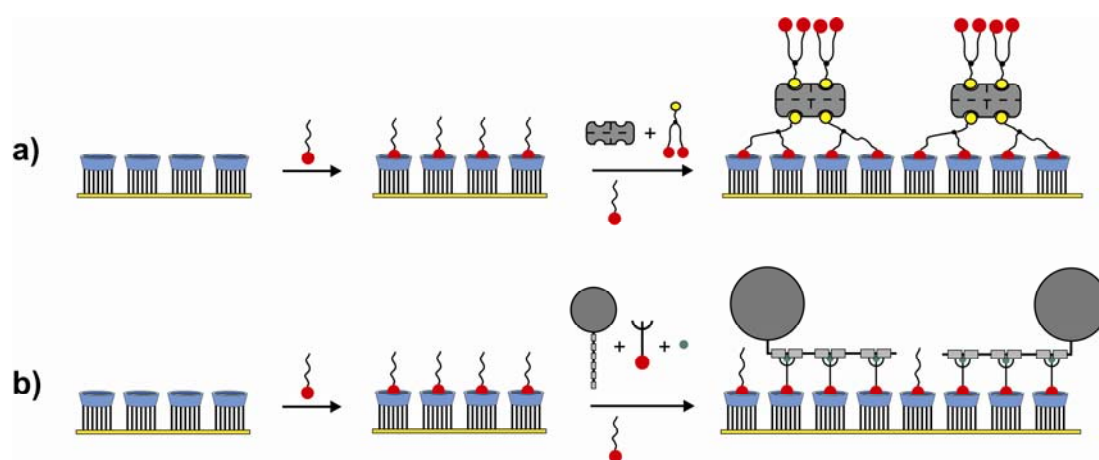***Chart 6.1*** *Compounds used in this study: hexa(ethylene glycol) mono(adamantyl ether) (**1**), divalent adamantyl-biotin linker (**2**), mono(adamantyl) N-Nitrilo-triacetic acid-(NTA-Ad) linker (**3**), the proteins SAv and His$_6$-MBP, and Ni^{2+}.*

Scheme 6.1 *Adsorption schemes for the assembly of SAv(**2**)$_4$ (a) and MBP(Ni•**3**)$_3$ at the molecular printboard in the presence of **1** (b).*

6.2.2 Binding studies

Isothermal titration calorimetry (ITC) experiments were performed to investigate the possible aggregation of **1**, and to determine the binding constant of **1** and **3** to βCD in solution. When 5 mM of **1** was titrated to PBS buffer (Figure 6.1a), only very small constant heat effects were observed which are attributed to dilution. Thus aggregation of **1** is not observed and this indicates that **1** can be used at least up to 1 mM in order to suppress nonspecific protein adsorption at molecular printboards. An ITC titration of 10 mM βCD to 1 mM **1** gave a titration curve typical of a 1:1 binding event (Figure 6.1b). Fitting to a 1:1 binding model yielded $K_a = (6.6 \pm 0.3) \times 10^4$ M^{-1}, and $\varDelta H° = $ -5.2 $\pm$ 0.4 kcal mol^{-1}. An ITC titration of 10 mM βCD to 1 mM **3** (Figure 6.1c) similarly led to $K_a = (5.5 \pm 1.3) \times 10^4$ M^{-1}, and $\varDelta H° = $ -6.5 $\pm$ 0.4 kcal mol^{-1}. In both cases these values are typical for βCD-adamantyl interactions.[15] As a test protein, 0.1 mM BSA was used to investigate a possible interaction with **1** by ITC. Notably, an interaction of **1** with BSA is absent (Figure 6.1d).
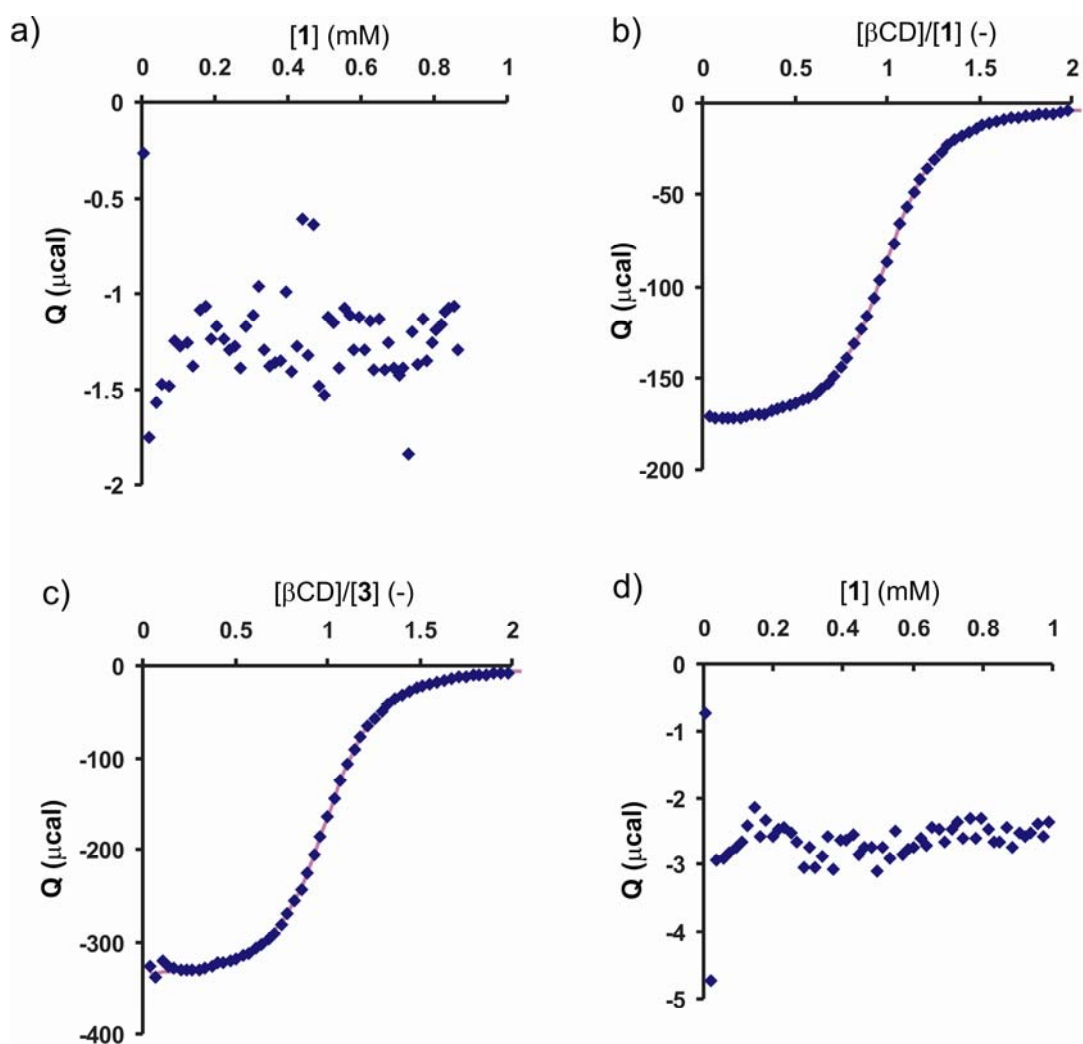
Figure 6.1 *Heat evolved per injection (markers) and fits to a 1:1 model (lines) for the isothermal calorimetric titrations of 5 mM **1** in PBS to PBS (a), of 10 mM βCD in PBS to **1** in PBS (b), 10 mM βCD in PBS to **3** in PBS (c), and 5 mM **1** in PBS to 0.1 mM BSA in PBS (d).*

Surface plasmon resonance (SPR) titrations were performed by adding solutions with different concentrations of **1** and **3** to the molecular printboard, while in between the additions, rinsing steps with 10 mM βCD in PBS were applied. The SPR data (Figure 6.2) were fitted to a 1:1 Langmuir type model, giving $K_a = (2.6 \pm 0.9) \times 10^4$ M^{-1} for **1**, and $K_a = (1.2 \pm 0.2) \times 10^4$ M^{-1} for **3**, which are comparable to the values found for binding βCD in solution.
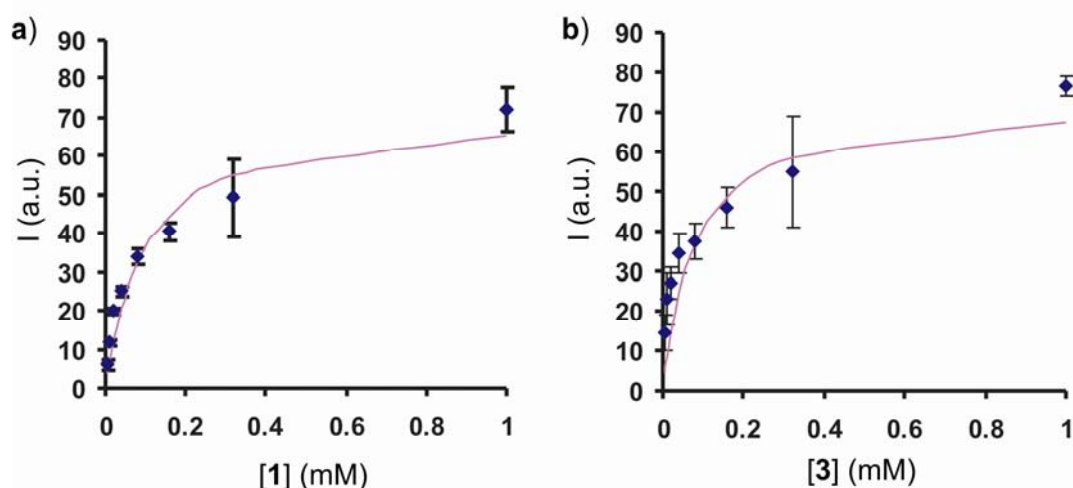
Figure 6.2 *SPR titration (markers) and corresponding fits (solid lines) to a 1:1 Langmuir-type binding model for the binding of **1** in PBS to the molecular printboard (a) and of **3** in PBS to the molecular printboard (b). Error bars indicate the 50% confidence interval.*

Figure 6.3 shows the SPR sensograms for the binding of SAv, His$_6$-MBP, and BSA in the absence and presence of **1**. Whereas SAv, MBP, and BSA showed significant nonspecific adsorption in the absence of **1** (black curves), already low concentrations (0.1 mM) of **1** appear to be sufficient for the suppression of nonspecific interactions. It is to be noted that at 0.1 mM approximately > 80 % of all βCD sites are already occupied by **1** (see Scheme 6.1), albeit in a dynamic fashion. Experiments in which 0.1 mM of hexa(ethylene glycol) (HEG) was used instead of **1**, showed that the amount of protein adsorption to the molecular printboard is comparable to the amount in the absence of HEG. This indicates that the main interaction through which nonspecific adsorption is inhibited, is via the binding of **1** to the surface, thereby temporarily blocking the βCD cavities, and exposing the hexa(ethylene glycol) tails to the solution.
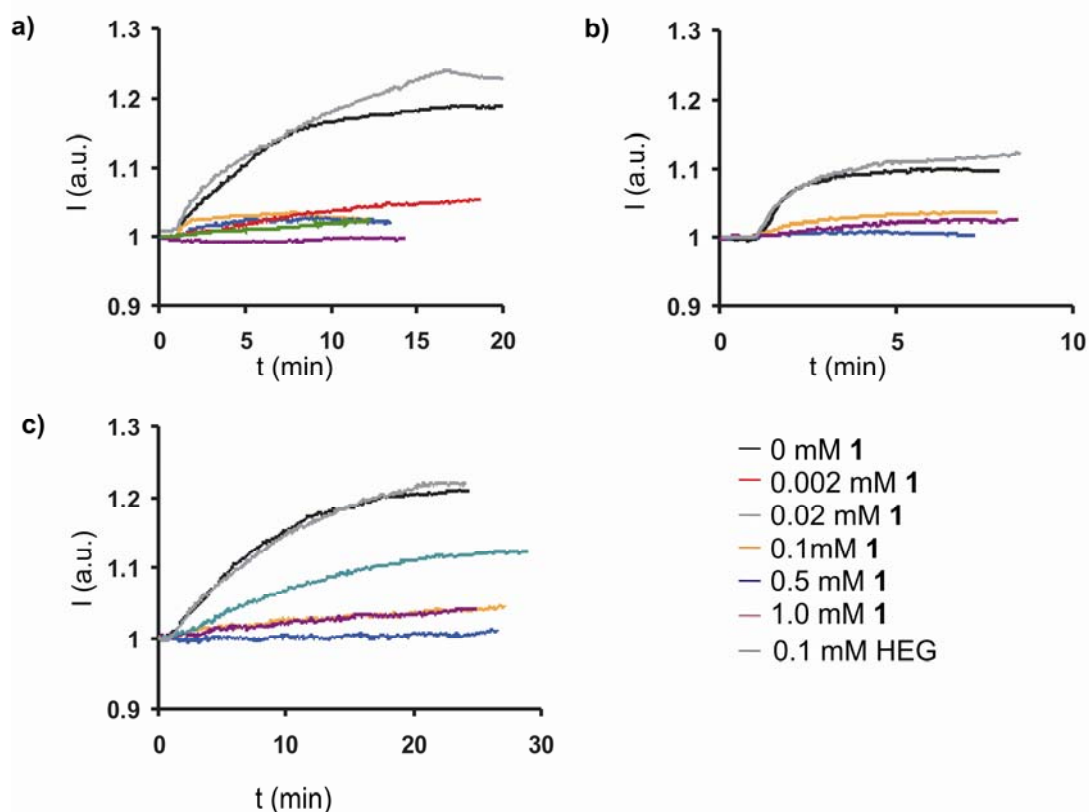
Figure 6.3 *SPR sensograms of the adsorption of 0.1 μM of SAv (a), 0.1 μM of His$_6$-MBP (b), and 0.1 μM of BSA (c) at the molecular printboard in PBS in the absence (-) and presence of 0.002 mM (-), 0.02 mM (-), 0.1 mM (-), 0.5 mM (-), and 1 mM (-) of 1 or 0.1 mM hexa(ethylene glycol) (HEG) (-).*

Earlier work by Whitesides showed that mixed SAMs with OEG thiols resist the nonspecific adsorption of proteins when the fraction of the OEG thiol is at least 0.4-0.6, corresponding to an absolute coverage of about 4×10^{-10} mol/cm^2.[8] When this value is compared to the surface coverages of **1** achieved here, it appears that much lower densities of OEG moieties can be effective in our case (max. about 5×10^{-11} mol/cm^2 for full βCD SAM coverage). This may be in part attributed to the dynamic nature of the supramolecular approach presented here. Moreover, although no surfactant behavior of **1** has been detected (see above), interactions of **1** with proteins in solution cannot be ruled out completely. Further protein binding experiments were performed at 0.1 mM of **1**.

To investigate whether the application of **1** still allows the specific attachment of proteins via orthogonal linkers, the binding of SAv at the molecular printboard through the orthogonal multivalent biotin-functionalized linker **2** (Scheme 6.1a and

Figure 6.4a) was studied by SPR as well as the specific adsorption of His$_6$-MBP through the Ni^{2+}-complexed NTA-Ad linker **3** (Scheme 6.1b, Figure 6.4b). SAv is a homo-tetrameric protein with four identical biotin-binding sites, and thus can bind four equivalents of **2**. Because of the geometry of SAv and the length of the used divalent adamantyl-linker, only two of the linkers, and thus four adamantyl moieties bind four neighboring βCD cavities of the molecular printboard.[4] Because of the multivalency effect, the binding of the SAv(**2**)$_4$ complex to the molecular printboard is expected to be much stronger than the binding of **1**, also when applying **1** in excess. Figure 6.4a shows the adsorption of 0.1 μM of SAv(**2**)$_4$ in the presence of 0.1 mM of **1**. After attempted desorption with 10 mM βCD, most of the SAv(**2**)$_4$ complex remained, proving the strong interaction of the complex to the molecular printboard. The beginning of the SPR curve indicates a βCD SAM already covered with **1**, which means that the absolute intensity change of the SPR signal is caused by the exchange of **1** for the SAv(**2**)$_4$ complex. Therefore, the intensity change is lower compared to the attachment of SAv(**2**)$_4$ to an empty βCD SAM in the presence of 1 mM βCD (see Chapter 4).[4]
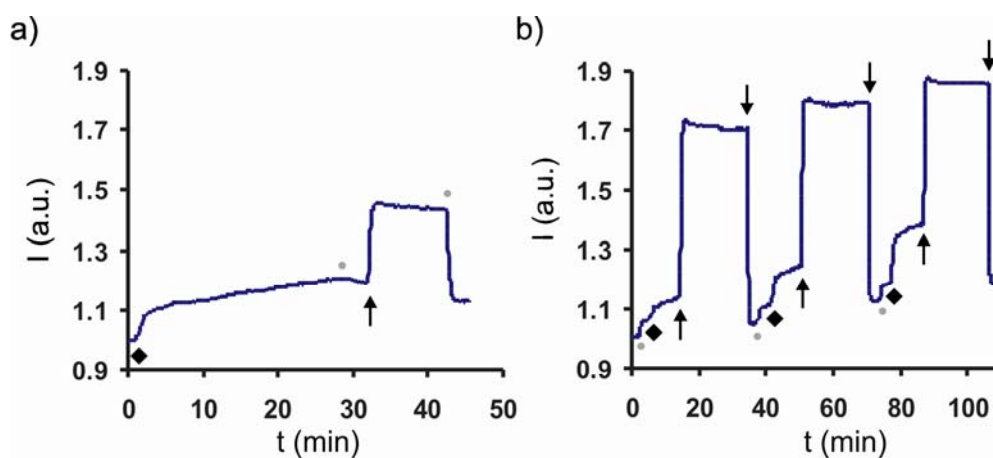
Figure 6.4 *SPR sensograms of the adsorption of 0.1 μM SAv and **2** (ratio 1:6) (a) and of different concentrations of His$_6$-MBP, Ni^{2+}•**3** (ratio 1:5:5) (b) at βCD SAMs in the presence of 0.1 mM **1** in PBS. In the latter case, the His$_6$-MBP concentrations were 2.0 μM, 5.0 μM, and 10 μM, respectively. Symbols indicate switching of solutions in the SPR flow cell to SAv + **2** (ratio 1:6) + 0.1 mM **1** in PBS, or MBP + Ni^{2+} + **3** (ratio 1:5:5) + 0.1 mM **1** in PBS (♦), 0.1 mM **1** in PBS (●), 10 mM βCD + 0.1 mM **1** (+ 10 mM EDTA in the case of MBP) in PBS (↑), or PBS (↓).*

In the case of His$_6$-MBP, the protein was premixed with Ni^{2+} and **3** (ratio 1:5:5) and 0.1 mM **1** in solution, and this solution was flowed over βCD SAMs already covered with **1**. Figure 6.4b shows the adsorption of His$_6$-MBP. Rinsing with 10 mM βCD and 10 mM EDTA led to complete recovery of the baseline signal The slight increase in the baseline is attributed to drift. This procedure was repeated at different concentrations of His$_6$-MBP and **3** (see also Chapter 7). It shows the specific binding of His$_6$-MBP in the presence of the monovalent blocking agent **1**. Moreover, it shows that it is possible to vary the surface coverage of His$_6$-MBP.

6.3   Conclusions

In this chapter the development of a new supramolecular blocking agent that inhibits nonspecific protein adsorption at βCD molecular printboards is described. It is shown that this compound has similar binding constants to βCD in solution and at the surface, and that a 0.1 mM concentration is already sufficient to inhibit nonspecific protein adsorption, which corresponds with a significantly lower coverage than obtained for standard protein repelling surfaces. Moreover, it is still possible to attach proteins to the surface using multivalent orthogonal linkers, which ensure specific binding by exchange of **1**. This was shown for two proteins which are bound via differently functionalized linkers to the molecular printboard, exemplifying the versatility of this method. In conclusion, the implementation of this supramolecular nonspecific protein inhibition scheme demonstrates the strong potential for the use of molecular printboards as a general platform for the immobilization of proteins. Future directions will be to develop models for describing the multivalent thermodynamics of such orthogonal systems, and to increase the complexity of the protein architectures to antibodies and cells.

6.4   Experimental section

General
All materials and reagents were used as received, unless stated otherwise. All moisture sensitive reactions were carried out under an argon atmosphere. ^{1}H-NMR spectra were recorded on Varian Unity 300 MHz and Varian Inova 400 MHz

spectrometers. Spectra are reported in ppm downfield from TMS as an internal standard. FAB-MS and MALDI-MS spectra were recorded with a Finnigan MAT 90 spectrometer using *m*-NBA as a matrix and a PerSpective Applied Biosystems Voyager-De-RP spectrometer, respectively. Analytical TLC was performed using Merck prepared plates (silica gel 60 F-254 on aluminum). Biotin-4-fluorescein was bought from Sigma and used as received. Streptavidin was bought from Aldrich and used as received. Maltose binding protein (MBP) with a C-terminal hexahistidine tag was expressed and purified as previously described.[14] For all experiments 10 mM phosphate buffer, pH 7.5 with 100 mM NaCl, phosphate buffered saline (PBS), was used.

Synthesis

1-Biotin-3-(3,5-di(tetra(ethylene glycol) adamantyl ether) benzylamide 2 was synthesized as described before.[4]

Hexa(ethylene glycol) mono(adamantyl ether) (**1**) was synthesized by the reaction of hexa(ethylene glycol) (12.5 ml, 49.9 mmol) with 1-bromoadamantane (1.1 g, 5.0 mmol) at 180 °C in the presence of Et$_3$N (2.0 ml, 15 mmol). After cooling to room temperature, dichloromethane (50 ml) was added. The solution was washed with 2 M hydrochloric acid (4 × 50 ml) and once with brine (50 ml). The organic layer was dried over MgSO$_4$ and the solvent was evaporated under reduced pressure to give **1** as a yellow-brown oil (1.9 g, 4.5 mmol; 90 %). ^{1}H NMR (300 MHz, CDCl$_3$, 20°C, TMS) δ: 3.70 (t, 2H, AdO*CH$_2$*CH$_2$), 3.66-3.62 (m, 16H, HEG CH$_2$), 3.61-3.54 (m, 6H, AdOCH$_2$*CH$_2$* + *CH$_2$*CH$_2$OH), 3.02 (s, 1 H, CH$_2$*OH*), 2.10 (m, 3H, CH$_2$*CH*CH$_2$Ad), 1.75-1.70 (m, 6H, CH*CH$_2$*CAd, 1.65-1.53 (m, 6H, CH*CH$_2$*CHAd); ^{13}C NMR (400 MHz, CDCl$_3$): δ 72.8, 72.5, 71.5, 70.8, 70.6, 70.4, 61.9, 59.5, 41.7, 36.7, 30.7. MS (FAB): *m/z* calcd for [M+H]$^+$ 417.3; found 417.1.

Mono(adamantyl) L-lysine-nitrilo-tri(acetic acid)-(O*t*Bu)$_3$ (**3**)-(O*t*Bu)$_3$ L-Lys-NTA(O*t*Bu)$_3$[16] (1.0 g, 2.3 mmol) was dissolved in dichloromethane (50 ml) and DIPEA (0.50 ml, 2.4 mmol) and adamantyl acid chloride (0.4 g, 2.2 mol) were added subsequently. The solution was stirred at room temperature for 2 h, washed with 1N NaOH (2 × 75 ml), 1 N HCl (2 × 75 ml), and brine (75 ml), dried over MgSO$_4$ and

evaporated to dryness. The residue was purified by column chromatography (SiO_2, cyclohexane/ethylacetate [3:1]) to give the desired product in 99% yield as a colorless oil (1.3 g, 2.2 mmol).

^{1}H NMR (300 MHz, $CDCl_3$, 20ºC, TMS) δ: 5.82 (t, 1H, NH), 3.50 (m, 4H, CH_2COO), 3.25-3.36 (m, 3H, NCH + CONH*CH₂*), 2.09 (m, 3H, AdCH), 1.87 (m, 6H, $AdCH_2$), 1.63-1.79 (m, 8H, $AdCH_2$ + *CH₂*CH), 1.40-1.58 (m, CH₂*CH₂CH₂*CH₂ + CH_3); ^{13}C NMR (400 MHz, $CDCl_3$): δ 178.0, 172.3, 170.6, 81.1, 80.7, 65.1, 53.8, 40.5, 39.2, 39.0, 36.6, 30.2, 29.0, 28.2, 28.1, 26.9, 23.2; MS (MALDI-TOF): *m/z* calcd for [M] 593.8, found [M+H]+ 594.0.

Mono(adamantyl) L-lysine-nitrilotri(acetic acid) (**3**) was synthesized as follows. (**2**)-(O*t*Bu)₃ (0.70 g, 1.1 mmol) and triethylsilane (1.4 ml, 8.4 mmol) were dissolved in trifluoroacetic acid (20 ml). The solution was stirred at room temperature for 4 h and diethylether (20 ml) was added to give a white precipitate. The precipitate was isolated by filtration over a glass filter (pore 4) and rinsed thoroughly with diethylether to give the desired product in 71 % yield as a white powder.

^{1}H NMR (300 MHz, DMSO, 20 ºC, TMS) δ: δ 11.70 (bs, 3H, COOH), 7.29 (t, 3H, 1H, NHCO), 3.51 (m, 4H, CH2COO), 3.36 (t, 1H, NCH), 3.01 (m, 2H, NHC<u>H</u>₂), 1.95 (m, 3H, AdCH), 1.55-1.77 (m, 14H, $AdCH_2$ + $AdCH_2$ + *CH₂*CH), 1.25-1.42 (m, 4H, CH₂*CH₂CH₂*CH₂); ^{13}C NMR (400 MHz, DMSO): δ 175.0, 174.8, 66.4, 55.7, 41.3, 39.8, 39.6, 37.2, 30.6, 29.1, 24.4; MS (MALDITOF): *m/z* calcd for [M] 424.6, found [M+H]+ 425.8.

Monolayer preparation

Gold substrates for SPR (BK7 glass/2-4 nm Ti/50 nm Au) were obtained from Ssens B.V., Hengelo, the Netherlands. Gold substrates were cleaned by dipping them into piranha (1:3 mixture of concentrated H_2SO_4 and 30% H_2O_2) for 5 s. (*Warning:* piranha should be handled with caution; it can detonate unexpectedly.) After thorough rinsing with Millipore water, they were placed for 10 min in absolute EtOH. Subsequently SAMs were prepared as described before.[17] All solvents used in the monolayer preparation were of p.a. grade.

Calorimetric titrations

Calorimetric titrations were performed at 20 °C using a Microcal VP-ITC titration microcalorimeter. Aggregation studies were performed by adding 5 µl aliquots of a 5 mM solution of **1** in PBS to PBS or 0.1 mM BSA. Titrations were performed by adding 5 µl aliquots of a 10 mM βCD solution to a 1 mM solution of **1** or **3**. The titrations were analyzed with a least-squares curve fitting procedure. Each ITC experiment was repeated at least two times.

SPR

SPR measurements were performed on a Resonant Probes GmbH SPR instrument equipped with a flow pump as described before.[4] A continuous flow of 0.5 ml/min was used.

6.5 References

1. G. MacBeath, S. L. Schreiber, *Science* **2000**, *289*, 1760-1763.

2. H. Zhu, J. F. Klemic, S. Chang, P. Bertone, A. Casamayor, K. G. Klemic, D. Smith, M. Gerstein, M. A. Reed, M. Snyder, *Nat. Genet.* **2000**, *26*, 283-289.

3. E. Katz, I. Willner, *Angew. Chem. Int. Ed.* **2004**, *43*, 6042-6108.

4. M. J. W. Ludden, M. Péter, D. N. Reinhoudt, J. Huskens, *Small* **2006**, *2*, 1192-1202.

5. C. P. Quinn, *et al.*, *Emerg. Infect. Dis.* **2002**, *8*, 1103-1110.

6. M. Kyo, T. Yamamoto, H. Motohashi, T. Kamiya, T. Kuroita, T. Tanaka, J. D. Engel, B. Kawakami, M. Yamamoto, *Genes to Cells* **2004**, *9*, 153-164.

7. S. Herrwerth, W. Eck, S. Reinhardt, M. Grunze, *J. Am. Chem. Soc.* **2003**, *125*, 9359-9366.

8. K. L. Prime, G. M. Whitesides, *J. Am. Chem. Soc.* **1993**, *115*, 10714-10721.

9. K. L. Prime, G. M. Whitesides, *Science* **1997**, *252*, 1164 -1167.

10. W. Senaratne, L. Andruzzi, C. K. Ober, *Biomacromolecules* **2005**, *6*, 2427-2448.

11. E. Ostuni, L. Yan, G. M. Whitesides, *Colloids Surf. B* **1999**, *15*, 3-30.

12. J. Huskens, A. Mulder, T. Auletta, C. A. Nijhuis, M. J. W. Ludden, D. N. Reinhoudt, *J. Am. Chem. Soc.* **2004**, *126*, 6784-6797.

13. S. Lata, J. Piehler, *Anal. Chem.* **2005**, *77*, 1096-1105.

14. A. Tinazli, R. Valiokas, S. Picuric, S. Lata, J. Piehler, B. Liedberg, R. Tampé, *Chem. Eur. J.* **2005**, *11*, 5249-5259.

15. M. V. Rekharsky, Y. Inoue, *Chem. Rev.* **1998**, *98*, 1875-1917.

16. I. T. Dorn, K. R. Neumaier, R. Tampé, *J. Am. Chem. Soc.* **1998**, *120*, 2753-2763.

17. M. W. J. Beulen, J. Bügler, B. Lammerink, F. A. J. Geurts, E. M. E. F. Biemond, K. G. C. van Leerdam, F. C. J. M. van Veggel, J. F. J. Engbersen, D. N. Reinhoudt, *Langmuir* **1998**, *14*, 6424-6429.

7

Attachment of histidine-tagged proteins to molecular printboards*

In this chapter, the multivalent binding of histidine$_6$- (His$_6$-) tagged proteins to the molecular printboard by using a hetero-divalent orthogonal adamantyl N-nitrilotriacetic acid (NTA) linker (2) is discussed. Nonspecific interactions were suppressed using the monovalent adamantyl-hexa(ethylene glycol) derivative 1. With the mono-His6-tagged maltose binding protein (His6-MBP), thermodynamic modeling based on SPR titration data showed that the MBP molecules in solution were linked on average to one linker. On the surface, however, the majority of His$_6$-MBP became linked to surface βCDs via three linker molecules. This difference is explained by the high effective βCD concentration at the surface, and is a new example of supramolecular interfacial expression. Patterning of (His$_6$)$_4$-DsRed-FT, a tetrameric, auto-fluorescent protein, was carried out in the presence of Ni•2. Fluorescence measurements showed that the (His$_6$)$_4$-DsRed-FT is bound strongly via Ni•2 to the molecular printboard. In a similar adsorption scheme, surface plasmon resonance (SPR) proved that the α-proteasome could be attached to the molecular printboard in a specific manner.

7.1   Introduction

Proteins can be immobilized at surfaces by covalent immobilization or physisorption,[1,2] but these methods leave little room for control over the adsorption process. Control over the immobilization of proteins can be reached, however, by supramolecular chemistry (see Chapters 4, 5, and 6). Ultimate control over protein immobilization can be reached through the insertion, by bioengineering, of a histidine$_6$- (His$_6$-) tag to a protein. These His tags can bind to Ni-*N*-nitrilotriacetic acid (NiNTA) self-assembled monolayers (SAMs). In this manner, there is control over many factors, such as thermodynamics, orientation, and function.[3-5]

Originally, the NiNTA system has been developed for the purification of proteins *via* NiNTA columns as discussed in Chapter 2. Nowadays, the technology is more and more applied for the immobilization of His-tagged proteins to surfaces.[6-16] Multivalency, which is the simultaneous interaction between multiple functionalities on one entity to multiple complementary functionalities on another entity,[17] is an important concept when proteins are immobilized to surfaces by this method.[5,6,18-20]

When His-tagged proteins are immobilized to NiNTA SAMs it is possible to reverse the immobilization.[4,21,22] Also control over the orientation of His-tagged proteins is possible.[19,21,23-26] In case of the 20S proteasome for instance, this was achieved using NiNTA SAMs on gold.[27] The 20S proteasome is a large protein complex, and is responsible for the degradation of misfolded proteins. It can be His-tagged in two manners, end-on (α) and side-on (β). When immobilizing the 20S proteasome on the NiNTA SAMs, there was a clear distinction between the α and β immobilization. With the α-immobilization of the 20S proteasome on the surface, it was possible to elucidate the substrate association step of the mechanism of the 20S proteasome.[19]

The enhancement of a multivalent species at the βCD molecular printboard was previously proven by surface plasmon resonance (SPR) titration experiments in which a heterotopic,[28,29] orthogonal motif was used.[30] In that study an adamantyl-functionalized ethylenediamine ligand complexed to M(II) (M being Cu or Ni) was assembled at the surface.[30] In solution, the metal-ligand complex was monovalent. On the surface, however, a multivalent complex was formed. The formation of multivalent complexes at the βCD molecular printboard is governed by the effective concentration (C_{eff}), which results in an increased stability of multivalent complexes at

the molecular printboard compared to monovalent complexes. Enhancement factors of ~100 for the multivalent complex formation at the surface compared to solution were observed.[31-32]

The versatility of the molecular printboard for the attachment of proteins and for the inhibition of nonspecific protein adsorption to those surfaces became already apparent in the previous Chapters (4 and 5). The ability of AdPEG (**1**) to inhibit nonspecific interactions of proteins to the molecular printboard was shown in Chapter 6.

In this Chapter, the advantages of protein attachment to the molecular printboard, e.g. controllable binding constants (K_a), and the suppression of nonspecific interactions, are combined with His-tagged proteins. The His$_6$-tagged proteins are immobilized on molecular printboards by the adamantyl-NTA linker (**2**) presented in Chapter 6.

In this chapter, the advantages of protein attachment to the molecular printboard, e.g. controllable binding constants (K_a), and the suppression of nonspecific interactions, will be combined with His-tagged proteins. The His$_6$-tagged proteins are immobilized on the molecular printboard by the adamantyl-NTA linker (**2**) presented in Chapter 6. Titration experiments with the maltose binding protein (MBP) containing a single His$_6$ tag are described, as well as the modeling of these experiments in which the valency of the complex formation in solution and at the surface is compared. The possibility to pattern multiple His-tagged proteins will be explored with (His$_6$)$_4$-DsRed-FT, a variant of the tetrameric reef coral visible fluorescent protein DsRed. For the α-His-tagged 20S proteasome, the possibility of specific immobilization is discussed.

7.2 Results and discussion

7.2.1 System

The molecular printboard has been introduced in Chapter 2. A linker is employed with an adamantyl moiety and an NTA group (Chart 7.1) for the specific immobilization of His-tagged proteins to the molecular printboard. The adamantyl moiety ensures interaction with the molecular printboard, while the NTA moiety, when complexed to Ni(II), can interact with the His$_6$-tagged proteins.
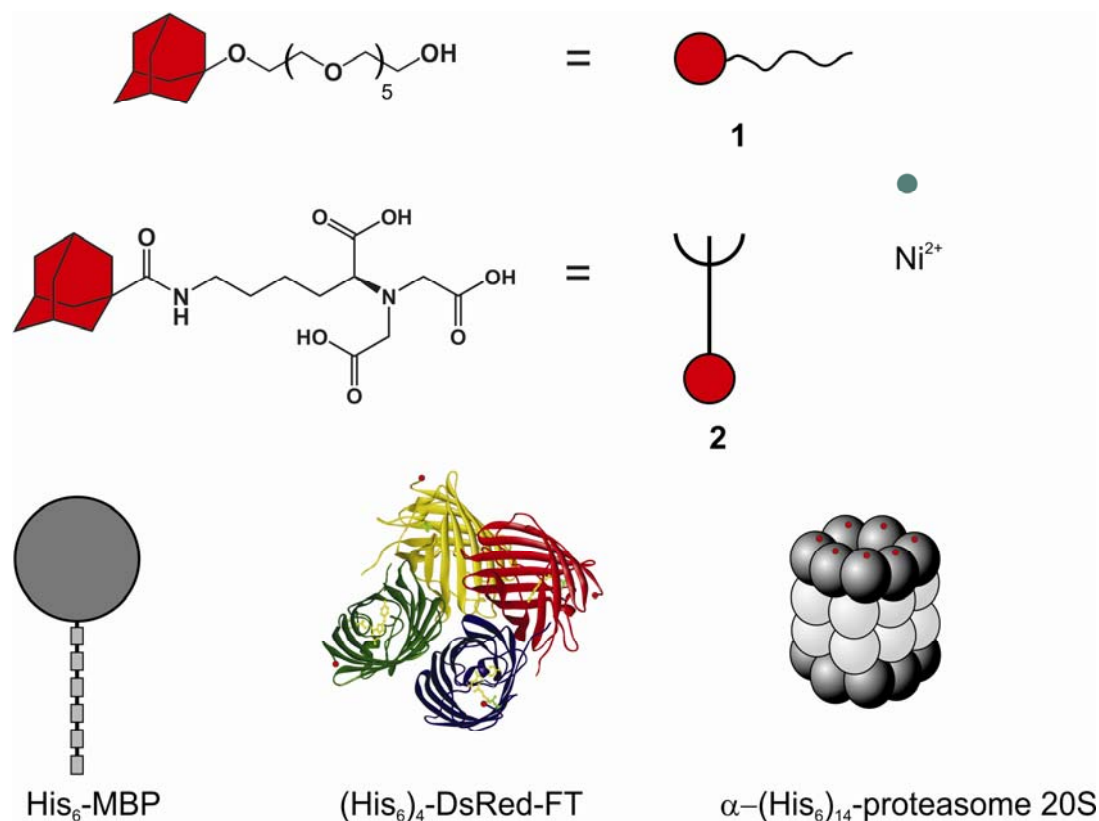
Chart 7.1 *Compounds used in this study. AdPEG (1), AdNTA (2), Ni(II), His$_6$-MBP, (His$_6$)$_4$-DsRed-FT, α-(His$_6$)$_{14}$-20S proteasome.*

Three different proteins with varying size and number of His$_6$ tags have been examined in this study: the maltose binding protein (MBP), the fluorescent timer mutant of DsRed (DsRed-FT), and the 20S proteasome (Chart 7.1). MBP is a protein with a molecular weight of 41 kDa (3 × 4 × 6.5 nm)[33] which is part of the maltose/maltodextrin system of *Escherichia coli* which is responsible for the uptake and efficient metabolism of maltodextrins.[34] The version employed here bears one His$_6$ tag. The His$_6$ tag spans ~2 nm and the βCD cavities are spaced about 2.1 nm from each other, which means that the Ni(II)•**2** complexes resided at the His$_6$ tag are spaced far enough from each other to form multiple host-guest complexes at the βCD surface. Considering the size of the protein, and the surface area of the surface-confined βCD cavities, it should be noted that MBP is somewhat larger than three βCD cavities, which corresponds to the maximum number of linkers **2** through which His$_6$-MBP can be bound. Therefore, a closed packed layer of protein is expected. The experiments presented in this chapter, were performed at a pH of 7.5. At this pH, the

Ni(II)•**2** complex is formed for > 90% when [Ni]$_{tot}$ = [**2**]$_{tot}$ > 50 nM, which is true for every data point shown. In the modeling (shown below) it is therefore assumed that Ni(II)•**2** is always formed completely.[35,36]

The fluorescent timer mutant of DsRed (DsRed-FT) is an fluorescent, tetrameric protein,[37-40] and in each monomer a His$_6$ tag was inserted via bio-engineering. When this protein is attached to a surface, at least two His$_6$ tags will be facing the surface, and possibly three or four, due to deformation of the protein's tertiary or quaternary structure. The fluorescent properties of this protein are sensitive to changes in the tertiary structure, and the protein may lose its fluorescent properties, upon large conformational changes.

The 20S proteasome is a large protein complex (700 kDa) which consists of two different subunits with high homology. The size of the protein is about 15 nm in height and 10 nm in diameter, which means that, if the 20S proteasome is immobilized end-on to the molecular printboard, it spans about 20 βCD cavities. The two outer rings consist of seven α-subunits, while the two inner rings consist of seven β-subunits. In the proteasome employed here the His$_6$ tags are inserted at the α-subunits. Binding to the surface is therefore expected via 7 His$_6$ tags, and thus 21 NTA linkers bound to 21 βCD cavities, which fits well with the cross-section of the proteasome.[19]

7.2.2   The binding of His$_6$-MBP to molecular printboards

The immobilization of His$_6$-MBP to the molecular printboard via Ni(II)•**2** was first studied with SPR titration experiments using His$_6$-MBP. The assembly is schematically depicted in Scheme 7.1, Figure 7.1 shows the corresponding surface plasmon resonance (SPR) titration curve.
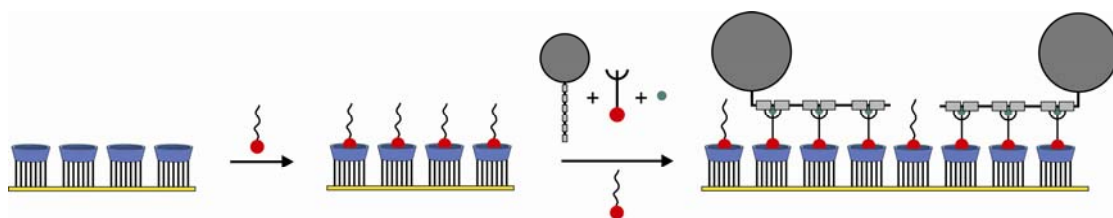
Scheme 7.1 *Binding of His$_6$-MBP via Ni(II)•2 to the molecular printboard, in competition with the monovalent blocking agent 1.*
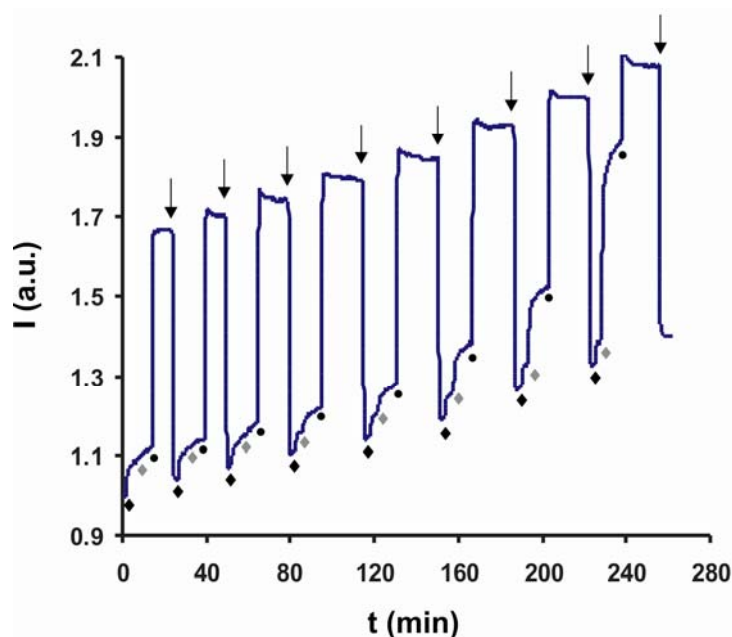
Figure 7.1 *SPR sensogram of a titration experiment of His₆-MBP to the molecular printboard (Scheme 7.1). Symbols indicating switching to: (♦) 0.1 mM **1** in PBS, (♦) increasing concentrations of His₆-MBP + Ni(II)•2 (ratio 1:5) + 0.1 mM **1** in PBS, (●) 10 mM βCD + 10 mM EDTA in PBS, (↓) PBS.*

The SPR titration experiment was performed by monitoring additions of increasing concentrations of His₆-MBP and Ni(II)•2 at a background of 0.1 mM **1** in PBS, which is suitable to suppress nonspecific interactions (see Chapter 6). Throughout this study the Histag:Ni(II)•2 ratio was kept at 1:5, *i.e.* a two-equivalent excess relative to the 3 equivalents that are maximally expected to interact with a His tag. After an addition an increase of the SPR signal was observed indicative of adsorption (Figure 7.1). The adsorption was followed for 10 min, after which the surface was regenerated with 10 mM βCD and 10 mM EDTA, which led to restoration of the baseline indicating the desorption of the His₆-MBP complex of the surface.

Figure 7.1 shows a steady increase in the baseline, which is attributed to drift, because every addition of **1** before the addition of His₆-MBP and Ni(II)•2 resulted in a similar increase of the SPR signal. Furthermore, each flow, with an increasing concentration of His₆-MBP, resulted in a higher increase of the SPR signal. The data points generated with the SPR titration experiment shown in Figure 7.1 were fitted using a model accounting for the interactions of **1** and Ni(II)•2 with βCD in solution (βCD₁) and at the βCD SAM (βCDₛ), as well as the interaction of Ni(II)•2 with His₆-MBP. A

complete description of the model employed can be found in the Appendix to this chapter. From isothermal titration calorimetry (ITC) measurements, the binding constants for **2** and **1** with βCD in solution (βCD$_l$) were determined to be K_a = (6.6 ± 0.3) × 10^4 M^{-1}, and K_a = (5.5 ± 1.3) × 10^4 M^{-1}, respectively (see Chapter 6). These are typical binding constants for monovalent βCD-adamantyl interactions.[41] The binding constants of complexation of **1** and Ni(II)•**2** with βCD$_s$ were determined by SPR titrations. Fitting of the data led to binding constants (K_a) of (2.6 ± 0.9) × 10^4 M^{-1} and (1.2 ± 0.2) × 10^4 M^{-1} for **1**•βCD$_s$ and **2**•βCD$_s$, respectively. These binding constants are comparable to the ones found in solution, and are also typical for monovalent βCD-adamantyl interactions. In the model, K_a values of Ad binding to βCD$_s$ and βCD$_l$ were used as determined in the different SPR and ITC experiments.

The main fit parameter in the modeling was the value of the first interaction of Ni(II)•**2** to the His$_6$ tag (K_1). The second (K_2) and third (K_3) binding constants of Ni(II)•**2** to the His$_6$ tag are linked to K_1 by statistical factors i.e. (6/25) and (7/225), respectively (see Supporting Information). Fitting of the curve in Figure 7.2 resulted in K_1 = 7.8 × 10^4 M^{-1}, and thus to K_2 = 1.9 × 10^4 M^{-1} and K_3 = 2.4 × 10^3 M^{-1}. These are close to the binding constants found in literature (K_i = 7.8 × 10^4 M^{-1}).[20]
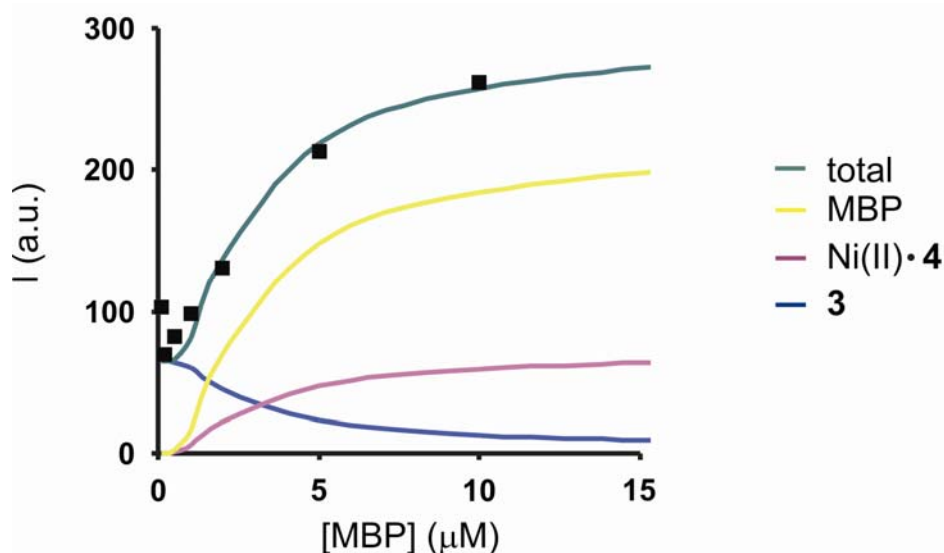

Figure 7.2 *Equilibrium values of the SPR intensities (markers) of the titration shown in Figure 7.1 and corresponding fit to the model and contributions by different components to the signal (solid lines).*

The modeled data presented in Figure 7.2 show that the concentrations of His$_6$-MBP and **2** at the surface increase and that the concentration of **1** decreases at the surface, which is in agreement with the expected competition. This enhancement is efficient because the complex of His$_6$-MBP bound to Ni(II)•**2** at βCD SAMs is multivalent, governed by C_{eff}, which is stronger than the monovalent binding of **1**. The total SPR signal is the sum of the intensity change of the three different components (His$_6$-MBP, **1**, Ni(II)•**2**). With the equilibria shown in Scheme 7.2 (see Appendix) and the binding constants obtained for **1** and **2** in solution and at the surface, it is possible to determine the speciation in both phases. Figure 7.3 shows the speciations of all MBP species bound to x (x = 0-3) Ni(II)•**2** complexes in solution and at the surface. Thus the valency of the MBP complexes can be determined.
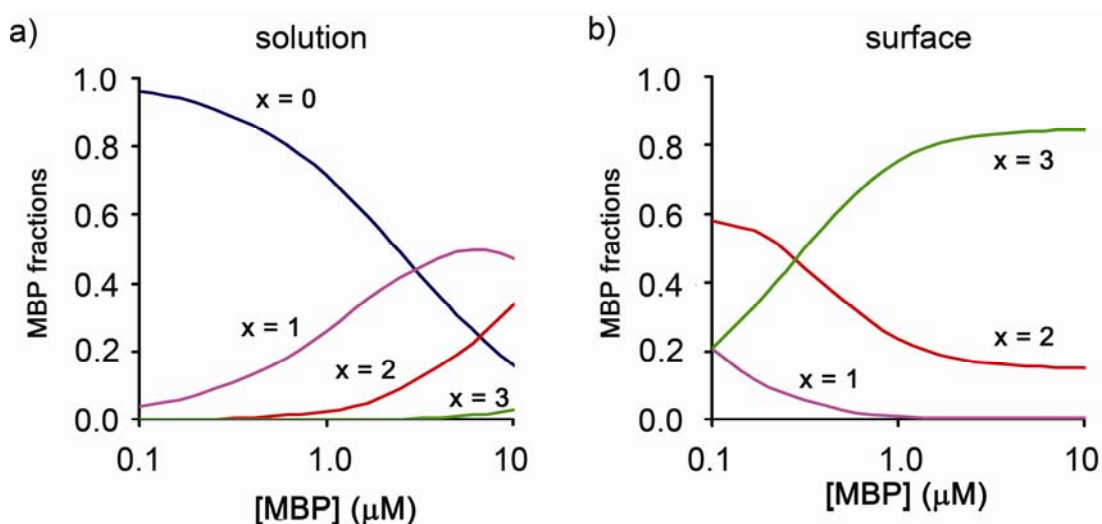
Figure 7.3 *Thermodynamic data modeling showing fractions of His$_6$-MBP•(Ni•2) (i.e. complexed to different numbers, x, of (Ni(II)•2) as a function of [His$_6$-MBP] in solution (a) and at the surface (b).*

From the modeled data presented in Figure 7.3 several observations can be made. At sub-μM concentrations, there is almost no interaction between His$_6$-MBP and Ni(II)•**2** in solution. At higher concentrations the majority of His$_6$-MBP is complexed in a monovalent fashion to Ni(II)•**2**. A smaller fraction is bound to two Ni(II)•**2** moieties and there is hardly any His$_6$-MBP present that is bound to three NiNTA moieties. On the surface however, the situation is completely different. At low concentrations, the occupation of the molecular printboard with His$_6$-MBP is still low which is due to the

way the experiments are performed, *i.e.* by variation of the concentrations of both His$_6$-MBP and Ni(II)•**2** simultaneously. Nevertheless, the valency of binding of His$_6$-MBP to the molecular printboard is already for about 60% in a divalent fashion, and 20% in a trivalent fashion. Above 0.15 μM the concentration of surface-immobilized His$_6$-MBP increases rapidly, and this increase can almost completely be attributed to trivalently bound His$_6$-MBP. Above 1 μM, the majority (~85%) of His$_6$-MBP is bound in a trivalent fashion to the molecular printboard, while a smaller fraction (~15%) is bound in a divalent fashion. The amount of monovalently bound His$_6$-MBP is negligible.

The surface multivalency enhancement observed here resembles the enhancement observed before,[30] and can be ascribed to the effective concentration at the surface promoting multivalent binding. The enhancement can be expressed in an enhancement factor (*EF*), which can be calculated according to equation 1, in which *f* is the fraction of MBP in solution (l) or surface (s) bound in a mono- or multivalent fashion to Ni(II)•**2**.

$$EF_{multi} = \left(\frac{f_{s,multi}}{f_{s,mono}} \right) \Big/ \left(\frac{f_{l,multi}}{f_{l,mono}} \right) \tag{1}$$

At low concentrations the enhancement factor for divalent binding to the printboard is 300, and decreases at higher concentrations (Figure 7.4). For the trivalent species, the surface multivalency effect is a lot larger. The EF_{tri} is close to 10^4 at low concentrations and also decreases gradually. It can therefore be concluded that the multivalent βCD host surface favors the formation of multivalent complexes, and that this effect is stronger for complexes with a higher valency.
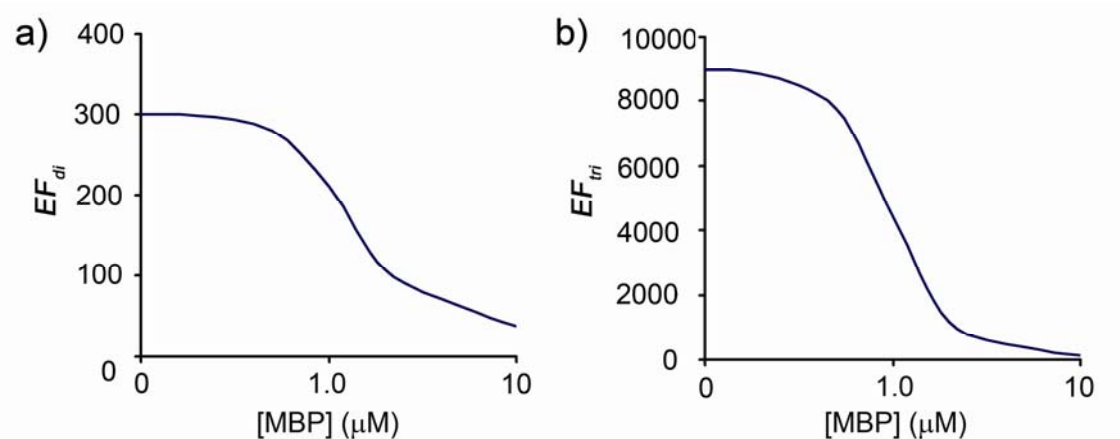
Figure 7.4 *Enhancement factors (EF) for the divalent (a) and trivalent (b) species present at the molecular printboard, relative to the corresponding solution species.*

7.2.3 Adsorption of the 20S proteasome at the molecular printboard

Nonspecific interactions of the 20S proteasome to the molecular printboard were investigated by SPR. Since control over protein orientation is targeted eventually, α-His-tagged 20S proteasome was used to target an end-on immobilization. For the SPR experiments of the 20S proteasome to the molecular printboard **1** was tested for the suppression of nonspecific interactions to the surface (Figure 7.5).

Figure 7.5 *SPR sensograms of the nonspecific (a) and specific (b) adsorption, of the α-(His₆)₁₄-20S proteasome (0.1 μM) onto βCD SAMs, in the presence of **1** (a) and in the presence of **3** (1 mM) in the absence and presence of 7 μM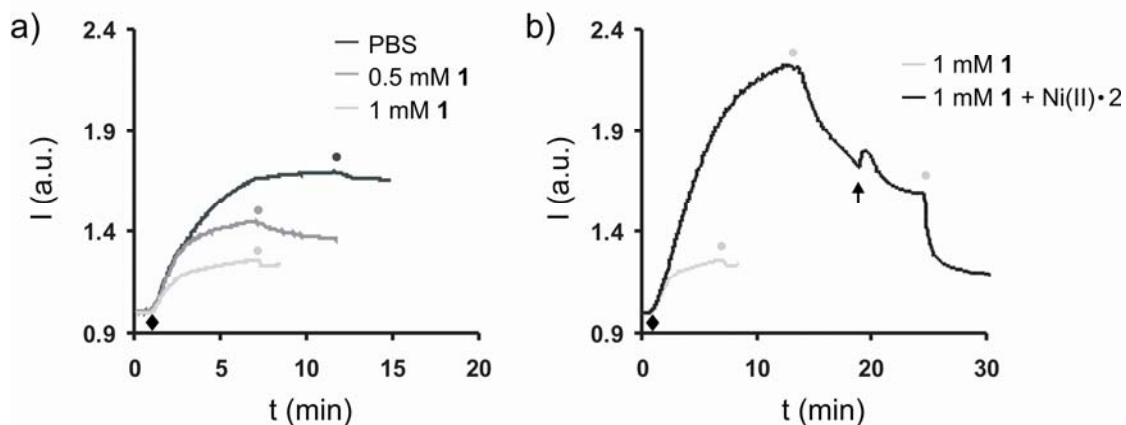 Ni•**2** (b). Symbols indicate switching solutions to: (●) PBS, (●) 0.5 mM **1** in PBS, (●) 1.0 mM **1** in PBS, (♦) 0.1 μM 20S proteasome in PBS, 0.5 mM **1** in PBS + 0, 0.5, or 1.0 mM **1** in PBS (▲) 0.1 μM 20S proteasome + 7 μM Ni(II)•**2** in PBS + 1 mM **1**,(↑) 10 mM βCD and 10 mM EDTA in PBS.*

In Figure 7.5a, SPR sensograms are depicted, which show that the 20S proteasome adsorbs nonspecifically at the molecular printboard in the absence of **1**. Addition of 0.5 mM and 1 mM **1** reduced the amount of nonspecific adsorption by respectively 36% and 62%. Experiments in which Ni(II)•**2** was used were performed to check if the 20S proteasome could be immobilized in a specific manner (Figure 7.5b). Therefore, the 20S proteasome was premixed with Ni(II)•**2** (ratio 1:70) and 1 mM **1** before the SPR experiments. Thereafter, this mixture was flowed over the βCD SAM. The increase of the SPR signal was much higher in this case, indicating that the 20S proteasome is immobilized to a large extent in a specific manner. In theory, the 20S proteasome is attached in a multivalent fashion, which should be stable against rinsing with PBS. Possibly, the position of the His₆ tag in combination with the length of linker **2**, does not allow a high valency to be achieved here. This is to be investigated in another study, by varying the linker length of linker **2**.

7.2.4 Patterning of DsRed-FT at the molecular printboard

Patterning of a His₆-tagged protein was carried out with (His₆)₄-DsRed-FT. Experiments in which (His₆)₄-DsRed-FT was patterned at the surface by microcontact

printing (μCP) were performed with oxidized PDMS stamps. These stamps were inked for 2 min with a solution containing 1×10^{-6} M (His$_6$)$_4$-DsRed-FT and 2×10^{-6} M Ni(II)•**2** in PBS buffer. After inking, the stamp was blown dry, and put into conformal contact with a βCD SAM on glass for 1 min. After printing, the sample was imaged with fluorescence microscopy (Figure 7.6, top). A reference experiment as performed in which the oxidized stamp was inked with 1×10^{-6} M (His$_6$)$_4$-DsRed-FT without Ni(II)•**2** (Figure 7.6, bottom).
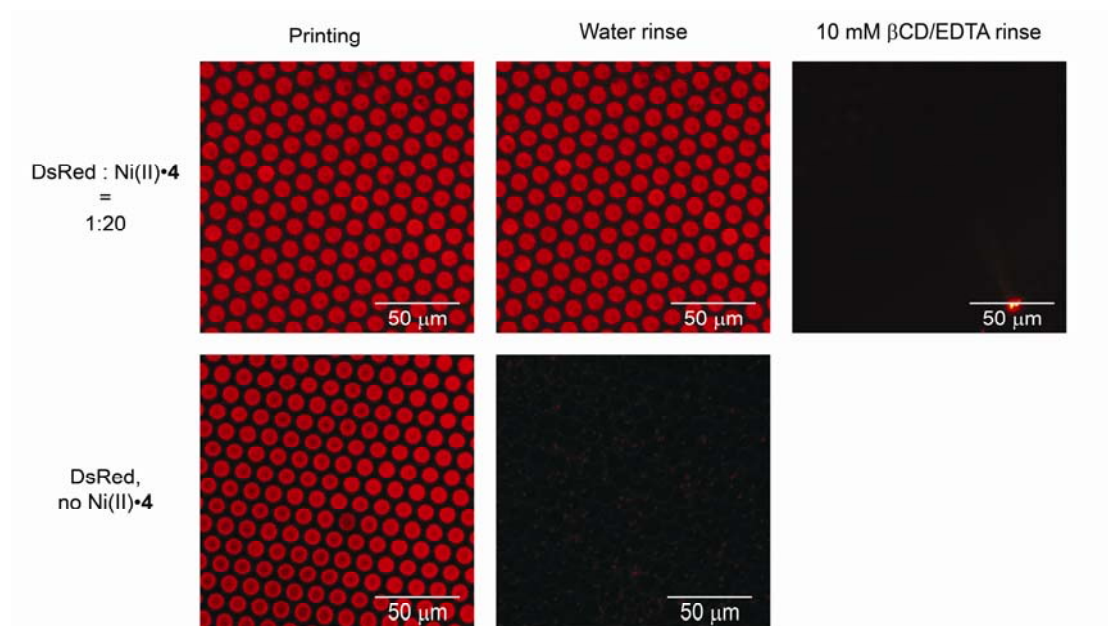
Figure 7.6 *Fluorescence microscopy images of (His$_6$)$_4$-DsRed-FT at the molecular printboard patterned by μCP with (top) and without Ni(II)•2 (bottom), directly after printing (left), rinsing with water (center), and subsequent rinsing with 10 mM βCD and 10 mM EDTA (right).*

After printing, patterns were clearly visible both with and without Ni(II)•**2** present, indicating (i) that the attachment to the molecular printboard did not disrupt the tertiary structure of the protein, and (ii) that the transfer occurred regardless of specificity of interaction. On the sample prepared with Ni(II)•**2** present in the inking solution, rinsing with water did not remove the pattern from the surface, only prolonged rinsing with a PBS solution containing 10 mM βCD and 10 mM EDTA appeared to be sufficient for removing (His$_6$)$_4$-DsRed-FT from the surface. This indicates that the complex stability is governed by the specific, multivalent interactions. In contrast, the surface that was patterned with the inking solution which

did not contain Ni(II)•**2** could be cleared from (His_6)_4-DsRed-FT by just rinsing with water, indicating that the protein was not attached in a specific manner.

An open issue is with how many His tags the (His_6)_4-DsRed-FT protein is bound to the surface. In principle, estimating the thermodynamic binding strength of a protein with multiple His tags is a doubly nested multivalent problem: 2 His_6 groups are anchored to a single N(II)•**2** complex, 1-3 Ni(II)•**2** complexes can be attached to a single His_6 tag (and we show here that the majority binds in a trivalent fashion), and 1-4 His_6 tags of DsRed-FT can be bound (via mostly) 3-12 Ni(II)•**2** complexes to the βCD substrate. For a single His_6 tag, the overall stability constant for trivalent binding via Ni(II)•**2** is given by (See Appendix) equation 2.

$$K = (K_i)^3 K_1 K_2 K_3 C_{eff}^2 [\text{Ni} \cdot \mathbf{2}]^3 \tag{2}$$

An apparent binding constant is therefore strongly dependent on [Ni(II)•**2**], and can be estimated, based on the data given above, to be approximately 10^5 M^{-1} when [Ni(II)•**2**] = 1 μM.[42] This stability of the DsRed-FT patterns towards rinsing with water may indicate binding with multiple (2-4) His_6 tags, and thus explain the behavior that is observed qualitatively similar to the binding of a divalent adamantyl derivative.[42,43] However, kinetic effects, *i.e.* slow dissociation and redissociation of the protein, can not be excluded at this stage. More experimental work, both regarding the thermodynamics and the kinetics of such nested multivalent systems as well as the thermodynamic modeling of such systems, is needed before firm conclusions can be reached.

7.3   Conclusions

This chapter shows that His_6-tagged proteins can be attached to the molecular printboard in a selective manner by using the supramolecular blocking agent **1** and Ni(II)•**2**. Modeling of SPR data of His_6-MBP binding to the molecular printboard showed that the enhancement of surface multivalency upon binding of His_6-MBP to the molecular printboard is present. Although the binding of His_6-MBP to Ni(II)•**2** in solution is mainly absent or monovalent, the binding of His_6-MBP to Ni(II)•**2** on the molecular printboard is mainly trivalent. Surface enhancement factors for the divalent

species are up to ~300, and for the trivalent species up to 10^4. Patterning experiments with the auto-fluorescent protein $(His_6)_4$-DsRed-FT showed that the protein, complexed to Ni(II)•**2**, can be patterned by means of µCP on the molecular printboard in a specific, stable, multivalent manner. SPR studies with the 20S proteasome showed that nonspecific interactions of the protein to the molecular printboard can be suppressed up to 62%. Nevertheless the possibility of specific adsorption became apparent in the presence of Ni(II)•**2**, although the final stability appeared to be rather low. This work shows that different layers of non-covalent interactions can lead to very stable attachment of surfaces. The research presented here, forms a basis from which the attachment of His-tagged proteins to molecular printboards can be extended, e.g. the development of protein arrays.

7.4   Acknowledgements

7.5   Experimental section

General

The synthesis of **1** and **2** has been described in Chapter 6. Maltose binding protein (MBP) with a C-terminal hexahistidine tag was expressed and purified as previously described.[5] The Fluorescent Timer mutant of DsRed (DsRed-FT) was produced by standard site-directed mutagenesis approaches as reported previously.[45] The PCR product was cloned into pQE-30/BamHI/Hind III vector. *Escherichia coli* JM101 cells were transformed with the plasmid. The expression of His_6-tagged DsRed-FT was induced by 1 mM IPTG for various lengths of time (3–24 h).

To purify $(His_6)_4$-DsRed-FT the clarified cell lysate was adsorbed on Ni(II)NTA agarose overnight at 4 °C, and the protein was eluted with 250 mM imidazole. The eluted fractions were dialyzed against 100 mM Tris-HCl, pH 8.5, 100 mM NaCl overnight. The α-Histagged-20S proteasome was expressed and purified as described

before.[19] For all experiments 10 mM phosphate buffer, pH 7.5 with 150 mM NaCl, phosphate buffered saline (PBS), was used.

Monolayer preparation

Gold substrates for SPR (BK7 glass/2-4 nm Ti/50 nm Au) were obtained from Ssens B.V., Hengelo, The Netherlands. Gold substrates were cleaned by dipping them into piranha (1:3 mixture of concentrated H_2SO_4 and 30% H_2O_2) for 5 s. (*Warning: piranha should be handled with caution; it can detonate unexpectedly.*) After thorough rinsing with Millipore water, they were placed for 10 min in absolute EtOH in order to remove the oxide layer. Subsequently SAMs were prepared as described before.[46] SAMs on glass were prepare, using βCD heptamine, as described before.[47] All solvents used in the monolayer preparation were of p.a. grade.

SPR

SPR measurements were performed on a Resonant Probes GmbH SPR instrument. The instrument consists of a HeNe laser (JDS Uniphase, 10 mW, λ = 632.8 nm) of which the laser light passes through a chopper that is connected to a lock-in amplifier (EG&G 7256). The modulated beam is directed through two polarizers (OWIS) to control the intensity and the plane of polarization of the light. The light is coupled via a high index prism (Scott, LaSFN9) in the Kretschmann configuration to the backside of the gold-coated substrate which is optically matched through a refractive index matching oil (Cargille; series B; $n_D^{25°C}$ = 1.7000 ± 0.0002) at the prism, mounted on a θ-2θ goniometer, in contact with a Teflon cell with a volume of 39 μl and a diameter of 5 mm. The light that leaves the prism passes through a beam splitter, subsequently, the s-polarized light is directed to a reference detector, and the p-polarized light passes through a lens which focuses the light onto a photodiode detector. Laser fluctuations are filtered out by dividing the intensity of the p-polarized light (I_p) by the intensity of the s-polarized light (I_s). All measurements were performed at a constant angle by reflectivity tracking.

A Reglo digital MS-4/8 Flow pump from Ismatec with four channels was used. In this flow pump, Tygon R3607 tubings with a diameter of 0.76 mm were used, obtained from Ismatec.

The SPR experiments were performed in a flow cell with a volume of 3.9×10^{-2} ml, under a continuous flow of 0.5 ml/min. Before a new experiment was started, the gold substrates were rinsed thoroughly with 10 mM βCD in 10 mM PBS containing 150 mM NaCl, and 10 mM PBS containing 150 mM NaCl. Experiments were started after the baseline was stable. When the solution had to be changed, the pump was stopped, and immediately after changing the solution the pump was switched on again. Stock solutions (1×10^{-4} M) of the different proteins were prepared in PBS, and diluted just before every experiment. In those cases were protein was used in combination with **2**, the solution was left standing for 20 min before use.

Microcontact printing (μCP)

PDMS stamps were prepared by casting a 10:1 (v/v) mixture of poly(dimethylsiloxane) and curing agent (Sylgard 184, Dow Corning) against a patterned silicon master. The master employed had hexagonally oriented 10 μm circular features separated by 5 μm. After curing of the stamps overnight, they were mildly oxidized in an oxygen plasma reactor for 30 s to render them hydrophilic. Subsequently, they were inked by soaking them in a 10^{-6} M aqueous solution of (His$_6$)$_4$-DsRed-FT for 2 min. Before printing, the stamps were blown dry in a stream of N$_2$. The stamps were applied manually and without pressure control for 2 min onto the βCD SAMs on gold and then carefully removed.

Fluorescence Microscopy

Fluorescent images were made using an Olympus inverted research microscope IX71 equipped with a mercury burner U-RFL-T as light source and a digital camera Olympus DP70 (12.5 million-pixel cooled digital color camera) for image acquisition. Green excitation light (510 nm $\leq \lambda_{ex} \leq$ 550 nm) and red emission light ($\lambda_{em} \geq$ 590 nm) was filtered using a U-MWG Olympus filter cube.

7.6   Appendix: multivalency model at interfaces for His-tagged proteins

The binding of His$_6$-MBP to βCD SAMs via Ni•**2** can be monovalent, divalent, or trivalent. In Scheme 7.2 all possible equilibria are presented, assuming the Ni(II)•**2** complex forms completely, as discussed in the main text. At βCD SAMs, all His$_6$-

MBP units complexed to one Ni(II)•**2** will behave as monovalent guests, binding to surface-confined βCD (βCD$_s$) in a similar fashion as to βCD in solution (βCD$_l$). For His$_6$-MBP units that are bound via two or three Ni(II)•**2** complexes, the binding to βCD SAMs will be governed by an effective concentration term (C_{eff}), which is the driving force for the formation of multivalent complexes at βCD SAMs.

A general description is given for the multivalent binding of His$_6$-MBP•(Ni(II)•**2**)$_x$ (x = 1-3) to the molecular printboard. The stepwise adsorption of e.g. His$_6$-MBP•(Ni(II)•**2**)$_3$ to the surface involves an intermolecular adsorption step and two intramolecular binding steps, the latter of which are both governed by C_{eff}. All solution and surface species of MBP are shown in Scheme 7.2. All intrinsic stability constants for βCD$_l$ and βCD$_s$ are assumed equal for all steps given in Scheme 7.2.[32]

As described before,[31,31] SPR titrations performed for the binding to βCD SAMs are fitted here, yielding K_1 values for the His$_6$ tag-NiNTA interaction, while $K_{i,l}$ and $K_{i,s}$, the intrinsic binding constant of an adamantyl guest to βCD in solution and the intrinsic binding constant of an adamantyl guest to a surface-confined βCD cavity, respectively, are fixed to the values determined by ITC and SPR.

The statistical factors relating K_2 and K_3 for additional Ni(II)•**2** were determined by noting that: (i) binding Ni(II)•**2** to His$_6$-MBP is 5 times as likely than binding to a His$_2$ unit (which is the intrinsic interaction motif in this case), (ii) there are 2 or 3 His$_2$ sites free for interaction of a second Ni(II)•**2** to MBP•Ni•**2** in 60% and 40% of the MBP•Ni(II)•**2** complexes, respectively, (iii) only for 46.7% of the MBP•(Ni•**2**)$_2$ complexes there is an additional free His$_2$ site available for a third Ni•**2** unit (See Scheme 7.3), and (iv) the assumption is made that Ni(II)•**2**•NTA binds to neighboring histidines in the His$_6$-tag. This leads to the prefactors of $K_2 = \dfrac{6}{25}K_1$ and $K_3 = \dfrac{7}{225}K_1$ as given in Scheme 7.2.
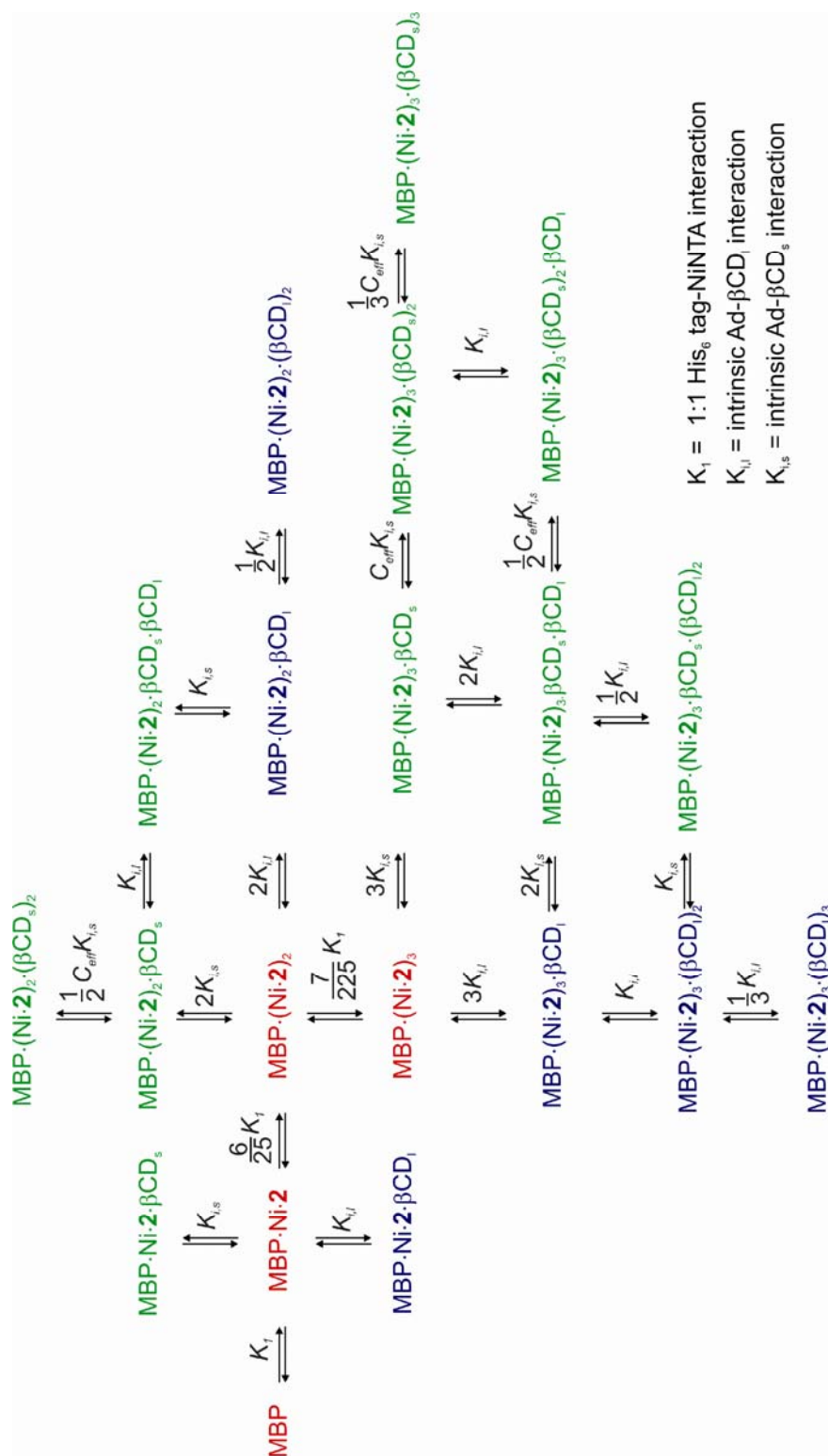
Scheme 7.2 *Equilibria for all species (solution ($_l$) and surface ($_s$)) for the attachment of His$_6$-MBP at the molecular printboard (charges are omitted for clarity). Subsequent complexation steps of Ni(II)•2 to His$_6$-MBP are shown in red, and all surface species are given in green.*
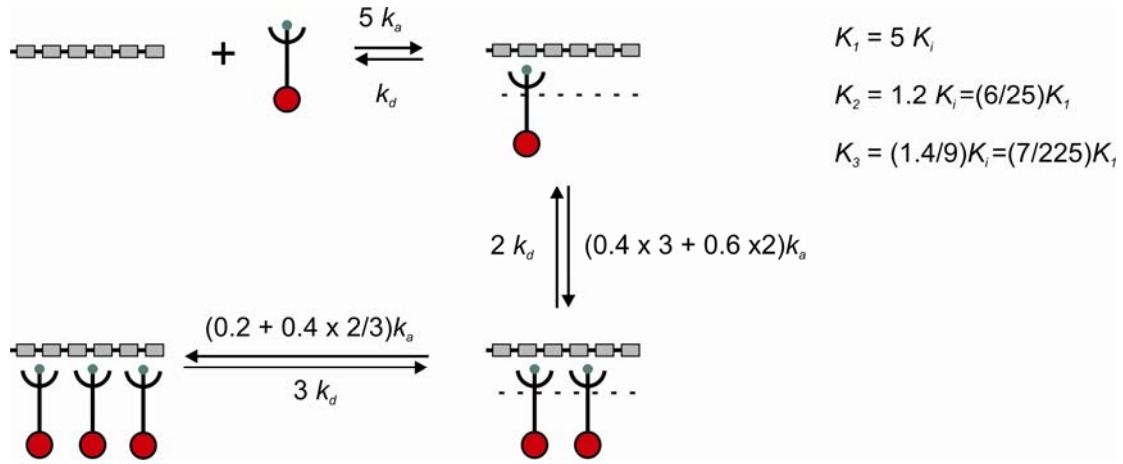
Scheme 7.3 *The statistical factors relating K_1, K_2 and K_3 to K_i. In the model is assumed that Ni(II)•2 binds to two neighboring histidines.*

Since all measurements are performed at pH = 7.5, Ni(II)•**2** is always formed completely (See main text). The mass balances that can be constructed based on Scheme 7.2 are the following (charges are omitted for clarity):

$$[MBP]_{tot} = [MBP]_{free} + [MBP•Ni•\mathbf{2}] + [MBP•Ni•\mathbf{2}•\beta CD_l] + [MBP•Ni•\mathbf{2}•\beta CD_s] +$$
$$[MBP• (Ni•\mathbf{2})_2] + [MBP•(Ni•\mathbf{2})_2•\beta CD_s] + [MBP•(Ni•\mathbf{2})_2•(\beta CD_s)_2] +$$
$$[MBP•(Ni•\mathbf{2})_2•\beta CD_l] + [MBP•(Ni•\mathbf{2})_2•(\beta CD_l)_2] +$$
$$[MBP•(Ni•\mathbf{2})_2•\beta CD_s\beta CD_l] + [MBP•(Ni•2)_3•(\beta CD_s)_2] + [MBP•(Ni•\mathbf{2})_3] +$$
$$[MBP•(Ni•\mathbf{2})_3•\beta CD_l] + [MBP•(Ni•\mathbf{2})_3•(\beta CD_l)_2] +$$
$$[MBP•(Ni•\mathbf{2})_3•(\beta CD_l)_3] + [MBP•(Ni•\mathbf{2})_3•\beta CD_s] +$$
$$[MBP•(Ni•\mathbf{2})_3•\beta CD_s\beta CD_l] + [MBP•(Ni•\mathbf{2})_3•\beta CD_s(\beta CD_l)_2] +$$
$$[MBP•(Ni•\mathbf{2})_3•(\beta CD_s)_2\beta CD_l] + [MBP•(Ni•\mathbf{2})_3•(\beta CD_s)_2] +$$
$$[MBP•(Ni•\mathbf{2})_3•(\beta CD_s)_3] \tag{3}$$

$$[\mathbf{2}]_{tot} = [Ni•\mathbf{2}]_{free} + [Ni•\mathbf{2}•CD_l] + [Ni•\mathbf{2}•CD_s] + [MBP•Ni•\mathbf{2}] + [MBP•Ni•\mathbf{2}•CD_s] +$$
$$[MBP•Ni•\mathbf{2}•CD_l] + 2([MBP•(Ni•\mathbf{2})_2] + [MBP•(Ni•\mathbf{2})_2CD_s] +$$
$$[MBP•(Ni•\mathbf{2})_2•(\beta CD_s)_2] + [MBP•(Ni•\mathbf{2})_2•\beta CD_l] +$$
$$[MBP•(Ni•\mathbf{2})_2•(\beta CD_l)_2] + [MBP•(Ni•\mathbf{2})_2•\beta CD_l•\beta CD_s]) +$$
$$3([MBP•(Ni•\mathbf{2})_3] + [MBP•(Ni•\mathbf{2})_3•\beta CD_s] + [MBP•(Ni•\mathbf{2})_3•(\beta CD_s)_2] +$$
$$[MBP•(Ni•\mathbf{2})_3•(\beta CD_s)_3] + [MBP•(Ni•\mathbf{2})_3•\beta CD_l] +$$

[MBP•(Ni•**2**)$_3$•(βCD$_l$)$_2$] + [MBP•(Ni•**2**)$_3$•(βCD$_l$)$_3$] +

[MBP•(Ni•**2**)$_3$•βCD$_s$•βCD$_l$] + [MBP•(Ni•**2**)$_3$(βCD$_s$)$_2$$\beta$CD$_l$] +

[MBP(Ni•**2**)$_3$$\beta$CD$_s$($\beta$CD$_l$)$_2$]   (4)

[**1**]$_{tot}$ =   [**1**]$_{free}$ + [**1**•βCD$_l$] + [**1**•βCD$_s$]   (5)

[βCD$_s$]$_{tot}$ =   [βCD$_s$]$_{free}$ + [MBP•Ni•**2**•βCD$_s$] + [MBP•(Ni•**2**)$_2$•βCD$_s$] +

[MBP•(Ni•**2**)$_2$•βCD$_s$•βCD$_l$] + [MBP•(Ni•**2**)$_3$•βCD$_s$] +

[MBP•(Ni•**2**)$_3$•βCD$_s$•βCD$_l$] + [MBP•(Ni•**2**)$_3$•βCD$_s$•(βCD$_l$)$_2$] +

2([MBP•(Ni•**2**)$_2$•(βCD$_s$)$_2$] + [MBP•(Ni•**2**)$_3$•(βCD$_s$)$_2$] +

[MBP•(Ni•**2**)$_3$•(βCD$_s$)$_2$$\beta$CD$_l$]) + 3[MBP•(Ni•**2**)$_3$•($\beta$CD$_s$)$_3$]   (6)

[βCD$_l$]$_{tot}$ =   [βCD$_l$]$_{free}$ + [MBP•(Ni•**2**)$_2$•βCD$_s$$\beta$CD$_l$] + [MBP•(Ni•**2**)$_2$•$\beta$CD$_l$] +

[MBP•(Ni•**2**)$_3$•βCD$_l$] + [MBP•(Ni•**2**)$_3$•βCD$_s$$\beta$CD$_l$] +

[MBP•(Ni•**2**)$_3$•(βCD$_s$)$_2$$\beta$CD$_l$] + 2([MBP•(Ni•**2**)$_2$•($\beta$CD$_l$)$_2$] +

[MBP•(Ni•**2**)$_3$•(βCD$_l$)$_2$] + [MBP•(Ni•**2**)$_3$•βCD$_s$(βCD$_l$)$_2$]) +

3[MBP•(Ni•**2**)$_3$•(βCD$_l$)$_3$]   (7)

Species involving βCD$_s$ are expressed in volume concentrations.[32] The binding of the divalent MBP•(Ni(II)•**2**)$_2$ and trivalent MBP•(Ni(II)•**2**)$_3$ to βCD$_l$ involves statistical factors (Scheme 7.2) arising from the probabilities for binding relative to the monovalent species, in this case according to a normal 1:3 complexation sequence.

The binding constants for first intermolecular binding events of the divalent and trivalent species at the surface are:

$$K = \frac{[\mathrm{MBP} \cdot (\mathrm{Ni} \cdot \mathbf{2})_2 \cdot \beta \mathrm{CD}_s]}{[\mathrm{MBP} \cdot (\mathrm{Ni} \cdot \mathbf{2})_2][\beta \mathrm{CD}_s]} = 2K_{i,s}$$ (8)

$$K = \frac{[\mathrm{MBP} \cdot (\mathrm{Ni} \cdot \mathbf{2})_3 \cdot \beta \mathrm{CD}_s]}{[\mathrm{MBP} \cdot (\mathrm{Ni} \cdot \mathbf{2})_3][\beta \mathrm{CD}_s]} = 3K_{i,s}$$ (9)

The second, intramolecular, binding event for the di- and trivalent species, and third, intramolecular binding event for the trivalent species, (equation 11, 12, and 13) are governed by the effective concentration term, which is defined as in equation 10.[31,32] The effective concentration is given by multiplying the maximum effective concentration, $C_{eff,max}$, which is the number of accessible host sites in the probing volume, with the fraction of free host sites at the surface.

$$C_{eff} = C_{eff,max} \frac{[\beta CD_s]}{[\beta CD_s]_{tot}} \tag{10}$$

$$K = \frac{[MBP \cdot (Ni \cdot \mathbf{2})_2 \cdot \beta CD_{s,2} \beta CD_l]}{[MBP \cdot (Ni \cdot \mathbf{2})_2 \cdot \beta CD_s \beta CD_l][\beta CD_s]} = \tfrac{1}{2} C_{eff} K_{i,s} \tag{11}$$

$$K = \frac{[MBP \cdot (Ni \cdot \mathbf{2})_3 \cdot \beta CD_{s,2}]}{[MBP \cdot (Ni \cdot \mathbf{2})_3 \cdot \beta CD_s][\beta CD_s]} = C_{eff} K_{i,s} \tag{12}$$

$$K = \frac{[MPB \cdot (Ni \cdot \mathbf{2})_3 \cdot \beta CD_{s,3}]}{[MBP \cdot (Ni \cdot \mathbf{2})_3 \cdot \beta CD_{s,2}][\beta CD_s]} = \tfrac{1}{3} C_{eff} K_{i,s} \tag{13}$$

Since the SPR experiments were performed in a flow system, all solutions species concentrations can be calculated from simplified forms of equations 3-5 and 7. After numerical optimization of these, the values of the solution species concentrations were used in the full equations 1-5 for calculations of the surface species.

Substitution of the equilibrium constant definitions into the mass balances for [MBP]$_{tot}$, [CD$_s$]$_{tot}$, [CD$_l$]$_{tot}$, [$\mathbf{1}$]$_{tot}$, and [$\mathbf{2}$]$_{tot}$ (equations 3-7) provides a set of numerically solvable equations with [MBP], [CD$_s$], [CD$_l$], [$\mathbf{1}$], and [$\mathbf{2}$] as the variables.

Starting from an initial estimate for K_l, (defined as: $K_1 = \dfrac{[MBP \cdot (Ni \cdot \mathbf{2})]}{[MBP][Ni \cdot \mathbf{2}]}$) using fixed values for $C_{eff,max}$ (0.1 M) and the other stability constants, this set of equations is solved numerically using a Simplex algorithm in a spreadsheet approach.[48] When fitting SPR data, K_l is optimized in a least-squares optimization routine, assuming that the SPR response (intensity) is linearly dependent on the coverages of MBP, $\mathbf{1}$, and $\mathbf{2}$

adsorbed to the βCD SAM, regardless of the type of species. The maximum intensity (I_{max} of MBP) is then optimized as an independent fitting parameter as well while those of **1** and **2** were determined by independent SPR measurements.

The overall stability constant of His$_6$-MBP•(Ni•**2**)$_3$•(βCD$_s$)$_3$ can, based on Scheme 7.2, be given by equation 14:

$$K = (K_{i,s})^3 K_1 K_2 K_3 C_{eff}^2 \cdot [\text{Ni} \cdot \textbf{2}]^3 \tag{14}$$

Assuming $K_{i,s} = 1.2 \times 10^4$ M^{-1}, $K_1 = 7.8 \times 10^3$ M^{-1} ($K_2 = \dfrac{6}{25} K_1$ and $K_3 = \dfrac{7}{225} K_1$), $C_{eff} = C_{eff,max} = 0.1$ M (at relatively low coverages), and [Ni•**2**] = 1 μM, an apparent conditioned binding constant can be estimated of ~ 10^5 M^{-1}.

7.7 References and notes

1. A. Biebricher, A. Paul, P. Tinnefeld, A. Gölzhäuser, M. Sauer, *J. Biotech.* **2004**, *112*, 97-107.

2. K. M. McLean, S. L. McArthur, R. C. Chatelier, P. Kingshott, H. J. Griesser, *Coll. Interface Sci. B* **2000**, *17*, 23-35.

3. R. Valiokas, G. Klenkar, A. Tinzali, R. Tampé, B. Liedberg, J. Piehler, *ChemBioChem* **2006**, *7*, 1325-1329.

4. E. L. Schmid, T. A. Keller, Z. Dienes, H. Vogel, *Anal. Chem.* **1997**, *69*, 1979-1985.

5. S. Lata, J. Piehler, *Anal. Chem.* **2005**, *77*, 1096-1105.

6. G. Klenkar, R. Valiokas, I. Lundstrom, A. Tinazli, R. Tampé, J. Piehler, B. Liedberg, *Anal. Chem.* **2006**, *78*, 3643-3650.

7. A. Tinazli, J. Tang, R. Valiokas, S. Picuric, S. Lata, J. Piehler, B. Liedberg, R. Tampé, *Chem. Eur. J.* **2005**, *11*, 5249-5259.

8. R. Gamsjaeger, B. Wimmer, H. Kahr, A. Tinazli, S. Piruric, S. Lata, R. Tampé, Y. Maulet, H. J. Gruber, P. Hinterdorfer, C. Romanin, *Langmuir* **2004**, *20*, 5885-5890.

9. R. Blankespoor, B. Limoges, B. Schöllhorn, J. L. Sysa-Magalé, D. Yazidi, *Langmuir* **2005**, *21*, 3362-3375.

10. E. Gizeli, J. Glad, *Anal. Chem.* **2004**, *76*, 3995-4001.

11. J. K. Lee, Y. G. Kim, Y. S. Chi, W. S. Yun, I. S. Choi, *J. Phys. Chem. B* **2004**, *108*, 7665-7673

12. K. Kato, H. Sato, H. Iwata, *Langmuir* **2005**, *21*, 7071-7075.

13. D. Kröger, M. Liley, W. Schiweck, A. Skerra, H. Vogel, *Biosens. Bioelectr.* **1999**, *14*, 155-161.

14. U. Rädler, J. Mack, N. Persike, G. Jung, R. Tampé, *Biophys. J.* **2000**, *79*, 3144-3152.

15. L. Schmitt, T. M. Bohanon, S. Denzinger, H. Ringsdorf, R. Tampé, *Angew. Chem. Int. Ed.* **1996**, *35*, 317-320.

16. G. J. Wegner, H. J. Lee, G. Marriott, R. M. Corn, *Anal. Chem.* **2003**, *75*, 4740-4746.

17. M. Mammen, S.-K. Choi, G. M. Whitesides, *Angew. Chem. Int. Ed.* **1998**, *37*, 2754-2794.

18. M. J. W. Ludden, M. Péter, D. N. Reinhoudt, J. Huskens, *Small* **2006**, *2*, 1192-1202.

19. S. Hutschenreiter, A. Tinazli, K. Model, R. Tampé, *EMBO* **2004**, *23*, 2488-2497

20. S. Lata, M. Gavutis, R. Tampé, J. Piehler, *J. Am. Chem. Soc* **2006**, *128*, 2365-2372.

21. N. Haddour, S. Cosnier, C. Gondran, *J. Am. Chem. Soc.* **2005**, *127*, 5752-5753.

22. G. Zhen, D. Falconnet, E. Kuennemann, J. Vörös, N. D. Spencer, M. Textor, S. Zürcher, *Adv. Funct. Mat.* **2006**, *16*, 243-251.

23. A. Tinazli, J. Tang, R. Valiokas, S. Picuric, S. Lata, J. Piehler, B. Liedberg, R. Tampé, Chem. Eur. J. **2005**, *11*, 5249-5259.

24. I. T. Dorn, K. Pawlitschko, S. C. Pettinger, R. Tampé, *Biol. Chem.* **1998**, *379*, 1151-1159.

25. C. Dietrich, L. Schmitt, R. Tampé, *Proc. Natl. Acad. Sci. USA* **1995**, *92*, 9014-9018.

26. A. Thess, S. Hutschenreiter, M. Hofmann, R. Tampé, W. Baumeister, R. Guckenberger, *J. Biol. Chem.* **2002**, *277*, 36321-36328.

27. I. T. Dorn, R. Eschrich, E. Seemüller, R. Guckenberger, R. Tampé, *J. Mol. Biol.* **1999**, *288*, 1027-1036.

28. M. C. T. Fyfe, J. F. Stoddart, *Coord. Chem. Rev.* **1999**, *183*, 139-155.

29. H. Hofmeier, U. S. Schubert, *Chem. Comm.* **2005**, 2423-2432.

30. O. Crespo-Biel, C. W. Lim, B. J. Ravoo, D. N. Reinhoudt, J. Huskens, *J. Am. Chem. Soc.* **2006**, *128*, 17024-17032.

31. A. Mulder, T. Auletta, A. Sartori, S. Del Ciotto, A. Casnati, R. Ungaro, J. Huskens, D. N. Reinhoudt, *J. Am. Chem. Soc.* **2004**, *126*, 6627-6636.

32. J. Huskens, A. Mulder, T. Auletta, C. A. Nijhuis, M. J. W. Ludden, D. N. Reinhoudt, *J. Am. Chem. Soc.* **2004**, *126*, 6784-6797.

33 J. D. Fikes, G. A. Barkocy-Gallagher, D. G. Klapper, P. J. Bassford, *J. Biol. Chem.* **1990**, *265*, 3417-3423.

34. W. Boos, H. Shuman, *Microbiol. Mol. Biol. Rev.* **1998**, *62*, 204-229.

35. L. G. Sillen, A. E. Martell, *Stability Constants of Metal-Ion Complexes. Section 2: Organic Ligands*, The Chemical Society, London, UK, **1964**.

36. The conditional stability constant for the complex Ni(II)•**2**, $K_{cond} = \dfrac{[\text{Ni(II)}\cdot\mathbf{2}]}{[\text{Ni(II)}][\mathbf{2}]_{\text{free}}}$, where $[\mathbf{2}]_{\text{free}}$ represents the concentration of **2** and its protonated forms, is given by: $\log K_{cond} = \log K_{Ni\bullet\mathbf{2}} - \log K_{H\bullet\mathbf{2}} + \text{pH}$ (for pH = 3-10). Assuming values for NiNTA ($\log K_{NiNTA}$ = 11.5, $\log K_{HNTA}$ = 9.7), $\log K_{cond}$ = 9.3 at pH = 7.5.

37. M. V. Matz, K. A. Lukyanov, S. A. Lukyanov, *BioEssays* **2002**, *24*, 953-959.

38. N. C. Shaner, R. E. Campbell, P. A. Steinbach, B. N. G. Giepmans, A. E. Palmer, R. Y. Tsien, *Nat. Biotech.* **2004**, *12*, 1567-1572.

39. V. V. Verkhusha, K. A. Lukyanov, *Nat. Biotech.* **2004**, *22*, 289-296.

40. J. Wiedenmann, A. Schenk, C. Röcker, A. Girod, K. D. Spindler, G. U. Nienhaus, *Proc. Natl. Acad. Sci.* **2002**, *99*, 11646-11651.

41. M. V. Rekharsky, Y. Inoue, *Chem. Rev.* **1998**, *98*, 1875-1917.

42. C. M. Bruinink, C. A. Nijhuis, M. Péter, B. Dordi, O. Crespo-Biel, T. Auletta, A. Mulder, H. Schönherr, G. J. Vancso, J. Huskens, D. N. Reinhoudt, *Chem. Eur. J.* **2005**, *11*, 3988-3996.

43. T. Auletta, B. Dordi, A. Mulder, A. Sartori, S. Onclin, C. M. Bruinink, M. Péter, C. A. Nijhuis, H. Beijleveld, H. Schönherr, G. J. Vancso, A. Casnati, R. Ungaro, B. J. Ravoo, J. Huskens, D. N. Reinhoudt, *Angew. Chem. Int. Ed.* **2004**, *43*, 369-373.

44. S. Lata, A. Reichel, R. Brock, R. Tampé, J. Piehler, *J. Am. Chem. Soc.* **2005**, *127*, 10205-10215.

45. A. Terskikh, A. Fradkov, G. Ermakova, A. Zaraisky, P. Tan, A. Kajava, X. Zhao, S. Lukyanov, M. Matz, S. Kim, I. Weissman, P. Siebert, *Science* **2000**, *290*, 1585-1588.

46. M. W. J. Beulen, J. Bügler, B. Lammerink, F. A. J. Geurts, E. M. E. F. Biemond, K. G. C. van Leerdam, F. C. J. M. van Veggel, J. F. J. Engbersen, D. N. Reinhoudt, *Langmuir* **1998**, *14*, 6424-6429.

47. S. Onclin, A. Mulder, J. Huskens, B. J. Ravoo, D. N. Reinhoudt, *Langmuir* **2004**, *20*, 5460-5466.

48. J. Huskens, H. van Bekkum, J. A. Peters, *Comp. Chem.* **1995**, *19*, 409-416.

Summary

This thesis describes the selective attachment of proteins to β-cyclodextrin (βCD) self-assembled monolayers (SAMs), termed molecular printboards through multivalent orthogonal interactions. It is shown that the molecular printboards allow different assembly pathways for the build-up of (complex) bionanostructures. In the assembly of these bionanostructures, control over stability, stoichiometry of binding, and orientation is achieved. A monovalent supramolecular blocking agent can be applied to prevent nonspecific immobilization of proteins to the molecular printboard, while the specific attachment of proteins via multivalent interactions is still possible.

A review of the development of the βCD molecular printboard is given in Chapter 2. It is shown that the stable (reversible) attachment of molecules to the molecular printboard is based on the valency of the interaction. In multivalent binding to βCD molecular printboards, the high effective concentration of βCD at the surface is responsible for the high stability. This allows the patterning and the build-up of 3-dimensional (3D) structures on these molecular printboards. Furthermore, protein and cell attachment to surfaces in general is reviewed. Prerequisites are selectivity, function, stability, and control over orientation. Surfaces consisting of poly(ethylene glycol), as developed by amongst others Whitesides, are discussed as a manner to avoid nonspecific protein immobilization. Control over orientation is possible by making use of bio-engineered His_6-tags in proteins. These proteins can be attached to surfaces which contain Ni-*N*-nitrilotriacetic acid. This is also a method which yields a high coverage of functional protein, in contrast to immobilization methods in which lithography is used.

The stepwise reversible attachment of a noncovalent capsule on the molecular printboard is discussed in Chapter 3. The capsule is based on two calix[4]arenes. The bottom halve of the capsule being a calix[4]arene modified with four adamantyl functionalities at the lower rim to ensure stable positioning at the molecular

printboard, and four guanidinium groups at the upper rim, the top part calix[4]arene modified with four sulfonate groups at the upper rim to ensure binding to the guanidinium groups at the lower halve of the capsule. The association constants (K_a) for capsule formation in solution and at the surface are comparable. The possibility of stepwise adsorption and desorption of the capsule on the molecular printboard is shown using surface plasmon resonance spectroscopy (SPR) experiments.

The attachment of streptavidin (SAv) to the molecular printboard via orthogonal linkers and the hetero-functionalization of surface-confined SAv is shown in Chapter 4. SAv is assembled via orthogonal linkers bearing a biotin moiety on one side and either a single (monovalent) or two (divalent) adamantyl groups on the other. The tetravalent linker-protein complex is much more stable at the surface than the divalent linker-protein complex, as demonstrated in competition experiments. The divalent linker allowed the stepwise adsorption of SAv to the molecular printboard, which is confirmed by SPR and atomic force microscopy (AFM) measurements. The availability of the free biotin-binding pockets in the stepwise immobilized SAv at the printboard is shown by patterning studies in which the divalent ligand is patterned to which SAv is attached. The subsequent attachment of biotin-4-fluorescein showed the availability of the free binding pockets. Cytochrome *c* (cyt *c*) is the first functional protein that is attached to stepwise immobilized SAv. It is proven that the cyt *c* coverage at the molecular printboard is similar to the theoretical coverage.

In Chapter 5, the possibility of antibody (AB) attachment to the molecular printboard via multiple orthogonal binding motifs is described. Patterning studies in which a bionanostructure of SAv, biotinylated protein A (bt-PA), and a fluorescently labeled Fc fragment of a human immunoglobin (IgG-Fc) are built up, show that the assembly process is selective. AB bionanostructures are built on top of the molecular printboard via two different assembly schemes: via a biotinylated immunoglobin and via an Fc receptor protein. Both SPR and AFM measurements confirm the build-up of these bionanostructures. AB-coated surfaces are used as a platform for specific cell attachment. From fluorescence studies it appears that CD3^{+} lymphocytes can be attached to the molecular printboard in a specific manner. Cell attachment appeared to be approximately linear with concentration. For the attachment of proteins inside microchannels, a chip with a large channel splitting up into four smaller, parallel channels is designed. In this chip, a βCD SAM is immobilized in a stepwise fashion.

The four smaller channels can be addressed individually by the stepwise and selective immobilization of the bionanostructures.

The development of a supramolecular method for the inhibition of nonspecific protein interactions to surfaces is shown in Chapter 6. To this purpose an adamantyl-modified hexa(ethylene glycol) guest molecule (AdHEG) has been synthesized. The hexa(ethylene glycol) chain prevents nonspecific protein adsorption, while the adamantyl part ensures specific interaction to the molecular printboard. It is shown that AdHEG is efficient in preventing the nonspecific interactions of SAv, the histidine-tagged maltose binding protein (His$_6$-MBP), and bovine serum albumin (BSA) to the molecular printboard. The concentration of AdHEG functional for the inhibition of nonspecific protein immobilization is about an order of magnitude lower than for the standard protein-repellent poly(ethylene glycol) PEG-surfaces, as developed by, amongst others, Whitesides. Furthermore, AdHEG still allows the specific immobilization of SAv and His$_6$-MBP through the divalent adamantyl-biotin linker and an adamantyl-modified Ni-*N*-nitrilotriacetic acid (Ni-NTA) linker, respectively.

The attachment of His$_6$-tagged proteins to the molecular printboard in a specific fashion is described in Chapter 7. Titration experiments with His$_6$-MBP to the molecular printboard were modeled, and from these modeling studies it could be concluded that the binding of Ad-NiNTA to His$_6$-MBP in solution is to a large extent monovalent. On the surface, however, the majority of the His$_6$-MBP is bound in a trivalent fashion, via three Ad-NTA-Ni linker complexes. This difference is caused by the high effective concentration of βCD at the surface, which induces a high stability of binding in a multivalent fashion, to molecular printboards. The surface enhancement factor for the formation of the trivalent species at the surface is a factor 30 higher than for the divalent species. Patterning of His$_6$-tagged proteins is shown with (His$_6$)$_4$-DsRed-FT. This auto fluorescent protein was patterned on the molecular printboard with a high level of specificity. When (His$_6$)$_4$-DsRed-FT is patterned on the molecular printboard in the absence of Ad-NiNTA, the patterns were not stable upon rinsing. In contrast, the formed patterns were stable when (His$_6$)$_4$-DsRed-FT is premixed with Ad-NiNTA. SPR experiments showed that the nonspecific interactions for the α-(His$_6$)$_{14}$-20S proteasome could be suppressed by about 60%.

This thesis shows that the molecular printboard can be used as a general platform for the attachment of proteins and cells. It is possible to build up complex bionanostructures at the molecular printboard, consisting of multiple orthogonal binding motifs, which resulted in control over thermodynamics, orientation, and functionality. It is shown that, by means of supramolecular chemistry and multivalency, a very effective scheme for the blocking of nonspecific protein immobilization is possible, while maintaining the specific binding via multivalent interactions. These results constitute a starting point for the development of applications for the immobilization of proteins, such as ABs, cells, and the selective immobilization of proteins inside microchannels. The results described in this thesis can be applied in the development of optical and electrochemical biosensors, which may be useful for medical and environmental applications. Another possibility is the development of more complex protein or DNA assays based on the immobilization schemes that have been developed in this thesis.

Samenvatting

Het onderzoek beschreven in dit proefschrift behelst de specifieke hechting van eiwitten op zelf-geassembleerde monolagen (SAMs) van β-cyclodextrine (βCD), door middel van multivalente orthogonale linkers. Er is aangetoond dat het mogelijk is om op deze moleculaire printplaten complexe bionanostructuren op te bouwen. In dit assemblageproces is er controle over de stabiliteit, de stoichiometrie en de oriëntatie van de bionanostructuren. Een monovalente supramoleculaire inhibitor kan gebruikt worden om niet-specifieke eiwit-adsorptie op de moleculaire printplaat te verhinderen, waarbij tegelijkertijd de hechting van eiwitten op een specifieke manier via de gebruikte assemblageschema's met behulp van multivalentie wel mogelijk is.

In Hoofdstuk 2 wordt een literatuuroverzicht gegeven over de ontwikkeling van de moleculaire printplaat. Daar wordt onder meer getoond dat de (reversibele) hechting van moleculen op de moleculaire printplaat gebaseerd is op de valentie van de interactie tussen een molecuul met gast-groepen en het oppervlak. De hoge effectieve concentratie van βCD op de moleculaire printplaat is verantwoordelijk voor de hoge stabiliteit van multivalent gehechte moleculen. Dit maakt het mogelijk om 3-dimensionale (3D) structuren op de SAMs op te bouwen, en om van deze 3D-structuren patronen op deze SAMs te maken. Verder wordt de hechting van eiwitten en cellen op oppervlakken in algemene termen besproken. Belangrijke vereisten zijn onder andere selectiviteit, functie, stabiliteit en controle over de oriëntatie. Eiwit-afstotende oppervlakken, bestaande uit poly(ethyleen glycol) (PEG), zoals ontwikkeld door onder andere Whitesides, worden besproken als een methode om niet-specifieke eiwit-adsorptie tegen te gaan. Controle over de oriëntatie kan bijvoorbeeld worden verkregen door een 6-voudige histidine-keten (His$_6$) te verankeren aan een eiwit door middel van bio-engineering. Deze eiwitten kunnen worden gehecht op oppervlakken welke Ni-N-nitrilotriazijnzuur (Ni-NTA) bevatten. Het is gebleken dat deze methode

in een hoog percentage functioneel gehecht eiwit resulteert, dit in tegenstelling tot methoden waarbij van lithografie gebruik wordt gemaakt.

De stapsgewijze, reversibele hechting van een niet-covalente capsule op een moleculaire printplaat wordt beschreven in Hoofdstuk 3. De capsule bestaat uit twee verschillende calix[4]arenen. De onderste helft van de capsule is een calix[4]areen die aan de onderkant gemodificeerd is met vier adamantyl groepen, en aan de bovenkant met vier guanidinium-groepen. De bovenste helft van de capsule is aan de bovenrand gemodificeerd met vier sulfonaat-groepen, die een interactie kunnen aangaan met de vier guanidinium-groepen op de onderste helft van de capsule. De bindingsconstantes (K_a) van de capsule vorming in oplossing en aan het oppervlak zijn vergelijkbaar. De mogelijkheid om de capsule stapsgewijs te adsorberen op, en te desorberen van het oppervlak is aangetoond met behulp van oppervlakte-plasmonresonantie-spectroscopie (SPR).

De hechting van streptavidine (SAv) op de moleculaire printplaat via orthogonale linker-moleculen en de hetero-functionalisering van gebonden SAv worden besproken in Hoofdstuk 4. SAv kan op het oppervlak gehecht worden via monovalente en divalente orthogonale linker-moleculen. Het tetravalente linker-eiwit-complex is veel stabieler op het oppervlak dan het divalente linker-eiwit-complex, zoals is aangetoond met behulp van competitie-experimenten. De divalente linker maakt de stapsgewijze assemblage van SAv op het oppervlak mogelijk, hetgeen is aangetoond met behulp van SPR en atomaire kracht-microscopie (AFM). De mogelijkheid om de vrije biotine-bindings plaatsen in het stapsgewijs gehechte SAv te gebruiken, is aangetoond met behulp van experimenten waarin de divalente linker in patronen op het oppervlak is aangebracht door middel van microcontact-druk (μCP). Na het stempelen van de divalente linker, is SAv op dit oppervlak vastgezet, waarna biotine-4-fluoresceïne is gehecht op de vrije biotine-bindingsplaatsen. Cytochroom *c* (cyt *c*) is het eerste functionele eiwit waarmee het stapsgewijs gehechte SAv is gefunctionaliseerd. Er is aangetoond dat de experimenteel gevonden bezettingsgraad van cyt *c* vergelijkbaar is met de theoretische bezettingsgraad.

In Hoofdstuk 5 is de hechting van antilichamen op moleculaire printplaten via meerdere orthogonale bindingsmotieven beschreven. Er zijn experimenten beschreven waarin een bionanostructuur bestaande uit SAv, gebiotinyleerd proteïne A en een fluorescent gemerkt Fc-fragment van een menselijk immunoglobine, in patronen op

het oppervlak is opgebouwd. Deze experimenten laten zien dat deze bionanostructuur met een hoge selectiviteit op het oppervlak kan worden opgebouwd. Antilichaamstructuren kunnen via twee verschillende assemblage-routes op de moleculaire printplaat worden opgebouwd: via een gebiotinyleerd immunoglobine en via een Fc-receptor-eiwit. Zowel AFM als SPR hebben de opbouw van de bionanostructuren aangetoond. Moleculaire printplaten kunnen ook als basis worden gebruikt voor specifieke cel-hechting. Uit fluorescentie-experimenten is gebleken dat $CD3^+$-lymfocyten op een specifieke manier op de printplaat kunnen worden vastgezet. De cel-hechting blijkt bij benadering lineair met de concentratie. Een microchip bestaande uit een groot kanaal, dat gesplitst wordt in vier kleinere, parallelle kanalen, is gebruikt voor de hechting van eiwitten in microkanalen. In deze chip kan op stapsgewijze manier een βCD-monolaag worden gemaakt. De vier kleinere kanalen kunnen individueel worden aangestuurd door middel van de stapsgewijze opbouw van de bionanostructuren en de hoge selectiviteit van dit groeiproces.

De ontwikkeling van een supramoleculaire methode voor het tegengaan van niet-specifieke eiwit-adsorptie op oppervlakken wordt geïntroduceerd in Hoofdstuk 6. Voor dit doel is een adamantyl-gemodificeerd hexa(ethyleen glycol)-gastmolecuul (AdHEG) gesynthetiseerd. De hexa(ethyleen glycol)-keten verhindert niet-specifieke eiwit-adsorptie, terwijl de adamantylgroep zorgt voor specifieke binding met het oppervlak. Er wordt aangetoond dat AdHEG effectief is in het voorkomen van niet-specifieke eiwitadsorptie op de βCD-oppervlakken van SAv, het met een histidine-keten gefunctionaliseerde maltose bindings eiwit (His_6-MBP), en met runder-serum-albumine (BSA). De bezettingsgraad van AdHEG om niet-specifieke eiwit-adsorptie te verhinderen is ongeveer een orde van grootte lager dan voor de standaard eiwit-afstotende PEG-oppervlakken, zoals ontwikkeld door Whitesides. Verder is ook aangetoond dat AdHEG de specifieke hechting van SAv en His_6-MBP door middel van de divalente adamantyl-biotine-linker en een adamantyl-gemodificeerde Ni-NTA linker niet in de weg staat.

De hechting van eiwitten met een His_6-keten op βCD-SAMs wordt beschreven in Hoofdstuk 7. Titratie-experimenten van His_6-MBP op het oppervlak zijn uitgevoerd en gemodelleerd. Uit deze studie blijkt dat de binding van Ad-NiNTA aan His_6-MBP in oplossing grotendeels monovalent is. Op het oppervlak is de meerderheid van His_6-MBP echter op trivalente wijze gebonden aan Ad-NiNTA. Dit verschil wordt

veroorzaakt door de hoge effectieve concentratie van βCD aan het oppervlak, hetgeen zorgt voor een grote stabiliteit van multivalente complexen op βCD-monolagen. De toename van de vorming van de trivalente complexen op het oppervlak is een factor 30 hoger dan voor de divalente complexen. Het maken van patronen op een oppervlak is aangetoond met behulp van $(His_6)_4$-DsRed-FT. Dit autofluorescente eiwit kon met een hoge graad van specificiteit in patronen op een oppervlak worden gebracht. Wanneer de patronen werden gemaakt in afwezigheid van Ad-NiNTA, dan konden de patronen worden weggespoeld met water. Daarentegen waren patronen bestaande uit $(His_6)_4$-DsRed-FT in aanwezigheid van Ad-NiNTA wel stabiel. Controle over de oriëntatie van eiwitten met een His_6-keten op de moleculaire printplaat kon worden aangetoond door middel van de hechting van het α-$(His_6)_{14}$-20S proteasoom complex. SPR-experimenten hebben aangetoond dat de niet-specifieke interactie van het α-$(His_6)_{14}$-20S-proteasoom met het βCD-oppervlak met ongeveer 60% kon worden gereduceerd.

Dit proefschrift beschrijft het gebruik van moleculaire printplaten voor de hechting van eiwitten en cellen. Het is mogelijk om complexe bionanostructuren op te bouwen, gebruik makend van meerdere orthogonale interacties, hetgeen resulteert in controle over de thermodynamica, oriëntatie en functionaliteit. Door middel van supramoleculaire chemie en multivalentie is een zeer effectieve methode ontwikkeld om niet-specieke eiwit-adsorptie te voorkomen, terwijl specifieke hechting door middel van multivalente interacties nog steeds mogelijk blijft. Deze resultaten vormen een aanzet tot de ontwikkeling van toepassingen voor de hechting van funtionele eiwitten, zoals antilichamen, en cellen, en de specifieke hechting van eiwitten in microkanalen op βCD-monolagen. De resultaten beschreven in dit proefschrift kunnen worden toegepast in de ontwikkeling van optische en electronische biosensoren, die onder andere medische en milieu-technische toepassingen kunnen hebben. Een andere mogelijkheid is de ontwikkeling van complexere DNA-assays gebaseerd op de assemblageroutes beschreven in dit proefschrift.

Dankwoord

Net als veel promovendi die me zijn voorgegaan, realiseer ik me dat het werk beschreven in dit proefschrift niet alleen tot stand is gekomen door mijn persoonlijke inspanningen. Gedurende de afgelopen vijf jaar, heb ik veel verschillende mensen ontmoet en met een aantal van hen samengewerkt. Ze hebben allemaal gezorgd voor meer begrip omtrent de materie en hebben mijn leven hebben verrijkt. Het gaat te ver om iedereen bij naam te noemen, maar een aantal mensen wil ik in dit dankwoord noemen.

Als eerste wil ik David Reinhoudt bedanken voor de kans die hij me heeft geboden om in zijn groep onderzoek te verrichten. Zeker toen het allemaal wat moeilijker liep, gaf je me alle vertrouwen op een goede afloop, hetgeen ik zeer waardeer.

Dan wil ik graag Jurriaan Huskens, mijn dagelijks begeleider en promotor, bedanken. Je hebt er voor gezorgd dat ik alle rust en ruimte had om mijn onderzoek uit te voeren. De vele ideeën en suggesties die je hebt gegeven zijn zeer waardevol geweest. Bedankt voor je steun en vertrouwen.

The research described in Chapter 3 was performed in cooperation with Francsesca Corbellini and Alart Mulder. Thanks for the help with experiments and the discussions about the work in this chapter. Op het moment dat ik begon te werken aan de projecten waar eiwitten in voor kwamen, was Rolf Vermeij een bron van informatie, Rolf, bedankt voor alle hulp en discussies, ik heb het zeer gewaardeerd. Mária Péter wil ik bedanken voor de AFM experimenten beschreven in Hoofdstuk 4. The cytochrome c experiments, described in Chapter 4, were performed in collaboration with professor Gunther Wittstock and Jatin Sinha from the University of Oldenburg in Germany. Thank you very much for the pleasant collaboration. I also would like to thank Carolina Neunes-Kircher in this respect. Voor de antilichaamexperimenten, beschreven in Hoofdstuk 5 heb ik onder andere samen gewerkt met Aart van Amerongen van de Universiteit Wageningen. Bedankt voor alle

goede tips, en de prettige samenwerking. The cell experiments described in Chapter 5, were performed in collaboration with Xiao Li from the Biophysical engineering group. I would like to thank Wojchiech Bula and Han Gardeniers for the fabrication of the microchips described in Chapter 5. The experiments described in Chapter 6 and 7, were performed in collaboration with the group of prof. Robert Tampé in Frankfurt, Katrin Schulze expressed and purified the 20S proteasome and Alart Mulder the synthesis of the Ad-NTA linker and expressed and purified His_6-MBP.

I would like to thank the "βCD-group", Alart, Olga, Christian, Xing Yi, and Steffen, for the pleasant cooperation and good discussions.

Dan zijn er nog de vaste steunpunten van de SMCT en MnF groep die ik graag zou willen bedanken. Marcel, de ondersteunende werkzaamheden die je uitvoert zijn onmisbaar. Bedankt voor je inzet. Richard, bedankt voor de hulp bij allerhande computerprobleempjes. Carla, Izabel, Marieke en Daniëlle wil ik graag bedanken voor de secretariële ondersteuning.

Ik wil Alart, Rolf en Aldrik graag bedanken voor het zorgvuldige corrigeren van mijn conceptproefschrift.

Jan-Willem en Sabrine wil ik graag bedanken omdat ze naast me zullen staan op 21 september als paranimf.

Dan wil ik mijn familie bedanken voor de interesse die ze in mij en mijn onderzoek hebben getoond.

Mijn ouders hebben me de afgelopen paar jaar steeds gesteund en geholpen daar waar nodig was. Voor mij was het allemaal niet makkelijk, voor jullie waarschijnlijk nog iets moeilijker. Ik hoop dat jullie, net als ik, trots zijn dat ik dit werk tot een goed einde heb weten te brengen. Bedankt!

Lieve Vincent, jij hebt je steeds gerealiseerd hoe belangrijk dit werk voor me was. Meer dan eens heb je je voor me weggecijferd. Je hebt altijd in mij en mijn onderzoek geloofd, met alle ups en downs. Bedankt voor alles.

Manon

Curriculum vitae

Manon Julia Wilhelmina Ludden werd geboren op 29 oktober 1977 te Oldenzaal. In 1995 behaalde zij haar MAVO diploma aan de MAVO "San Salvator", te Denekamp. Na het behalen van haar VWO diploma aan het "Twents Carmellyceum" te Oldenzaal in 1997 is zij scheikunde gaan studeren aan de Universiteit Leiden. In 2002 is zij afgestudeerd onder supervisie van prof. dr. J. Reedijk, dr. J. Haasnoot en dr. M.J.J. Mulder. Haar afstudeerwerk betrof de synthese en karakterisering van moleculaire geleiders gebaseerd op $M(dmit)_2$. Vanaf oktober 2002 verrichte zij promotieonderzoek in de groepen Supramoleculaire Chemie en Technology en Molecular Nanofabrication aan de Universiteit Twente, onder supervisie van prof. dr. ir. J. Huskens en prof. dr. ir. D. N. Reinhoudt. De resultaten van haar promotie onderzoek zijn beschreven in dit proefschrift. Vanaf september 2007 is zij werkzaam als post doc in de Mesoscale Chemical Systems groep onder leiding van prof. dr. J.G.E. Gardeniers, aan de Universiteit Twente.